Faculty of Engineering and Science

Department of Civil and Construction Engineering

Collapse Behaviour of Cold-Formed Steel Structure at Elevated Temperatures

Yong Pei Ming

This thesis is presented for the Degree of
Master of Philosophy (Civil Engineering)
of
Curtin University

September 2018

Declaration

To the best of my knowledge and belief this thesis contains no material previously published by any other person except where due acknowledgment has been made.

This thesis contains no material which has been accepted for the award of any other degree or diploma in any university.

Signature: ………………………….

Date: …08/08/2018……………

Collapse Behaviour of Cold-formed Steel Structure at Elevated Temperatures

Abstract

Cold-formed steel is increasingly used as primary and secondary members in residential and industrial buildings due to the advantages of high strength to weight ratio and ease in installation. With increasing number of cold-formed steel buildings, it is becoming critical to ensure the occupant's safety due to unpredictable fire event. Currently, there is lack of understanding and research on collapse behaviour of cold-formed steel structures in fire. Most of the researches focused on the behaviour of hot-rolled steel portal frames at elevated temperatures. In fire, rapid heating of cold-formed steel members causes loss of strength and stiffness which lead to structural collapse. Therefore, cold-formed steel is usually installed with one or multilayers of fire-rated gypsum as protection. Numerous researches have been carried out to investigate cold-formed steel wall panels via furnace test. However, the furnace test only limited to wall components and prescriptive fire emitted by furnace may not reflect the actual behaviour during in real fire condition. Therefore, this thesis describes a full-scale, non-uniform natural fire test carried out on a cold-formed steel structure with roof truss supported by the studs and framing wall. Finite element modelling to investigates the collapse behaviour of a cold-formed steel structure with and without protection of fire-rated gypsum board is also presented in this thesis.

The cold-formed steel structure tested spans 10m with seven equally spaced frames. The width of the structure is 8m, whereas the eaves height is 2.0 m with roof pitch of 15-degree. The members and connections of the cold-formed steel structure were fabricated from G550 high strength cold-formed steel sections. Fire rated gypsum boards were used to protect the cold-formed steel sections at the southern wall of the structure whereas the northern wall was fully exposed to the fire. Approximately 3.5 tons of timber pallets were used as fire source. The temperatures and side-sway displacements of the cold-formed steel structure were recorded. The structure collapsed with an inwards asymmetrical collapse mechanism at 622.5 ˚C where the collapse is being due to the member buckling rather than failure of the connections. The behaviours of collapse demonstrated by northern and southern walls are different as predicted.

Full-scale fire tests are expensive and time consuming, a finite element (FE) model of cold-formed steel structure was developed as an alternative way to study the thermal and structural performance of the structure. Besides, the material properties of cold-formed steel and gypsum board were determined through laboratory tests for modelling purposes. In the FE model, one of the walls was protected by a layer of fire-rated gypsum board while the other wall was directly exposed to fire. The FE model was validated against the existing full-scale fire test results. The comparison shows that the FEA results were in good correlation with the existing full-scale fire test results. The results presented in this thesis can contribute to practical design guidance for fire safety engineering and also the cold-formed steel industry.

Acknowledgement

First and foremost, I would like to express my gratitude to my supervisor Ir. Professor Dr. Lau Hieng Ho for his invaluable expertise, encouragement, rigorous discussions, questions and helpful guidance throughout the course in this research project. I would also like to acknowledge and thank EcoSteel Sdn. Bhd for technical and financial support in this research.

Many thanks to laboratory technicians who assisted me throughout the project. I wish to thank my fellow friends who helped me throughout this project. Special thanks to Darren Cheong Yaw Kwong, Aim Pei Fong, Daniel Tie, Tan Wei Hong, Chin Mei Chuo, Timothy Ting, Kok Ka Yee, Victor Cai, Yong Hoi Kai and others had made every endeavour to help me in the full-scale fire test. I am also grateful to Mr Kelvin Hew Qi Rong for providing technical support and assisting me in using the finite-element software (ABAQUS).

I would like to express my deep and sincere gratitude to my family, their love gave me strength to accomplish this research.

Table of Contents

List of Figures

List of Tables

Nomenclature

BCA	Building Code of Australia
C	Damping matrix
C_p	Specific heat (constant pressure) per unit mass at a given temperature
$C_{p,ref}$	Aluminium oxide specific heat capacity at a given temperature
CFS	Cold-formed steel
DSC	Differential Scanning Calorimetry
E	Young's modulus
E_{ambient}	Young's modulus at ambient temperature
E_T	Young's modulus at a given temperature
ΔF	Incremental of external applied forces
FE	Finite element
FEA	Finite element analysis
HF_{blank}	Heat flow of the empty crucible at a given temperature
HF_{ref}	Heat flow of reference material aluminium oxide at an instantaneous temperature
HF_{sample}	Heat flow of the gypsum specimen at a given temperature
HRR	Heat Release Rate
f_y	Yield Stress
f_u	Ultimate Stress
G	Distance between end of haunches
h	Coefficient of convection
k	Thermal conductivity
K	Stiffness matrix
L	Span
l	Original length
Δl	Changes of length
M	Mass matrix

n_t	Ramberg-Osgood hardening coefficient
$Mass_{ref}$	Mass of the aluminium oxide
$Mass_{sample}$	Mass of the gypsum specimen
M_c	Plastic moment of resistance of column
M_p	Plastic moment of resistance of rafter
H_R	Horizontal reaction force
q	Heat flux per unit area
r	Heat supplied externally into the body per unit volume
S	Surface area
S	Distance between frame centres
T	Temperature
TGA	Thermogravimetric Analysis
t	Time
u	Displacement
$\dot{u}$	Velocity
$\ddot{u}$	Acceleration
Δu	Displacement at the nodes
U	Internal heat generation rate per unit volume
$\dot{U}$	Material time rate of the internal energy
V	Volume of solid material
V_R	Vertical reaction force
W_f	Load at time of collapse
Y	Vertical height of end of haunch
α	Numerical damping parameter
β	Newmark’s parameter
β	Coefficient value of 0.86 for strain yield strain at a given temperature
γ	Newmark’s parameter
ε	Emissivity
ϵ	Strain
$\epsilon_{nominal}$	Nominal Strain
ϵ_{true}	True Strain
ε_T	Strain at a given temperature
θ	Temperature

θ_s	Sink temperature
λ	Thermal conductivity tensor
ρ	Density
σ	Stefan-Boltzmann constant ($5.67\ \times 10^8$ W/m^2/°C^4)
σ	Stress
σ_{ambient}	Stress at ambient temperature
σ_{nominal}	Nominal stress
σ_{true}	True stress
σ_{yT}	Yield stress at a given temperature
σ_T	Stress at a given temperature

1 Introduction

1.1 Background

Applications of cold-formed steel (CFS) are increasing in residential, industrial, and commercial due to due to the advantages of high strength to weight ratio and ease in installation. Figure 1.1 shows a typical CFS framings used in residential and commercial buildings which comprised of roof trusses with purlins supported by CFS wall framings. CFS wall panels are made of CFS studs, track sections, and wallboards as shown in Figure 1.2. In addition, roof truss is mostly a triangulated system comprised of interconnected CFS sections to support load transferred from purlin and roof sheets. These structural components are usually prefabricated in factory to reduce construction time and labour costs.

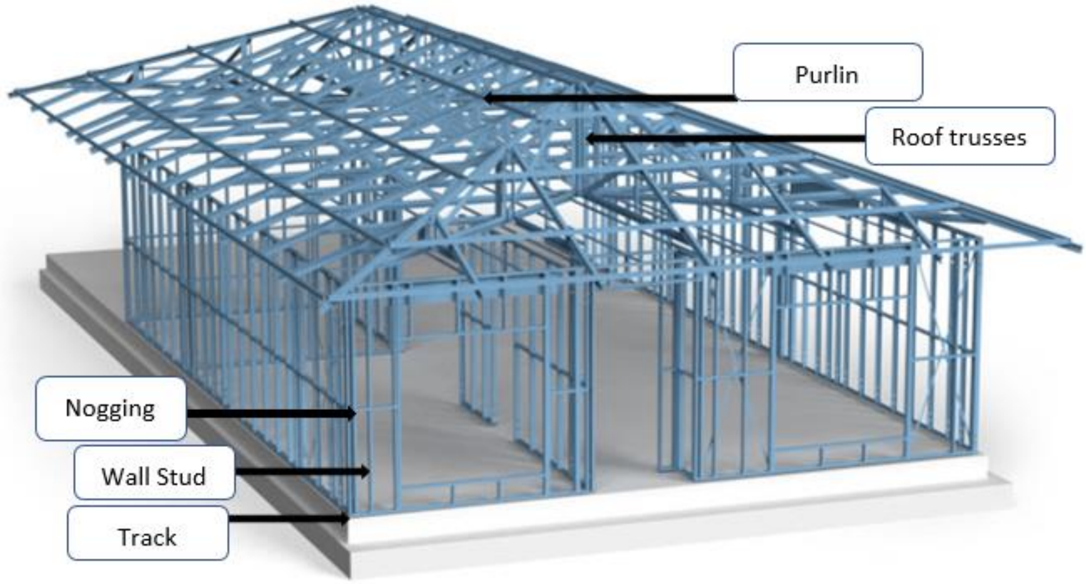

Figure 1.1: Cold-formed Steel Structure ("Supaloc Steel Building System," n.d.)

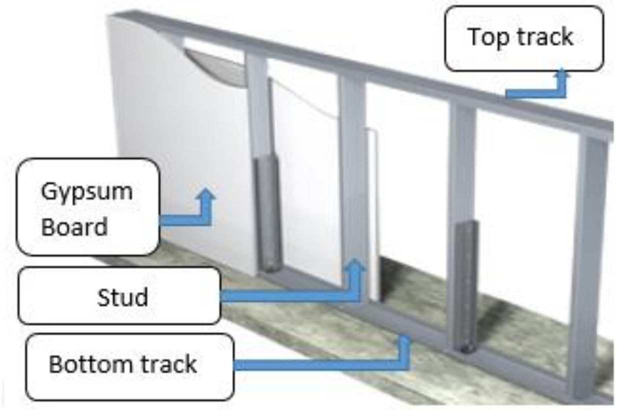

Figure 1.2: CFS Wall framings ("DrywallTrims," n.d.)

1.2 Cold-formed Steel Sections

Cold-formed Steel (CFS) sections are made from thin sheet of steel through different manufacturing process such as cold roll forming, press brake operation, and bending brake operation at room temperature. American Iron and Steel Institute (AISI) and American Institute for Steel Construction (AISC) design specifications defines the CFS members as ‘‘shapes manufactured by press-braking blanks sheared from sheets, cut lengths of coils or plates, or by roll forming cold- or hot-rolled coils or sheets; both forming operations being performed at ambient room temperature, that is, without manifest addition of heat such as would be required from hot forming" (AISI, 2007, Javed *et al.*, 2007). There are various types of CFS sections available in the market today. Cee lipped sections are commonly used to form roof trusses and wall panels in low rise building constructions. Figure 1.3 shows different types of CFS sections.

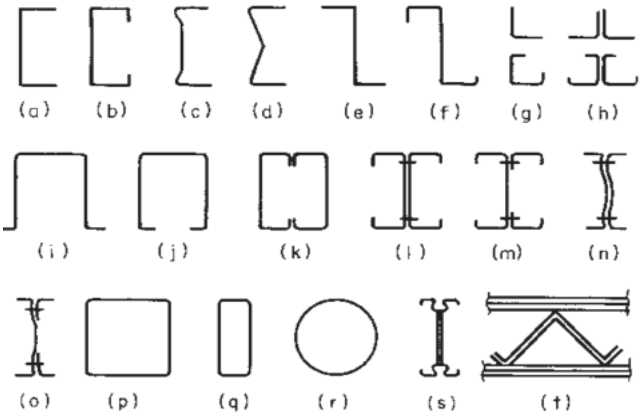

Figure 1.3: Various CFS Sections (Yu and LaBoube, 2010)

1.3 Cold-formed Steel Structure in Fire

Increasing use of CFS framings in residential and commercial buildings, it becomes critical to ensure the occupant's safety due to unpredictable fire event. It is well known that the steel is a high thermal conductivity material. In fire, the rapid heating of CFS sections leads to immediate loss of strength and stiffness, which caused the CFS structure to collapse prematurely. An inappropriate outward collapse of the CFS framings further threaten live of occupants and rescuers during the evacuation. Currently, there is lack of studies and understanding on collapse behaviour of cold-formed steel structures in fire.

To date, most of the research was mainly focused on hot-rolled steel portal frames. A few researchers such as, Rubert and Schaumann (1986), Cooke and Latham (1987) and Wong (2001) carried out full-scale fire test to investigate the collapse behaviour, thermal and structural performance of hot-rolled steel portal frames. The costs of full-scale fire tests are often expensive and time consuming. Alternatively, finite element (FE) models for hot-rolled steel portal frames in fire were developed by numerous researchers (O'Meagher *et al.*, 1992; Simms and Newman., 2002; Bong *et al.,* 2005; Vassart *et al.*, 2004b; Moss *et al.*, 2006; Song, 2008; Rahman, 2012; Sun, 2012; Gentili, 2013; Iqbal, 2016) for a more economical solution. They reported that FE software ABAQUS, VULCAN, SAFIR and ANSYS can model the hot-rolled steel portal frames in fire with good correlation between FE results and full-scale fire tests results.

Currently, only Pyl *et al.* (2012) and Johnston *et al.* (2014) investigated the collapse behaviour, thermal and structural performance of CFS portal frames through a full-scale fire test and FE modelling. However, the research and relevant literature on the behaviour of a cold-formed steel structure with roof truss supported by the studs and framing wall under fire is still limited.

The strength of steel deteriorates over the time in elevated temperature condition. Hence, fire protection materials are widely used to protect the CFS from fire. This is usually achieved by installing a layer or multi-layer of fire-rated gypsum board on CFS wall assembly to delay the temperature rise. Many researchers conducted studies on CFS wall assembly to improve the structural and thermal performance (Alfawakhiri *et al.,* 1999; Ariyanayagam and

Mahendran., 2014a; Chen *et al.*, 2013; Feng *et al.*, 2003a; Gerlich, 1995; Gunalan, 2011; Keerthan and Mahendran, 2012; Kesawan and Mahendran, 2015; Kolarkar and Mahendran, 2012; Park *et al.*, 2011; Rusthi *et al.*, 2015; Shahbazian and Wang, 2013; Zhao *et al.*, 2005). These researches are mainly carried out component testing of cold-formed steel wall panels utilizing a large furnace in laboratory. However, the behaviour of single component test of CFS wall assembly may not reveal the actual behaviour in-service condition at elevated temperatures.

1.4 Aim and Objectives

The aim of this research is to study the collapse behaviour of cold-formed steel structure with roof truss supported by the studs and framing wall assembled with and without fire-rated gypsum board under elevated temperatures.

Finite element modelling was carried out to investigate the collapse behaviour of a cold-formed steel framing structure with and without protection of fire-rated gypsum board.

The objectives of this project are:

1. Carried out a full-scale, non-uniform natural fire test on a cold-formed steel building structure with roof truss supported by the studs and framing wall. In the building, one side of the wall was protected by fire rated gypsum board and, without gypsum board on the opposite side of the wall.

2. Develop a finite element(FE) model to assess the collapse modes, thermal performance, and structural performance of CFS building structure as described in objective 1.

3. Compare the thermal and structural performance of CFS framing structure under elevated temperatures of the finite element model results with the full-scale non-uniform natural fire test results.

1.5 Scope of Work

1. The scope of work for this research covers constructing a cold-formed steel structure with overall dimension of 8 m × 10 m × 3.58 m for fire test. This includes a foundation, cold-formed steel wall framings assembled with and without fire-rated gypsum boards and roof trusses.

2. To carry out laboratory material properties tests for cold-formed steel and gypsum board to acquire material properties for finite element modelling. These tests include: Tensile coupon tests for cold-formed steel; furnace tests, Thermogravimetric analysis (TGA) and Differential Scanning Calorimetry (DSC) for gypsum board.

3. To develop a finite element model using ABAQUS version 6.14 software to model the collapse behaviour of a cold-formed steel structure with roof truss supported by the studs and framing wall assembled with and without fire-rated gypsum boards under fire condition.

1.6 Thesis Outlines

The outline of this thesis as follows:

Chapter 1 presents the introduction and background for this research of cold-formed steel structure under fire and also description of research problems to form the research statements, aims and objectives for this research.

Chapter 2 reviews the up to date literatures on collapse behaviour of hot-rolled steel portal frame structures and cold-formed steel structures. This chapter identifies the research gaps from the literatures to justify the aims and objectives of this research.

Chapter 3 illustrates the methodology used for the full-scale, non-uniform natural fire test carried out on a cold-formed steel structure with roof truss supported by the studs and framing wall assembled with and without fire-rated gypsum boards. The specification of CFS framings, details of instrumentation and testing method are described in this chapter.

Chapter 4 describes the experiment methodology including details of tensile coupon tests on CFS sections at ambient temperature; details of gypsum board furnace tests; thermogravimetry analysis (TGA) and Differential Scanning Calorimetry (DSC) tests to determine thermal properties of a fire-rated gypsum board.

Chapter 5 presents the development of FE model of CFS structure under elevated temperatures using ABAQUS version 6.14 software. The validation of material properties for gypsum board are presented. The modelling method described including geometrical modelling, input of CFS material properties, thermal properties, and mesh studies.

Chapter 6 explains and discuss the results of the full-scale fire test and also the FE results. The results of full-scale fire test and FE model were described in terms of the collapse mode, thermal performance, and structural performance. Details of the results including the critical temperatures, side-sway deflection against time are presented and discussed. Verification and discussion of FE results with full-scale fire test results are also presented in this chapter.

Chapter 7 concludes the significant findings of this research and the recommendations were made for further research.

2 Literature Review

2.1 Introduction

This chapter reviews the literatures review related to this research. This chapter consists of two parts. Firstly, literature review on the collapse behaviour for steel portal frames and cold-formed steel structure at elevated temperatures. Secondly, literature review on material properties of cold-formed steel and fire rated gypsum board at elevated temperatures.

2.2 Natural Fire

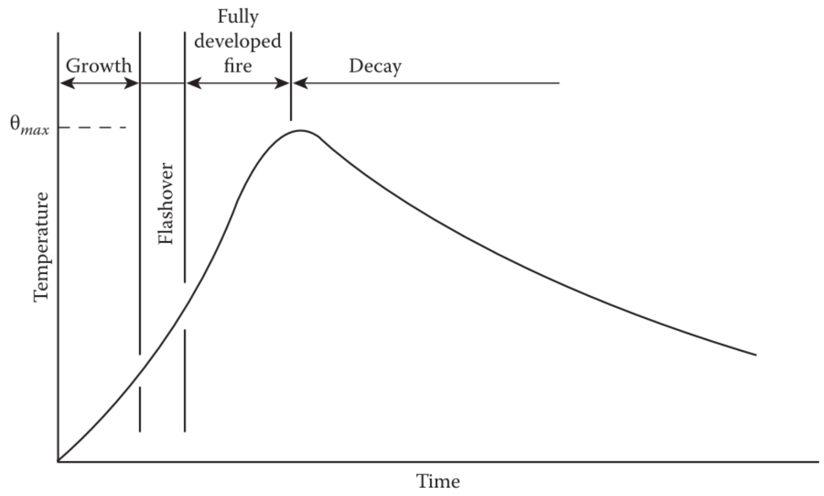

Figure 2.1: Temperature against Time Profile of a Natural Fire Development (Purkiss and Li, 2013)

Natural fire can be created in any compartment by ignition sources such as electrical sparks and cigarettes. The development of natural fire in a compartment is described by Purkiss and Li (2013) where the temperature against time curve is shown in Figure 2.1. The development of natural fire is sub-divided into three stages namely, fire growth, fully developed fire and decay of fire. The fire growth stage usually initiated with ignition of fire and smokes are released from the combustible materials. The temperature in the compartment rises as the fire continues to develop with sufficient air ventilation. Thereafter, flashover is the phenomenon of fire spreads spontaneously within the compartment due to a layer of hot gases accumulated around the ceiling approximately at 600 ˚C (Buchanan, 2001). The flashover leads to an increase in burning rate and progress to a fully developed fire in the compartment. The collapse of a steel structure is very likely in a fully developed fire. Eventually, the decay stage of natural fire is resulted by the decrease of the rate of fuel combustion.

2.3 Standard Fire

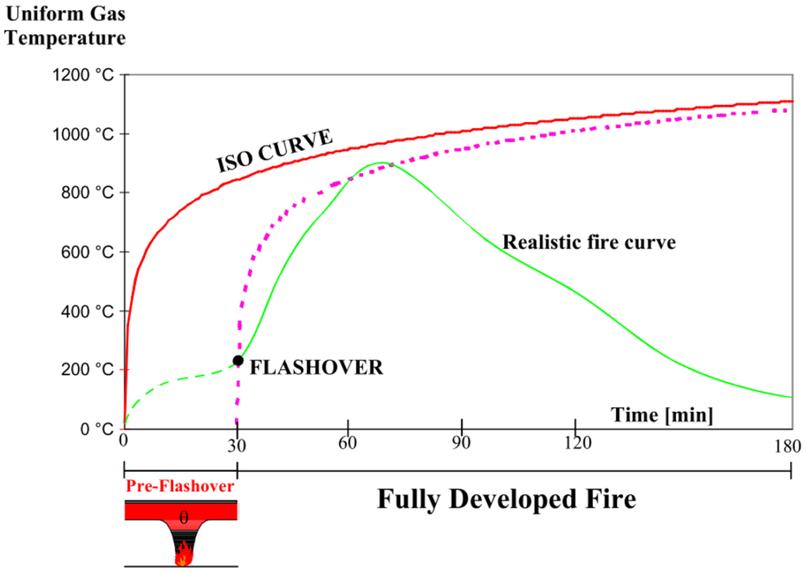

Figure 2.2: ISO Fire Curve and Natural Fire (Vassart *et al*., 2014)

The assessment of fire-resistant rating of structural elements is commonly tested by furnace in according to standard fire ISO 834 (ISO, 1999). The standard fire curve was originated from wood burning furnace and the fire curve was amended to provide rapid rise in temperature at first ten minutes (Nyman, 2002). The ISO 834 (ISO, 1999) fire curve is expressed in Eq. 2-1.

$$T_g = 345 \log_{10}(8t_{min} + 1) + T_0 \qquad \text{Eq. 2-1}$$

Where, T_g is the gas temperature, t_{min} is the time in minutes and, T_0 is the room temperature.

However, the test specimen is often limited by the size of furnace. In case of fire test for large structure, it is uneconomical to build a large furnace. Furthermore, the prescriptive nature of ISO 834 (ISO, 1999) curve only assumes exponential heating and neglected effects of building size, ventilations, decay period and flash-over period. Figure 2.2 shows the comparison of standard fire curve and real fire curve.

The modern buildings are increasingly occupied by synthetic materials. For example, fabric sofa, plastic chairs and tables. In accidental fire, these synthetic materials increase the heat release rate (HRR) in the building compartment. As a result, the fire severity increases and therefore, the realistic fire may be severe than standard fire ISO 834 (ISO, 1999).

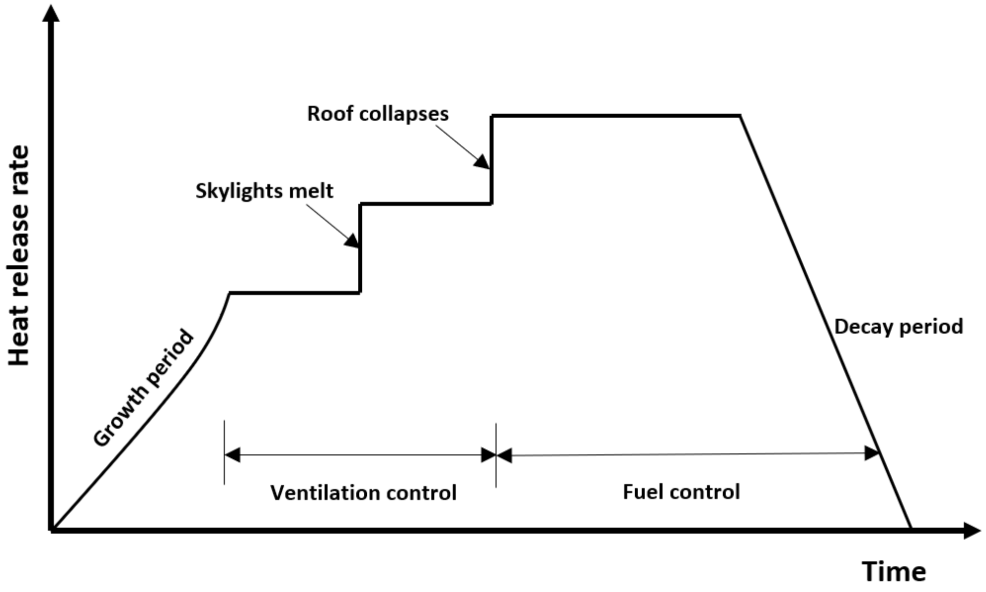

Figure 2.3: Heat Release Rate for a Fire in an Industrial Building (Buchanan, 2001)

Buchanan (2001) described the uncontrolled fire in single storey industrial building using HRR and time relationship as shown in Figure 2.3. In initial stage, the ventilations including door, window and small openings are limiting the heat release rate of fire. In ventilation control phase, Buchanan explained the rate of combustion is limited by the volume of cold air that can enter and the volume of hot gases that can leave the compartment. The increase in HRR is due to additional ventilations that allow the outside air mix with hot unburned gaseous fuel when roof collapses. After that, the fuel control phase is dependent on the available energy remains in the combustible items. Finally, the decay period shows the HRR decreases when the energy of combustible items is depleting in the building.

2.4 Design Guidelines

Fire protection is commonly used to protect steel structure from fire. However, it is uneconomical to apply fire protection to the entire structure. To remit this problem, Simms and Newman (2002) recommended the hot-rolled steel roof structure to be left unprotected and, they assumed a symmetrical inward collapse mechanism will take place. A set of empirical formula also proposed by Simms and Newman to estimate the overturning moment of steel columns as shown in Eq. 2-2 to Eq. 2-5. Their guideline can allow engineers to design the column base to resist the overturning of the steel columns under fire. The steel structure referred by Simms and Newman are double pitched steel portal frame and truss framed roof as shown in Figure 2.4 and Figure 2.5 respectively. Nevertheless, the design recommendation only limited to steel portal frames only and, there is lack of guidelines on the collapse of the cold-formed steel structure. The availability of fire tests results, and finite element model results are also limited. Therefore, this research developed a finite element model of cold-formed steel structure based on validated full-scale fire test results.

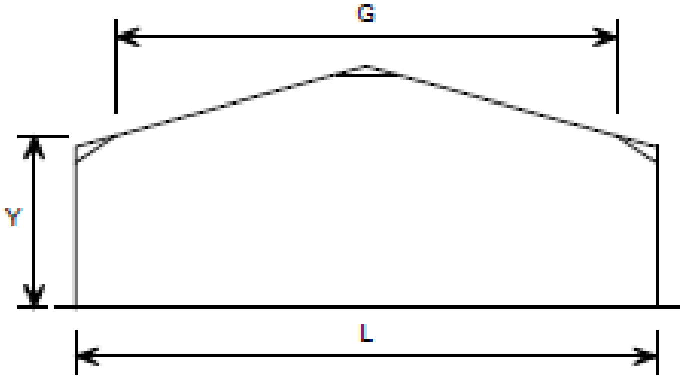

Figure 2.4: Steel Portal Frame (Simms and Newman, 2002)

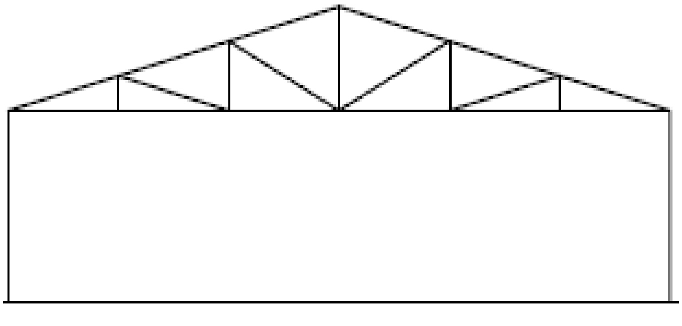

Figure 2.5: Truss Framed Roof (Simms and Newman, 2002)

Vertical reaction $V_R = 0.5\ W_f SL$ + dead weight of wall Eq. 2-2

Horizontal reaction $H_R = K[\ (W_f\ SGA - \frac{CMp}{G}) \ > \ \frac{Mc}{10}\ ]$ Eq. 2-3

Over turning moment $= K[\ (W_f\ SGA\ (A+ \frac{B}{Y}) \ - M_p\,(\frac{CY}{G} - 0.065) \ > \ \frac{Mc}{10}\ )]$ Eq. 2-4

$B=\frac{L^2-G^2}{8G}$ Eq. 2-5

Where,

W_f = load at time of collapse

S = distance between frame centers

G = distance between end of haunches

Y = vertical height of end of haunch

L = span

M_p =plastic moment of resistance of rafter

M_c = plastic moment of resistance of column

K = 1 for single bay frames or adopted from SCI publication 087 Newman (1990)

A and C are frame geometry parameters (Simms and Newman, 2002, pp. 10)

Furthermore, Eurocode 3 part 1.2 (CEN, 2005) provided a structural fire design guideline for cold-formed steel members as class 4 cross-section. The design of cold-formed steel section under elevated temperature was based on critical temperature of 350 ˚C. The critical temperature is defined as the temperature at which failure is expected to occur in a structural steel member given a uniform temperature distribution and load level (Xiong *et al.*, 2017, p.1). Numerous researchers (Zhao *et al.*, 2005; Gunalan and Mahendran, 2014; Kankanamge and Mahendran, 2011; Cheng, 2015) where standard fire ISO-834 (ISO, 1999) was adopted in their experimental tests and finite element models. From their tests results, it is revealed that the design of cold-formed steel section using critical temperature of 350 ˚C is over conservative. Zhao *et al.* (2005) claimed a very slender cold-formed steel member could have a critical temperature exceeding 400 ˚C under a high load.

Nevertheless, these investigations are limited to component furnace testing in the laboratory by applying standard fire ISO-834 (ISO, 1999). This is because: (1) The fire tests on component are limited in capturing the realistic interactions. Abreu *et al.* (2014) and Javed *et al*. (2017) reviewed the current research on cold-formed steel including beam, columns and wall component. However, most of the research are focused on the testing of wall component and isolated member in laboratory. They recommended more research are required to investigate the cold-formed steel structures in real fire such as carrying out a full-scale fire test. (2) The standard fire ISO-834 (ISO, 1999) used in laboratory furnace test did not represent the behaviour of real fire due to absence of compartment ventilation, type of combustible and pre-flashover fire considerations. All these shortcomings of standard fire ISO-834 were addressed by Grosshandler (2007) as cited by Abreu *et al*. (2014).

To overcome these shortcomings, Park *et al.* (2011) used a realistic fire to test a compartment that consisted of cold-formed steel wall framings protected with two layers of gypsum boards. The realistic fire was created from burning of timber cribs and sofa (polyurethane foam supplemented with wood). Hydraulic jacks loaded the cold-formed steel wall framings to simulate imposed loads. The results show the maximum temperature recorded in the wall framings exceeded results by the standard fire ASTM E119 (ASTM, 1988) which is similar to ISO-834 fire (ISO, 1999) curve. This shows that the use of standard fire might be under conservative. They reported the cold-formed steel wall framings protected by two layers of gypsum board survived the test. However, the structural failure of cold-formed steel was not fully understood. Therefore, this research carried out a full-scale fire test utilizing real fire to investigate the collapse behaviour cold-formed steel structure with roof truss and wall framing. The structural performance of wall framings with and without the protection of a layer of gypsum board were also investigated.

Pyl *et al*. (2012) carried out a full-scale test using a real fire on cold-formed steel portal frames. They concluded that the cold-formed steel portal frames collapsed at a critical temperature of 750 ˚C. Pyl's results revealed the design of cold-formed steel section using critical temperature of 350 ˚C is over-conservative. Johnston *et al*. (2014) also reported a collapse temperature of 714 ˚C based on the result of a full-scale fire test on cold-formed steel portal frames using real fire. However, it is found that the critical temperature and structural behaviour of cold-formed steel wall structure with roof truss and wall framing is not studied extensively. Therefore, this research carried out a full-scale fire test adopting real fire to investigate the collapse behaviour and the collapse temperature of cold-formed steel structure with roof truss and wall framing.

2.5 Fire Tests of Hot-Rolled Steel Portal Frames

The research on collapse behaviour of cold-formed steel portal frames in fire follow the conventional hot-rolled steel portal frames.

Bisby *et al*. (2013) reviewed most of the notable full-scale non-standard structural tests around the world such as BRE Caridington Steel Building Tests (Steel, 1999), FRACOF Fire Test (Vassart and Zhao, 2011), and Harbin Institute of Technology Tests (Dong and Prasad, 2009). Most of these buildings tested in a real fire are composite steel structure that comprised of steel frames and composite slab. However, there are limited numbers of full-scale fire test conducted on steel portal frames and cold-formed steel structures. Kodur *et al.* (2012) noted only a small number of tests carried out on steel portal frames in the 1980's and 90's. Only Rubert and Schaumann (1986) and Cooke and Latham (1987) carried out full scale test on steel frame with zero pitch in real fire. For the case of double pitched portal frame, a few researchers like O'Meagher *et al*. (1992), Wong (2001) and, Santiago *et al.* (2008) conducted experimental investigation on steel portal frames in a real fire.

Cooke and Latham (1987) conducted a full-scale fire test to assess structural performance of a single steel frame under elevated temperatures at Fire Research Station Cardington Laboratory. The aim of the research was to generate data to aid in preparation of design guidelines which will able to assist engineers to design steel frames under fire condition. Their research also improved the understanding of fire and structural performance of steel portal frames under a real fire condition as the BS476 (BS 476, 1972): Part 8 standard fire test method did not consider fire growth and decay. In other words, the structural response of steel frame is more realistic by adopting real fire test in field compared to furnace test in laboratory.

The steel frame tested by Cooke and Latham (1987) is comprised of two unprotected columns having 3.53 m length of 203 mm × 203mm × 52 kg/m (9.2/12.5 mm) section pinned on the ground and joined by one unprotected beam having 4.55 m length of 406 × 178 mm × 54 kg/m (7.6/10.9 mm) section. Both beam and columns were made of BS 4360 (BS 4360, 1986) Grade 43A. Bracing was applied in-plane direction of the frame to provide stability. 1.32 tonne of timber cribs were used as burning agent to produce fire load of 25 kg/m^2 and ventilated with one-eighth area of two walls in compartment to ensure the steel to attain critical temperature of 630 ˚C. The frame was loaded with constant load of 552 kN compression axial force at the column and 39.6 kN at four different position for the beam to represent dead load. Thermocouples were used to attached on to the steel surface to measure the temperature profile. Linear displacement transducers were applied to measure the vertical and side displacement of beam and column respectively. The thermocouples and linear displacement transducers were connected to computer-controlled data acquisition system. They concluded the maximum temperature recorded on the hot flange was 775 ˚C and a maximum compartment temperature of 830 ˚C.

Later, CONSTRADO (1979) investigated the collapse behaviour of double pitched steel portal frame in fire. They described when the steel portal frame is exposed to fire, the heated frame expanded and moved outwards in initial stage. The increasing thermal expansion contributed extra moment in the rafters and, yield strength continuously deteriorated by elevated temperatures. Consequently, this caused the plastic hinges to form at the maximum moment position on rafters also, at the ends of the haunches and near to the apex. The plastic hinge in this context is referred as “fire hinges”. The collapse of the pitched roof was subjected by formation of two or three fire hinges to complete the collapse mechanism.

As the roof apex has deformed below eaves level, the rafter is in catenary due to loss of stiffness. Figure 2.6 shows the rafter is in catenary which is analogous to a curve of a hanging chain under gravitational force. In this instance, the tension force and gravitational force exerted on the rafters induced an overturning moment on columns which may lead to collapse of entire frame.

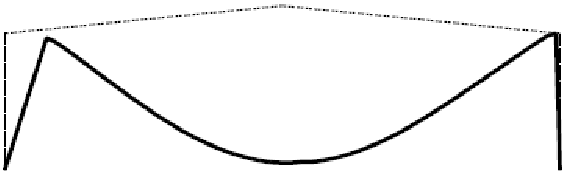

Figure 2.6: Inward Collapse (O’Meagher *et al.*, 1992)

Figure 2.7: Outward Collapse (O’Meagher *et al.*, 1992)

O’Meagher *et al.* (1992) carried out an investigation on the collapse behaviour of steel portal frames at elevated temperatures through two-dimensional (2D) finite element analysis

(FEA) using ABAQUS software. The research was intended to provide improvements to the Building Code of Australia (BCA). In FEA, the author investigated the effect of haunches, effects of column fire protection, different heating scenario and lateral restrains on the roof. They emphasized on the collapse modes of steel portal frame includes inward and outward collapse as shown in Figure 2.6 and Figure 2.7, respectively. O’Meagher concluded the collapse behaviour of steel portal frame was governed by a symmetrical collapse. This is because undesired outward collapse induced by fire may harm the adjacent buildings, fire fighters and exit for occupants. However, the collapse behaviour of cold-formed steel portal frame might be different to conventional steel portal frame due to thin walled nature of cold-formed steel. Therefore, this research is carried out to investigate the collapse behaviour of cold-formed steel structure.

Wong (2001) carried out full-scale field tests on steel portal frames made of 127 mm × 76 mm × 13 mm, Grade 43 steel. Overall dimension of the steel structure is 6 m in span, 7.5 m in length with four portal frames spaced evenly, 2 m in height (to eave) and 15 ^{o} roof pitch. A dead load of 2.16 kN/m was applied on the roof to ensure collapse of the steel portal frames. The steel temperatures and displacements were measured using thermocouple type K and position sensors respectively. Natural fire was created from the burning of liquid heptane and timber cribs.

In Wong’s first and second full-scale field tests, no collapse was observed. For the third test, a combined collapse mechanism was observed. Wong described that the rafter was deflected outward initially due to thermal expansion, until the roof collapse in snap-through buckling of the rafter. Formation of fire hinges or plastic hinge caused by the snap-through effect due to the degradation of steel’s material properties as shown in Figure 2.8. Wong also found that the steel portal frame collapsed asymmetrically within 8 minutes 20 seconds and maximum steel temperature of 1040 ˚C. Wong’s results revealed the steel portal frame did not always collapsed symmetrically as assumed by Simms and Newman (2002). Nonetheless, the collapse mode of cold-formed steel framing remains unclear due to limited research in the literature. Hence, this research addressed the concerns on the collapse behaviour of cold-formed steel structure.

Figure 2.8: Asymmetrical Collapse (Wong, 2001)

Whereas, Lou *et al.* (2018) performed a full-scale fire test on 36 m × 12 m steel portal frames exposed to natural fire. The steel portal frame height is 6.6 m to apex and 5.4 m to knee joint level. A 4 m × 6 m fire compartment storing 8 m^3 of wooden cribs located was built as shown in Figure 2.9 and Figure 2.10. A total of 0.6 kN/m^2 live load was imposed on the roof using 30 sand bags hung on each 18 m span rafter. Fire was set in the fire compartment as shown in Figure 2.10. The frames collapsed in-plane symmetrically after 15 minutes of fire exposure and, a maximum temperature of 1100 ˚C was recorded on the column. An out of plane movement of the end frame column was observed. Figure 2.10 shows the structural collapse at 15 minutes.

Figure 2.9: Before Test (Lou *et al.*, 2018)

Figure 2.10: Test at 15 Minutes (Lou *et al.*, 2018)

2.6 Fire Tests of Cold-formed Steel Portal Frames

There are only a few test data of cold-formed steel building structures. Currently, only Pyl *et al*. (2012) and Johnston *et al*. (2014) conducted full scale fire test on cold-formed steel frames. Pyl *et al*. (2012) conducted a full-scale field test to investigate the collapse behaviour of cold-formed steel portal frames under a natural fire. The structure tested was specifically for application in industry. The cold-formed steel structure is 8 m in span, height-to-eaves of 2.5 m with a roof pitch of 10^o. The building length was 20 m, including five frames with frame spacing of 5 m and constructed using cold formed steel sigma section made of steel grade 350 MPa. Approximately 6 tons of timber cribs with net caloric value of 14 MJ/kg were used as source of burning. Fire load density of 625 MJ/m^2 is in accordance to fire regulation for industrial buildings in Belgium. Twenty-two thermocouple type K were placed at apex, rafter, purlins, wind bracings and wall bracings. Linear variable differential transducer (LVDT) were utilized to record the vertical deflection of the rafter for the central frame. At the end of the test, temperature against time graph and displacement time graph were plotted. They also concluded that the portal frames collapsed inward symmetrically at 750 ˚C by 62 minutes. Figure 2.11 shows the cold-formed steel portal frames during and after the fire test. It is found that severe buckling occurred at the mid-height of the cold-formed steel column.

Figure 2.11: During Fire Test and After Fire Test (Pyl *et al.*, 2012)

Johnston *et al.* (2015) portal frame is spanning 8 m, 2.2 m height-to-eaves with a roof pitch of 10˚. The total structure length was 10 m, comprising five evenly spaced frames. These frames were assembled entirely with back to back C lipped channel sections. The steel grade is 550 MPa. The steel temperatures and side sway displacements of the columns were measured using eight thermocouple type K and two laser range meters, respectively. Johnson concluded that the cold-formed steel portal frame collapsed asymmetrically at 714 ˚C. The collapse of the structure was due to the buckling of the knee joint.

The collapse behaviour cold-formed steel portal frames have been investigated experimentally by Pyl *et al*. (2012) and Johnston *et al*. (2014). However, the collapse behaviour of cold-formed steel structure with roof truss and wall framing is remained unclear. This is because the cold-formed steel wall framings are increasing used in the industry and attention must be paid to the structural performance of cold-formed steel wall framings under fire. Therefore, this research investigates the thermal and structural performance of cold-formed steel structure which comprised of roof trusses and wall framings.

2.7 Numerical Modelling of the Collapse of Hot-Rolled and Cold-formed Steel Structures

Carrying out full-scale test on steel structures are expensive and time consuming. Therefore, many researchers (Simms and Newman, 2002; Bong, 2005; Vassart *et al.*, 2004a; Moss *et al.*, 2006; Song, 2008; Rahman *et al.*, 2009; Sun, 2012; Gentili, 2013; Iqbal, 2016) used finite element (FE) software to model and study the collapse behavior of hot-rolled steel structures together with full-scale fire test results.

The full-scale fire tests conducted by Wong (2001) were investigated numerically using finite element software, VULCAN developed at University of Sheffield. Wong compared the 2-Dimensional and 3-Dimensional FE model and reported 3-Dimensional FE model is more realistic compared to 2-Dimensional FE model. Figure 2.12 illustrates the 3-Dimensional FE steel portal frame model before and after FE analysis. Secondary members such as purlins are modelled. The failures of the steel portal frame are captured in the FE analysis was the formation of plastic hinges near the apex and the eave joints. At the apex, the failure temperature in FE was approximately 775 ˚C whereas the full-scale fire test shows apex failure temperature approximately at 1040 ˚C. Wong reported the FE analysis was terminated after the formation of plastic hinge. It is found that the general static analyser is unable to further model and analyse the collapse of the structure when the structural instability occurred.

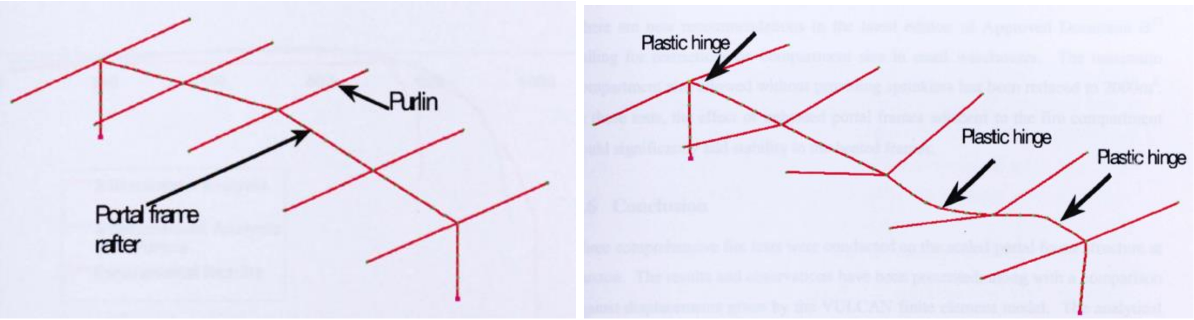

Figure 2.12: Before and After Analysis of FE Model for Steel Portal Frame (Wong, 2001)

The issues of un-convergence in general static analysis for the full collapse behaviour of steel structures are identified and discussed by Bong (2005), Vassart *et al.* (2007), Sun (2012) and Song (2008). To overcome the numerical difficulties and to enable a convergence in collapse modelling of a structure, they suggested a dynamic approach for FE model. This is because the dynamic approach can handle the numerical instability.

In addition, the real behaviour of portal frames in fire are non-linear in terms of geometry, material and, the fire is also non-linear. Considering these factors in finite element program, time integration operators are required to solve the dynamic equilibrium equations incrementally through time. The integration operators are defined as the implicit dynamic method or the explicit dynamic method. Wang *et al*. (2012) described the explicit dynamic analyses use the known(explicit) state of a numerical model at the end of one incremental time step to calculate its state at the next time step. Whereas the implicit dynamic analyses solve the dynamic equilibrium equations by direct integration in an iterative manner to estimate the solution at the next time step. Furthermore, Rahman (2012) investigated and compared the efficiency of implicit and explicit dynamic method used in the ABAQUS software. The aim was to provide computational techniques and solutions for studying the possible behaviour of different hot rolled steel portal frames. The FE model of Song (2008) tested by Wong (2001). The results of FEA for both implicit and explicit dynamic were compared and correlated well with the FEA results of Song (2008). Rahman concluded the implicit dynamic method is more accurate and significantly more computationally efficient and viable than the explicit dynamic method when modelling the collapse of steel portal frame in fire. Johnston *et al*. (2015) also used the implicit dynamic method in the FE model for cold-formed steel portal frame and they reported a good correlation between the FE results and full-scale fire test results. Therefore, implicit dynamic method is adopted in the FE modelling for this research.

De Souza Junior *et al.* (2002) conducted computational simulation using SAFIR software (Franssen, 2005) to study single storey industrial building in elevated temperature. The sizes of the portal frame are 20 m wide, 46 m long and 8 m height from ground to apex as shown in Figure 2.13. Two-dimensional (2D) and three-dimensional(3D) model were modelled respectively. The modelling is taken account of purlin and it is very susceptible to fire effect. Figure 2.14 shows the purlins and side rails in the FE model. They concluded that the 2D modelling is unrealistic because the lateral instability of members of portal frames is not measurable. This is due to the effect of purlin preventing out of plane instability of portal frame. Therefore, the FE model in this research used 3D model to consider the effect of the lateral member such as purlins and side rails.

For the numerical studies of cold-formed steel, numerous studies have been undertaken on beam models (Kankanamge and Mahendran, 2008; Laím *et al*., 2013; Cheng, 2015; Martins *et al.*, 2015; Landesmann and Camotim, 2016). Whereas, the research of CFS studs and columns were also carried out by Feng (2003b), Ranawaka (2006), Chen and Young (2007) and, Gunalan (2011). It is found that the numerical studies on the collapse behaviour of cold-formed steel building structure is scarce.

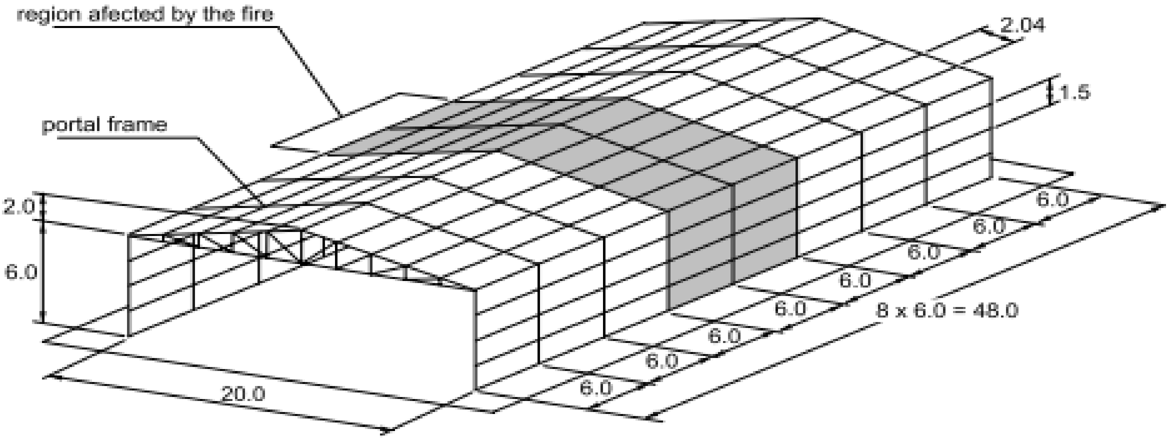

Figure 2.13: **Steel Portal Frames Dimensions (De Souza Juniour *et al.*, 2002)**

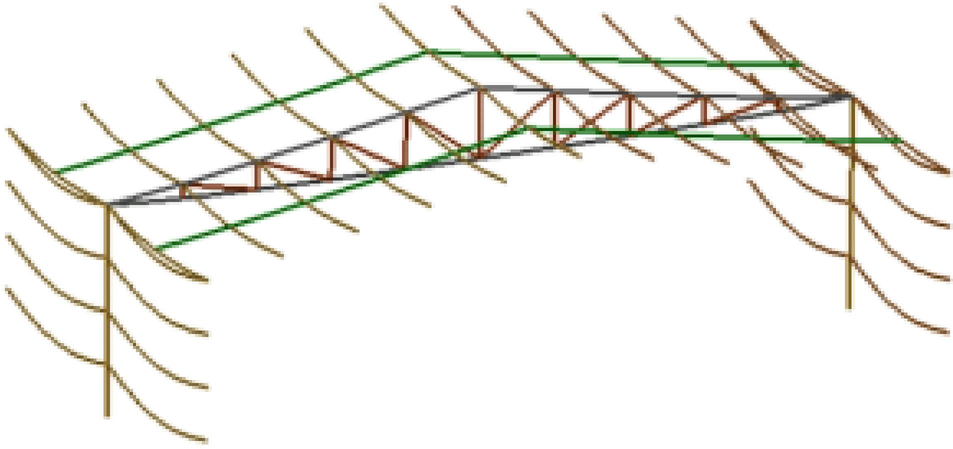

Figure 2.14: **Catenary Action of Secondary Members (De Souza Juniour et al., 2002)**

Later, the full-scale fire test of cold-formed steel portal frames conducted by Pyl *et al.* (2012) were predicted using finite element program, SAFIR (Franssen, 2005). The cold-formed steel members were modelled using beam elements. Johnston *et al.* (2015) further clarified the use of shell elements instead of beam elements in order to capture the effects of plate buckling. The 3-D FE model developed by Pyl *et al.* (2012) consisted of five evenly spaced portal frame and the secondary members are modelled. Pyl's FE results shows the collapse of the 3D FE model occurred about 688 ˚C within 54 minutes. The FE results close to the full-scale test results where the cold-formed steel portal frame collapsed at 750 ˚C around 66 minutes and 40 seconds. Figure 2.15 shows the collapse of cold-formed steel portal frames in 3D FE model and the full-scale fire test.

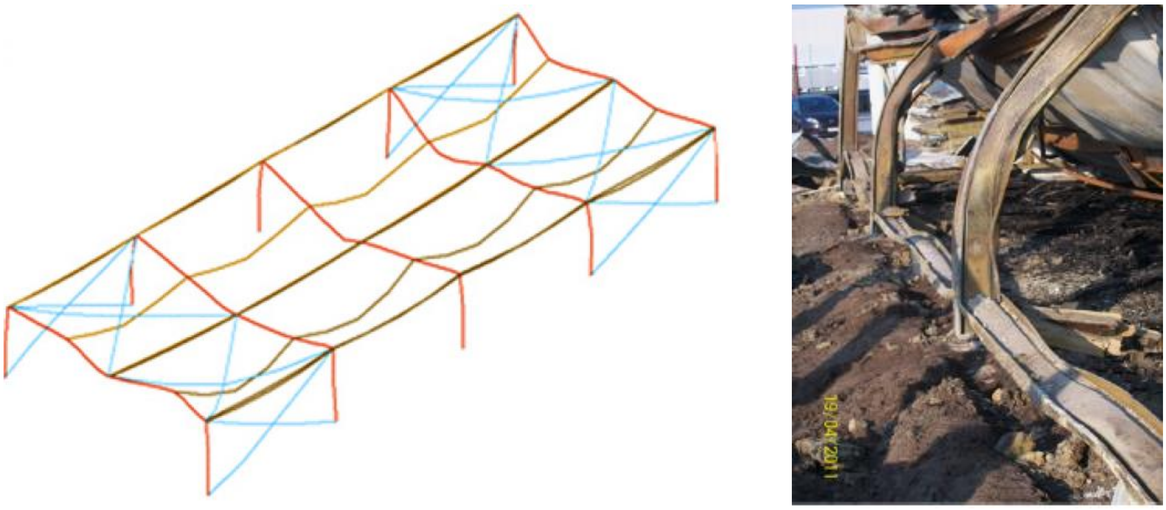

Figure 2.15: Comparison of FE Model and Full-Scale Fire Test (Pyl *et al.*, 2012)

Johnston *et al*. (2015) investigated the collapse behaviour cold-formed steel portal using a non-linear elasto-plastic finite-element shell model. The FE model was developed using ABAQUS finite element software to simulate and validate the FE model results against their existing full-scale test results. They adopted material model of cold-formed steel at elevate temperatures from Ranawaka and Mahendran (2009). The FE model was discretised by shell element S4R which accounts for finite membrane strains and arbitrarily large rotations. Since the element S4R accounted for large strain analyses, the authors included the non-linear geometrical (NLGEOM) in the FE model.

In the finite element analysis, static general solver was used in first step to simulate the permanent loading and, the second step used the implicit dynamic solver to simulate the collapse of cold-formed steel FE model. In addition, quasi-static application was used to handle the temporary instability of the structural collapse. Figure 2.16 shows the local failure of knee joint in FE model and full-scale fire test. They reported their FE model predicted collapse temperature of 682 ˚C at a time of 15 minutes and 53 seconds. The FE results agree well with full-scale test collapse temperature of 714 ˚C at a time of 15 minutes and 53 seconds.

The finite-element model of cold-formed steel portal frames have been developed and investigated by Pyl *et al.* (2012) and Johnston *et al*. (2015). Nevertheless, there is limited FE model of cold-formed steel structure with roof truss and wall framing. Therefore, this research developed a FE model of cold-formed steel structure consisted of wall framing with and without gypsum board and, roof truss. Shell element S4R with geometrical non-linearity was applied in the FE model however, convergence study was carried out to determine the optimum mesh size. The implicit dynamic solver with quasi-static application also adopted in ABAQUS FE model to capture snap-through buckling effect of cold-formed steel members.

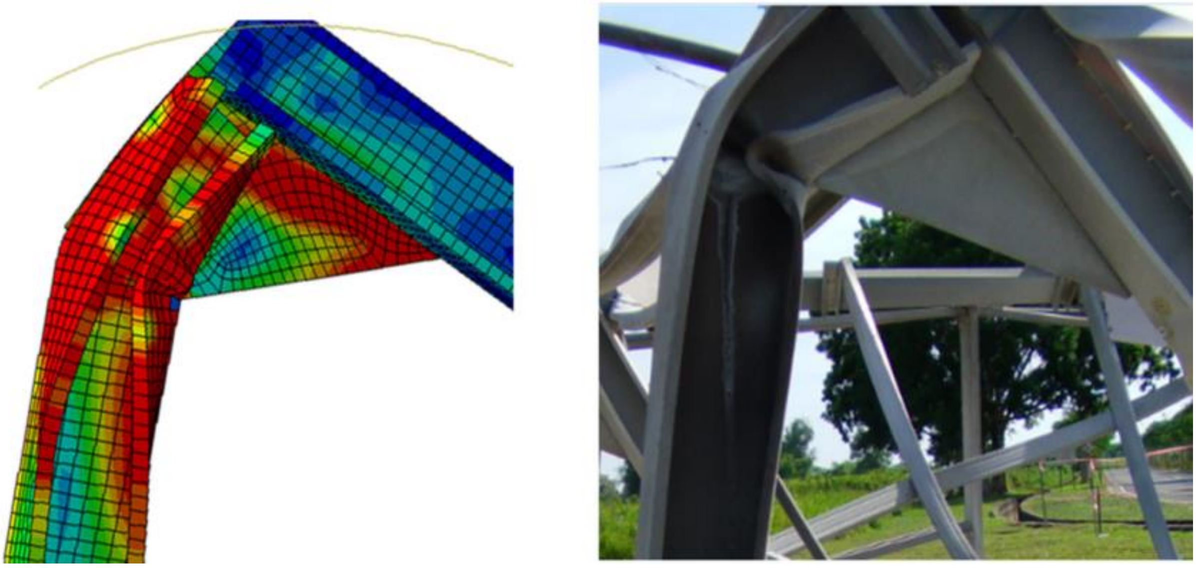

Figure 2.16: Comparison of FE model and Full-Scale Fire Test (Johnston *et al.*, 2015)

2.8 Thermal-Mechanical Properties of Cold-formed Steel at Elevated Temperature

Yield strength and elasticity modulus of cold-formed steel will continuously deteriorate when subjected to elevated temperatures. The deteriorations of strength are typically introduced as the ratio of mechanical properties at elevated temperature to the mechanical properties at ambient temperature which is known as the reduction factors.

Eurocode 3 (CEN, 2005) part 1-2 provides a set of predictive equations to calculate the yield strength, young’s modulus, and strains of cold-formed steels at elevated temperatures. However, the reduction factor suggested by Eurocode 3 part 1-2 (CEN, 2005) used the same reduction factor for hot-rolled steel. The thermomechanical response of cold-formed steel is different as compared to hot-rolled steel (Chen and Young, 2007; Kankanamge and Mahendran, 2011). Sidey and Teague (1988) claimed that the cold-formed steel reduces 10-20% more than hot rolled steels at elevated temperatures due to metallurgical composition and molecular surface effects. In addition, most of the research on thermomechanical properties are focused on hot-rolled steels. Therefore, many researchers; Lee *et al*. (2003), Ranawaka and Mahendran (2009), and Kankanamge and Mahendran (2011) have investigated the thermomechanical properties of cold-formed steel to check its difference against the hot-rolled steel.

Three methods are used for coupon test at elevated temperatures: steady state test, transient test and ISO test. Steady state test is based on a constant load under increasing static loading. Whereas, transient test and ISO test are in accordance to temperature variations under a constant load, where creep effect was also considered.

Lee *et al*. (2003) carried out the coupon tests in elevated temperatures to assess the mechanical properties such as yield strength, ultimate tensile strength, elastic modulus, and strain of light steel gauges under elevated temperature up to 800 ˚C. They also proposed equations for reduction factors and a stress-strain curve model which is applicable from 20 ˚C to 800 ˚C. In their experimental, 189 tests were carried out on different thicknesses of 0.4, 0.6, 1.0 mm and 1.2 mm, and different steel grades of G300, G500 and G550. Only steady state test method was conducted due to its simplicity. Different strain levels were used to compare with 0.2% proof stress method to derive on empirical equation for yield strength at temperature from 20 ˚C to 800 ˚C. The stress-strain model at elevated temperatures is based on Ramberg-Osgood (1943) formulation. They concluded that the stress-strain curve from their test was in good agreement with the proposed new stress-strain model for cold-formed steel at elevated temperatures.

Chen and Young (2007) carried out coupon tests at elevated temperatures to determine the material properties for cold-formed steel grade G550 and G450. The coupon thickness of 1.0 mm and 1.9 mm were tested in temperature range from 20 ˚C to 1000 ˚C using both steady and transient state methods. The material properties of cold-formed steel at elevated temperatures such as elastic modulus, yield strength at different strain levels and ultimate strength were compared with the Australian, British, European standards and other researcher results. They also proposed empirical equations for yield strength, elastic modulus, ultimate strength, and full strain range expression up to ultimate tensile strain of cold-formed steel. The empirical equations based on the Ramberg-Osgood (1943) formulae and further modified based on Mirambell and Real (2000) and Rasmussen (2003) findings. They concluded that the proposed equation accurately predicted the yield strength, elastic modulus, and ultimate strength of the cold-formed steel at elevated temperatures.

Ranawaka and Mahendran (2009) revealed the works carried out by Lee *et al.* (2003) have some drawbacks including; the furnace measuring device overestimated the temperature; strain measurement using modified extensometer clip was inadequate. Ranawaka and Mahendran (2009) claimed the equation used to assess stress-strain curve of CFS proposed by Lee was inaccurate due to errors in the proposed reduction factors. Therefore, Ranawaka and Mahendran (2009) overcame these shortcomings using improved strain measurement device named contact-free Laser Speckle Extensometer to obtain more accurate elongation data. A total of 115 tests were conducted on two different steel grades G550 and G250 having different thicknesses of 0.6, 0.8 and 0.95 mm. These coupon samples were tested in range from 20 ˚C to 800 ˚C in steady test method. They concluded that the steel grade is dependent on the yield strength of cold-formed steel. However, the elastic modulus shows no dependency to steel grade or the thickness of cold-formed steel.

Furthermore, Kankanamge and Mahendran (2011) used the improved measurement method developed by Ranawaka and Mahendran (2009) in coupon tests at elevated temperatures. The coupon specimens cover the steel grade of G250 having thicknesses of 1.55 mm and 1.95 mm; steel grade of G450 with thicknesses of 1.50 mm and 1.90 mm. Steady state method was used where the coupon specimens were heated from 20 ˚C to 700 ˚C. They combined their results with the results from Ranawaka and Mahendran (2009) and improved the predictive equations for high to low strength cold-formed steels. Therefore, this study use the predictive equation to obtain stress-strain curves at elevated temperatures developed by Kankanamge and Mahendran for finite-element modelling purposes.

2.8.1 Yield Stress and Young’s Modulus Reduction Factor

Figure 2.17 and Figure 2.18 show the reduction factors of yield strength and Young’s modulus at elevated temperatures for G550 steel (CEN, 2005; Kankanamge and Mahendran, 2011; Makelainen and Miller, 1983; Chen and Yong, 2007; Ranawaka and Mahendran, 2009; Lee, 2003). It is noted that the yield strength reduction factors curve at elevated temperatures varies as compared to Young’s modulus reduction factor curves at elevated temperatures. Thus, the yield strength reduction factors at elevated temperatures is critical. The comparison of the yield strength at elevated temperatures is able to determine the suitable prediction equations for G550 cold-formed steel. Figure 2.17 shows the yield stress reduction factor suggested by Eurocode 3 Part 1.2 (CEN, 2005) is the upper bound curve for cold-formed steel because it is the same reduction factors for hot-rolled steel. Whereas the lower bound is proposed by Chen and Young (2007).

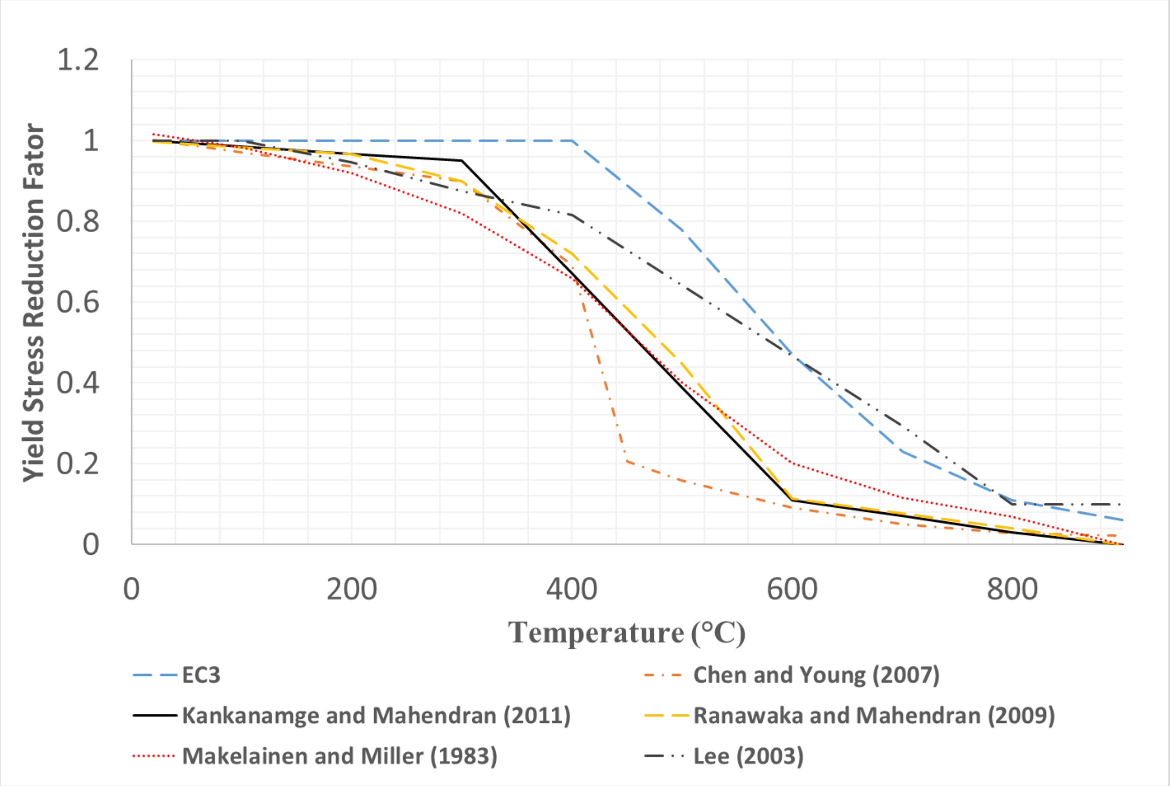

Figure 2.17: Comparison of Yield Strength Reduction Factors at Elevated Temperatures by Various Researchers

The yield strength reduction curve obtained by Kankanamge and Mahendran (2011) is bounded in between the upper bound and lower bound curve. The empirical equations proposed by Kankanamge and Mahendran were used in this study to determine yield strength at elevated temperatures. In addition, the steel grade and thickness (G550 with 0.95 mm thickness) used by Kankanamge and Mahendran (2011) are similar to the steel grade and thickness (G550 with 1 mm thickness) in this study.

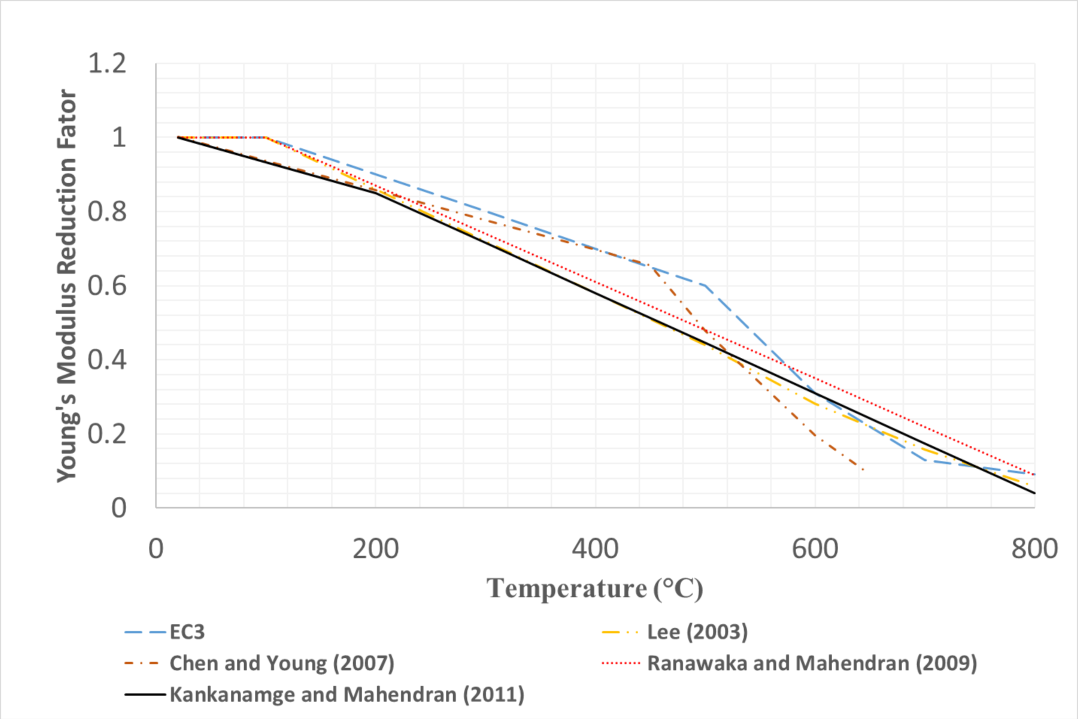

Figure 2.18: **Comparison of Young's Modulus Reduction Factors at Elevated Temperatures by Various Researchers**

2.9 Thermal Properties of Cold-formed Steel

The thermal properties of cold-formed steel are important in developing heat transfer finite-element model. Thermal properties of cold-formed steel are specific heat capacity, thermal conductivity and thermal expansion. Specific heat capacity measures the heat required to increase the temperature of a substance per unit of mass. Thermal conductivity is the parameter that controls the heat conduction. Whereas the thermal expansion is considered when thermal strains are induced by the heating of cold-formed steel.

Many researchers (Zhao *et al*., 2005; Gunalan, 2011; Cheng, 2015; Johnston *et al.*,2015) used the thermal properties of cold-formed steel proposed in the Eurocode 3 Part 1-2 (CEN, 2005) for finite-element modelling purposes. They reported a good correlation between their finite-element results and experimental results. Therefore, these data from Eurocode 3 Part 1-2 (CEN, 2005) for specific heat, thermal conductivity and, thermal expansion of cold-formed steel are used. Figure 2.19, Figure 2.20 and Figure 2.21 show the specific heat, thermal conductivity and thermal expansion of cold-formed steel, respectively.

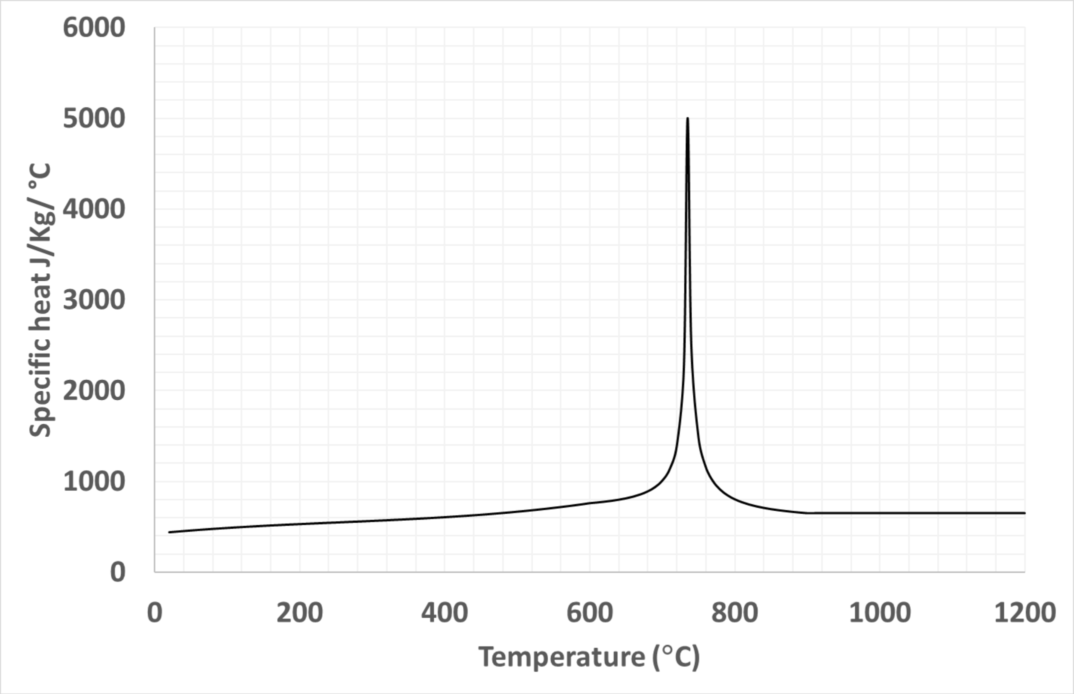

Figure 2.19: Specific Heat of Cold-Formed Steel at Elevated Temperatures (CEN, 2005)

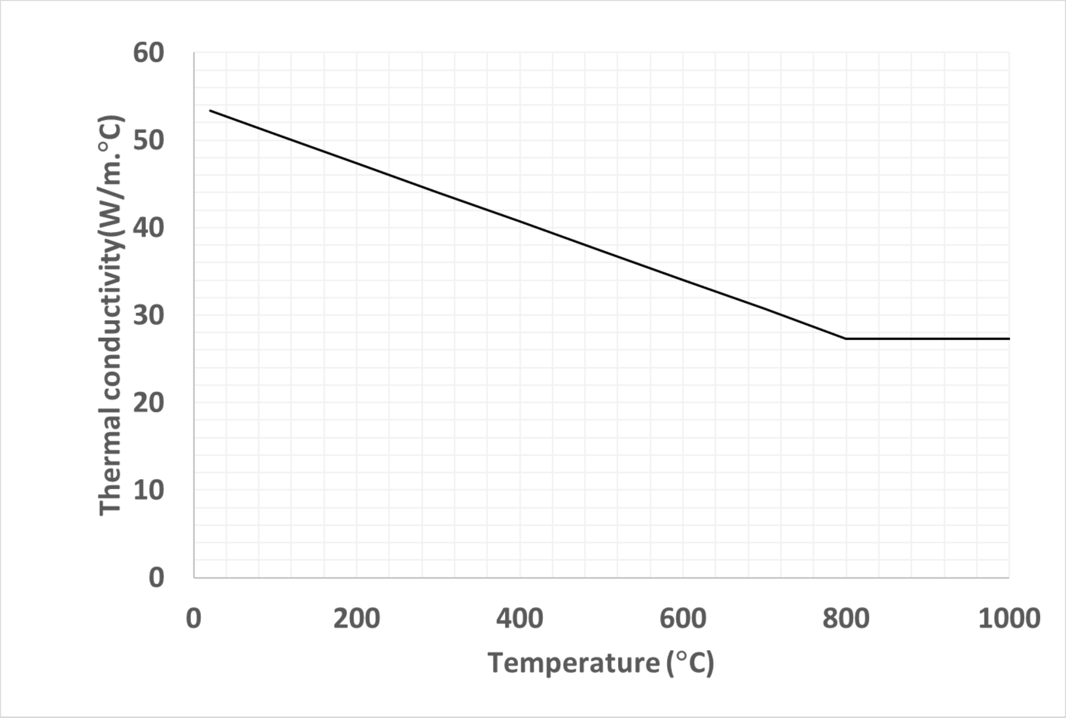

Figure 2.20: Thermal Conductivity of Cold-Formed Steel at Elevated Temperatures (CEN, 2005)

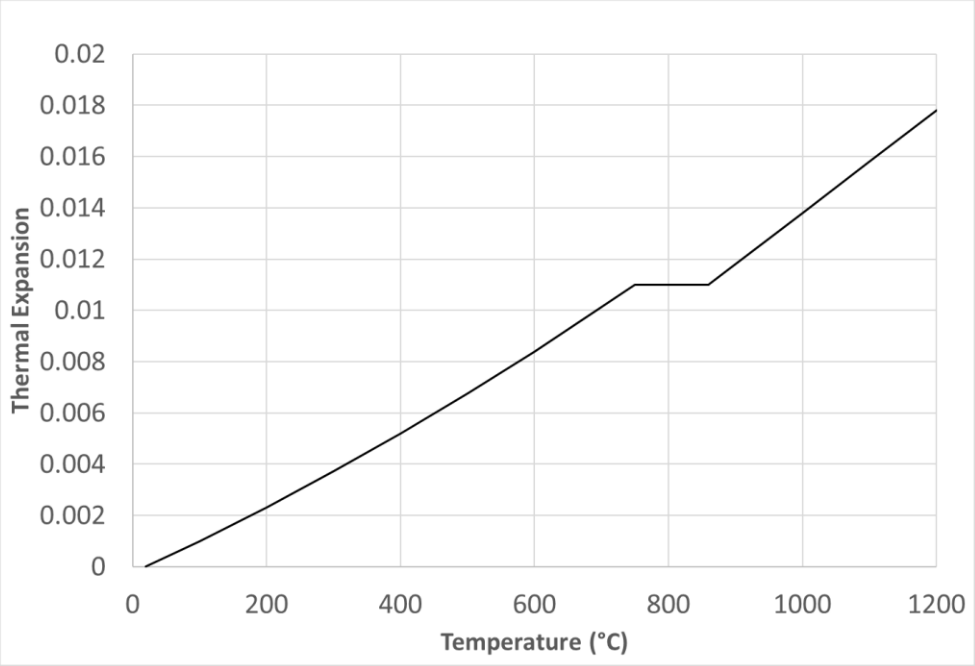

Figure 2.21: Thermal Expansion of Cold-Formed Steel at Elevated Temperatures (CEN, 2005)

2.10 Gypsum Board

Gypsum boards are widely used to protect cold-formed steel wall framings from fire due to its ability to absorb heat and delay temperature rise in the cold-formed steel sections. The gypsum board is composed of a gypsum core with laminated papers as shown in Figure 2.22.

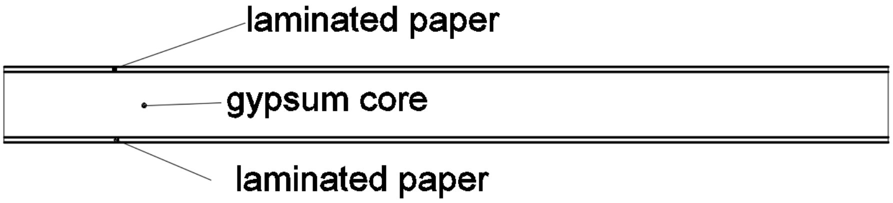

Figure 2.22: Gypsum Board

There are different types of gypsum board available in market today, they are regular gypsum board, Type X gypsum board and, special purpose Type C gypsum board. These gypsum boards are mainly depending on the material composition of gypsum core. The regular gypsum board has lower density gypsum core and it is not stipulated to any fire-resistant rating. Whereas, Type X gypsum boards are more commonly used in framing construction as it is fire rated to provide 60 minutes of fire resistance depending on its thickness. Type X gypsum board consists of some glass fibre reinforcing and other additive to enhance its thermal performance (Buchanan, 2001). The thermal performance of Type C gypsum board is superior than regular gypsum board and Type X. This is because Type C gypsum board contains greater gypsum core density, higher composition of glass fibre and more additives (Jones, 2001). Since the Type X gypsum board is commonly used in framings construction, therefore this research investigates the structural performance of CFS wall framings with protection of Type X gypsum boards.

2.10.1 Furnace Test on Gypsum Board

Small-scale fire test for gypsum board is commonly carried out in a laboratory using a furnace. The fire resistance of the gypsum board was assessed based on the failure time. However, the fire resistance based on time domain does not fully reveal the thermal performance of the gypsum board. Therefore, this leads to the application of a performance-based approach where the temperature against time relationship at the fire exposed and unexposed surface of gypsum boards are obtained using thermocouple during the small-scale fire tests.

Researchers such as Mehaffey *et al.* (1994), Sultan (1996), Rahmanian (2011) and, Kolarkar and Mahendran (2012) have conducted small-scale fire tests on different gypsum board to investigate its thermal performances. Different gypsum board tested by various researchers are tabulated in Table 1. It is found that the small-scale fire test on 15 mm Gyproc Fireline is limited and therefore this research carried out small-scale fire test on 15 mm thick Gyproc Fireline. The testing method of small-scale fire test by Rahmanian (2011) was followed because same product was used in this research.

The results of small-scale fire tests are used to validate the thermal properties of gypsum board in finite-element analysis. The laboratory tests for thermal properties for gypsum board are reviewed in Section 2.12.

Table 1: Different Manufacturer of Gypsum Boards Tested by Various Researchers

Authors	Manufacturer	Thickness(mm)
Sultan (1996)	Canadian gypsum board (Type X)	12.7
Sultan (2010)	Canadian gypsum board (Type X)	15.9
Rahmanian (2011)	British gypsum board (Gyproc Fireline)	12.5
Kolarkar and Mahendran (2012)	Australian gypsum board (FireSTOP, Boral Industry)	13 and 16

2.10.2 Thermochemistry of Gypsum

The chemical formula of gypsum is calcium sulphate dihydrate ($CaSO_4{\cdot}2H_2O$). Pure gypsum contains 3% of free water and 20% of chemically combined water of crystallisation (Mehaffey *et al.*, 1994; Gerlich, 1995). In fire, the heat is absorbed by gypsum board and the moisture content in the gypsum board are evaporated. When most of the moisture in the gypsum board is lost, cracks will be formed on its surface and no longer provide fire resistance to the cold-formed steel wall framings.

It is important to understand the dehydration process of gypsum board that occurred at different temperatures. The density loss, specific heat and thermal conductivity of gypsum board are interrelated with the temperature of dehydration. Rahmanian and Wang (2012) claimed 75% of chemically combined water in gypsum board is driven off in first dehydration at about 100 ˚C. Whereas, 25% of chemically combined water is evaporated in second dehydration approximately at 200 ˚C. The chemical formula of first and second hydration are expressed in Eq. 2-6 and Eq. 2-7, respectively.

$$CaSO_4 \cdot 2H_2O + Q_1 \rightarrow CaSO_4 \cdot \frac{1}{2}H_2O + \frac{3}{2}H_2O \qquad \text{Eq. 2-6}$$

$$CaSO_4 \cdot \frac{1}{2}H_2O + Q_2 \rightarrow CaSO_4 + \frac{1}{2}H_2O \qquad \text{Eq. 2-7}$$

Where $CaSO_4 \cdot 2H_2O$ is gypsum or calcium sulphate dihydrate, H_2O is water and Q_1 and Q_2 are the heat of first and second hydration respectively.

2.10.3 Thermal Properties of Gypsum Board

The main thermal properties of gypsum board are density loss of gypsum board, specific heat and thermal conductivity. Many researchers (Thomas, 2002; Feng, 2003a; Wakili *et al.*, 2007; Rahmanian and Wang, 2012; Semitelos, 2014) tested the gypsum board in laboratory to determine thermal properties of gypsum board. These thermal properties are useful in the development of finite element model for cold-formed steel wall framings with gypsum board (Zhao *et al.*, 2005; Gunalan, 2011, Keerthan and Mahendran, 2012; Rusthi *et al.*, 2015).

2.10.3.1 Density Loss

The density of gypsum board is ranged from 550 to 850 kg/m^3 (Keerthan and Mahendran, 2012). The density of gypsum board varies with elevated temperatures due to loss of moisture content in gypsum. Thermogravimetric Analysis (TGA) is used by various researchers such as Mehaffey *et al.* (1994), Wakili *et al.* (2007) and Keerthan and Mahendran (2012) to obtain the mass loss of gypsum in elevated temperature. TGA is a method of thermal analysis that measures the weight of a sample over a time with elevated temperatures. Moreover, the TGA can provide details of thermal decomposition and phase changes of a tested material.

Mehaffey *et al.* (1994), Wakili *et al.* (2007) and Keerthan and Mahendran (2012) conducted TGA tests on Canadian, European and Australian Type X gypsum specimens. The heating rate of 20 ˚C/min was used in their tests. Mehaffey *et al.* (1994) reported 17.5% of mass loss of gypsum sample was due to dehydration at the temperature between 100 ˚C and 160 ˚C. Wakili *et al.* (2007) obtained 17% of mass reduction of gypsum sample around 150 ˚C to 220 ˚C. Whereas, Keerhan and Mahendran (2012) reported 10% of moisture loss of gypsum density approximately between 125 ˚C and 175 ˚C. It is found that the moisture loss of gypsum varies depending on the moisture content of gypsum specimens. Therefore, TGA tests were carried out in this study to determine the density loss of British gypsum board (Gyproc Fireline).

2.10.3.2 Specific Heat Capacity and Thermal Conductivity

Specific heat capacity and thermal conductivity are important parameters that affect the heat transfer of gypsum board. Figure 2.23 and Figure 2.24 show the specific heat capacity and thermal conductivity of gypsum by various researchers.

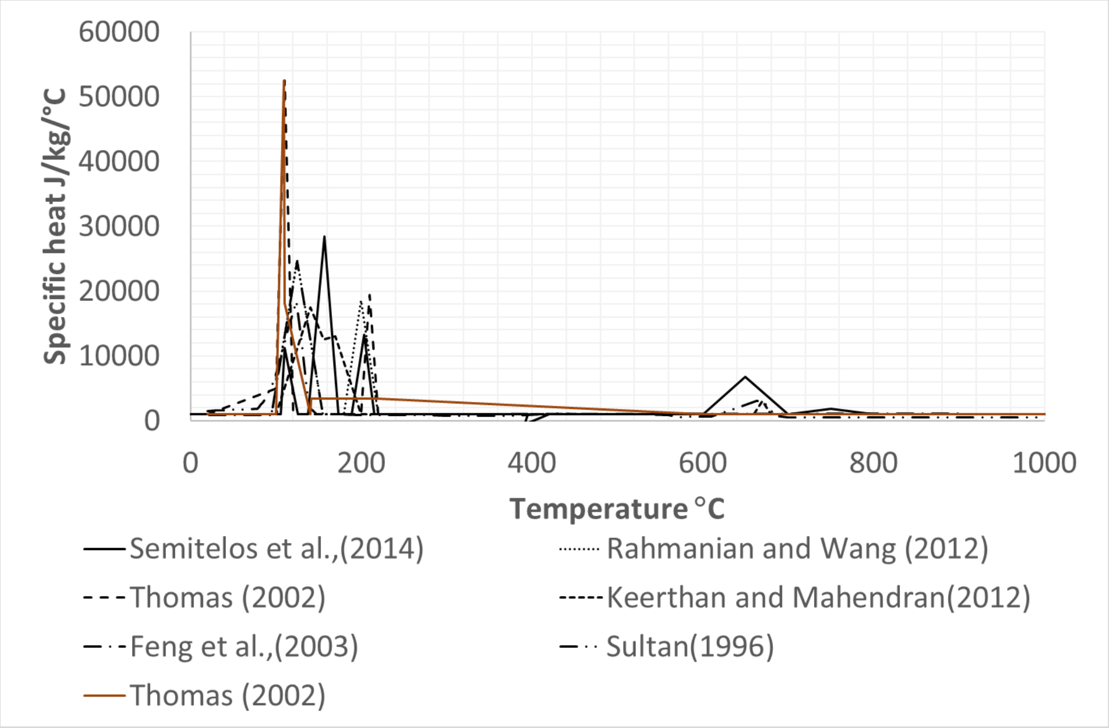

Figure 2.23: **Specific Heat Capacity of Gypsum by Various Researchers**

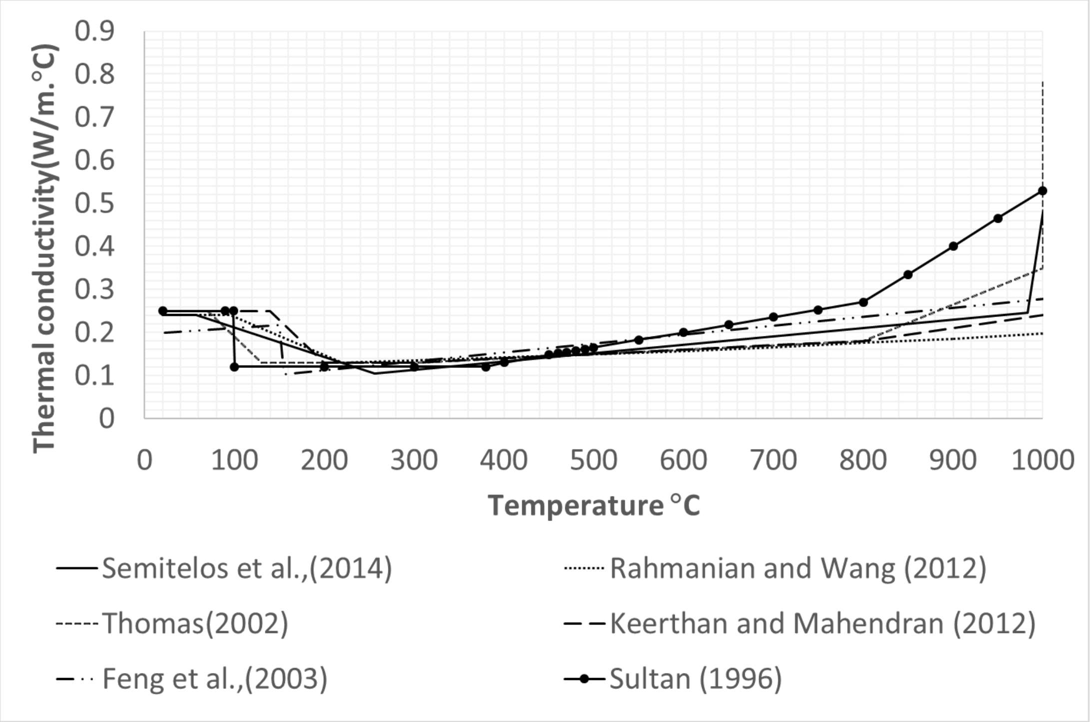

Figure 2.24: **Thermal Conductivity of Gypsum by Various Researchers**

In Figure 2.23, the peaks of specific heat curves indicate the first and second dehydration within 80 ˚C to 220 ˚C. The details of peaks of specific heat capacities corresponding to its temperatures for the occurrence of first and second dehydration are tabulated in Table 2. It is shown that the data of specific heat capacities and temperatures are dispersed among these researchers.

Table 2: Peak Values in Specific Heat Capacity Curves by Various Researchers

Authors	**Specific heat (1st dehydration) (J/kg/ ˚C)**	**Temperature (1st dehydration) (˚C)**	**Specific heat (2nd dehydration) (J/kg/ ˚C)**	**Temperature (2nd dehydration) (˚C)**
Sultan (1996)	18479	124	-	-
Thomas (2002)	52450	110	-	-
Thomas (2002)	52450	110	19450	210
Rahmanian and Wang (2012)	24775	125	18581	200
Keerthan and Mahendran (2012)	17500	140	13000	170
Semitelos *et al.* (2014)	28478	156	13255	203

In relation to the thermal conductivity curves in Figure 2.24, the variations of density loss and specific heat capacities also affect the thermal conductivity. The initial value of thermal conductivity of gypsum board varies from 0.218 to 0.25 W/m/˚C at ambient temperature. The decrease in thermal conductivity about 100 ˚C to 220 ˚C indicated the gypsum board underwent endothermic reaction and dehydration.

Keerthan and Mahendran (2012) conducted Differential Scanning Calorimetry (DSC) tests based on standard ASTM E1269 (ASTM, 2005) to obtain specific heat capacity of gypsum. Thermal conductivity was acquired by modifying the values in literature to reach a good agreement in validation between experimental and numerical result. The thermal properties extraction method is further explored in this research.

2.11 Mechanical Properties of Gypsum Board at Elevated Temperatures

Gypsum board can provide temporary lateral restrain to cold-formed steel wall framings before cracking and fall off in elevated temperatures. The data on the mechanical properties of gypsum boards at elevated temperatures is scarce (Abreu *et al*., 2014).

Cramer *et al*. (2003) carried out experimental tests on 15 mm thick type X gypsum board to obtain mass loss, shrinkage, bending strength and modulus of elasticity at elevated temperatures to 400 ˚C for 60 minutes of fire exposure. They proposed the values for elastic modulus and coefficient of thermal expansion at elevated temperatures up to 400 ˚C. Rahmanian (2011) performed experimental tests on 15.9 mm thick fire gypsum board to determine the elastic modulus, bending and compressive strengths and thermal expansion coefficient along and across the gypsum board. However, the data of elastic modulus is only up to 300 ˚C. Therefore, the elastic modulus at elevated temperatures and coefficient of thermal expansion proposed by Cramer *et al*. (2003) is applied in finite element modelling of this research.

2.12 Conclusions

The experimental and numerical investigations of hot-rolled steel and cold-formed steel structure at elevated temperatures have been reviewed. Most researches are focused on the hot-rolled steel structures. In addition, most of the gypsum board are based on component testing using furnace in laboratory. The understanding of the interaction of cold-formed steel structure remains scattered. Nevertheless, the experimental and numerical investigation of the collapse behaviour of a cold-formed steel structure with roof truss and wall framing is critical. It is therefore required to carry out a full-scale fire test and finite-element modelling to investigate the collapse behaviour of the cold-formed steel structure with roof truss and wall framing.

3 Methodology of Full-Scale Fire Test

3.1 Introduction

This chapter illustrates the details of full-scale fire test including building dimensions, construction method, instrumentations and test itself. The full-scale fire test was aimed to study to study the collapse behaviour of cold-formed steel structure with roof truss supported by the studs and framing wall assembled with and without fire-rated gypsum board under elevated temperatures which are exposed to a non-uniform fire. Temperatures and side sway displacements against time were recorded in the test. This full-scale fire test was carried out at Curtin University, Malaysia Campus.

3.2 Cold-formed Steel Building Specifications

3.2.1 Main Structure

The cold-formed steel building spans 10 m with seven equally spaced frames. The width of the structure is 8m, whereas the eaves height is 2.0 m with roof pitch of 15-degree. Figure 3.1 shows the cold-formed steel structure before installation of claddings. Figure 3.2 illustrates the CAD drawing of 3-dimensional cold-formed steel structure.

Cold-formed steel channel-sections were made of G550 steel grade. The cold-formed steel section designation, nominal dimensions and section properties are shown in Table 3. The wall studs and roof trusses were constructed using C07508 lipped channel section, where C07508 is notation of a section with 75 mm web depth and 0.8 mm thickness. The purlins, side rails and bracing members used C07510 sections, where C07510 is notation of a section with 75 mm web depth and 1.0 mm thickness. Figure 3.3 and Figure 3.4 shows the 2-dimensional view of the building at front and side view, respectively.

Figure 3.1: Cold-formed Steel Structure

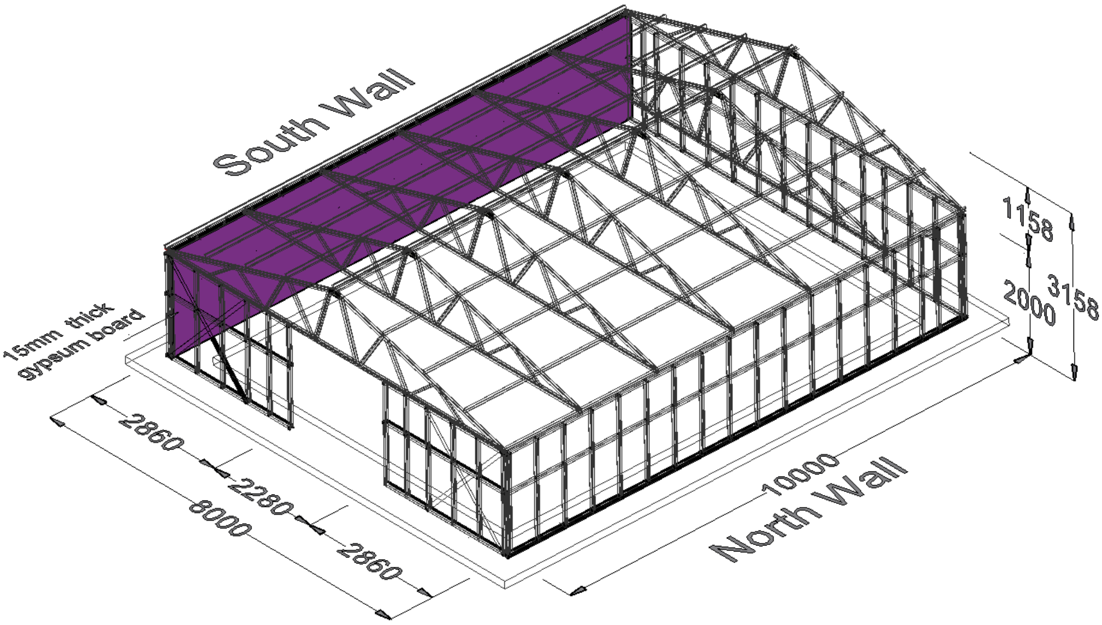

Figure 3.2: 3-Dimensional View of Cold-formed Steel Structure (All Dimension in mm)

Table 3: Nominal Dimensions of Cold-formed Steel Sections

Section Designation	Steel Grade	Flange width (mm)	Web depth (mm)	thickness (mm)	Lip length, (mm)
C07510	G550	40	75	1.0	14
C07508	G550	40	75	0.8	14

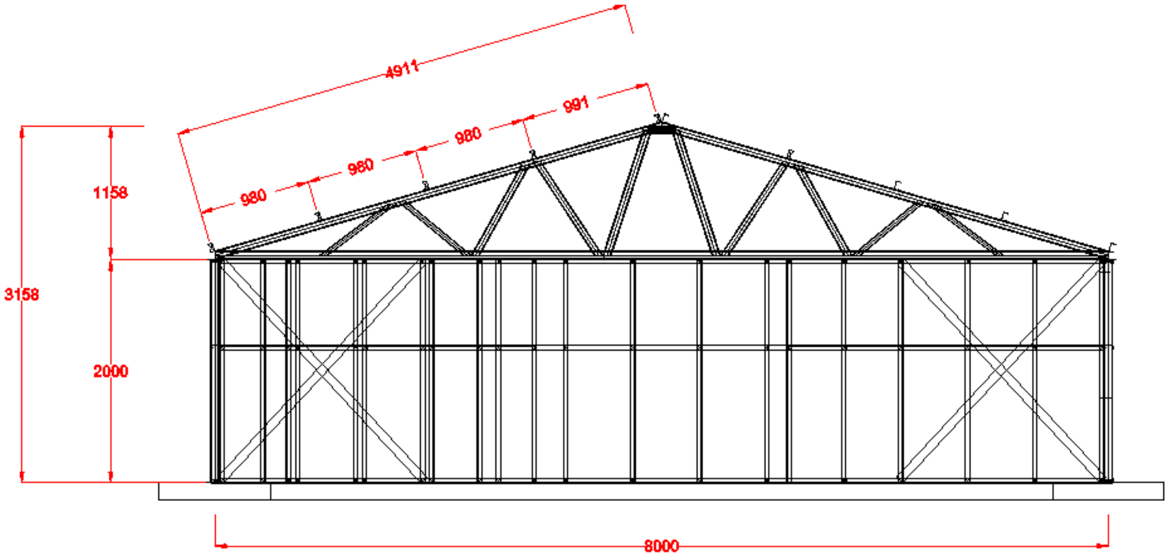

Figure 3.3: Details of Test Frame (All Dimensions in mm)

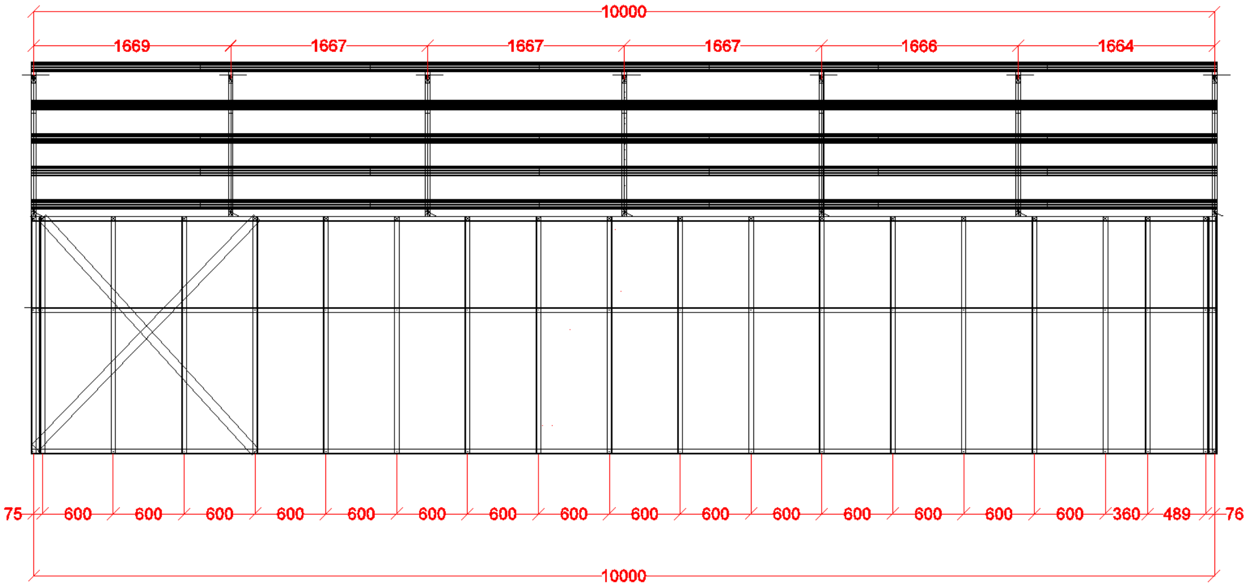

Figure 3.4: Cold-formed Steel Wall Framing Dimensions

3.2.2 Connection Details

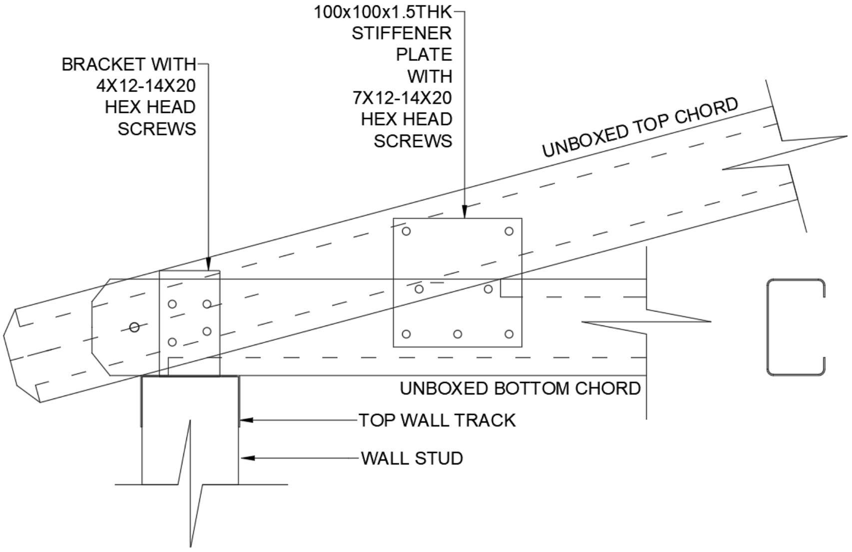

Figure 3.5: Eave Connection Details

Figure 3.5 illustrates the eave connection details. The top and bottom chord joints were formed through a 100 mm × 100 mm cold-formed steel plate with thickness of 1.5 mm. The joint was connected with three rows of seven-gauge #12 self-drilling screws. Besides, L angle bracket with thickness of 2.0 mm was used to connect the top chord and top wall track. The L angle bracket was connected using six-gauge #12 self-drilling screws, four fasteners were used to connect top and bottom chord, and the other two fasteners were used to tie down the roof truss to the top track of the wall. The apex joint joints were formed through a 420 mm × 75 mm cold-formed steel plate with thickness of 0.8 mm. Further details on the screw fasteners are given in Table 4.

Table 4: Fastener Details

Diameter	Gauge #12 (5.43mm diameter)
Thread form	14 Threads per inch
Drive	Hex Head 5/16 inch
Length	20 mm
Drill point	6.0 mm length / 4.50 mm dia.
Type of steel	C 1022 Steel, Hardened heat treated
Single shear	9.0 kN
Torsion	13 Nm

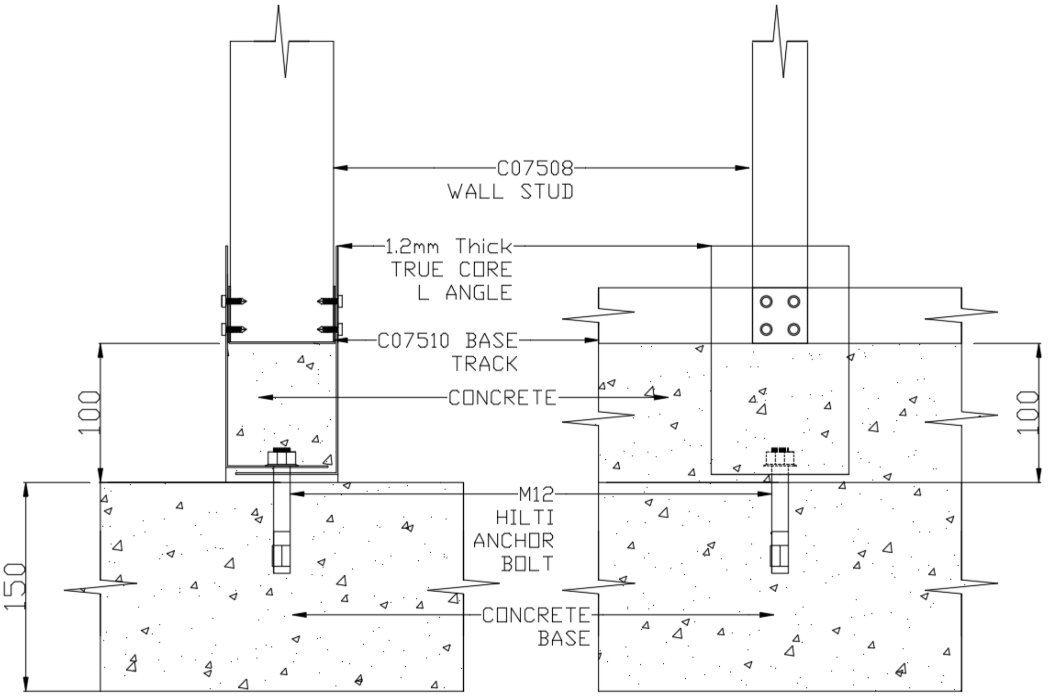

Figure 3.6: Front and Side View of Base Connection Details

Figure 3.6 shows the base connection details of the cold-formed steel wall framings. The cold-formed steel wall bottom track connection comprised of two 1.2 mm thick L angle brackets restrained by four self-drilling fasteners, in two rows. The L angle brackets were anchored by a Hilti M12 bolt through the concrete base with thickness of 150 mm. The void within the base track and L angle was filled with 25 MPa concrete.

3.3 Constructions of Cold-formed Steel Structure

3.3.1 Concrete Foundation

A concrete foundation was constructed to support the cold-formed steel structure. The foundation comprised of a layer of 50 mm thick aggregate at bottom level, and a layer of 50 mm thick lean concrete on top and finished with another layer of 150 mm concrete at top.

For the bottom layer of foundation, aggregates compacted manually on the top of the soil as shown in Figure 3.7 which comprised of coarse and fine aggregates to support a 50 mm thick lean concrete. After that, 150 mm height of cold-formed steel formworks were constructed as shown in Figure 3.8.

150 mm thick foundation was casted with 25 MPa concrete and cured for 14 days. Figure 3.9 shows the concrete base covered with plastic to prevent moisture loss in concrete. The formworks were stripped after 14 days as shown in Figure 3.10.

Figure 3.7: Ballast formed on Site

Figure 3.8: Formwork of Concrete Base

Figure 3.9: Concrete Base curing

Figure 3.10: Concrete Base Finishes

3.3.2 Cold-formed Steel Structure

3.3.2.1 Roof Trusses

The construction of the cold formed steel structure was aided from the technical support of EcoSteel Sdn Bhd. Initially, roof truss members including top chords, bottom chords and other internal truss members were arranged according to construction drawings. This was carried out to secure the triangular frame to ease the installation of internal members, then the internal chords were positioned and restrained by one self-drilling screws at each end of internal chord. Figure 3.11 shows the setup of the triangular framing and assembly of a unit of roof truss.

Connection between top chords and bottom chords were connected suing eight self-drilling screws along with 100 × 100 × 1.5 mm stiffener plate. Figure 3.12 shows an eave connection constructed on site. Specification and details of screws were specified in Figure 3.15 and Table 4. Each purlin cleat was restrained at the top chord by two self-drilling screws. Figure 3.13 shows the purlin cleats installed on the top chord for purlin installation later.

Figure 3.11: Roof Trusses Setup

Figure 3.12: Roof Truss Knee Connection

Figure 3.13: Purlin Cleat

3.3.2.2 Wall Framings

The wall frames comprised of G550 cold-formed steel wall studs, top tracks, middle side rails, and bottom tracks. Initially, wall studs were arranged accordingly to the drawings before the installation. The middle side rail consists of prefabricated openings on the surface to allow the stud joined perpendicularly at 1200 mm of stud length. The top and bottom tracks were capped at the top and bottom of cold-formed steel studs. Figure 3.14 shows the wall framings assemblies. Each of the perpendicular joint was restrained by a screw as shown in Figure 3.15. Lastly, the wall bracings were installed in eastern, northern, southern, and western side of wall. The wall bracing members were made of G550 cold-formed steel straps with a thickness of 2 mm. Figure 3.16 shows the wall bracing restrained by self-drilling screws, and Figure 3.17 shows a photograph of self-drilling screw used.

Figure 3.14: Wall Assemblies

Figure 3.15: Mid-Rail Fasteners

Figure 3.16: Wall Bracing

Figure 3.17: Self-drilling Screw

3.3.2.3 Wall Framings Base Connections

10 meters length of the wall was marked on concrete base. The locations of anchor bolts were marked, and 12 mm pre-drilled holes was created using an electric driller. Two pieces of L angle cleats were installed by a Hilti bolt as shown in Figure 3.18 and Figure 3.19.

Figure 3.18: L Angle Base Connection

Figure 3.19: M12 Hilti Bolt

Figure 3.20 Markings and Reference Points

Figure 3.21 Spirit Ruler Level

3.3.2.4 Installation of Wall Framings

Figure 3.20 shows a reference point marked on 1.18m height of the wall for adjustment purposes. In the adjustment procedures, a hydrometer and a spirit ruler were used to level the wall framings to ensure the bottom track is in flat position as illustrated in Figure 3.21. The wall framings were adjusted with reference to the hydrometer water level as such that the tip and tail of hydrometer matched a same level. After the adjustment has been completed, the L angle seats on the base was restrained as shown in Figure 3.23. Spirit level ruler was used to double confirm the level of the wall vertically and horizontally. Cold-formed steel members were restrained on the wall studs laterally to function as temporary structure after the wall framings were adjusted perpendicular to the concrete base. Figure 3.22 shows the lateral restrain of the wall stud with aid and spirit ruler. In addition, cold-formed steel plate with a thickness of 2 mm was used to join the wall corners where the end of each wall framing met perpendicularly. Figure 3.24 shows a total number of four-gauge #12 self-drilling screws restrained the plate and wall framing together. The end of the wall set up is shown in Figure 3.25. The base connections were casted with concrete as illustrated in Figure 3.26.

Figure 3.22: Wall Verticality

Figure 3.23: Base Connection

Figure 3.24: Plate Connection

Figure 3.25: Completion of Wall Installation

Figure 3.26: Concrete Fill

3.3.2.5 Roof Trusses Installation

To set up the roof trusses support positions, the top tracks of wall framings were marked according to truss spacings of 1.667 m. Figure 3.27 shows the eave connection comprised of back to back L brackets tied down by two AS Teks screws diagonally. Figure 3.28 shows the front and end frame were installed initially with aid of the lateral support to preventing the roof trusses from toppling.

The other inner trusses were installed with repeated levelling procedures to ensure the roof trusses are properly aligned. The roof trusses were joint by purlins and each purlin connection comprised of two AS Teks screws as shown in Figure 3.29. It was noted that the purlin did not overlapped in the L angle bracket. Figure 3.30 shows the completion of roof trusses installation and Figure 3.31 shows the overall cold-formed steel structure without cladding.

Figure 3.27: Eave Connection

Figure 3.28: End Frame

Figure 3.29: Purlin Connection

Figure 3.30: Completion of Trusses Installation

Figure 3.31: Cold-formed Steel Structure without Claddings

3.3.2.6 Installation of Cement Wall Cladding and Gypsum Board

Figure 3.32: Installation of Roof and External Wall Cladding

Figure 3.33: No. 8 x 1-1/8" Self-Drilling Screw

Figure 3.34: Silicone

The Primaflex cement board used in this project comprised sheet size of 1220 mm × 2440 mm and a thickness of 9 mm. Figure 3.32 illustrates the setup of roof and wall claddings. The self-drilling detailed with specification of No. 8 x 1-1/8" is shown in Figure 3.33. Silicone was used to seal the void between claddings to prevent water leakage. Figure 3.34 shows the silicone used in this project.

This research investigated the effect of gypsum board protection on one side of wall framings. Hence, Gyproc Fireline gypsum boards having thickness of 15 mm were installed in the southern wall. Figure 3.35 shows the gypsum board used in this study, Figure 3.36 shows the gypsum boards installed in the southern wall and, Figure 3.37 shows a complete building for the full-scale fire test.

Figure 3.35: 15 mm Gyproc Fireline Gypsum Board

Figure 3.36: Gypsum board in Southern Wall (Internal)

Figure 3.37: Completed Building (Southern Side View)

3.3.2.7 Thermocouple installation

A structure was built for thermocouple to protect from fire damage during the fire test. Figure 3.41 and Figure 3.38 illustrate the drawings and on-site thermocouple platform, respectively. The dimensions of thermocouple platform were surveyed in site for preparation of shop drawing. The shop drawing and joint details are outlined in appendix C. Firstly, the soil was excavated to form a 650 mm deep trench as a foundation for the thermocouple platform. Figure 3.39 shows the foundation of thermocouple platform. Besides, a circular tube was embedded below the concrete foundation at rear of the building to serve as an entrance for the thermocouple wire. Figure 3.40 shows the entrance created for thermocouple wires.

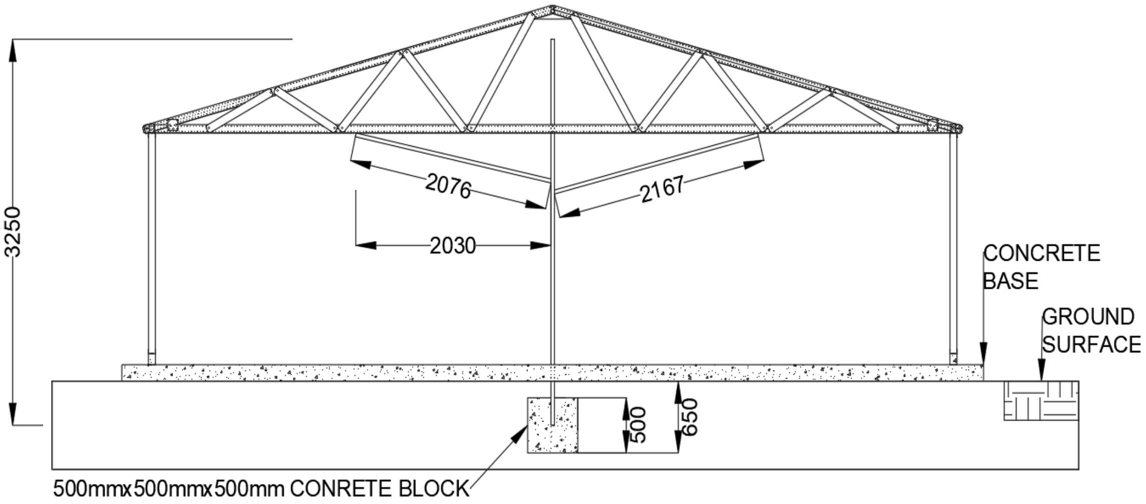

Figure 3.38: Thermocouple Tree

The thermocouple platform consisted of circular hollow steel section with a thickness of 5 mm. Two circular joint openings were formed at height of 1865 mm on left hand side, and 1965 mm on right hand side by using a flame cutting machine. The 2076 mm long member on the left-hand side was tilted to an angle of 12°. Whereby, the 2167 mm long member on the right-hand side was tilted to an angle of 14°. Before welding the connections, wire rope was used to tie the slanting members together with the roof bottom chord to provide temporary stability. Both connections were formed through a 6 mm fillet weld.

After the completion of welding tasks, 3:2:1 ratio of sand, aggregate and cement were mixed to produce 0.125 m^3 of concrete. Meanwhile, four pieces of plywood were inserted in the 650 mm deep trench laterally as a formwork. Finally, the concrete was casted in the ground as shown in Figure 3.42.

Figure 3.39: Trench in Compartment

Figure 3.40: Thermocouple Entrance

Figure 3.41: Thermocouple Platform

Figure 3.42: Concreting

3.4 Fire Source

Figure 3.43: Timber Pallets

Timber pallets were stacked to a height of 1.2 m across the ground in compartment, except for a 2.0 m corridor where the fire was ignited. Figure 3.43 shows the timber pallets stacked up to 1m. A total number of 176 timber pallets were weighted and stockpiled in the building. Total weigh recorded from 176-unit timber pallets was 3517 kg, which gives a total fire load per unit area of 1228.8 MJ/m^2. The caloric value of the timber was approximately 16000 KJ/kg. The timber pallets were estimated to burn out completely in 60 mins. The compartment and steel temperatures were also predicted using zone model "Ozone" developed by Cadorin and Franssen (2003) and, Cadorin *et al*., (2003). Detailed calculations were presented in Appendix A.

3.5 Roof Loading

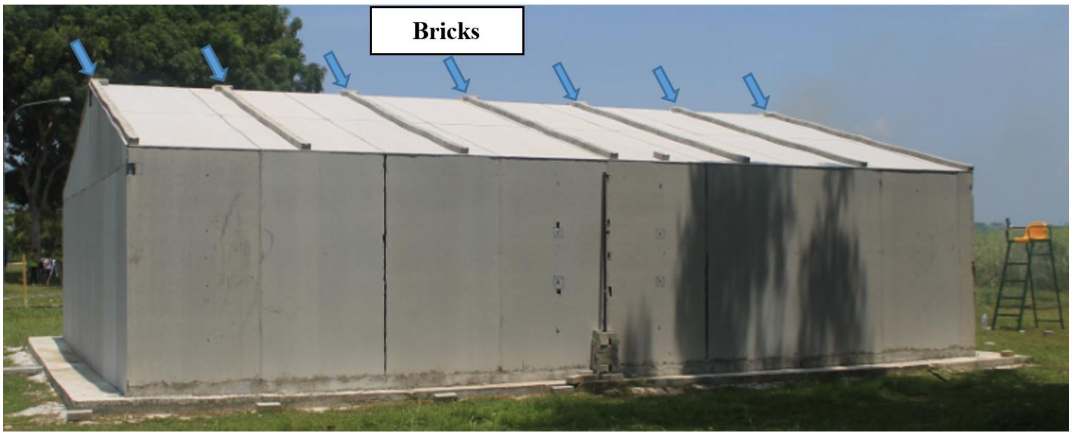

Figure 3.44: Permanent Load on Roof Top

As can be seen in Figure 3.44, cement bricks were loaded on the roof top. The cement brick load on top of roof was to ensure collapse of the cold-formed steel structure would occur during the fire. The load was applied on top of roof claddings, supported by purlins spanning between adjacent frames. 40 bricks were used to load on each frame which gives a total number of 280 unit of bricks applied on the roof. This is equal to 0.178 kN/m of permanent load applied on the roof. This load comprised self-weight of the members, cladding, purlins and the weight of the cement brick. Detailed calculations for permanent load are described in appendix B.

3.6 Full-Scale Fire Test Instrumentation and Setup

3.6.1 Temperature Measurement

One of the objectives in this study was to quantify the thermal performance of cold-formed steel structure. Thermocouple type K was used to measure the temperature development of cold-formed steel structure. Figure 3.45 shows 100 meter of thermocouple used in this project.

Thermocouple type K is a temperature measuring device with inclusion of two conductors that contact each other. A thermocouple type K wire comprised of nickel chromium alloy wire (positive side) and, nickel-silicium alloy wire (negative side). This indicates that both positive and negative wire must be tied in the head and tail of the thermocouple wire to allow thermal and electric conduction. One end of the thermocouple type K wire is usually connected to a data logger. Voltage is generated when there are temperature differences in the in conductor. As a result, the voltage signals received from thermocouple the data logger are converted to temperature readings. Details of the thermocouple type K is tabulated in Table 5.

Table 5: Thermocouple Type K Details (Bonnier and Devin, 1997)

Metal A(+)	Metal B(-)	Temperature Range (°C)	Standard Error (%)	Minimal Error (%)
Nickel-chromium alloy (Chromel)	Nickel-aluminium alloy (Alumel)	-270 to 1372	2.2-0.75	1.1-0.2

The purpose of thermocouple type K is used to measure the temperature development of cold formed steel members. The choice of selecting thermocouple type K as temperature measurement is because the highest temperature can be recorded up to 1372 °C. Thermocouple type K is a well-known instrument used by researchers Pyl *et al*. (2012) and Johnston *et al.* (2014) to measure the temperature development of cold-formed steel members.

Figure 3.45: Thermocouple type K

3.6.2 Displacement Measurement

The wall framings side sway displacements were record by measuring device named laser range meter as shown in Figure 3.46 and Figure 3.47. A total number of thirteen laser range meters were used in this project. Among thirteen laser range meters, there were nine “BOSH GLM80” and four “FLUKE 424D” laser range meters used in project. Both laser range meters are shown in Figure 3.46 and Figure 3.47. BOSH GLM80 laser range meter is capable to measure up to 80 meters with an accuracy of plus minus 1.5 mm. Besides, FLUKE 424D laser range meter having specification of measurement up to 100 m with an accuracy of plus minus 1 mm. Both laser range meters are integrated with inclination sensors which is essential for levelling works to ensure the laser is perpendicular to the target.

Figure 3.46: BOSH Laser Range Meter

Figure 3.47: FLUKE Laser Range Meter

3.6.3 Test Setup

3.6.3.1 Thermocouple installation and Laser Range Setup

Thermocouple type K was connected to a data logger to measure the temperature development of cold-formed steel. A total number of ten individual thermocouples were connected to the central roof truss, northern and southern wall. On one hand, thermocouple NT1, NT2 and NT3 were installed in the northern wall as shown in Figure 3.48. On the other hand, thermocouple ST1, ST2 and ST3 were installed in the southern wall as shown in Figure 3.59. The thermocouple configuration for northern wall is identical to the southern wall. Table 6 summarized all the locations of thermocouple around the structure.

Thermocouples installed on the northern and southern walls are protected by the hot-rolled steel circular tubes. The cladding was removed locally to expose the surface of the steel studs. The temperature measurements were taken on the outside flange of the wall studs at height of 2.0 m, 1.6 m and 0.9 m from the baseline. The thermocouple installation is shown in Figure 3.49, Figure 3.50 and, Figure 3.51. The self-drilling screw was used to restrain thermocouple wire to the cold-formed steel stud. On the other end of thermocouple wire was connected to a data logger to record the temperature readings at 10 sec intervals.

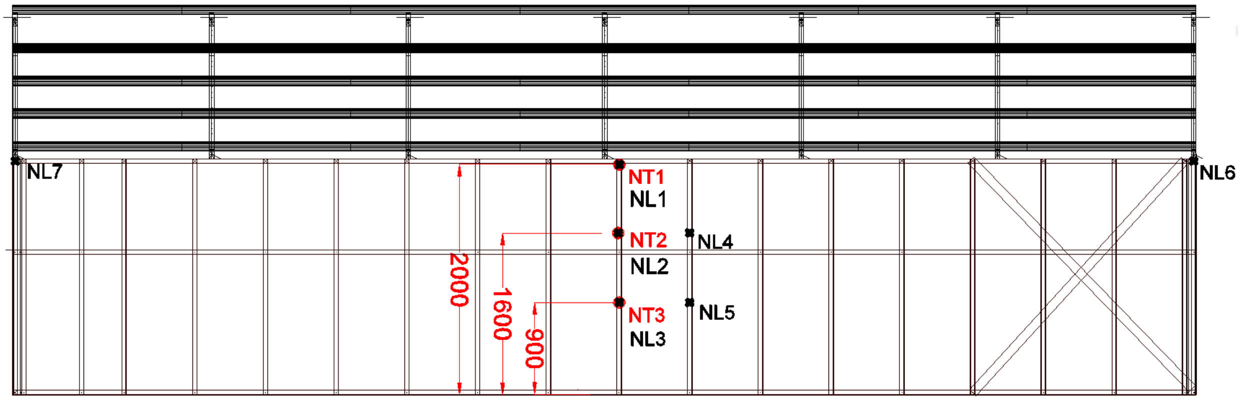

Figure 3.48: Northern Wall Thermocouple and Laser Range Target

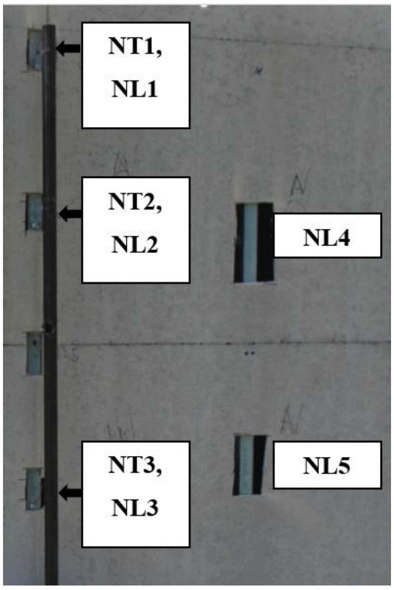

Figure 3.49: Northern Wall In-Situ Thermocouples

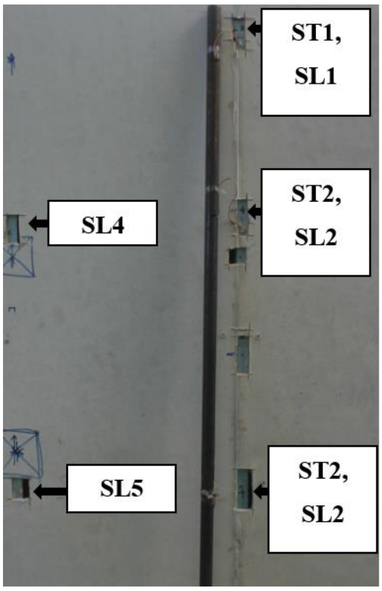

Figure 3.50: Southern Wall In-Situ Thermocouples

Figure 3.51: In-Situ Thermocouple

Table 6: Thermocouple Position around The Structure

Thermocouple	Position
NT1	Northern wall (top)
NT2	North side wall (mid)
NT3	North side wall (bottom)
ST1	Southern wall (top)
ST2	Southern wall (mid)
ST3	Southern wall (bottom)
RT1	Roof apex
RT2	Left bottom chord
RT3	Right bottom chord
RT4	Middle bottom chord

Furthermore, a total number of four thermocouple points RT1, RT2, RT3 and RT4 were inserted in a steel tube at rear of the building. Figure 3.52 shows the location of thermocouple installed in the roof truss. Figure 3.53 and Figure 3.54 shows the thermocouple wire located at rear and, inside of the building. These thermocouples were wired to the location RT1, RT2, RT3 and RT4 as shown in Figure 3.55 to Figure 3.58.

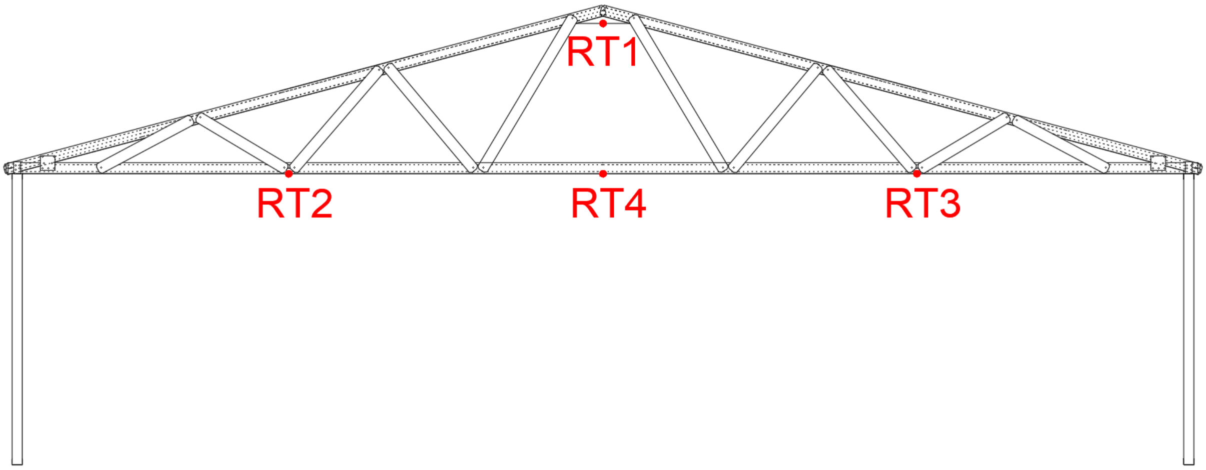

Figure 3.52: Central Roof Truss Thermocouple Locations

Figure 3.53: Thermocouple (Rear of building)

Figure 3.54: Thermocouple Inside Building

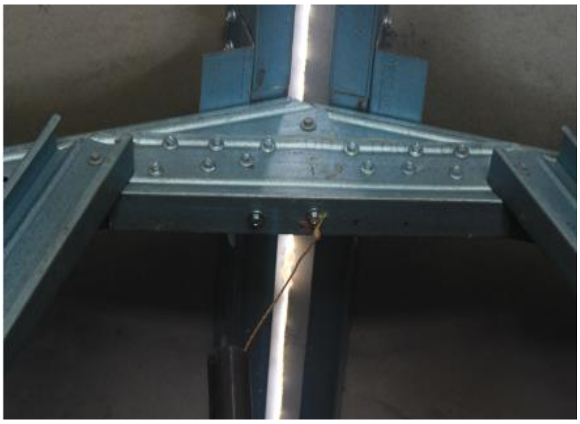

Figure 3.55: Thermocouple Location RT1

Figure 3.56: Thermocouple Location RT4

Figure 3.57: Thermocouple Location RT3

Figure 3.58: Thermocouple Location RT4

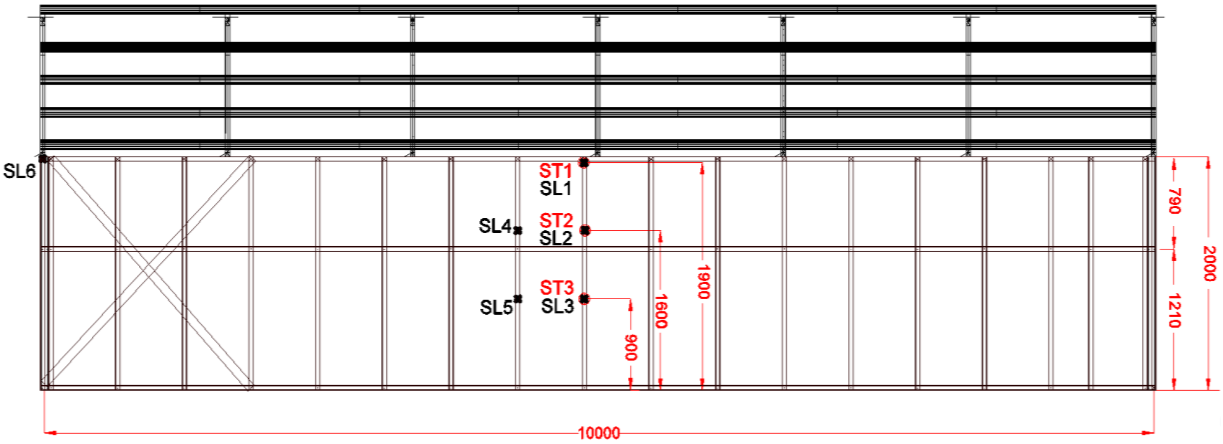

Figure 3.59: Southern Wall Thermocouple and Laser Range Target

Figure 3.60: Southern Side Laser Range Station

A total number of thirteen laser range meters were used to measure the side sway displacement of northern and southern wall. Figure 3.48 shows laser range targets of NL1 to NL7 and, Figure 3.59 shows laser range targets of SL1 to SL6. “N” or “S” denoted as northern or southern wall. Whereby, “L” indicates laser range meter. Figure 3.60 shows the laser range station at southern side. A centralized timing system was employed where readings for each instrument were taken and recorded at 10 second intervals. Volunteers monitored and recorded the displacement data for southern and northern laser range station.

3.7 Conclusions

The full-scale fire test programme for cold-formed steel structure has been described. The cold-formed steel structure is composed of roof truss and wall framing assembled with and without fire-rated gypsum board. Fire load survey has been conducted and, the fire test was designed for 60 minutes fire severity to ensure collapse of the structure. The details of cold-formed steel structure and instrumentation for fire test such as the thermocouple wires type K were used to obtain the temperature readings around the structure. Whereas, the laser range meters were used to obtain the northern and southern wall movement. A centralized timing system was used where readings for each instrument were taken and recorded at 10 second intervals. Many challenges and difficulties are overcome to complete the fire test.

4 Material Property Tests

The material properties tests of cold-formed steel and gypsum board carried out in the laboratory are described in this chapter. Coupon tests were carried out to obtain the stress-strain curve of G550 cold-formed steel. Whereas, Thermogravimetric analysis (TGA) and differential scanning calorimetry (DSC) were conducted to assess density loss and specific heat of gypsum board. Furnace tests were performed to determine the temperature development of cold and hot surfaces for gypsum boards. The results of furnace tests results were used to validate the thermal conductivity of gypsum board in finite element modelling as described in Chapter 5.

4.1 Coupon Tests

The material properties of cold-formed steel are required in the finite element modelling to simulate the behaviour of cold-formed steel. Tensile coupon tests were conducted to obtain the stress-strain curve of G550 cold-formed steel at ambient temperature. The conversion of stress-strain curve at ambient temperature to stress-strain curve at elevated temperature were further discussed in Chapter 5. The coupon specimens were prepared in accordance to standard AS1391 (SA, 2007) where Figure 4.1 shows the dimension of coupon specimen in accordance to AS1391 (SA, 2007) and, Figure 4.2 shows the zinc coating on the coupon specimens was removed using hydrochloric acid as the zinc coating provides additional yield strength to the specimens (Swanger and France, 1932).

Huang and Young (2014) suggested loading rate of 0.05 mm/min to obtain sufficient data for Young’s modulus. A loading rate of 0.05 mm/min was applied to the coupon specimen in this Instron 5882-E2 Universal Testing Machine. The failure of coupon specimen is shown in Figure 4.3 and Figure 4.4 shows the Instron 5882-E2 Universal Testing Machine used in tensile coupon tests. To obtain static stress-strain curve, it is recommended to reduce the strain rate as such, the loading is paused for 100 seconds at the levels of 0.2% proof stress and ultimate yield strength (Huang and Young, 2014).

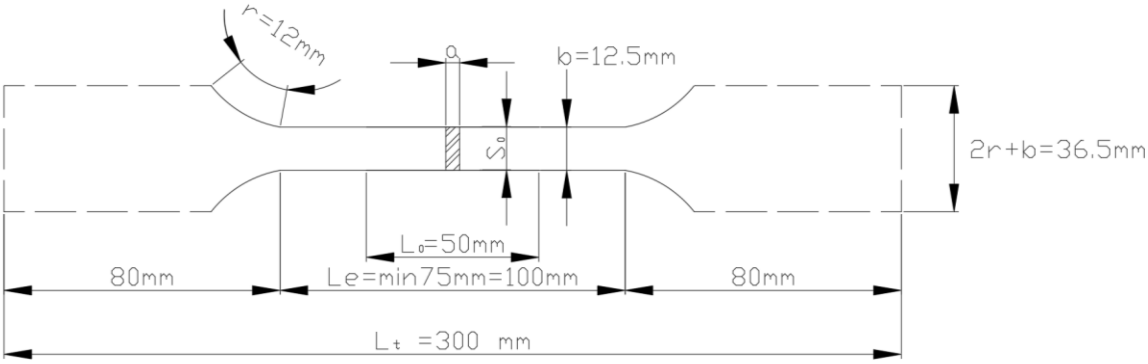

Figure 4.1: **Dimensions of Coupon Specimen According to AS1391 (SA, 2007)**

Figure 4.2: **Zinc Coating Removed from Coupon Specimens**

Figure 4.3: **Failure of a Coupon Specimen**

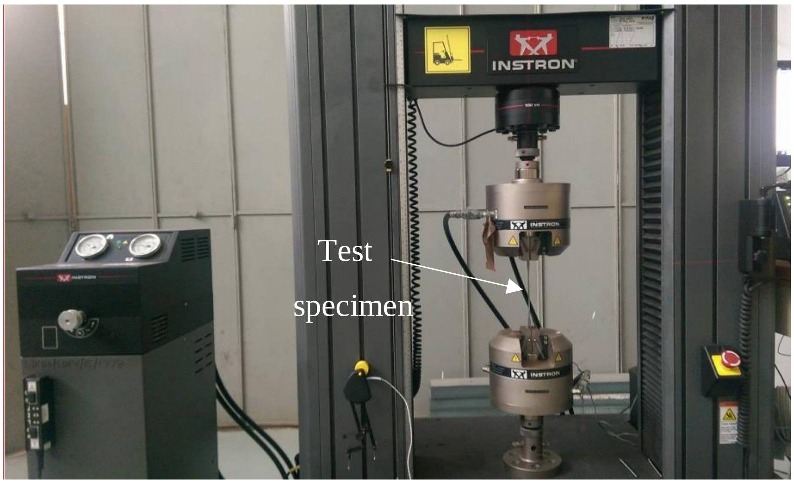

Figure 4.4: **Instron 5882-E2 Universal Testing Machine**

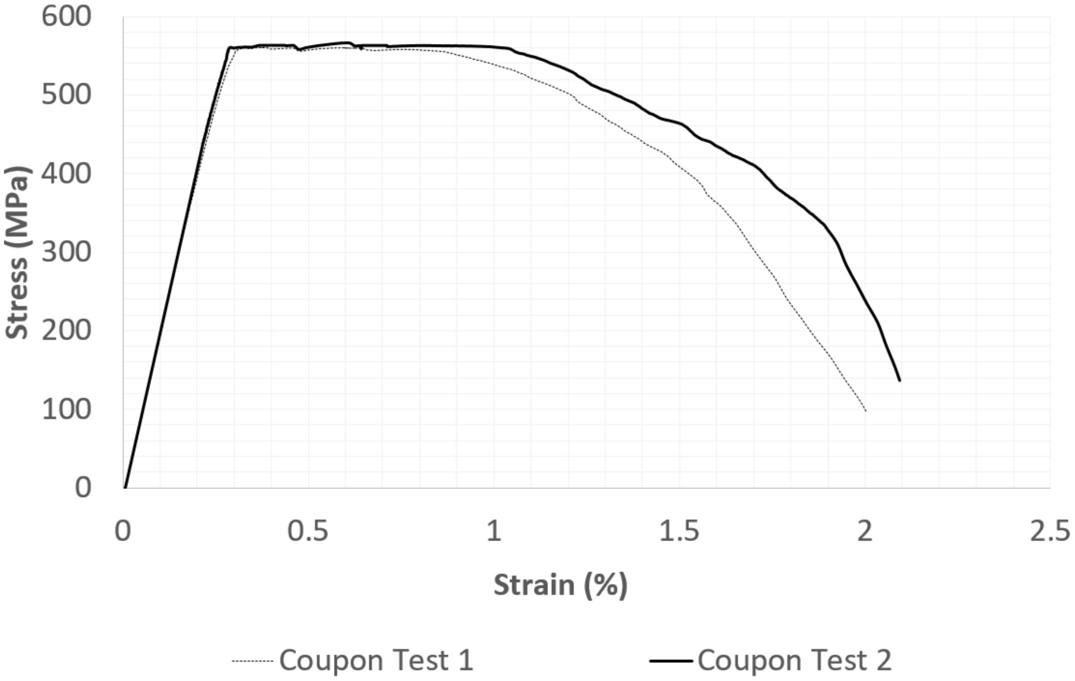

Figure 4.5: Stress-Strain Curves of Coupon Specimens

Table 7: Coupon Test Results

Specimen	Young's Modulus	Yield Stress	Ultimate Stress
	E (GPa)	f_y (MPa)	f_u (MPa)
Coupon Test 1	183.90	530.00	535.14
Coupon Test 2	194.30	563.00	571.60
Average	189.10	546.50	553.37

Figure 4.5 shows the obtained stress-strain curves of coupon specimens for this research. The coupon test results show similar trend up to proportional limit. The Young's modulus, yield strength and ultimate stress obtained in coupon test 1 are 183.9 GPa, 530 MPa, and 545.14 MPa, respectively. For coupon test 2, the results obtained for Young's modulus, yield strength and ultimate stress are 194.3 GPa, 563 MPa and 571.6 MPa, respectively. Average values of Young's modulus, yield strength and ultimate strength are 189.1 GPa, 546.5 MPa and 553.37 MPa, respectively.

Cold formed steel normally gives a range of 190 to 210 GPa for the modulus of elasticity of steel E. (Yu and LaBoube, 2010; Gere and Timoshenko, 1991). Roger and Hancock (1997) stated that Young's modulus, E, increases for test specimens obtained from the transverse direction, e.g. 252 GPa and decreases for test specimens obtained from the diagonal directions, e.g. 192 GPa in their tests. This is because of dependent on direction for fully recrystallised steels, because of the inability of the grain structure to return to a completely random orientation even after heat treatment. Thus, the results of 189 GPa for E are reasonable.

The Grade 550 steel used is low ductility steel with strain 2%-3%. Thus, the constant ratio of f_u/f_y is close value of f_y to f_u. This is because lack of a strain hardening range for the G550 materials. The G550 sheet steels doesn’t meet current design standard requirements for ultimate strength to yield stress ratio of $f_u/f_y \geq 1.08$.

4.2 Thermogravimetry Analysis (TGA) of Gypsum Powder

Thermogravimetric analyses (TGA) were carried out using TA instrument TGA Q500 as shown in Figure 4.9. TGA Q500 was used to heat the gypsum specimens up to 900 °C, the electronic balance integrated in TGA Q500 traced the mass loss of gypsum specimens at elevated temperatures. Seven gypsum specimens with a mass range between 12.12 mg to 12.14 mg were prepared. A scanning rate of 20 °C/minute was used to compare with the Mehaffey *et al.* (1994), Keerthan and Mahendran (2012) and Semitelos *et al.* (2014) tests.

4.2.1 Preparation of Gypsum Powder Specimen

The solid gypsum boards were grinded into a power form in accordance to ASTM E1269 (ASTM, 2005). A portion of gypsum solid was removed from gypsum board using a razor blade. The gypsum solid was crushed and grinded using mortar and pestle as shown in Figure 4.6 and Figure 4.7. The powered gypsum was sieved to produce finer powder as shown in Figure 4.8. A gypsum powder specimen was sampled from various parts and then mixed together to comply with ASTM 1269 (ASTM, 2005) sampling method. A total of fourteen gypsum specimens ranged between 8 mg to 13 mg were prepared and weighted by electronic balance. Half of the total specimens were tested for TGA, while the remaining were tested for differential scanning calorimetry (DSC).

Figure 4.6: Crushed Gypsum

Figure 4.7: Mortar and Pestle

Figure 4.8: Sieve

Table 8: TGA Specimens Weight

Thermogravimetric Analysis	
Specimen	Mass(mg)
1	11.11
2	8.11
3	14.00
4	8.44
5	11.11
6	18.88
7	13.90
Average	12.22

4.2.2 TGA Test Setup

Initially, the gypsum powder specimen was weighted and held by a platinum pan. Table 8 shows the weight of seven specimens. The platinum pan was hung using a hanger and inserted into furnace chamber as shown in Figure 4.9**.** The hanger is connected to an electronic balance which was used to trace the mass changes of gypsum specimen during the test. The TGA Q500 as shown in Figure 4.10 consists of a furnace chamber that can be heated up to 1000 ℃. Gas and water are required to heat up the furnace chamber. In this test, nitrogen gas was purged with a controlled flow rate of 2L per hour. The decomposition of gypsum powder was recorded in form of mass loss as a function of temperatures.

Figure 4.9: TGA TA Instrument Q500

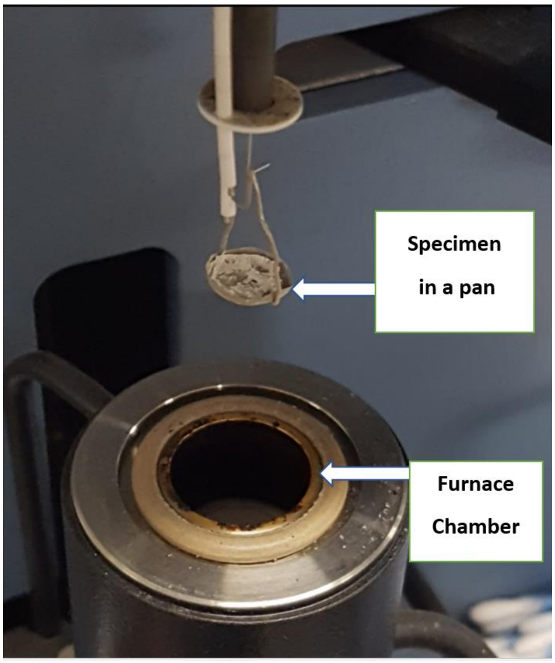

Figure 4.10: TGA Furnace Chamber

4.2.3 TGA Results

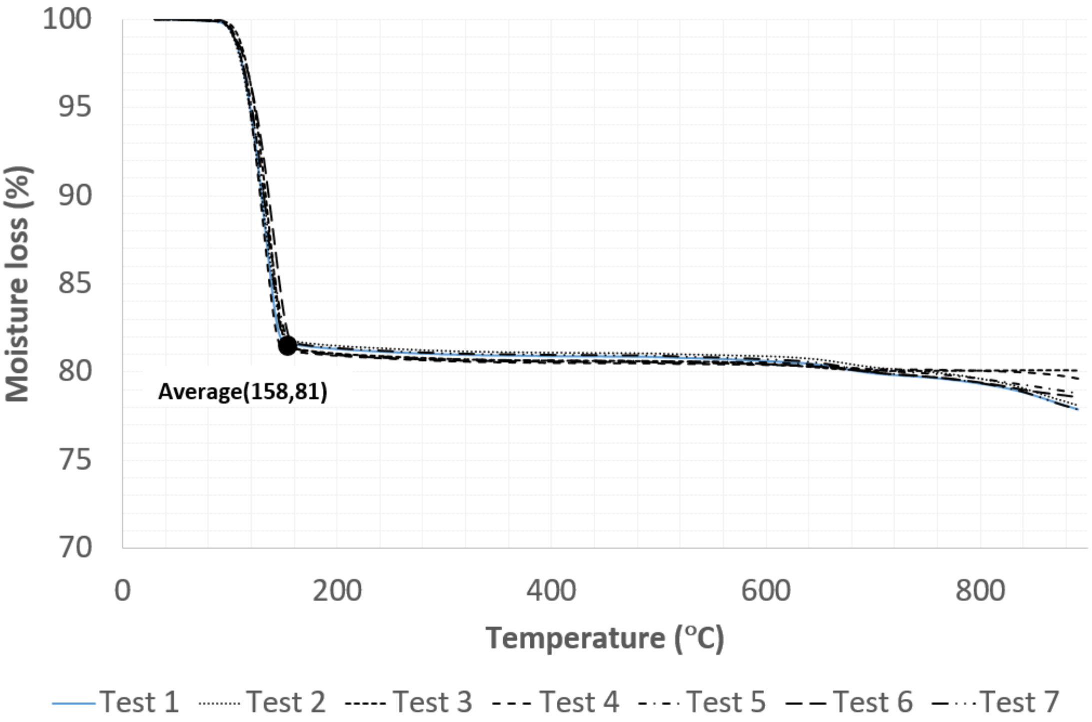

Figure 4.11: Moisture Loss of Gypsum

TGA tests have been conducted to determine the moisture loss of gypsum under elevated temperatures. Figure 4.11 shows the relationship between moisture loss and temperature of seven gypsum specimens. Initially, the moisture content of gypsum shows insignificant changes from 20 ℃ to 100 ℃. The evaporation of the water was commenced approximately at 100 ℃. The result shows the moisture content of gypsum samples dropped significantly from 100% to 81% at temperature of 100 ℃ to 158 ℃, respectively. In other words, 19% of moisture content was evaporated at a temperature of 158 ℃. Overall moisture lost recorded was 21.3%. The results show good correlation with other researchers (Mehaffey, 1994; Thomas, 2002; Kontogeorgos and Founti, 2010; Rahmanian, 2011), they reported the weight chemically bounded water of gypsum board is approximately 21%.

4.3 Differential Scanning Calorimetry (DSC)

Differential Scanning Calorimetry (DSC) was performed to determine the specific heat capacity of gypsum powder. DSC test is a thermo-analytical technique which involves measurement of heat difference required to increase the temperature of a specimen. Generally, the specific heat of gypsum board cannot be measured directly and hence, DSC testing machine is used to measure the heat flow of gypsum specimen up to 550 ℃. The specific heat of gypsum board is computed using Pyris computer software which is integrated with ASTM1269 (ASTM, 2005) calculation standards. Figure 4.12 shows the Perkin Elmer DSC7 machine used in this test. Figure 4.13 shows the heating chamber of DSC 7 which is located at the top of the machine. A schematic diagram of the test is shown in Figure 4.15.

Figure 4.12: Perkin Elmer DSC 7

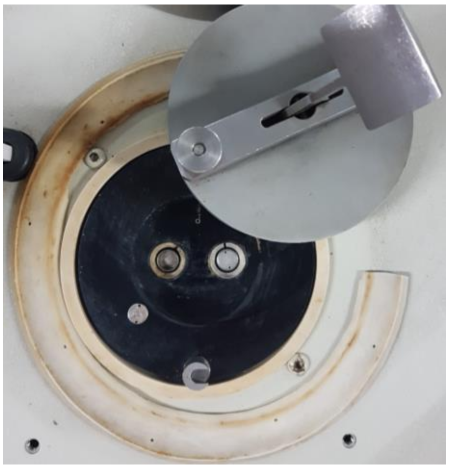

Figure 4.13: DSC 7 Heating Chamber

Table 9: Gypsum Board Specimens Weight

Differential scanning calorimetry	
Specimen	Mass(mg)
1	12.31
2	12.29
3	12.31
4	12.60
5	12.54
6	12.24
Average	12.38

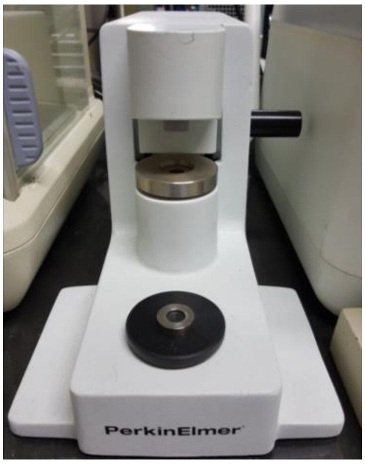

Figure 4.14: Pan Crimper

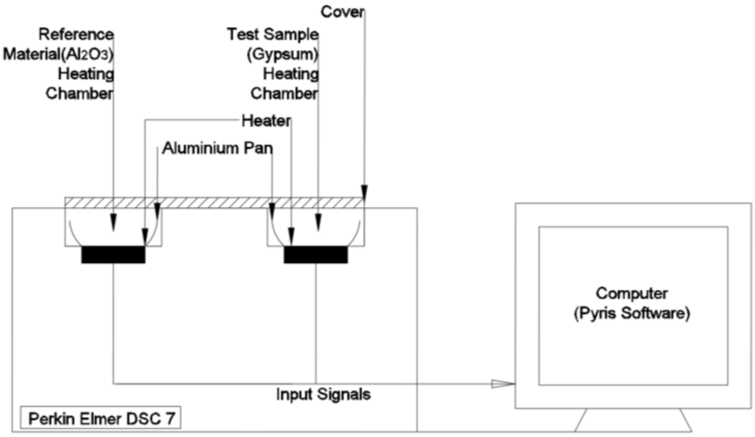

Figure 4.15: Schematic Diagram of DSC Test

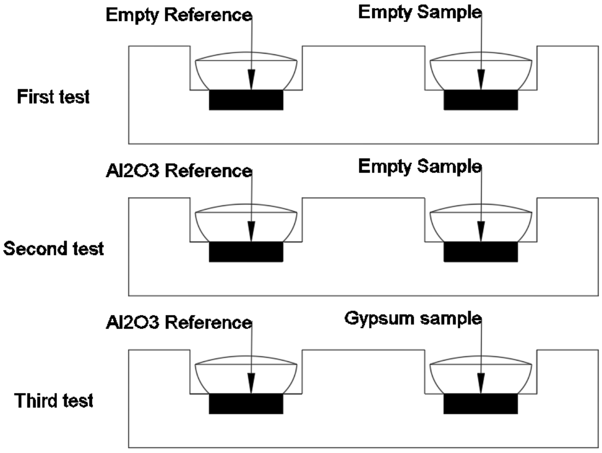

Figure 4.16: DSC Test Procedures for One Gypsum Specimen

Six gypsum specimens ranged from 12.29mg to 12.60mg were tested using DSC method. Table 9 shows the weight of six gypsum specimens. ASTM 1269 (ASTM, 2005) standardize the use of aluminium oxide (Al_2O_3) as a reference material for more reliable result in DSC test. This is because the aluminium oxide is a well-known material with standardized values of specific heat capacity given in ASTM1269 (ASTM, 2005).

The assessment of specific heat capacity of gypsum specimen is given in ASTM1269 (ASTM, 2005). Eq. 4-1 shows the mathematical expression of the specific heat capacity of gypsum determined by multiplying heat flow ratio and mass ratio as correction factors of aluminium oxide. Therefore, the heat flow of gypsum specimen, aluminium oxide and empty aluminium crucible are required in DSC tests.

$$C_p = \frac{HF_{sample} - HF_{blank}}{HF_{ref} - HF_{blank}} \times \frac{Mass_{ref}}{Mass_{sample}} \times C_{p,ref}(T) \qquad \text{Eq. 4-1}$$

Where: Cp(T) indicates the gypsum specimen specific heat per unit mass at a given temperature; HF_{sample} represents heat flow of gypsum at an instantaneous temperature; HF_{blank} denoted as the heat flow of the empty crucible at a given temperature; HF_{ref} indicates the heat flow of reference material aluminium oxide at an instantaneous temperature: $Mass_{Sample}$ represents the mass of the gypsum specimen; $C_{p,ref}$ (T) denoted as the aluminium oxide specific heat capacity at a given temperature.

The procedures of DSC test for a gypsum specimen is in accordance to ASTM1269 (ASTM, 2005). The test was conducted with two empty aluminium pans. Then, the test was performed with aluminium oxide power inserted in one pan, and the other aluminium pan is remained empty. The heat flow of aluminium oxide power was recorded. Lastly, the final test was performed with aluminium oxide powder inserted in one pan, and gypsum powder in the other pan.

Figure 4.15 shows a schematic diagram of DSC test includes a Perkin Elmer DSC7 connected to a computer. The aluminium oxide and gypsum powder were inserted into two aluminium pans, respectively. The aluminium pans were covered by lids using a pan crimper as shown in Figure 4.16. The DSC 7 comprised of two heating chambers, the reference material aluminium oxide (Al_2O_3) was inserted into left hand side heating chamber. Besides, the gypsum specimen was placed in the right-hand side heating chamber.

4.3.1 DSC Results

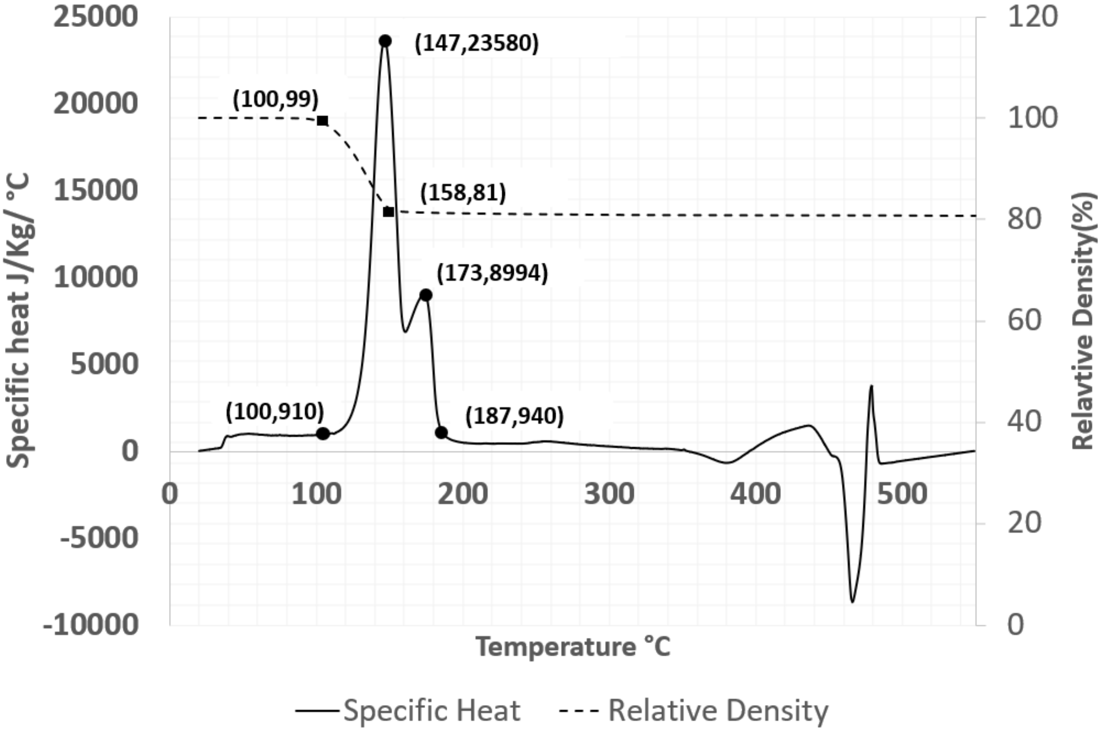

Figure 4.17: Specific Heat Capacity of Gypsum

Figure 4.17 shows the results of DSC test for gypsum powder. The relative density or moisture loss of gypsum was superimposed into the graph to aid the discussion of specific heat capacity of gypsum powder. There are three peak values observed in Figure 4.17. These are, first, second and third dehydration of gypsum specimens. The tested gypsum underwent first and second dehydration at the temperature of 147 °C and 173 °C, respectively. The temperatures of first and second dehydration are close to results of Keerthan and Mahendran (2012). They reported the temperature of first dehydration and second dehydration obtained around 140 °C and 170 °C, respectively.

When the gypsum specimen is heated, the water content in gypsum specimen absorbed heat and underwent evaporation which require 23,580 J/kg/ °C of specific heat capacity at 147 °C. The relative density curve shows 19% of water loss at a temperature of 158 °C. The first peak of specific heat curve agrees well with the relative density curve. The specific heat of first dehydration in this test had a difference of 7.2% relative to 22,000 J/kg/ ℃ of specific heat capacity which recorded by Keerthan and Mahendran (2012). For the case of second dehydration, the specific heat capacity obtained in this test was 8994 J/kg/ ℃. In contrast, Keerthan and Mahendran (2012) recorded 13,000 J/kg/ ℃ of specific heat capacity.

The third peak of specific heat curve occurred at a temperature of 466 ℃. This observation is similar to DSC test results obtained by Keerthan and Mahendran (2012), Gunawan (2011) and Manzello *et al.* (2007). The occurrence of third dehydration was due to the molecular structure of soluble crystal changed itself into a lower insoluble energy state (Gunawan, 2011; Manzello *et al.*, 2007).

4.4 Gypsum Board Furnace Tests

4.4.1 General

When gypsum is exposed to fire on one side, heat is transferred from hot surface to cold surface, or across the thickness of the gypsum board. It is necessary to determine the temperature development of hot surface and cold surface of gypsum board to investigate thermal performance of gypsum board. Therefore, four furnace tests were carried out to assess the temperature against time profile for hot and cold surfaces of gypsum board. In addition, the furnace test results are used to validate the thermal properties of gypsum board through application of heat transfer in finite element analysis later.

4.4.2 Gypsum Specimen

The gypsum board tested was 15 mm thick Gyprock Fireline manufactured by British Gypsum. The gypsum board originally manufactured with a dimension of 2400 mm × 1200 mm. Four 360 mm × 360 mm gypsum board specimens were prepared by using an electric saw cut.

4.4.3 Thermocouple Layout

Figure 4.18 shows a 360 × 360 mm gypsum specimen with a heating boundary of 200 × 200 mm. A total number of ten thermocouples were installed on hot and cold surface of gypsum specimens. Thermocouple wires T1, T2, T3, T4 and T5 were installed on the ambient surface. Whereby, Thermocouple wires T6, T7, T8, T9 and T10 were connected to the exposed surface. The thermocouple configuration followed Rahmanian (2012).

Rahmanian (2012) assumed the heat transfer from hot surface to cold surface of gypsum board as one-dimensional heat transfer. Temperature measurement focused on the centre point of the gypsum specimen. Figure 4.19 and Figure 4.20 show the horizontal cross-sectional view at middle of the gypsum specimen. Temperatures point T10 and T5 were recorded. In addition, other eight thermocouples located at four corners of a 150 x 150mm square were used to inspect the reasonability of one dimensional heat flow assumption as cited by Rahmanian (2012).

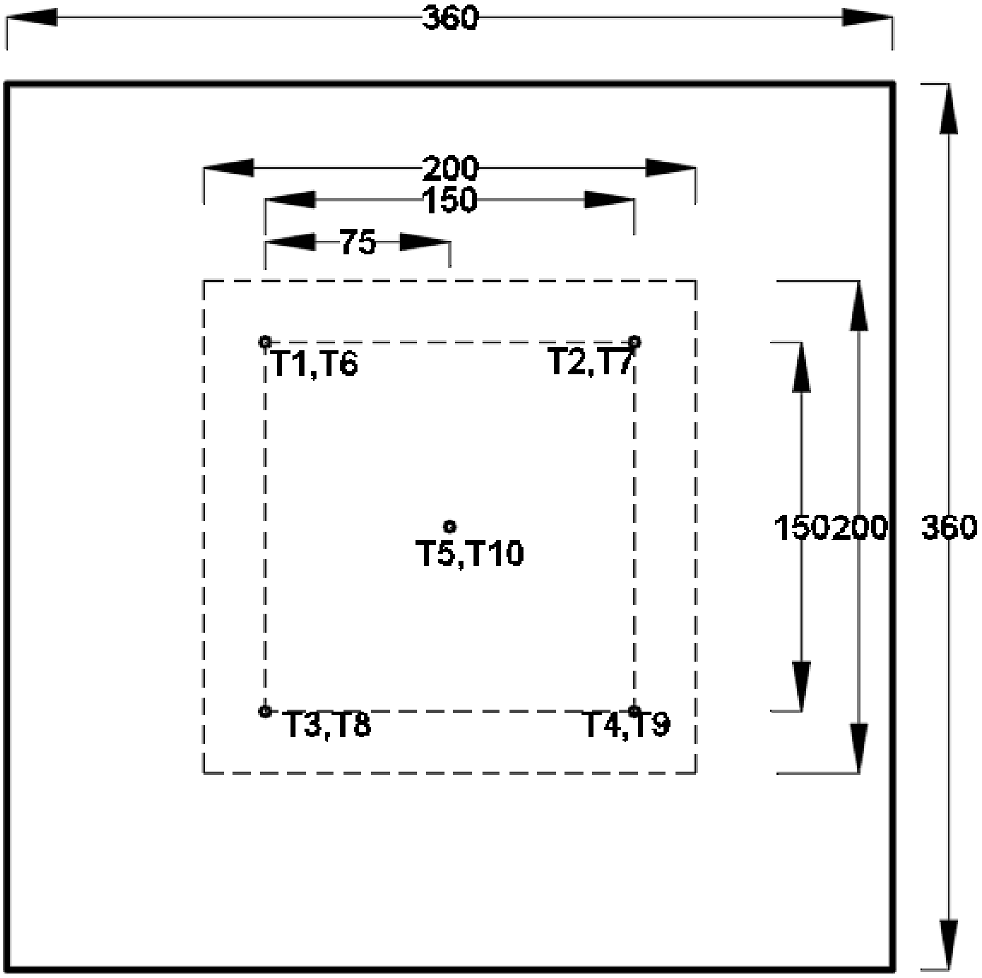

Figure 4.18: Plan View of Gypsum Board Specimen

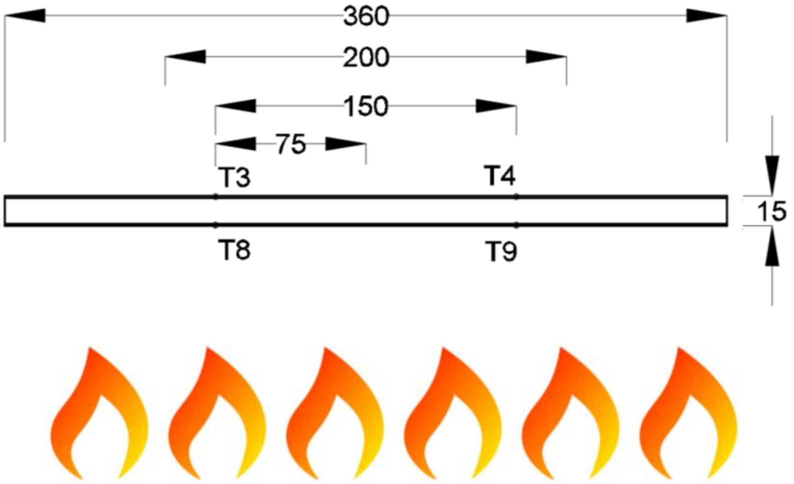

Figure 4.19: Horizontal Cross-Sectional View of Central Thermocouple

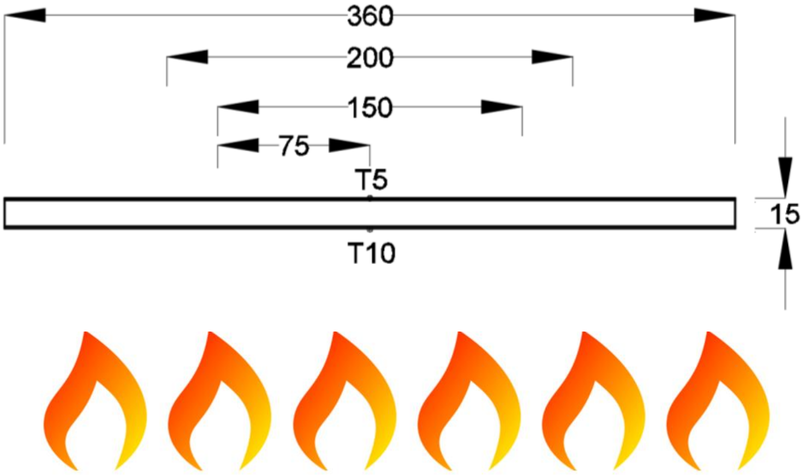

Figure 4.20: Horizontal Cross-Sectional View of Corner Thermocouples

4.4.4 Furnace Tests Instrumentations

4.4.4.1 Furnace

A LENTON furnace was in for four tests included a trial test. The LENTON AWF 12/12 having specification of maximum operating temperature of 1200℃. Figure 4.21 shows the furnace used in this test. Rapid heating and maximum temperature uniformity are provided by two side panel heating elements of ceramic fibre including wire spirals freely radiating from sinusoidal grooves. A door switch isolates power from the heating elements whenever the door is opened for maximum operator safety. Table 10 shows the furnace specification.

Figure 4.21: LENTON AWF12/12 Furnace Type 3216

Table 10: LENTON Furnace Specification

Model	AWF 12/12 Type 3216 Programmer
Maximum temperature (℃)	1200
Maximum continuous temperature (℃)	1150
Time to temperature (minutes)	80
Furnace chamber dimensions (h × w × d , mm)	200 × 200 × 300
External dimensions (h × w × d , mm)	700 × 555 × 615
Chamber capacity(*l*)	12
Maximum power (kW)	2.75
Net Weight (kg)	54

4.4.4.2 Data Logger

Thermocouple type K wires were connected to a data logger to record the temperature readings at 1 second interval. Figure 4.22 shows the GRAPTHEC Mini Logger G220 used in this furnace test. The data logger was capable in handling ten channels of thermocouple. The data logger was integrated with a LCD monitor to display the temperature development of each thermocouple channel. GL 220 data logger also has a built in 2GB of flash memory to store data.

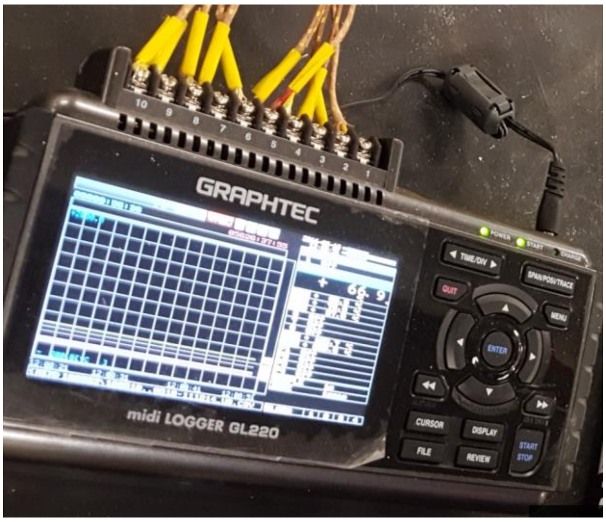

Figure 4.22: GRAPHTEC Mini Logger GL220

4.4.5 Small-Scale Fire Tests Setup

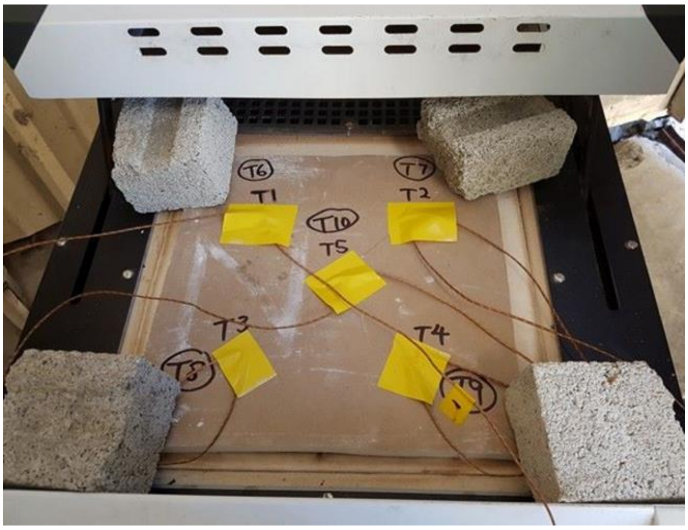

Figure 4.23: Furnace Test Setup

The furnace was programmed to deliver ISO-834 (ISO, 1999) heating profile. Figure 4.23 shows the test setup for the furnace test of the gypsum board. The furnace only allows eight different input of heat rates. Therefore, ISO-834 (ISO, 1999) curve was divided into eight different segments as shown in Figure 4.24. The heat rate of each segment was assessed linearly. Figure 4.24 shows the greater curvature of curve lied within 0 to 15 minutes. To obtain a better approximation, smaller sizes of segment number 1,2,3, and 4 were formed of 15minutes intervals. The larger segment number 5,6,7, and 8 were formed beyond 15min as the curve tends to vary almost linearly.

The heat rate inputs for furnace were tabulated in Table 11. The furnace was set to programmed ISO-834 (ISO,1999) heating profile. In trial run, the temperatures in the furnace were measured by using a thermocouple wire with programmed ISO-834 (ISO, 1999) heating profile. The result of the heating profile was compared to ISO-834 (ISO, 1999) curve as shown in Figure 4.25. The result shows the heating profile of furnace was in good agreement with ISO-834 heating profile.

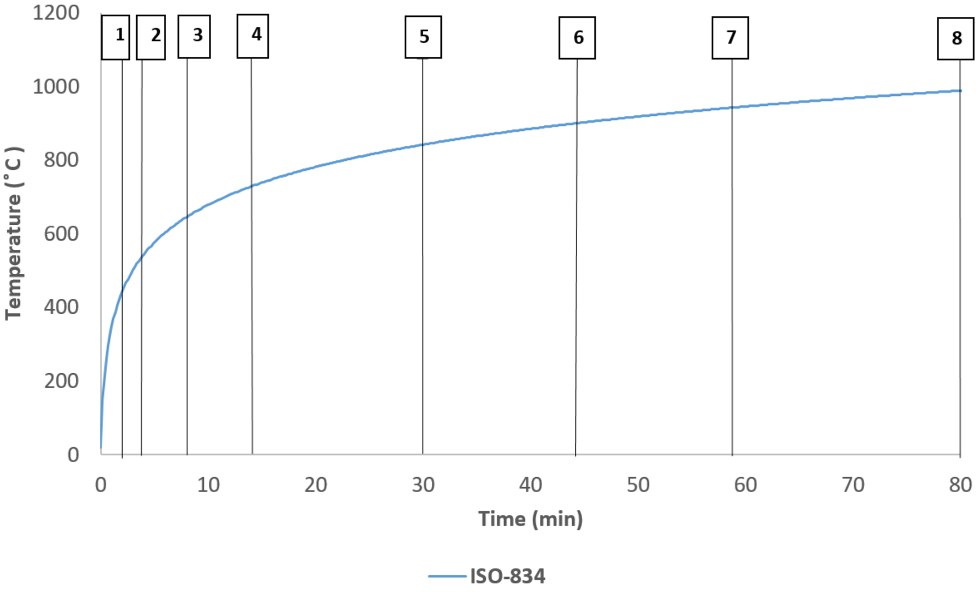

Figure 4.24: ISO-834 Heating Profile Input for Furnace (ISO, 1999)

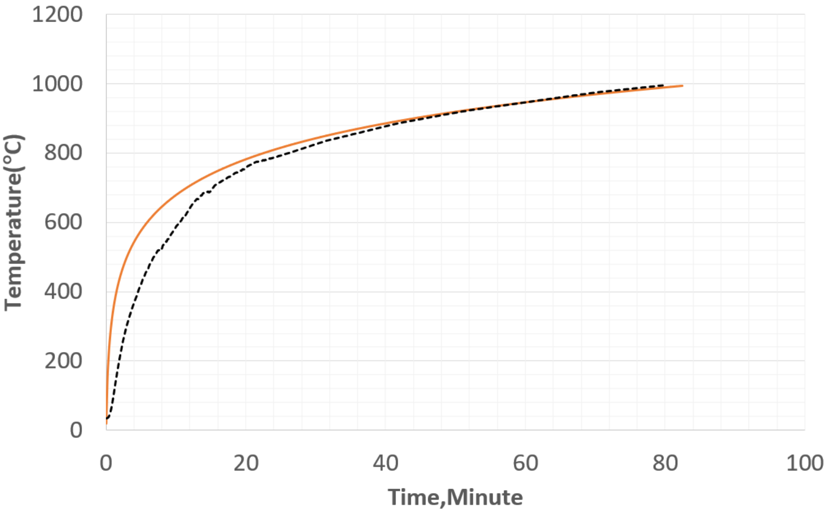

Figure 4.25: ISO-834 and Furnace Heating Curves

Table 11: Heat Rates Input for Furnace

Segment	1	2	3	4	5	6	7	8
Heat Rate (°C/min)	212	44	23	13	6.9	4	2.9	2.2

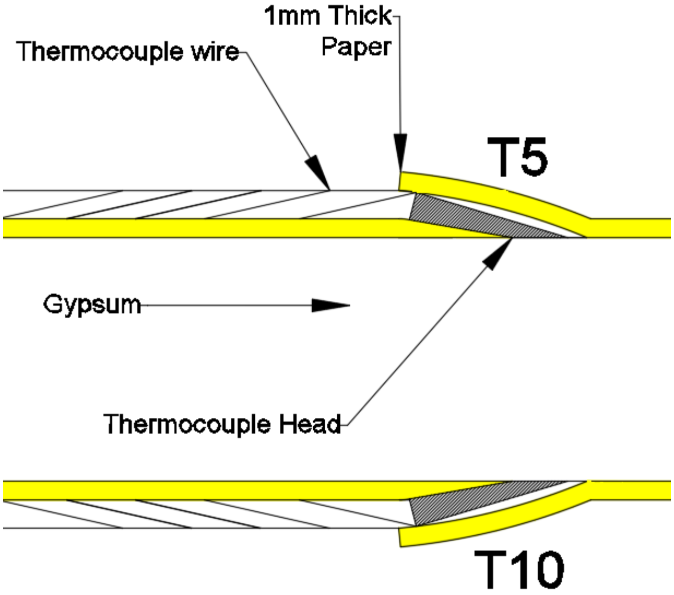

Figure 4.26: Thermocouple Installation of Gypsum Specimens

Figure 4.26 shows a typical installation of thermocouple wire at centre of the gypsum board specimen. A completed setup for gypsum specimen is shown in Figure 4.23.

4.4.6 Furnace Test Results

A total of 3 samples of gypsum board were tested under ISO 834 (ISO, 1999) for 80 minutes. The focus of the small-scale fire test is to obtain the temperature development at the ambient surface. More importantly, the temperature against time curve obtained at the ambient surface is used to verify the thermal properties of gypsum board as described later in Section 5.5. Observations of the test are documented in Appendix E.

The temperature against time curves recorded on the ambient surface shows the similar trend at thermocouple point T1 to T5 as shown in Figure 4.27. The results show the similar trend with the results obtained by Rahmanian (2012) and she claimed that the heat flow in the specimens is dominated in one dimension across the thickness of the gypsum board. The average temperature of the ambient surface for specimen 2 is plotted as in Figure 4.28. Test specimen 2 had failed due to the burning of laminated paper on its ambient side. The failure temperate of 267.62 °C was recorded at a time of 31 minutes and 28 seconds. Figure 4.29 shows the photograph of test specimen 2 at 31 minutes and 28 seconds. The standard ISO 834 (ISO, 1999) and AS 1530.4 (SA, 2005) specify the failure criteria of gypsum board when the average temperature rise on the unexposed surface exceeds 140 °C or the maximum temperature rise at any unexposed temperature point exceeds 180 °C. Thus, the tests shown that the failure criteria proposed by ISO 834 (ISO, 1999) and AS 1530.4 (SA, 2005) are conservative.

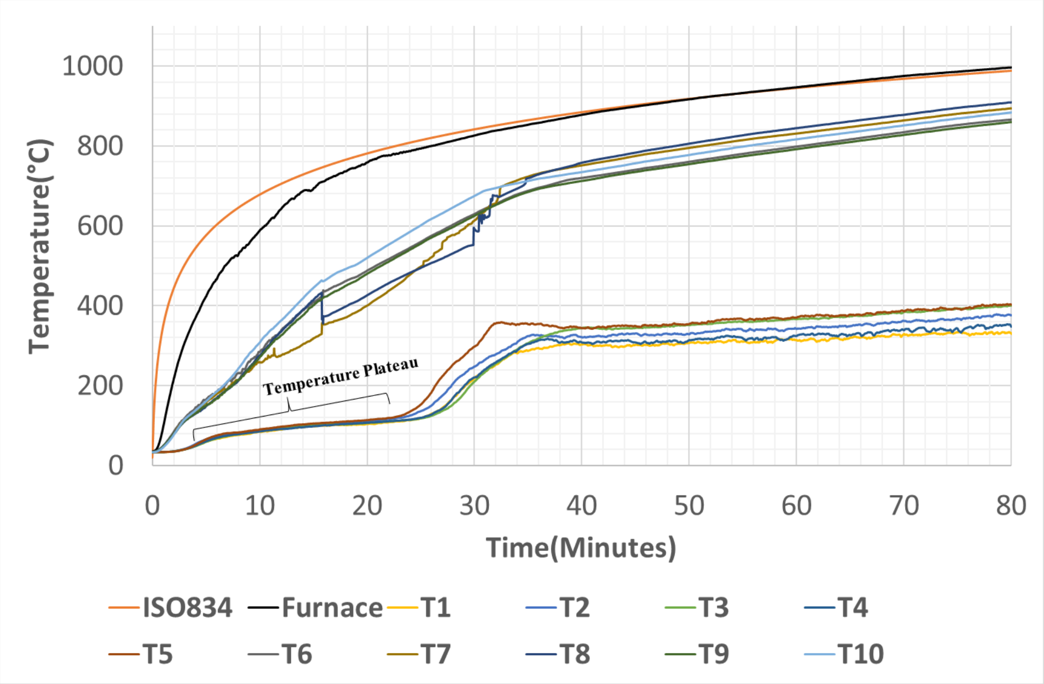

Figure 4.27: Temperature against Time Curves of Specimen 2

Moreover, the TGA results in Section 4.2.3 reported the evaporation initiated approximately at 100 °C and 19% of moisture has been lost at 158 °C. In Figure 4.27, the temperature plateau as described by Rahmanian (2012) shows the effect of chemically bound water in gypsum where most of the temperature and time are delayed in this region. The longer the temperature plateau, the more the time and temperature delay at ambient surface of gypsum board. Therefore, this is confirmed by the TGA results had shown the dehydration has occurred from 100 °C to 158 °C.

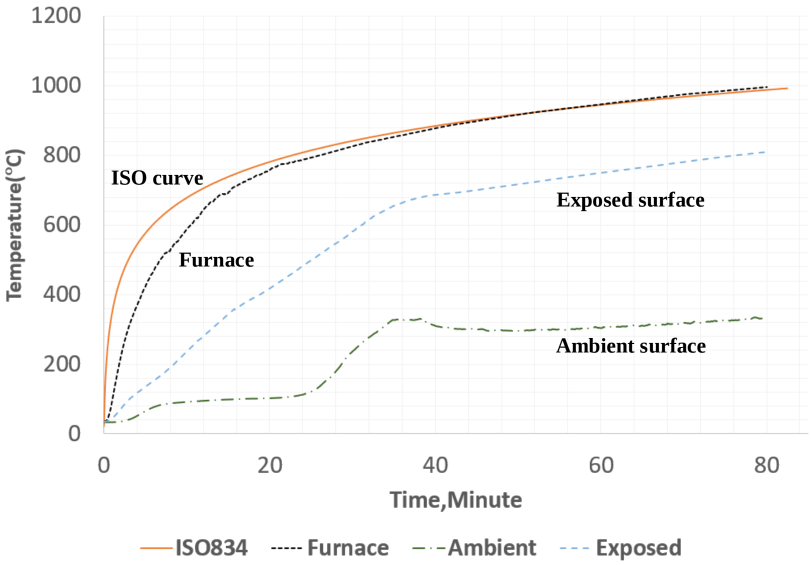

Figure 4.28: **Small-Scale Test Results Specimen 2 (Averaged Temperatures)**

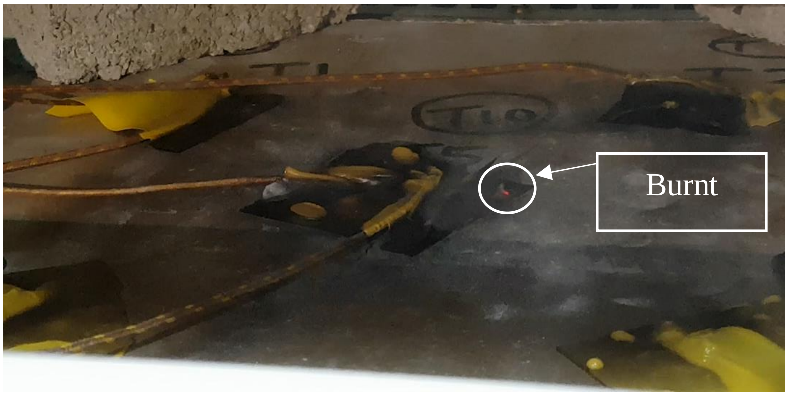

Figure 4.29: **Ambient Side Paper Burnt at 31 minutes 28 seconds**

4.5 Conclusions

Tests on cold-formed steel and gypsum board were carried out to obtain its material property for finite element modelling. For cold-formed steel, coupon tests were conducted to determine its stress-strain curve at ambient temperature. For gypsum board, thermogravimetric analysis (TGA) and differential scanning calorimetry (DSC) tests were performed to determine the density loss and specific heat of gypsum board. Furnace tests were conducted to obtain the temperature development of cold and hot surfaces for gypsum boards. The results of furnace tests were also used to validate the thermal conductivity of gypsum board in the finite element modelling as described in Chapter 5.

5 Finite-Element Modelling

5.1 Introduction

Full-scale field fire tests of cold-formed steel structure is often expensive and time-consuming. Nowadays, Finite Element Analysis (FEA) has been used by researchers (Pyl *et al.*, 2012, Johnston *et al.*, 2014) for economical solution to study the collapse behaviour of cold-formed steel (CFS) structures under natural fire. Their FE models were validated against experimental full-scale fire test. Such validated FE model can represent a close form of prediction for collapse behaviour of cold-formed steel structure.

This chapter describes the development of non-linear elastic-plastic implicit dynamic finite element (FE) model for CFS structure. Finite element software ABAQUS/CAE version 6.14 was used to model the cold-formed steel structure in the full-scale fire test as shown in Figure 5.1. The FE results were verified against the results obtained from the full-scale fire test as described in Chapter 6.

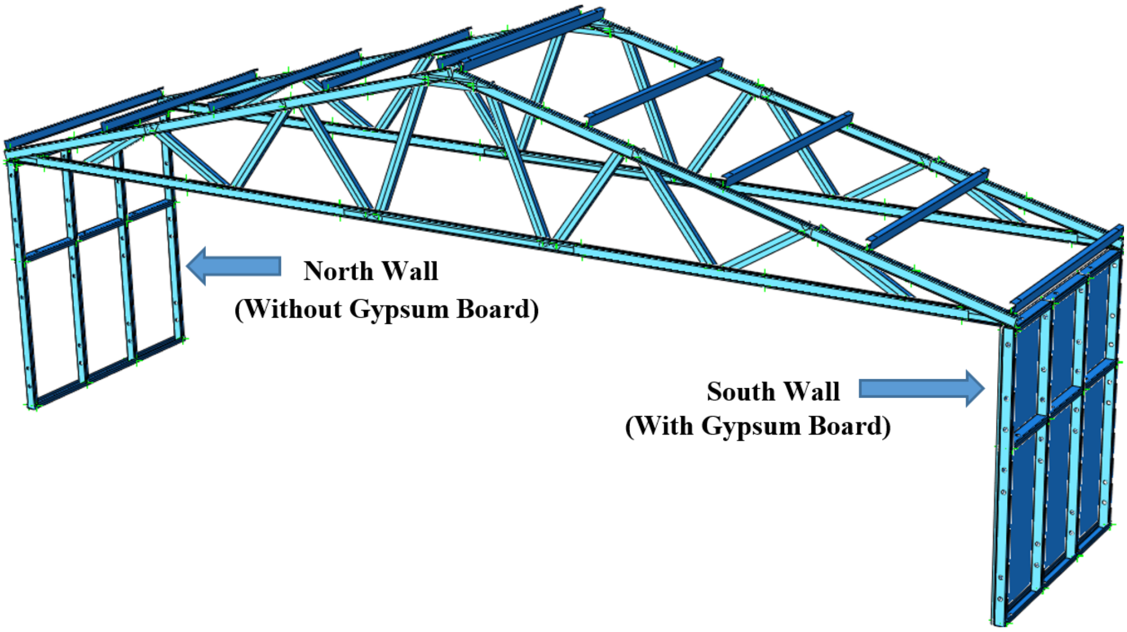

Figure 5.1: Cold-formed Steel Structure FE model

5.2 Overview of Numerical Modelling

In ABAQUS software used, sequentially coupled thermal-stress analysis has been carried out to simulate the collapse behaviour of the cold-formed steel structure. Figure 5.2 shows a flowchart of sequentially coupled thermal-stress analysis.

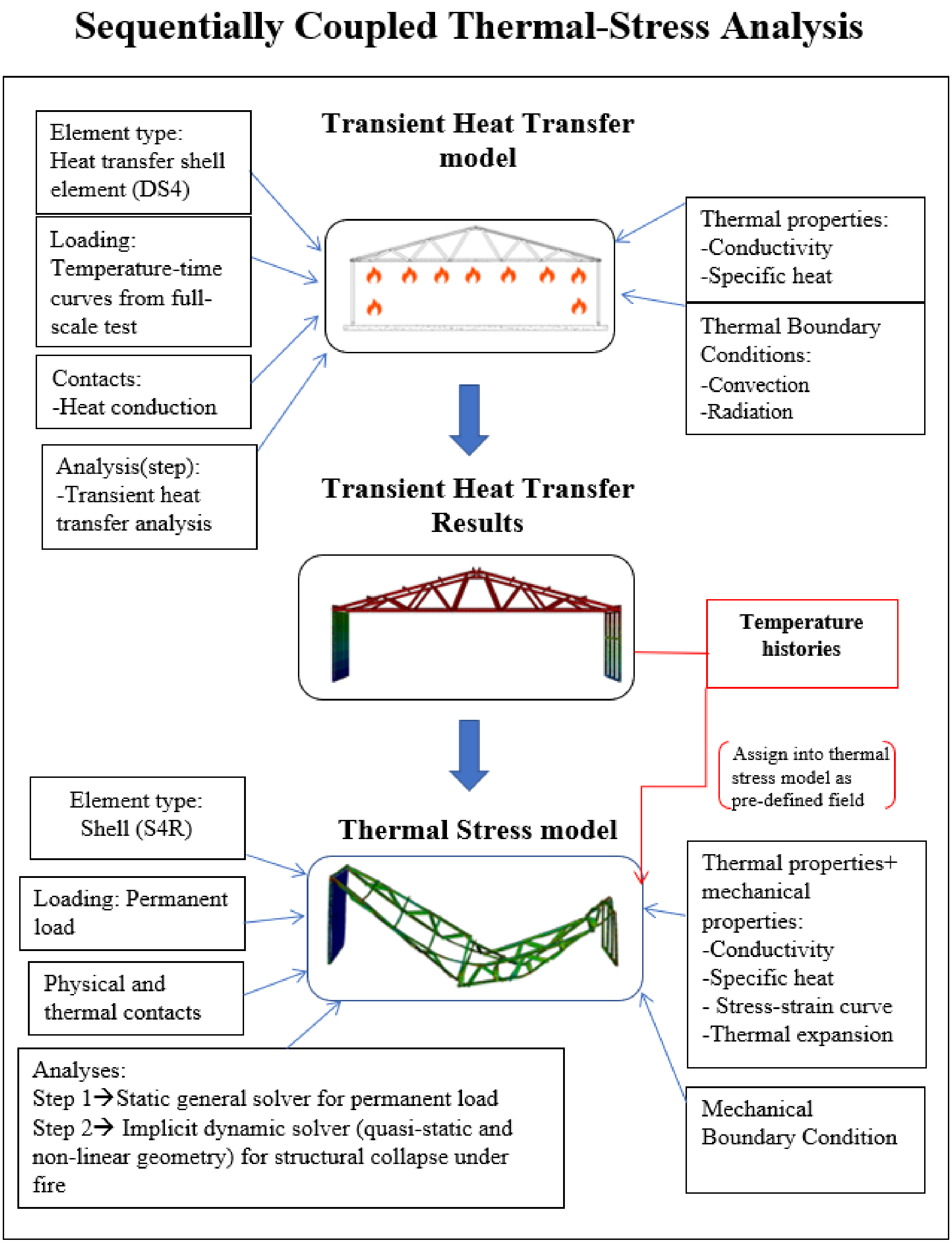

Figure 5.2: Sequentially Coupled Thermal-Stress analysis

In ABAQUS software, the transient heat transfer analysis was chosen and first performed in the transient heat transfer model to obtain the temperature field of the cold-formed steel members and gypsum board, without consideration of other mechanical load. This model requires the appropriate assignment of thermal properties of CFS and gypsum board, element type for heat transfer analysis, thermal boundary conditions in form of heat convection and radiation, contacts to enabling heat condition and, loading in terms of temperature against time curves obtained from the full-scale fire test.

Secondly, temperature histories obtained from transient heat transfer analysis were applied to thermal stress model. Thermal stress model undergoes two steps of analysis, i.e.:
(1) Step 1 used the static general solver to simulate permanent loads on the roof;
(2) Step 2 used the implicit dynamic solver with the quasi-static application and, non-linear geometry (NLGEOM) to simulate the collapse behaviour of the CFS structure.

The thermal stress model was developed with the appropriate assignment of thermal and mechanical properties of CFS and gypsum board, mechanical boundary conditions, physical contact between two bodies of steel-steel and steel-gypsum, thermal contact by means of heat conduction, and mechanical loads in terms of permanent load on the roof.

Assumptions for the FE model includes:

1) Initial geometric imperfections are not included in the CFS model. This is because the initial geometric imperfection has minimal effects on the CFS members at elevated temperatures as studied by Feng (2003), Ariyanayagam and Mahendran (2014b) and, Cheng (2015).

2) The focus of this study is not into connections. In the fire test, failure of the CFS structure was due to member buckling rather than failure of screws around the joint. Therefore, the connections in the CFS model were assumed as rigid connection.

3) The base of wall framings was assumed as pinned base condition to simulate the worst-case scenario. This may give lower bound results (i.e displacement against time curves). Whereas, using fully fixed base condition may lead to overestimation of FE results when compared to the fire test results.

5.3 Theoretical Background of Analyses used in FE Modelling

5.3.1 Transient Heat Transfer Analysis

Heat energy is transferred when two systems with different temperature contacted with each other. The basic energy balance equation used to formulate the heat exchange is shown in Eq. 5-1 (ABAQUS, 2014).

$$\int \rho \, \dot{U} dV = \int q \, dS + \int r \, dV \qquad \text{Eq. 5-1}$$

Where V is a volume of solid material, with surface area S; ρ is the density of the material; $\dot{U}$ is the material time rate of the internal energy; q is the heat flux per unit area of the body, flowing into the body; and r is the heat supplied externally into the body per unit volume. It is assumed that the thermal problems are independent of mechanical problems as such the $U = U(\theta)$, where θ is the temperature of the material and, q and r are independent on the strains or displacement of the body.

When structural member is exposed to fire, heat can be transferred in the form of conduction, convection and radiation. Purkiss and Li (2013) defined the heat conduction as the transfer of thermal energy from one place to another through a solid or fluid due to the temperature difference between the two places. The transfer of thermal energy occurs at the molecular and atomic levels without net mass motion of the material. The rate equation for heat conduction is formulated by Fourier's law as shown in Eq. 5-2. Using the energy balance equation with Fourier's law yields Eq. 5-3.

$$q = -\lambda \nabla \theta \qquad \text{Eq. 5-2}$$

$$\rho \, c \frac{\partial \theta}{\partial t} = \nabla \cdot (\nabla \lambda \theta) + U \qquad \text{Eq. 5-3}$$

Where q is the heat flux per unit area, λ is the thermal conductivity tensor, θ is the temperature, c is the specific heat, t is the time and, U is the internal heat generation rate per unit volume. It must be noted that the specific heat and thermal conductivity for steel and gypsum board are temperature dependent as described in Section 5.4.4. Therefore, the heat transfer was solved as a transient case due to non-linearity of specific heat and thermal conductivity of steel and gypsum board.

In addition, the heat convection and radiation emitted on the surfaces of structural member which usually treated as boundary conditions. Heat convection is transfer of thermal energy through a fluid due to motion of the fluid. Whereas radiation is transfer of thermal energy between two location by an electromagnetic wave that requires no medium (Purkiss and Li, 2013). The heat convection and radiation equations are expressed in Eq. 5-4 and Eq. 5-5, respectively.

$$q = h\,(\theta - \theta_s) \qquad \text{Eq. 5-4}$$

$$q = \varepsilon\sigma\,(\theta^4 - {\theta_s}^4) \qquad \text{Eq. 5-5}$$

Where h is the coefficient of convection or the film coefficient, θ_s is the sink temperature, ε is the emissivity of the material and σ is the Stefan-Boltzmann constant with a value of 5.67 × 10^8 W/m^2/°C^4.

5.3.2 Static and Non-Linear Implicit Dynamic Analysis

The step by step numerical analysis of structures in fire condition is traditionally performed by the succession of subsequent static analyses with reference to the changes of the temperature field (Vassart *et al.*, 2004b). If the loads at all degrees of freedom of a structure are denoted as “F” which corresponding to displacements “u”, then Eq. 5-6 is used to obtain the incremental displacements. In non-linear problems, the stiffness of the structure changes with the variation of the strain in the elements and therefore, Newton-Raphson method is used to solve the non-linear equilibrium equations to obtain the solution.

$$[\Delta F] = [K\,][\Delta u] \qquad \text{Eq. 5-6}$$

Where,

$[\Delta F]$	represents the incremental of external applied forces or the out of balance forces.
[K]	is the stiffness matrix of a structure.

$[\Delta u]$ denoted the displacement at the nodes.

It has been discussed in Section 2.7 that the collapse of steel structures in fire are triggered by snap-through buckling of steel members. In the FE analysis, the stiffness of the structure is positive in the pre-critical range as shown in Figure 5.3. However, the structure became unstable after the formation of snap-through in structural members. The stiffness of the structure is further reduced and changed from positive to negative which resulted in numerical failure or divergence. This condition has been observed by Song (2008), O'Meagher *et al.* (1992), Wong (2001) and De Souza Junior (2002). Therefore, the full collapse behaviour of steel structures in fire can only be obtained using implicit dynamic analysis because the static solution could not converge at the snap-through point as shown in Figure 5.3.

To overcome the un-convergence issue associated with the static analysis after the snap-through point in the post critical range, the implicit dynamic method is used after the pre-critical range. Thus, in ABAQUS software, the static solver was used for pre-critical stage and then the implicit dynamic solver was used for post-critical stage when the snap-through or structural instability is detected.

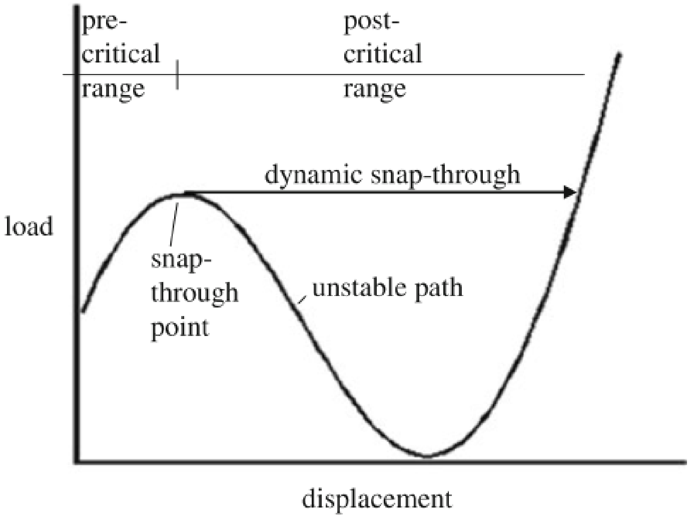

Figure 5.3 Snap-Through Problem (Rust, 2015)

The basic equation for the dynamic analysis is based on D'Alembert's equation as shown in Eq. 5-7.

$$F(t) = Ku + C\dot{u} + M\ddot{u} \qquad \text{Eq. 5-7}$$

Where,

$F(t)$	is the time dependent force
C	is the damping matrix
M	is the mass matrix
u	Is the displacement
$\dot{u}$	is the velocity
$\ddot{u}$	is the acceleration.

Sun *et al.* (2000) described the implicit dynamic method in ABAQUS software used an automatic increment strategy based on the success rate of a full Newton iterative solution method as shown in Eq. 5-8.

$$\Delta u^{i+1} = \Delta u^{i} + K_t^{-1}\,(F^{i} - I^{i}) \qquad \text{Eq. 5-8}$$

Where K_t is the current tangent stiffness matrix, F is the applied load vector, I is the internal force vector and Δu is the increment of displacement. The algorithm of implicit dynamic method defined by Hilber *et al*. (1978) is shown in Eq. 5-9.

$$F^{i+1} = M\ddot{u}^{i+1} + (1+\alpha)Ku^{i+1} - \alpha K u^{i} \qquad \text{Eq. 5-9}$$

Additionally, the algorithm of implicit dynamic is completed by the Newmark formulae for displacement and velocity integration are formulated in Eq. 5-10 and Eq. 5-11 respectively (ABAQUS, 2014).

$$u^{i+1} = u^{i} + \Delta t\dot{u}^{i} + \Delta t^{2}[\,(\tfrac{1}{2} - \beta)\ddot{u}^{i} + \beta\ddot{u}^{i+1}\,] \qquad \text{Eq. 5-10}$$

$$\dot{u}^{i+1}=\dot{u}^{i} + \Delta t[\,(1-\gamma)\ddot{u}^{i} + \gamma\ddot{u}^{i+1}\,] \qquad \text{Eq. 5-11}$$

$$\beta = \frac{1}{4}(1-\alpha^{2}) \qquad \gamma = \frac{1}{2} - \alpha \qquad \frac{1}{2} \leq \alpha \leq 0 \qquad \text{Eq. 5-12}$$

5.4 Development of FE model for Cold-formed Steel Structure

5.4.1 Geometrical Modelling

The FE modelling of the CFS structure was initiated by creating members in the ABAQUS software "Part" module. Figure 5.1 shows the simplified model of the cold-formed steel building. There are two types of elements in ABAQUS software: beam element and shell element. Figure 5.4 shows the beam element whereas Figure 5.5 shows the shell element. Beam elements are the elements that transfer lateral forces and bending moment, while shell element can transfer membrane forces and bending moment. In previous studies, Johnston *et al.* (2014) compared the beam element with shell element used in cold-formed steel portal frame model. Johnston et al concluded that the beam element was not able to accurately capture the effect of buckling on CFS members. Therefore, shell element was used in this model to capture the buckling effect of the cold-formed steel structure.

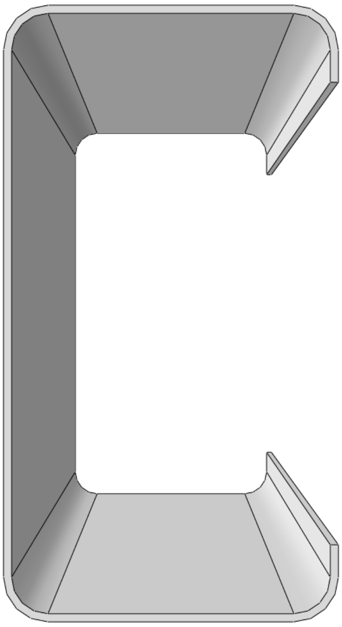

Figure 5.4: Beam Element

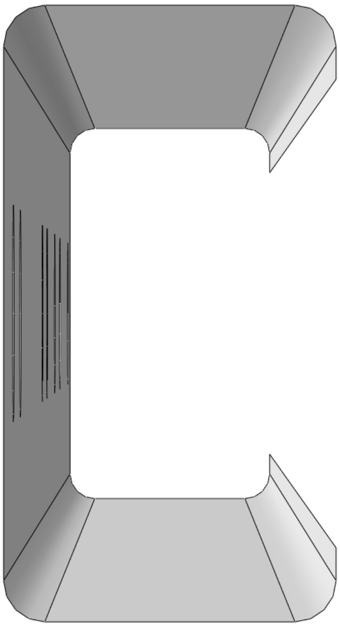

Figure 5.5: Shell Element

5.4.2 Element Type

Modelling of CFS structures involves discretization of the model into small elements or finite elements formed by nodes located at the element edges (Ellobody *et al.*, 2014). Heat transfer shell element DS4 (4-nodes heat transfer shell element) was chosen and used for heat transfer analysis as it provides temperature degree of freedom. For thermal-stress modelling, the mesh type S4R was used in this study. Element type S4R is a general-purpose shell element that includes transverse shear. The S4R element is a stress-displacement shell having four nodes with reduced integration. There are six degrees of freedom per node in S4R element.

Figure 5.6 and Figure 5.7 illustrates S4 shell element and S4R element respectively. Reduced integration shell elements use lower order integration to form the element stiffness which offers more economical computational time compared to the S4 element. Figure 5.7 shows only one integration point at the element centre, whereas Figure 5.6 shows four integration points at the corners. The S4R element also accounts for finite membrane strains and large rotation. The collapse of the cold-formed steel structure in fire test displayed large deformations and buckling. Therefore, the S4R element is suitable for large strain analyses and geometrically non-linear analyses (Ellobody *et.al*, 2014, Johnston *et al.*, 2015).

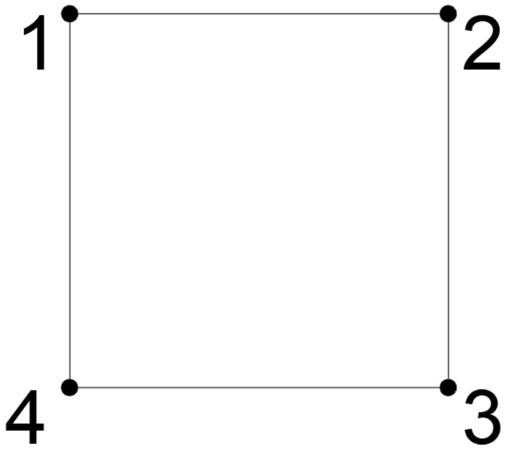

Figure 5.6: S4 Element

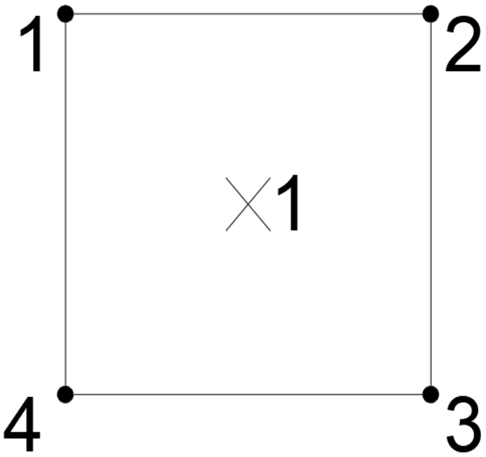

Figure 5.7: S4R Element

5.4.3 Element Size

Appropriate mesh is determined to obtain accurate results with lower computation time through mesh study. Finer mesh size produces a greater number of elements and, provides higher accuracy. But, it requires longer computation time. To determine an optimum mesh, mesh studies were carried out on 50 mm, 30 mm, 20 mm and 10 mm mesh size. Figure 5.8, Figure 5.9, Figure 5.10 and, Figure 5.11 show different mesh sizes created in the FE model.

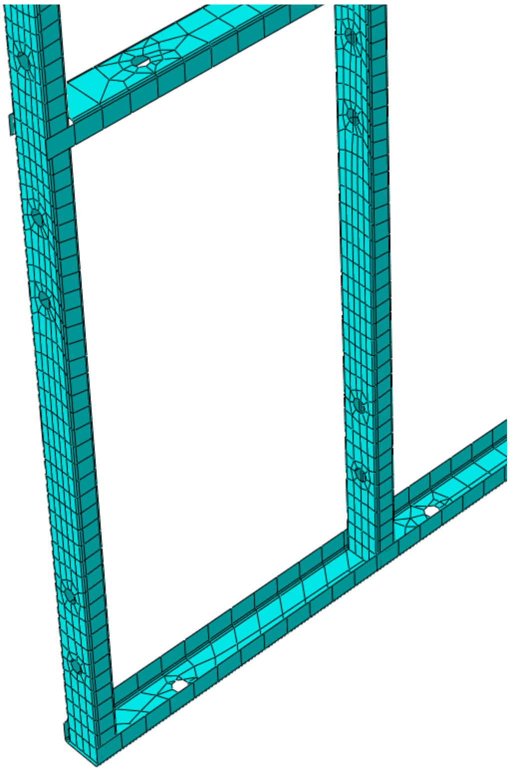

Figure 5.8: **50mm (29118 Elements)**

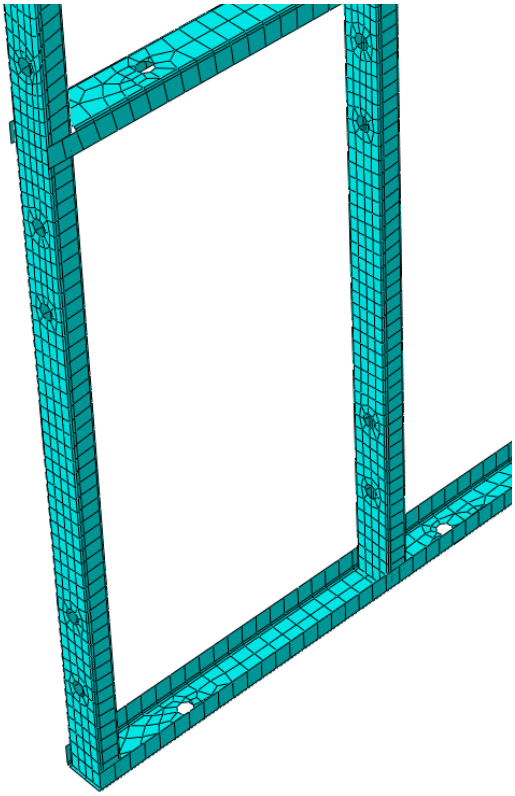

Figure 5.9: **30mm (33977 Elements)**

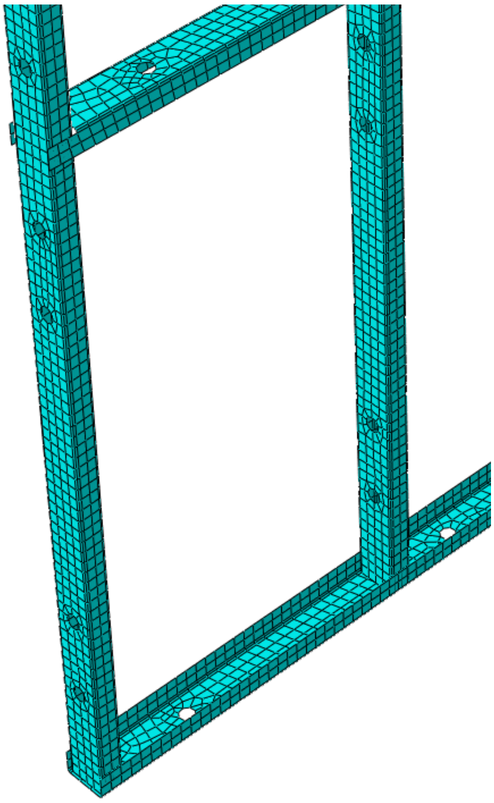

Figure 5.10: **20mm (46623 Elements)**

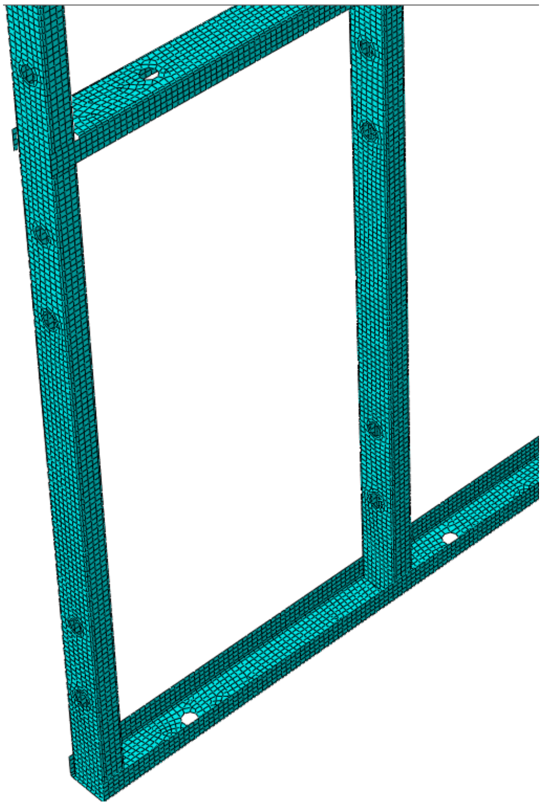

Figure 5.11: **10mm (119944 Elements)**

The results of the mesh study are tabulated in Table 12. The temperature at collapse against the number of elements are shown in Figure 5.12. A suitable mesh size was selected based on the good balance between this collapse temperature and the computational time. The collapse temperature obtained in full-scale field fire test was 622.5℃. In the FE model with 20 mm mesh, which has 46623 number elements, gave the closest collapse temperature of 627℃ with reasonable computational time and accuracy.

Table 12: Convergence Study

Mesh Size, mm	10	20	30	50
Number of Element	119944	46623	33977	29118
Computational Time, Hour	48	31	26	24
Collapse Temperature, ºC	640	627	575	571

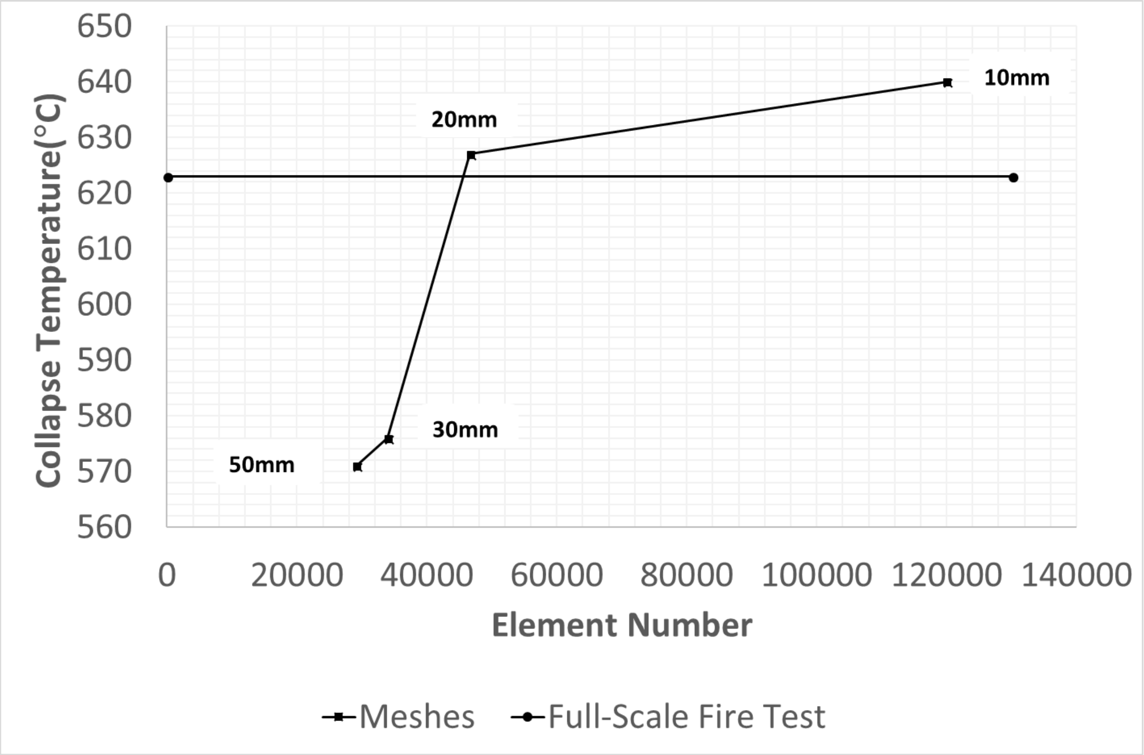

Figure 5.12: Collapse Temperature-Element Number Graph

5.4.4 Material Properties

To model the collapse of cold-formed steel structure, it is required to assign suitable material properties for cold-formed steel and gypsum board. The experimental works on material testing of cold-formed steel and gypsum boards were discussed in Chapter 4. Thermal properties of cold-formed steel and gypsum boards are crucial for heat transfer analysis and thermal-stress analysis. These include thermal stress-strain curves, thermal expansion, thermal conductivity, specific heat capacity and density as a function of temperature.

5.4.4.1 Mechanical Properties of Cold-formed Steel at Elevated Temperatures

To model cold-formed steel, ABAQUS software requires the assignment of true stress-strain curve. The true-stress strain curve equations require the data of nominal stress and nominal strains that obtained from the stress strain-curve as shown in Figure 5.13. To obtain true stress-strain curves, the results of coupon test mentioned in Chapter 4 were assessed using Eq. 5-13 to Eq. 5-15. The true plastic strain values were calculated using nominal plastic stress and plastic strain which are beyond the 0.2% proof stress. To determine true stress, true strain, and true plastic strain:

True Stress, $\sigma_{true} = \sigma_{nominal}\,(1 + \epsilon_{nominal})$ Eq. 5-13

True Strain, $\epsilon_{true} = \ln\,(1 + \epsilon_{nominal})$ Eq. 5-14

True Plastic Strain ,$\epsilon_{plastic} = \epsilon_{true} - \frac{\sigma_{true}}{E}$ Eq. 5-15

Where,

$\sigma_{nominal}$ indicates the nominal stress

$\varepsilon_{nominal}$ indicates the nominal strain

E indicates the young’s modulus of elasticity

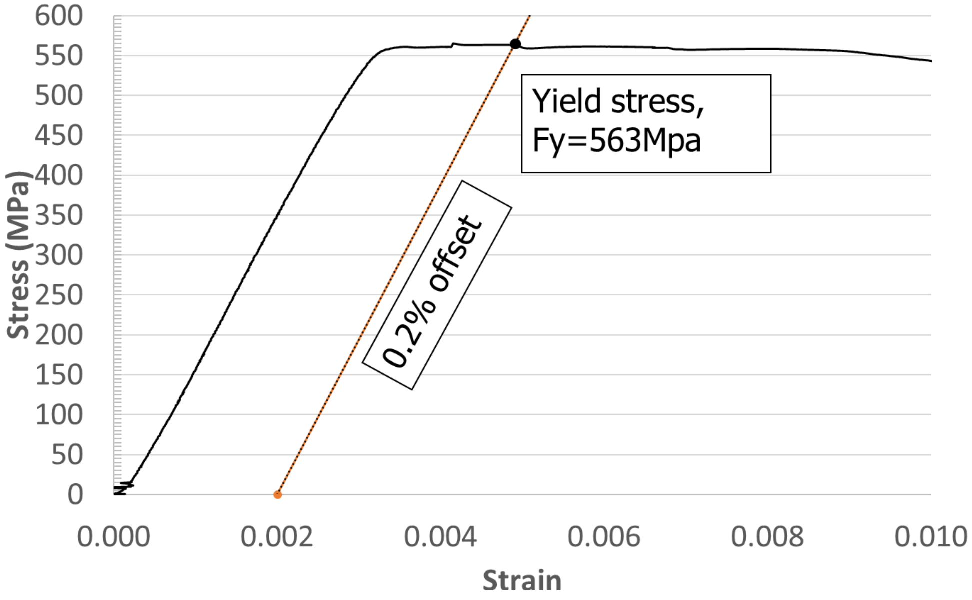

Figure 5.13: Stress-Strain Curve and 0.2% Proof Stress

Moreover, the true stress-strain curve at ambient temperature was converted into stress-strain curves at elevated temperatures using empirical formula proposed by Kankanamge and Mahendran (2011). The true stress-strain curves at elevated temperatures are shown in Figure 5.14. The stresses at elevated temperature σ_T were assessed by Eq. 5-16 to Eq. 5-18 with corresponding to 100 °C, 200 °C, 300 °C, 400 °C, 500 °C, 600 °C, 700 °C and 800 °C. The values of σ_{ambient} were taken as the true stresses at the ambient temperature calculated earlier.

To determine the reduction factors of yield strength for G550 steel,

$$\frac{\sigma_T}{\sigma_{\text{ambient}}} = -0.000179T + 1.00358 \qquad \text{for } 20\ °C \le T \le 300\ °C \qquad \text{Eq. 5-16}$$

$$\frac{\sigma_T}{\sigma_{\text{ambient}}} = -0.0028T + 1.79 \qquad \text{for } 300\ °C \le T \le 600\ °C \qquad \text{Eq. 5-17}$$

$$\frac{\sigma_{yT}}{\sigma_{\text{ambient}}} = -0.0004T + 0.35 \qquad \text{for } 600\ °C \le T \le 800\ °C \qquad \text{Eq. 5-18}$$

To identify the reduction factors of elasticity modulus for G550 steel,

$$\frac{E_T}{E_{\text{ambient}}} = -0.000835T + 1.0167 \qquad \text{for } 20\ °C \le T \le 200\ °C \qquad \text{Eq. 5-19}$$

$$\frac{E_T}{E_{\text{ambient}}} = -0.00135T + 1.1201 \qquad \text{for } 200\text{ °C} \leq T \leq 800\text{ °C} \qquad \text{Eq. 5-20}$$

The Young's modulus E_T, at elevated temperature, were assessed by Eq. 5-19 to Eq. 5-20 with corresponding to 100°C, 200°C, 300°C, 400°C, 500°C, 600°C, 700°C and 800°C. The Young's modulus at ambient temperature E_{ambient}, obtained from the coupon test results was 194.30 Gpa. To assess the value of strain at elevated temperature ε_T, the thermal stresses and thermal young's modulus were further used in Eq. 5-21 to calculate the thermal strain.

$$\varepsilon_T = \frac{\sigma_T}{E_T} + \beta\left(\frac{\sigma_{yT}}{E_T}\right)\left(\frac{\sigma_T}{\sigma_{yT}}\right)^{n_T}$$

$$n_T = -3.05 \text{ x } 10^{-7}T^3 + 0.0005\, T^2 - 0.2615T + 62.653 \qquad \text{for } 20\text{ °C} \leq T \leq 800\text{ °C} \qquad \text{Eq. 5-21}$$

Where,

T	indicates the temperature of steel
σ_T	indicates the applied stress at a defined temperature
σ_{yT}	indicates the applied yield stress at a defined temperature
E_T	indicates the elasticity modulus at respective temperature
β	indicates the coefficient value of 0.86

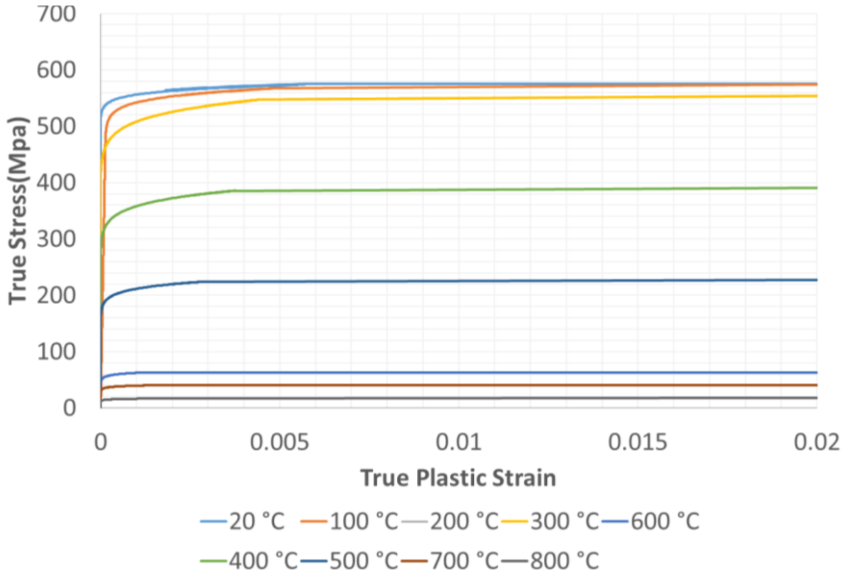

Figure 5.14: True Stress-Strain Curves at Elevated Temperatures

5.4.4.2 Mechanical Properties of Gypsum Board at Elevated Temperatures

The mechanical properties of gypsum board were adopted from Cramer *et al*. (2003). Cramer proposed a set of values for the Young's modulus of gypsum board at elevated temperatures. The relationship of the Young's modulus and temperatures is illustrated in Figure 5.15.

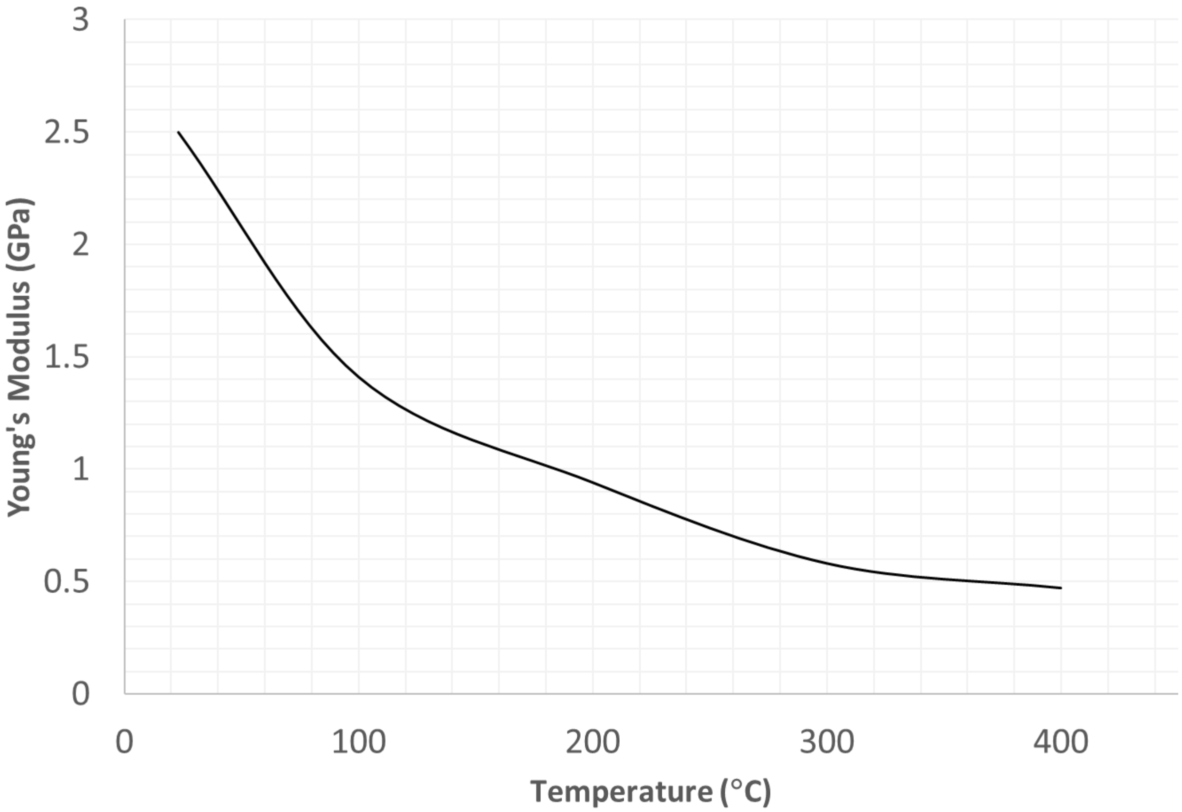

Figure 5.15: Young's Modulus against Temperature Graph of Gypsum Board (Cramer *et al*., 2003)

5.4.4.3 The Density of Cold-formed Steel and Gypsum Board

The density of cold-formed steel was taken as 7850 kg/m^3 and, a value of 0.3 was assigned for the Poisson's ratio (Zhao *et al*., 2005; Gunalan, 2011; Chen and Young, 2007; Johnston, 2014). The Poisson's ratio was assumed independent of temperature (Kaitila, 2002; Zha, 2003; Rahman, 2012).

On the other hand, the density of the gypsum board was taken as 770 kg/m^3 at ambient temperature. This value of density was adopted from Rahmanian (2013) due to the same product of gypsum board (Gyproc Fireline) used in this study. In the case of elevated temperature condition, the average of TGA tests results as described in Section 4.3.3, were assigned in the FE model. Figure 5.16 shows the average density changes at elevated temperatures.

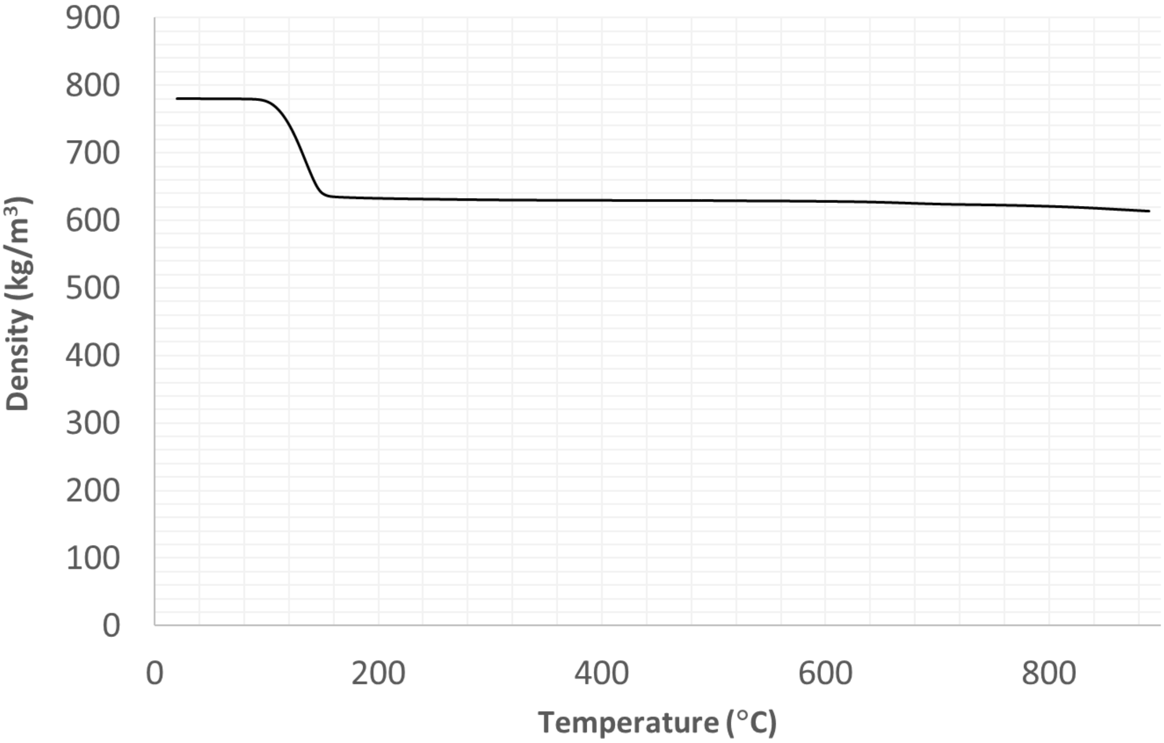

Figure 5.16: Average Gypsum Density-Temperature Graph

5.4.4.4 Cold-formed Steel Specific Heat Capacity

Specific heat capacity measures the heat required to increase the temperature of a substance per unit of mass. Specific heat of cold-formed steel at elevated temperatures was calculated by using Eq. 5-22 to Eq. 5-25 provided in Eurocode 3 Part 1-2 (CEN, 2005). To assess the specific heat of G550 cold-formed steel,

$$Cp = 425+7.73 \times 10^{-1}T-1.69 \times 10^{-3} T^2+ 2.22 \times 10^{-6} T^3 \quad \text{for } 20\ °C < T < 600\ °C \quad \text{Eq. 5-22}$$

$$Cp = 666 + \frac{13002}{738 - T} \quad \text{for } 600\ °C \le T < 735\ °C \quad \text{Eq. 5-23}$$

$$Cp = 545 + \frac{17820}{T - 731} \quad \text{for } 735\ ^\circ C \leq T < 900\ ^\circ C \qquad \text{Eq. 5-24}$$

$$Cp = 650 \quad \text{for } 900\ ^\circ C \leq T \leq 1200\ ^\circ C \qquad \text{Eq. 5-25}$$

Where,

T indicates the temperature of cold-formed steel

Cp indicates the specific heat of cold-formed steel

5.4.4.5 Cold-formed Steel Thermal Conductivity

Thermal conductivities of cold-formed steel at elevated temperatures were calculated by using Eq. 5-26 and Eq. 5-27 which are in accordance with Eurocode 3 Part 1-2 (CEN, 2005). To determine the thermal conductivity of G550 cold-formed steel,

$$k=54-3.33 \times 10^{-2}T \quad \text{for } 20\ ^\circ C < T < 800\ ^\circ C \qquad \text{Eq. 5-26}$$

$$k=27.3 \quad \text{for } 800\ ^\circ C < T \leq 1200\ ^\circ C \qquad \text{Eq. 5-27}$$

Where,

T indicates the temperature of the cold-formed steel

k indicates the thermal conductivity of the cold-formed steel

5.4.4.6 Thermal Expansion of Cold-formed Steel

One of the material properties concerned when steel exposed to elevated temperatures is thermal expansion. The fire induced extra thermal strains in the cold-formed steel members and its underwent thermal expansion. To include the effect of thermal expansion in the FE model, the values of thermal expansion for cold-formed steel at elevated temperatures were calculated by using Eq. 5-28 to

Eq. 5-30 which are in accordance with Eurocode 3 Part 1-2 (CEN, 2005).

$$\frac{\Delta l}{l} = 1.2 \text{ x } 10^{-5}\text{T} + 0.4 \text{ x } 10^{-8}\text{T}^2 - 2.416 \text{ x } 10^{-4} \qquad \text{for } 20\ ^\circ\text{C} \leq \text{T} < 750\ ^\circ\text{C} \qquad \text{Eq. 5-28}$$

$$\frac{\Delta l}{l} = 1.1 \text{ x } 10^{-2} \qquad \text{for } 750\ ^\circ\text{C} \leq \text{T} \leq 860\ ^\circ\text{C} \qquad \text{Eq. 5-29}$$

$$\frac{\Delta l}{l} = 2 \text{ x } 10^{-5}\text{T-}6.2 \text{ x } 10^{-3} \qquad \text{for } 860\ ^\circ\text{C} < \text{T} \leq 1200\ ^\circ\text{C} \qquad \text{Eq. 5-30}$$

Where,

T indicates the temperature of cold-formed steel

l Original length

Δl Changes of length

5.4.4.7 Specific Heat Capacity and Thermal Conductivity of Gypsum Board

The specific heat capacity and thermal conductivity of gypsum board affect the heat conduction. Many researchers (Semitelos *et al.*,2014; Thomas, 2012 ; Rahmanian and Wang, 2012; Keerthan and Mahendran, 2012; Sultan, 1996) carried out the investigations on specific capacity and thermal conductivity of gypsum board. However, the specific heat capacity, thermal conductivity, and its temperatures vary in the results among these researchers. In this research, an idealized specific heat capacity and conductivity were proposed based on the aforementioned experimental tests on gypsum board and, numerical verification. Figure 5.17 and Figure 5.18 shows the specific heat capacity and thermal conductivity curve of gypsum used in the FE model. The details of numerical verification on idealized specific heat capacity and thermal conductivity are described in Section 5.5.

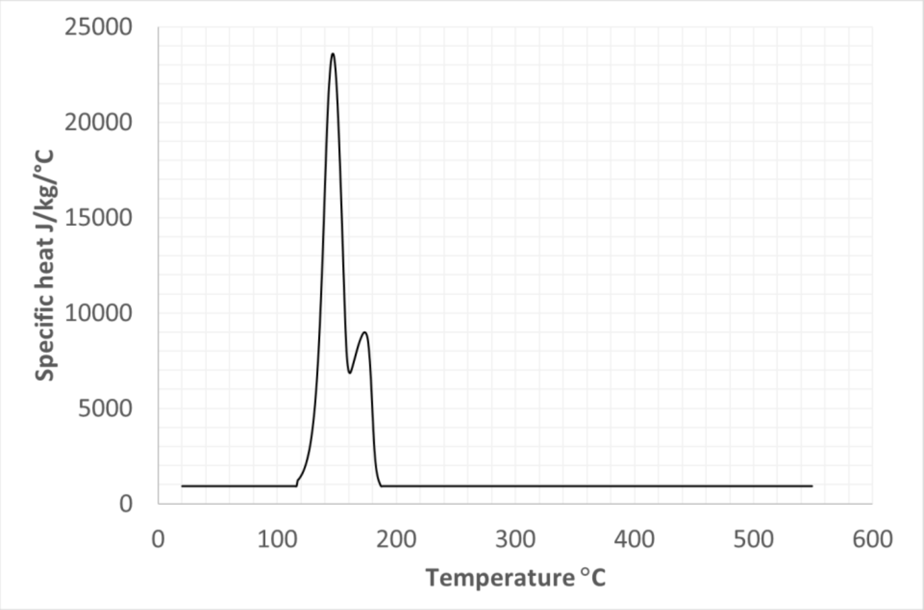

Figure 5.17: Idealized Specific Heat Capacity of Gypsum

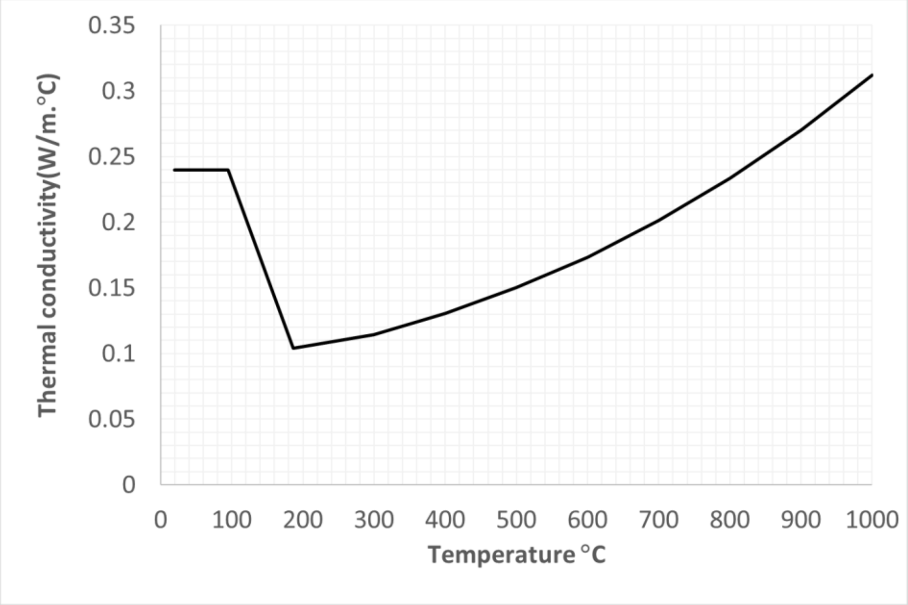

Figure 5.18: Idealized Specific Thermal Conductivity of Gypsum

5.4.4.8 Thermal Expansion of Gypsum Board

In the thermal-stress analysis, it is required to assign the coefficient of thermal expansion of gypsum board. Cramer *et al*. (2003) proposed a set of values for the coefficient of thermal expansion at elevated temperatures. In an elevated temperature condition, the gypsum board was subjected to thermal elongation and shortening as shown in Figure 5.19. To model these effects, the coefficient of thermal expansion was adopted from Cramer *et al*. (2003) in the FE model.

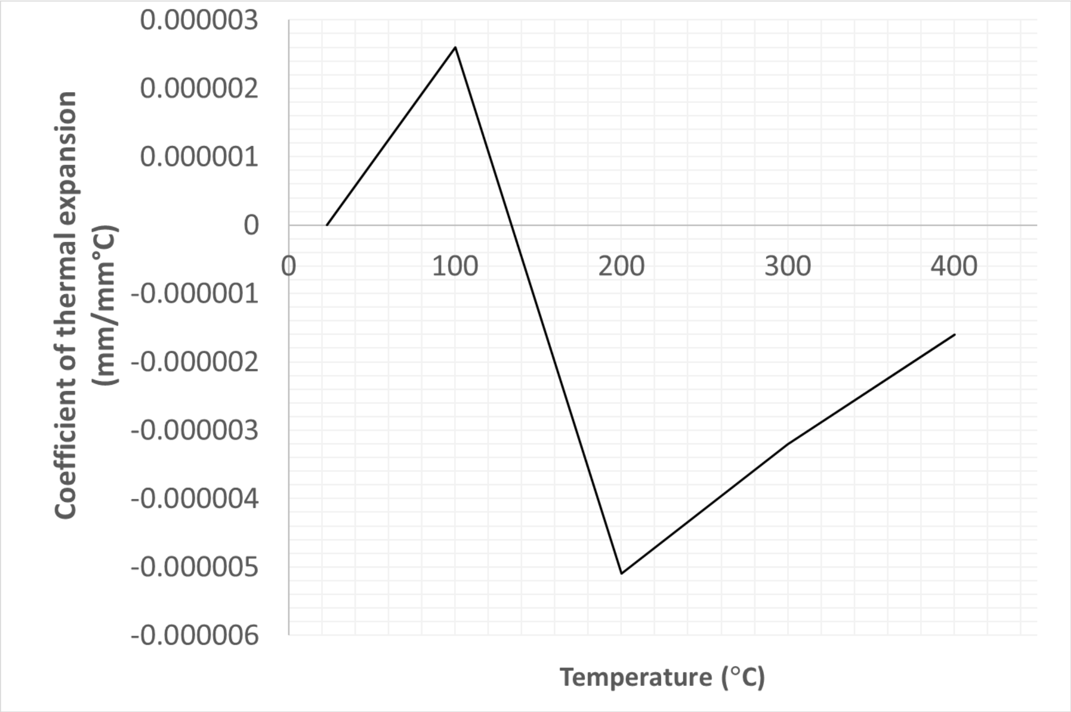

Figure 5.19: Coefficient of Thermal Expansion (Cramer *et al*., 2003)

5.4.5 Boundary Conditions

Boundary conditions are used in finite element models to identify the values of all basic solution variables such as temperature, displacement, and rotations at nodes (Ellobody *et al*., 2014). There are two types of boundary conditions used in this model: thermal boundary condition and mechanical boundary condition. In which, mechanical boundary condition involved restraining or releasing the degree of freedom at the wall base.

5.4.5.1 Thermal Boundary Conditions

There are three modes of heat transfer in the FE model namely, convection, radiation, and conduction. This section describes assignment of thermal boundary conditions in form of thermal convection and radiation in ABAQUS software. Whereas, the modelling of heat conduction of cold-formed steel and gypsum board were discussed in Section 5.4.6.

The thermal convection and radiation were modelled for the cold-formed steel with and without the protection of the gypsum board. Figure 5.20 and Figure 5.21 shows the boundary condition for cold-formed steel with and without gypsum board, respectively. The hot surface of gypsum board was considered as an exposed surface, while the remaining surfaces were taken as ambient surfaces. In the interaction module of ABAQUS software, the thermal convection coefficient at exposed and ambient surfaces was input as 25W/m^2 and 10W/m^2 respectively (Keerthan and Mahendran, 2012). The radiation emissivity on exposed and ambient surfaces was taken as 0.8 and 0.8, respectively. The sink temperature on the exposed side was assigned to follow the temperature against time curve obtained in the full-scale test. Lastly, a temperature of 33℃ was assigned for the ambient surface in according the site temperature in full-scale fire test.

5.4.5.2 Mechanical Boundary Conditions

To model mechanical boundary condition, the model assumed pinned support (U1=U2=U3=0) condition at bottom rails. Figure 5.22 shows the L angle cleats restraint at the base was modelled as the pinned joint in ABAQUS software. In addition, the top rails or, knee joint of the FE model was defined as free end. This allows the assemblies to deflect in-plane direction throughout the simulation.

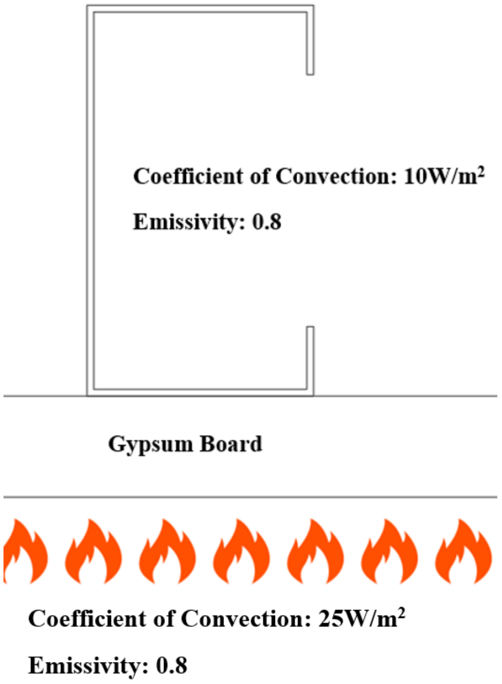

Figure 5.20: Case 1

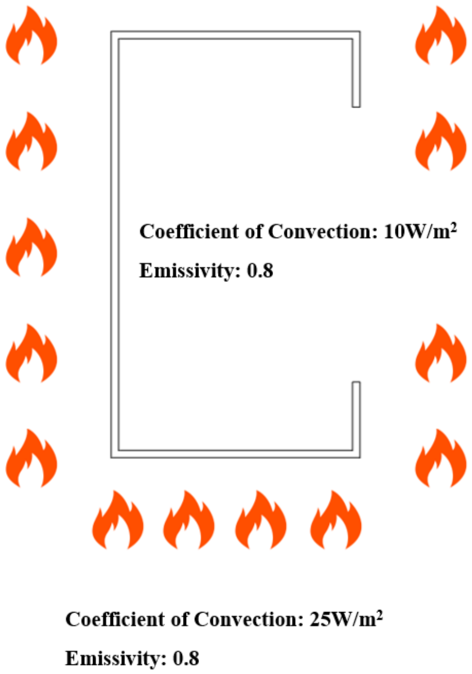

Figure 5.21: Case 2

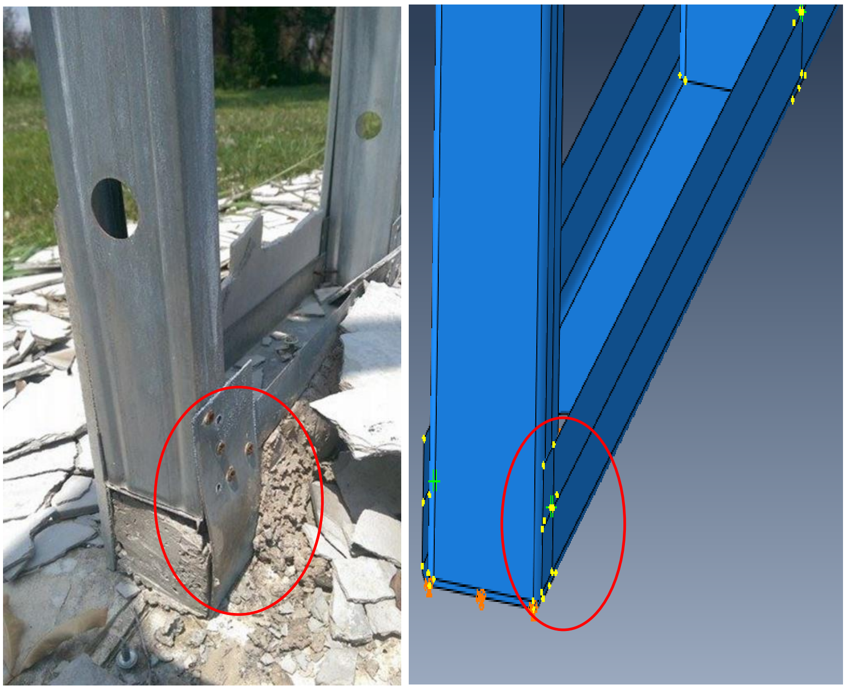

Figure 5.22: Pinned Base

5.4.6 Contact Modelling

The steel to steel and, gypsum to steel contacts were modelled to enable heat conduction also with the appropriate input of thermal conductivity as mention in section 5.4.2.5 and 5.4.2.7.

In the interaction module of ABAQUS software, the “surface to surface contact” was selected to assign the contact surfaces between two bodies. In addition, the surface to surface contact requires the input of interaction property. The contacts between these surfaces were assumed fully contact so that the heat conduction was mainly based on thermal conductivity input earlier. Therefore, the thermal conductance was assigned in interaction property to enable ABAQUS software to perform the heat conduction.

Likewise, the “surface to surface contacts” were also applied in the FE model to prevent the cold-formed steel member from intersecting to each other. The interaction property used in this case was mechanical contact property. To reduce the computational time, the tangential behaviour of contact surfaces was defined as frictionless in the mechanical interaction property. In addition, the normal behaviour of contact surfaces was defined as “HARD CONTACT”.

5.4.7 Connections

The cold-formed steel structure was composed of different joints at wall studs and wall tracks, eave joints, apex joints and gypsum board as shown in Figure 5.23 to Figure 5.27. To model these connections, “wire” function was used to connect two nodal points (i.e. the nodal point at wall stud and wall tracks) to form an idealization of a screw connection. These “wires” were applied according to the locations of the screw in the cold-formed steel connection. A similar method was applied to the eave joints, gypsum board wall joints and apex joints.

Furthermore, the connector section was assigned for “wires” to define the connector type. The connector type used for the screw connection was a combination of “cartesian” and “rotation” where the relative displacements and rotations of the screw were constraint kinematically. The connectors were assumed as rigid connectors due to failure of the CFS structure in fire test was due to member buckling rather than failure of screws around the joint. 2.5 mm physical radius of connectors was created with reference to the actual size of screws used in the full-scale fire test. Figure 5.23 and Figure 5.24 present the screw connections of in full-scale field test and FE model.

Figure 5.23: Screw connections in full-scale field test

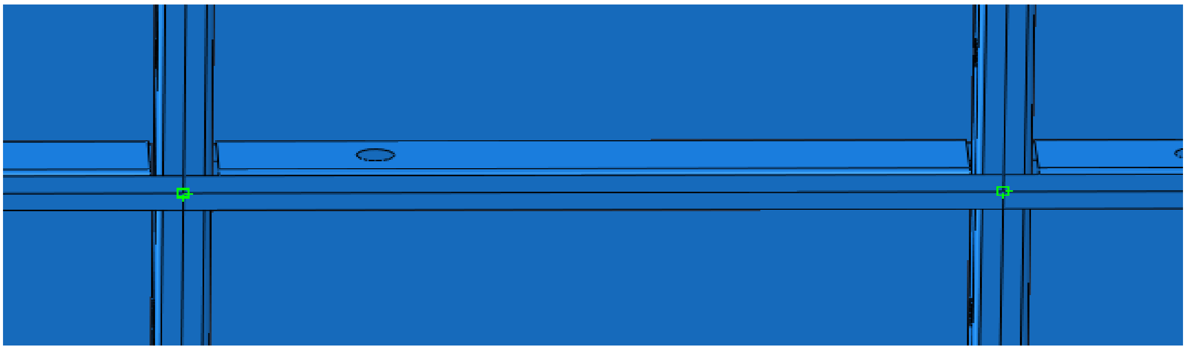

Figure 5.24: Screw connections in FE model

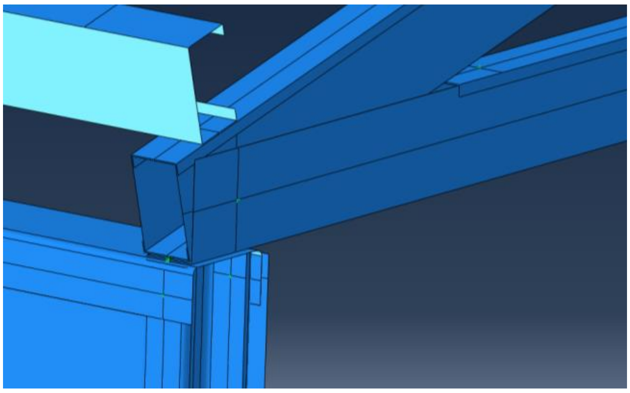

Figure 5.25: **Eave Joint**

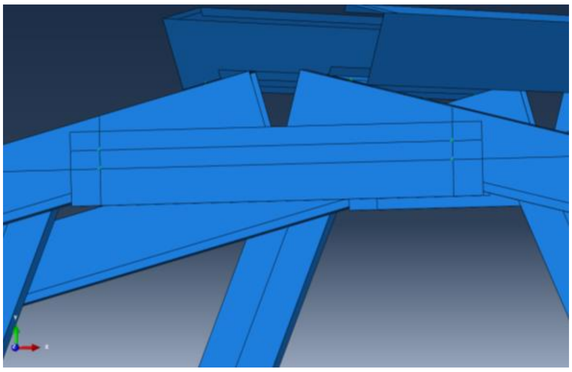

Figure 5.27: **Apex joint**

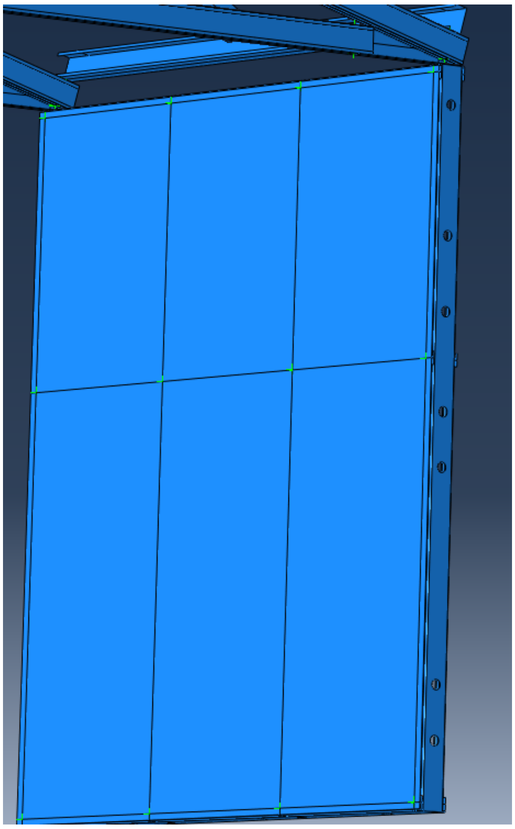

Figure 5.26: **Gypsum Board Connections**

5.4.8 Loadings

There are two types of loading applied to the FE model, they are fire and mechanical load. The temperature against time curve of the roof, northern and southern wall recorded in the full-scale field test were adopted as a heat source in the FE model. ABAQUS software allows the temperature against time curve input via "amplitude" function. Figure 5.28 shows the temperature against time curves of the roof (RT1), the northern wall (NT1) and, the southern wall (NT2) used in the model. The surfaces exposed to fire were assigned based on these amplitude curves under the "boundary condition" module.

The cold-formed steel structure in full-scale field test was loaded with bricks and cement claddings on top of the purlins. In the FE model, the weight of the bricks and cement cladding were assessed and defined as permanent loads. The detailed calculations were presented in Appendix. In load module of ABAQUS software, the permanent loads were applied as the concentrated loads on the purlins. Figure 5.29 shows the magnitude and location of permanent loads applied in the FE model.

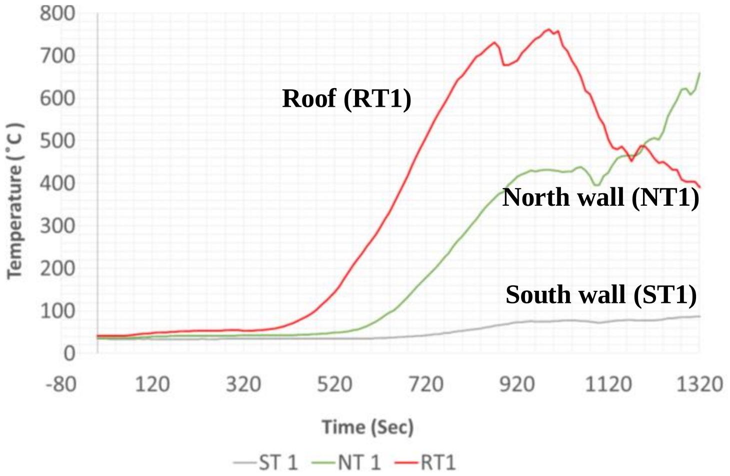

Figure 5.28: Heating Profiles used in FE model

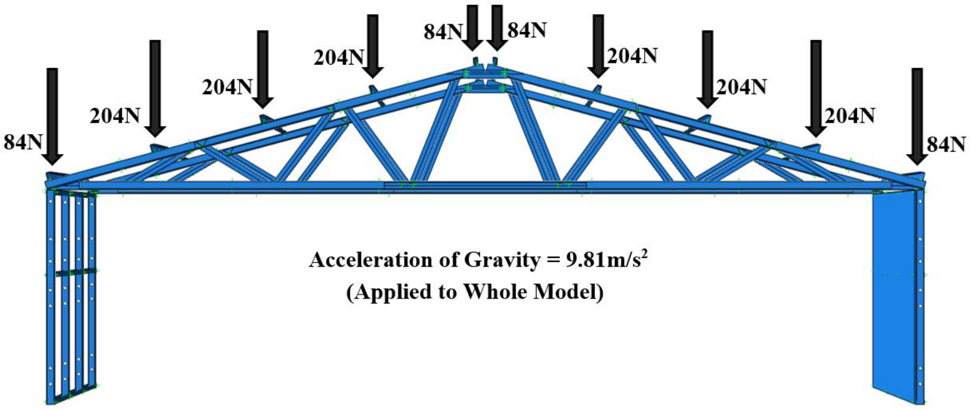

Figure 5.29: Roof Loads

5.4.9 Sequentially Coupled Thermal-Stress Analysis

In numerical modelling of the cold-formed steel structure, sequentially coupled thermal-stress was performed where the transient heat transfer analysis was first carried out to obtain the cross-sectional temperature field without accounting the effects of mechanical loads. Figure 5.30, Figure 5.31 and, Figure 5.32 show the temperature field of the entire model. The transient heat transfer analysis was selected due to the non-linearity of thermal properties (see section 5.4.4.3 to 5.4.4.7), thermal boundary conditions (see Section 5.4.5) and, temperature against time curve (see Figure 5.28). The duration of the simulation was set to 1320 seconds which referred to the instantaneous time of collapse for the cold-formed steel structure (see Figure 6.10).

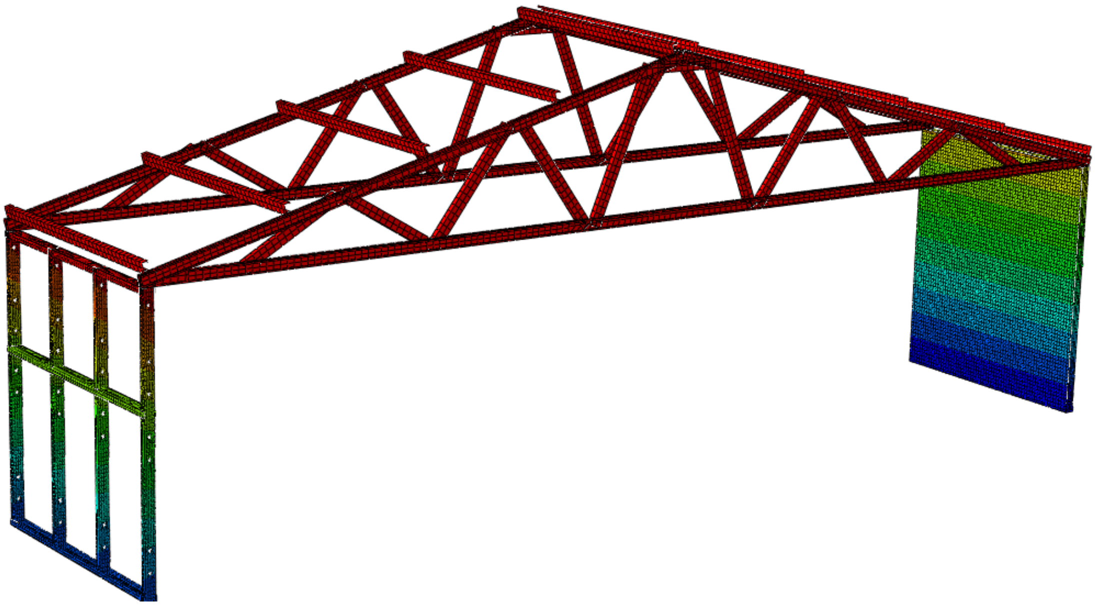

Figure 5.30: Heat Transfer Model

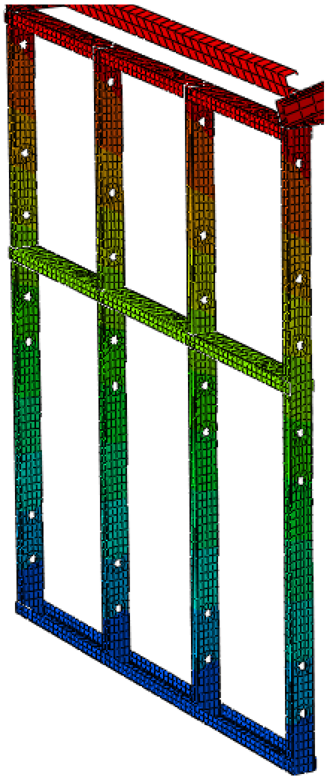

Figure 5.31: Temperature Field in North Wall

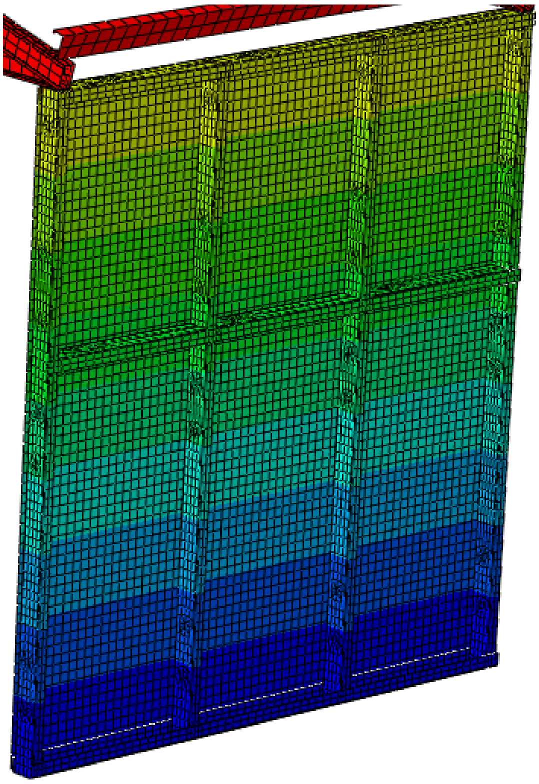

Figure 5.32: Temperature Field in South Wall

Secondly, the thermal-stress analysis was performed to simulate the structural behaviour of cold-formed steel structure under natural fire. The thermal-stress properties, mechanical contacts, thermal contact for heat conduction and connections discussed earlier were used in this analysis. In addition, there are two methods available to simulate the CFS structure at elevated temperatures: steady-state method and transient state method. It should be noted this transient state method shall not be confused with transient heat transfer analysis. The steady-state method is conducted by raising the temperature to a target level then followed by the load application. Whereas the transient state method is performed by the load application first, then followed by increasing the temperature. In the full-scale field test, the brick loads were applied to the roof and then followed by ignition of the fire. Therefore, the transient state method was adopted in this study which represents the actual condition in the full-scale field test. Cheng (2015) also claimed that the transient state method is more practical and, follows the experimental and actual structural condition. The similar method was adopted in the finite element model of Johnston *et al.* (2014).

To model the transient state method in thermal-stress analysis, the first step was to assign the loading step to simulate the permanent loads. Static general solver was used for the loading step and, the time step was input as 1 second. In the first step, the weight of bricks, weight of cement claddings and acceleration of gravity were applied. After that, all the assigned loads in step 1 were propagated to step 2.

The second step in the thermal-stress analysis is the temperature step to simulate the heating effect. Implicit dynamic solver incorporated with the quasi-static application was assigned in step 2. The implicit dynamic solver is capable to capture the snap-through effect of cold-formed steel members at elevated temperatures. Moreover, the quasi-static application was used to handle the instabilities of a structure by introducing inertia effect (Johnston, 2014). In step 2, the result file obtained from the transient heat transfer analysis was linked into this model using “PREDEFINED FIELD” function. The time step used in step 2 is simultaneous to transient heat transfer analysis which was 1320 seconds. The results obtained from the thermal stress analysis were validated by the full-scale fire test results.

5.5 Thermal Properties of Gypsum Board Model

This section describes the verification of thermal properties of fire rated gypsum board using heat transfer finite element analysis. The specific heat capacity and thermal conductivity used in the full model as in Section 5.4.4.7 were verified by the furnace test results.

The heat transfer of the gypsum board can be modelled in 2-dimension and 3 dimensions. Shahbazian (2013) carried out heat transfer modelling on 12 mm thick gypsum using ABAQUS software. The FE results are validated against the experimental results obtained by Rahmanian (2011). Shahbazian reported only a slight difference in the results of 3-dimensional and 2-dimensional gypsum board FE model. Hence, for simplicity, a two-dimensional model was used in this analysis. A 200 mm width and, 15 mm thickness solid part was created based on the dimension of gypsum board used in furnace test.

A 4-node linear heat transfer quadrilateral (DC2D4) element was used to allow for heat storage and, heat conduction in the gypsum board model. Convergence studies based on different mesh sizes were carried out to determine the optimum mesh. The gypsum FE model with element sizes of 15 mm, 7.5 mm, 3.75 mm, 2.5 mm, 1.5 mm and 1.2 mm were studied. Figure 5.35 shows an example of 6 layers meshes across the gypsum board thickness. The hot surface and cold surface are the exposed side and ambient side, respectively. The results on the ambient side based on different mesh size are shown in Figure 5.34. The temperature against time curve converged as the smaller mesh sizes were used. This is because smaller size mesh sizes generated a greater number of elements which yielding a more refined result. However, using higher number of elements required more computational time. Therefore, 6 layers of mesh across the thickness was adopted in this study.

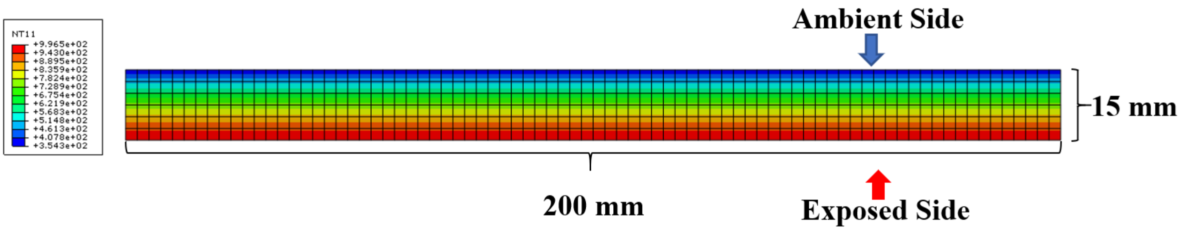

Figure 5.33: **6 Layers of Mesh across Gypsum Board Thickness**

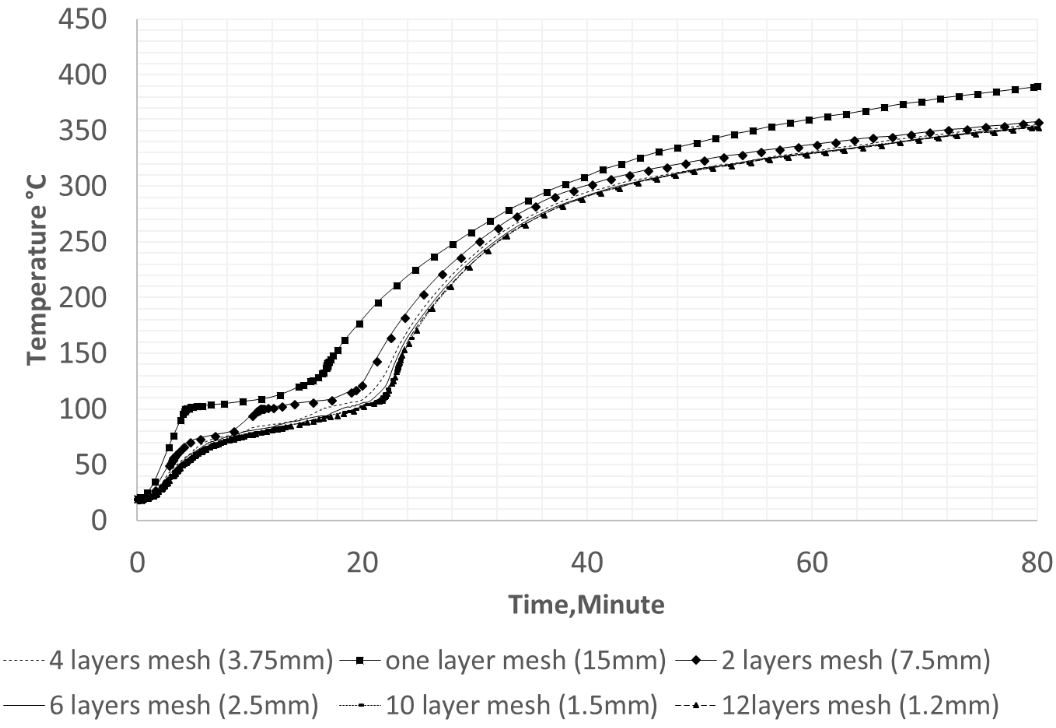

Figure 5.34: Mesh Size Studies of Gypsum Board

The furnace gas temperature which follows the ISO-834 (ISO, 1999) was assigned in FE model for benchmarking. (Semitelos *et al.*,2014; Thomas, 2012; Rahmanian and Wang, 2012; Keerthan and Mahendran, 2012; Feng, 2004)

Table 13: Various Convective Coefficient and Radiative Emissivity used by Various Researchers

Researchers	Convection coefficient at the ambient side (W/m^2)	Convection coefficient at the exposed side (W/m^2)	Radiation emissivity at ambient side	Radiation emissivity at exposed side
Semitelos *et al.* (2014)	Eliminated this parameter by directly input exposed surface temperature	10	0.9	Eliminated this parameter by direct input exposed surface temperature
Rahmanian (2011)	4	25	0.8	0.8
Thomas (2012)	9	25	0.6	0.8

Keerthan and Mahendran (2012)	10	25	0.9	0.9
Feng (2004)	10	25	0.8	0.3

The heat convection and heat radiation were input in the thermal boundary conditions. The convection coefficient and emissivity are the key parameters which affect the thermal convection and radiation, respectively. Table 13 shows the values of convection coefficient and emissivity used by different researchers (Semitelos *et al.*, 2014; Thomas, 2012; Rahmanian and Wang, 2012; Keerthan and Mahendran, 2012; Feng, 2004). It is shown that the convection coefficient of 25W/m^2 and 10W/m^2 at exposed and ambient side are conservative. Therefore, the coefficient of convection at exposed and ambient surfaces of 25W/m^2 and 10W/m^2 were taken respectively. Table 13 also shows the emissivity value of 0.8 is a norm for the ambient and exposed surface.

The gypsum board model is dependent on the input of appropriate thermal properties. The thermal properties of gypsum board include density loss, specific heat capacity and thermal conductivity. The values of density loss and specific heat capacity were obtained from Thermogravimetric Analysis (TGA) and DSC tests as discussed in section 4.3 and 4.4, respectively. The thermal conductivity values of gypsum board from Rahmanian (2010) were used in this model. Figure 5.35 shows the sequence of obtaining appropriate thermal conductivity based on an iterative method by Keerthan and Mahendran (2012). The heat transfer results, specifically the temperature against time profiles on the cold surface of gypsum board were compared to the furnace test results.

Furthermore, different specific heat and thermal conductivity curves proposed by various researchers (Semitelos *et al.*, 2014; Thomas, 2012 ; Rahmanian and Wang, 2012; Keerthan and Mahendran, 2012; Feng, 2004) were analysed by the gypsum FE model and the results were compared. It should be noted that two different specific heat curves proposed by Thomas (2002) were included for the comparison of FE results. The specific heat and thermal conductivity curves of various researchers are plotted as shown in Figure 5.36 and Figure 5.37. Table 13 shows the convection and radiation emissivity used by these researchers. The temperature against time curves of the ambient surface of various researchers were compared with the furnace test results as shown in Figure 5.40.

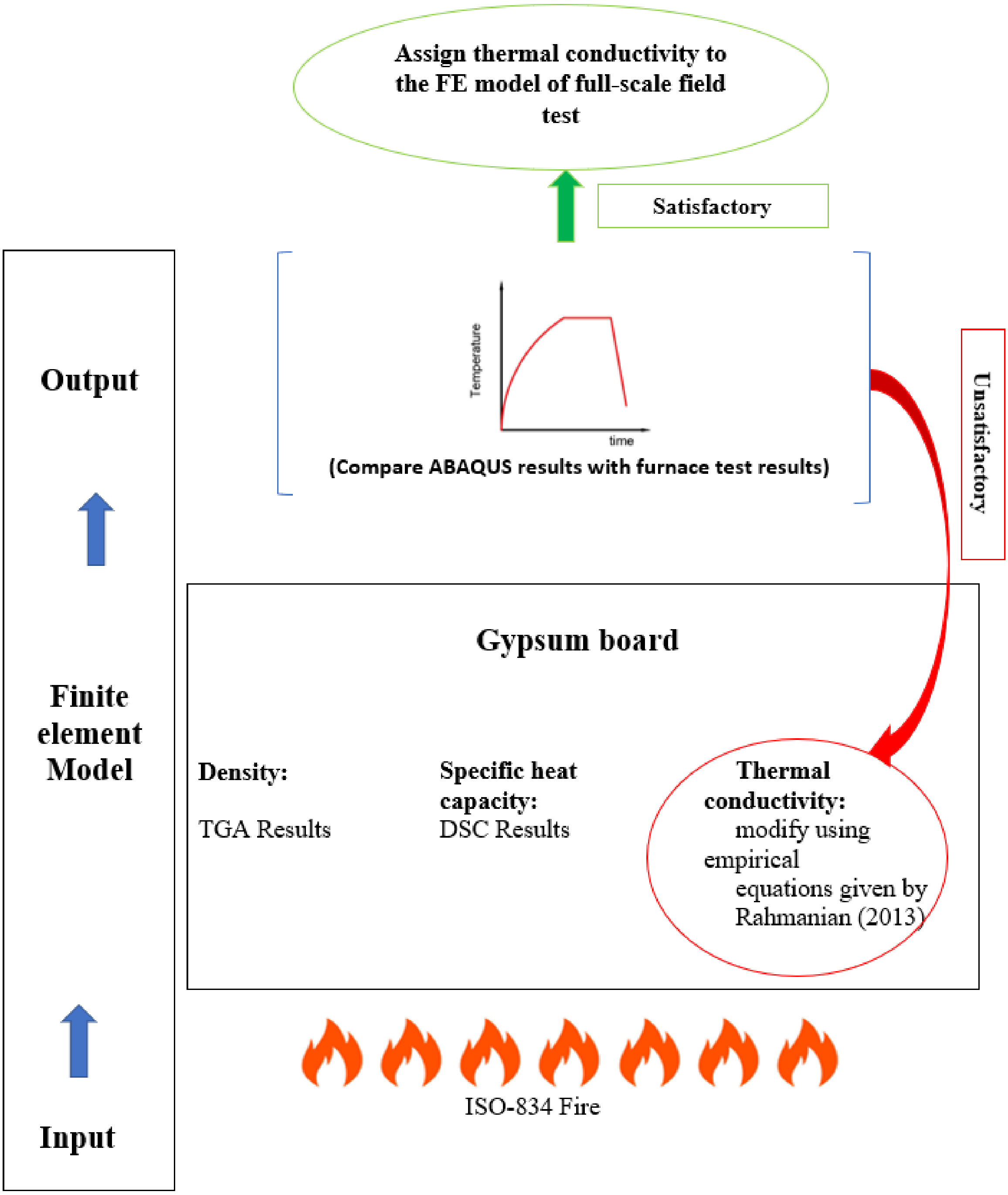

Figure 5.35: **Flow Chart of Gypsum Thermal Properties Validation**

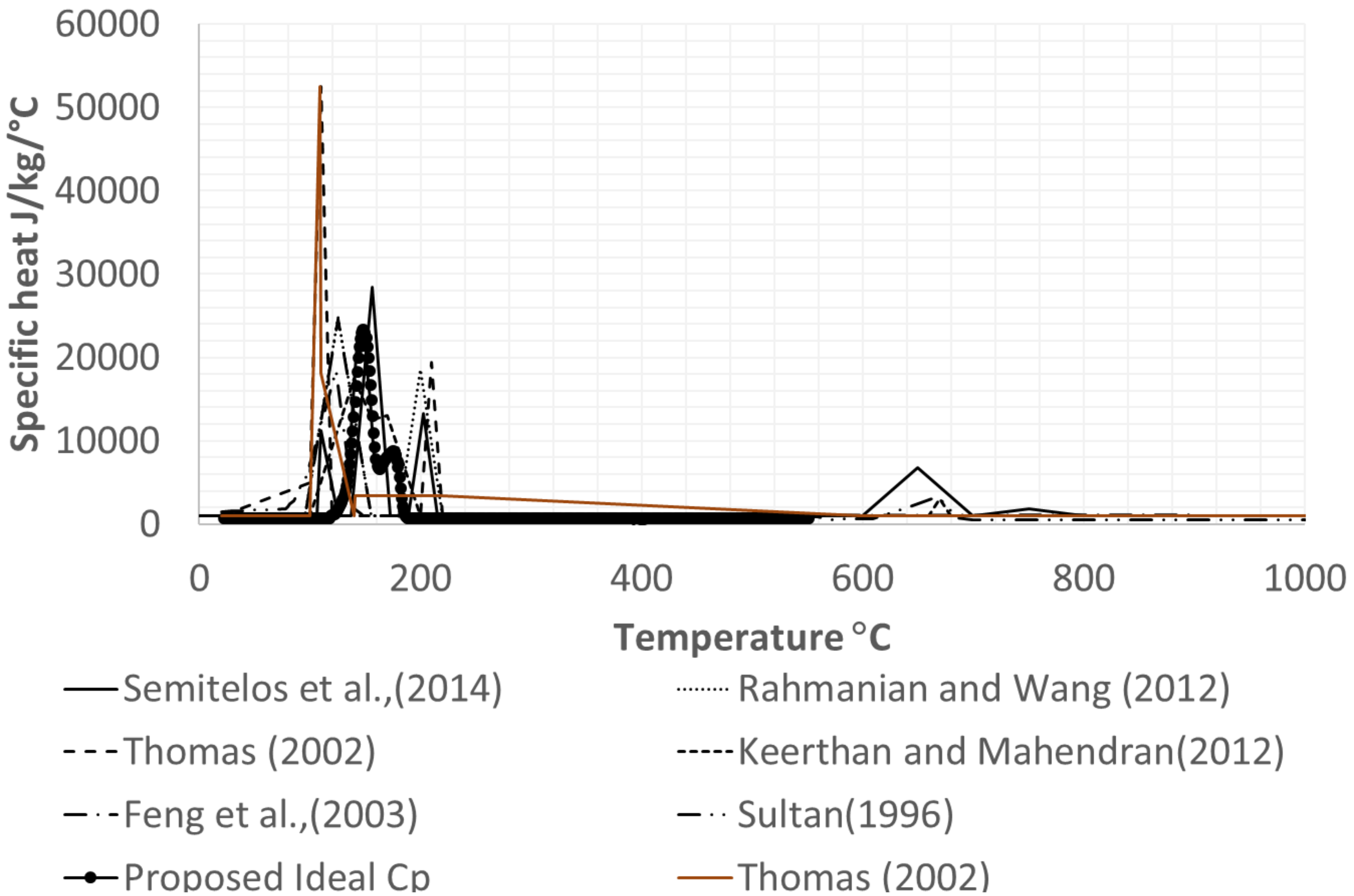

Figure 5.36: Proposed Specific Heat Capacity of Gypsum

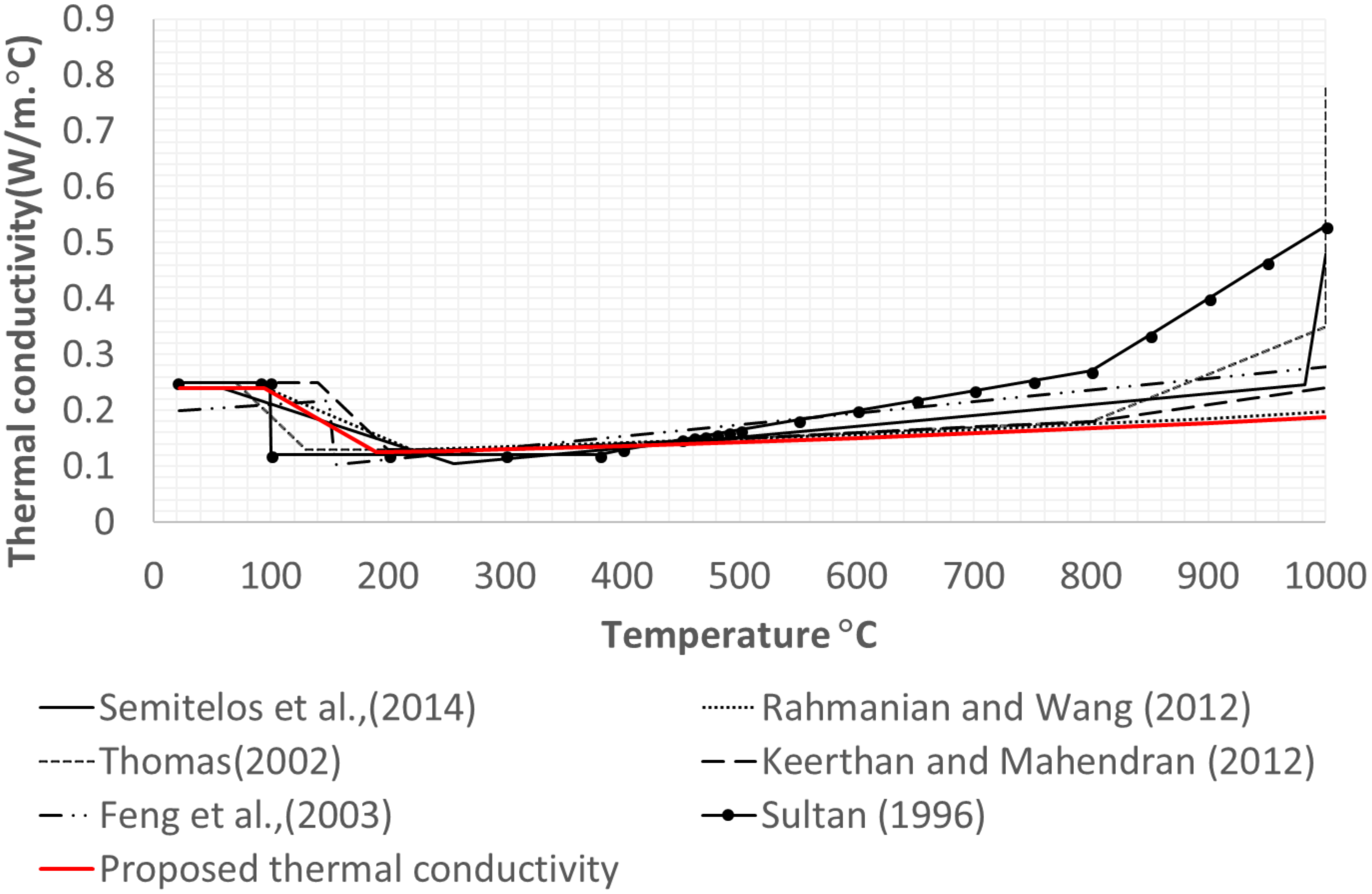

Figure 5.37: The Proposed Thermal Conductivity of Gypsum

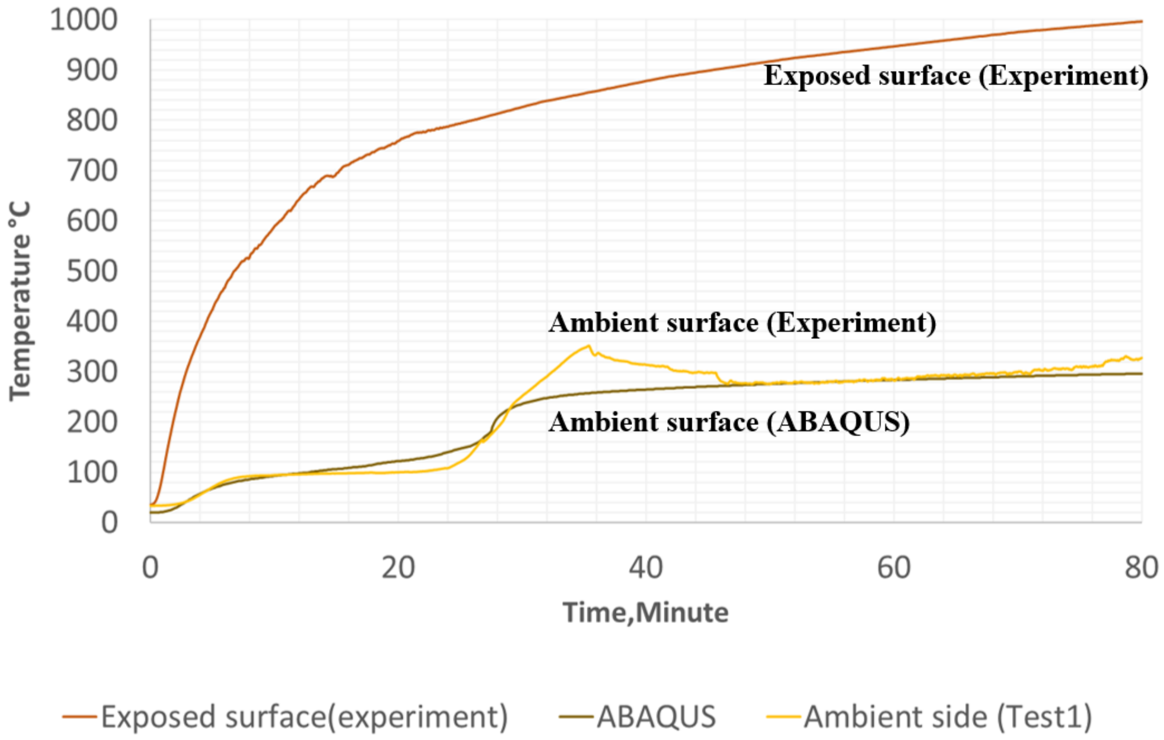

Figure 5.38: Ambient Surface Temperatures of FE and Furnace Test 1

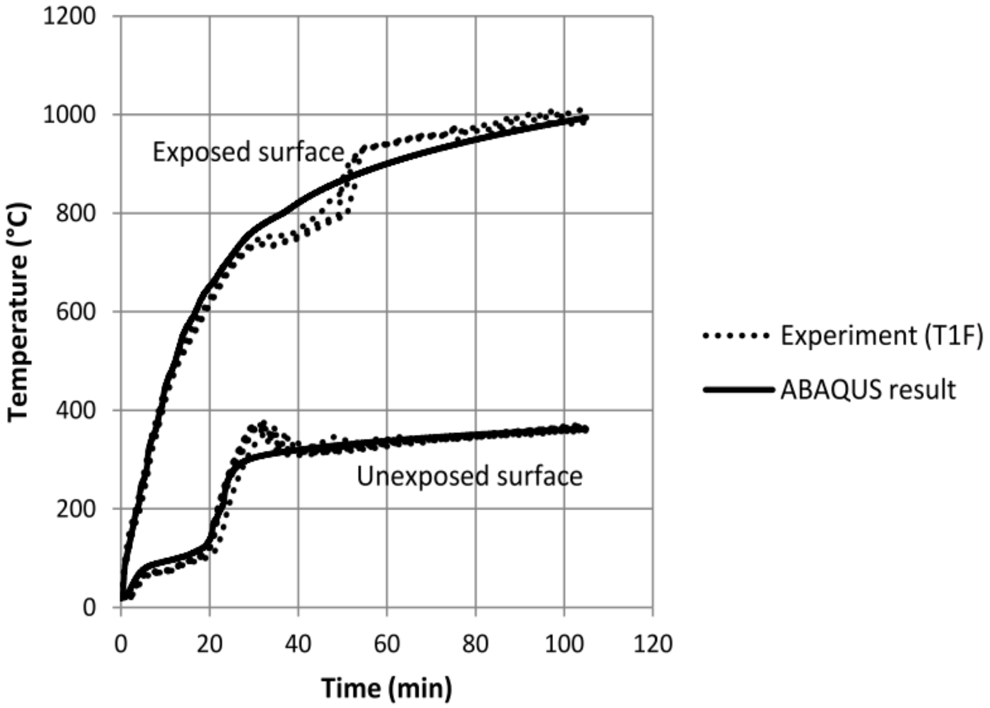

Figure 5.39 : Ambient Surface Temperatures of FE and Furnace test (Rahmanian 2012)

Figure 5.38 shows the comparison of FE results and furnace test results at the ambient surface for the FE gypsum board model. The proposed thermal conductivity and specific heat capacity used in the gypsum board model yield a close prediction between the ambient surface temperature of FE results and furnace test 1 results. This finding is similar to Rahmanian (2012) as shown which is shown Figure 5.39. The validation for the other two specimens is presented in Appendix E.

In addition, Figure 5.40 shows the various temperature against time curves of the ambient surface of the FE gypsum model. These ambient surface temperature against time curves are the outcome of gypsum FE analyses which utilizing different specific heat capacities curves and thermal conductivity curves proposed by various researchers (Semitelos *et al.*,2014; Thomas, 2012; Rahmanian and Wang, 2012; Keerthan and Mahendran 2012; Feng, 2004). It is found that the use of proposed specific heat and the proposed thermal conductivity in the FE model where the ambient surface temperature in FE results produced a good correlation with the experimental results. Therefore, these appropriate values of proposed specific heat capacities and the thermal conductivities were assigned to the large model as described in Section 5.4.4.7.

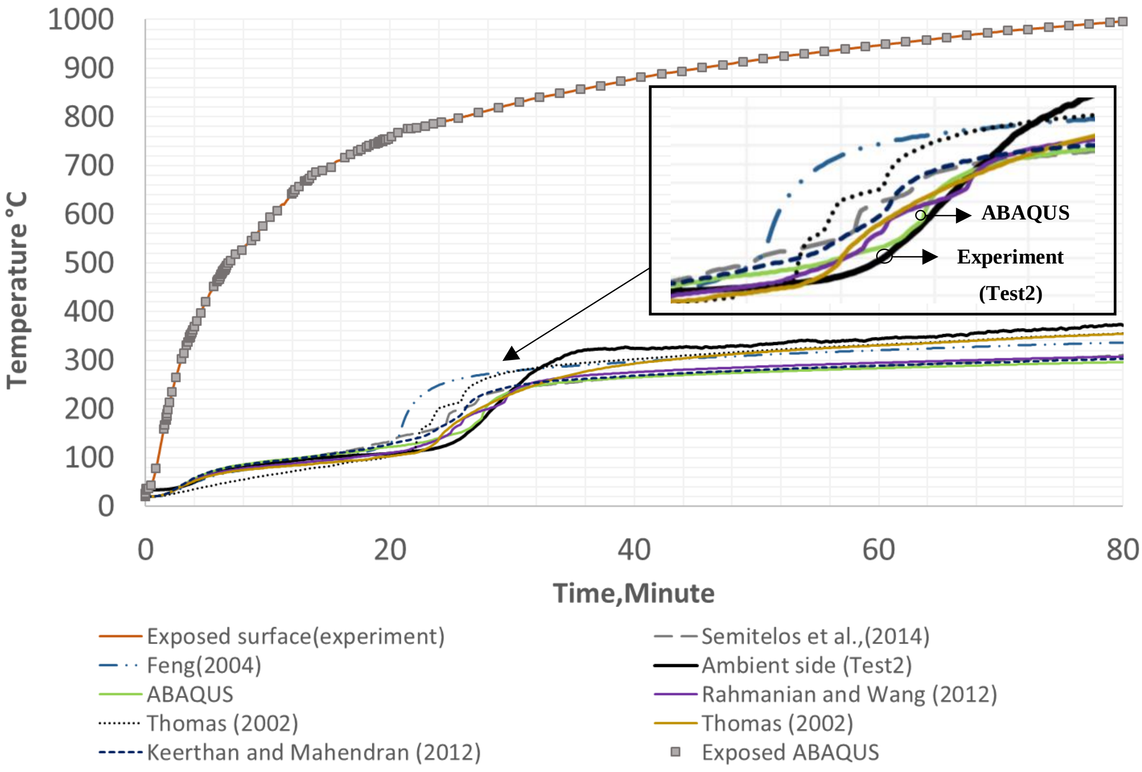

Figure 5.40: Comparison of Ambient Surface Temperature using Thermal Properties Proposed by Various Researchers

5.6 Conclusions

A non-linear elastic-plastic implicit dynamic finite element (FE) model for the cold-formed steel structure was developed. Important aspects of modelling were described. These include the appropriate assignment of thermal-mechanical properties for cold-formed steel and gypsum board, the optimum mesh size obtained from convergence studies, physical and thermal contacts, the modelling of connections, the fire source, and suitable analyses have been described. The validation of thermal conductivity and specific heat capacity of gypsum also described to justify the thermal properties used in the entire CFS structure model.

6 Results and Discussions

6.1 Introduction

This chapter presents the full-scale fire test results and finite element results of the collapse behaviour of cold-formed steel structure. The behaviour of the structure at initial and post-fire stages are described. The temperature against time profile of central roof truss, northern and southern wall are also presented in respect to thermal performance of the structure. Besides, the displacement-time profiles of northern and southern wall show the movement of walls against time of the collapse. Crucially, a combination of thermal and structural performance for northern and southern wall is described using these displacement-temperature profiles. Lastly, comparison of the finite element results and full scale-test results in terms of displacement-temperature and failure mode are presented.

6.2 Full-Scale Fire Test Results

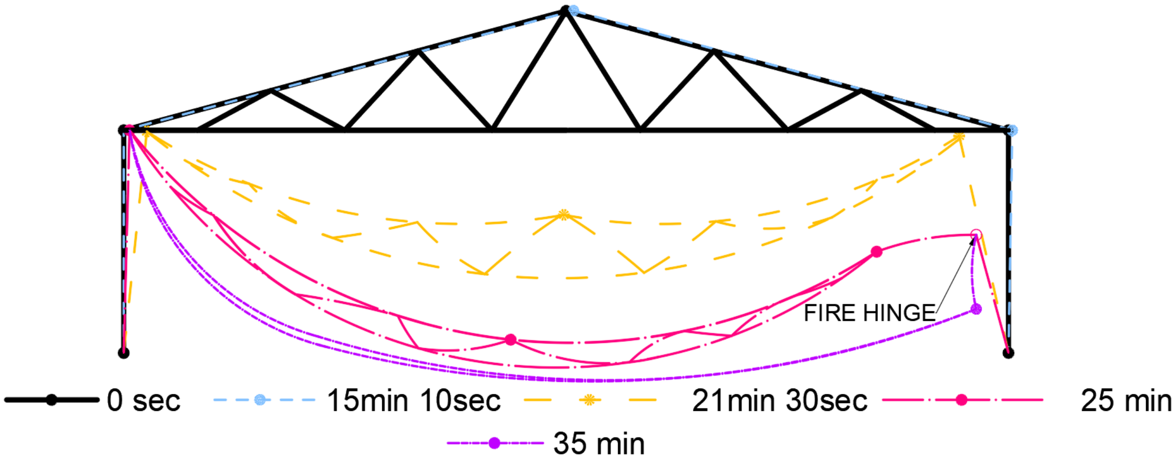

Figure 6.1: Highlights of Full-Scale Fire Test

Figure 6.1 shows displacements of the central frame against the time from ignition in term of collapse behaviour. The collapse mode was asymmetric with an initial thermal expansion of the frame, followed by an inward collapse at 659 °C by a time of 21 min 30 sec from fire ignition. Later, fire hinges were formed on the steel studs at a time of 22 min 30 sec, allowing upper part of the stud to rotate around these hinges. This mechanism is referred to as snap-through buckling of steel studs. The location of fire hinge was approximately located at one-third of the wall stud length. The snap-through mechanism was fully completed by a time of 35 min from fire ignition.

6.2.1 During the Fire Test

Figure 6.2: Ignition Stage (120 second)

The timber pallets were ignited at the base using a blow torch. Figure 6.2 shows the ignition stage of the fire proximity to the 1.8m wide corridor at the time of 120 seconds. The fire was started at the base, resulting in the compartment filled with smoke. A non-uniform fire was started in the compartment. The scenario above displays the incipient or fire growing stage, the fire was localized within the compartment and there is little rise in overall temperature.

Figure 6.3: Fire Test at 10 Minutes and 12 Seconds

Figure 6.4: Fire Test at 11 Minutes and 56 Seconds

Figure 6.3 shows the compartment was filled with smoke due to fire development at time 10 minutes and 12 seconds. However, there is no significant movement of the cold-formed steel structure. Later, two fire plumes were initiated at the left and right-hand side timber pallets. Figure 6.4 shows the initiation of two localized fire in the compartment at a time of 11 minutes and 56 seconds. As the fire continues to develop, it became fully engulfed and impinge on roof truss and roof cladding.

Figure 6.5: Fire Test at 13 minutes 37 Seconds

Figure 6.6: Fire Test at 14 Minutes 54 Seconds

Figure 6.5 and Figure 6.6 show the progress of fire development at 13 minutes 37seconds to 14 minutes 54 seconds. Buchanan (2001) explained the ventilation limiting the heat release rate of fire in the initial stage. The claddings were expanded from ignition to a time of 14 minutes. This is because the pressure in the compartment is increased due to heat accumulated in the compartment. As a result, the pressure in the compartment pushed the claddings away. The fire continuously reducing the mechanical properties of cold-formed steel members. However, the structural responses due to the thermal effects were not visible at this stage.

Figure 6.7: **Fire Test at 16 Minutes 16 Seconds**

Figure 6.8: **Fire Test at 17 Minutes 37 Seconds**

Movement of roof truss was observed at 16minutes and 16 seconds, to 17minutes and 37 seconds. Figure 6.7 and Figure 6.8 show the downward deflection of roof trusses. The roof truss sagged due to the intense temperature rising in the compartment. By observation, the roof truss has sagged asymmetrically. At the time 15 minutes and 20 seconds, the roof truss was gradually deflected downwards up to approximately half of the wall height level. The maximum temperature recorded was 765 ˚C at 17minutes and 5 seconds.

Figure 6.9: Fire Test at 21 Minutes 02 Seconds

Figure 6.10: Fire Test at 22 Minutes

Figure 6.11: Fire Test at 25minutes 20 Seconds

As the fire continued to intensify, the cold-formed steel material properties were deteriorated, and the roof truss lost its mechanical strength. The secondary members such as purlins provided temporary restrains to the roof trusses have failed to provide the restrains as the fire grows and material strength reduced. Figure 6.9 to Figure 6.11 show the roof trusses collapsed at first then followed by an inward collapse of the wall. Moreover, the front and rear trusses collapse inwards eventually after 20 minutes and 58 seconds due to fire and gravity load. After roof trusses collapsed, the northern wall also buckled and collapsed. However, the south wall did not collapse under 60 minutes of fire severity. The total time elapsed was 38 minutes for the structure to complete collapse as shown in Figure 6.13 and Figure 6.14.

Figure 6.12: Fire Test at 26 Minutes

Figure 6.13: Fire Test at 38 Minutes

Figure 6.14 : Fire Test at 38 minutes (Southern Side)

Table 14: Summary of Full-Scale Fire Test

Time(sec)	Time(min)	Description	Apex Temperature °C (RT1)	North wall °C (NT1)	South wall°C (ST1)
120	2	Ignition.	41.2	39.9	33.9
613 to 952	10.13 to 15.52	Localized fire plumes intensify.	279.4 to 718.4	75.4 to 430.7	35.5 to 75.2
976	16.16	Visible downward movement of roof trusses. The roof claddings cracked.	756.7	430.1	75.1
1258	20.58	The roof trusses gradually deflected downwards up to approximately half of the wall height level. The northern wall was pulled inwards where the southern wall did not collapse. It was observed the internal truss member detached from the roof truss.	431.4	577.8	83.3
1313	21.53	The purlins no longer provide temporary lateral restrain to the roof trusses, all the roof trusses	390.8	620.8	85.7

		were pulled inwards dynamically.			
1313, 1840 to 2100	21.53, 30.40 To 35	The formation of fire hinge approximately at one third the wall height from top. The upper part of northern wall rotated around the hinge.	390.8, 609.7 to 400.2	620.8 to N. A	86.4, 265.1 to 295.1
2280	38	Final collapse.	300.9	N. A	224.2

6.2.2 After the Fire Test

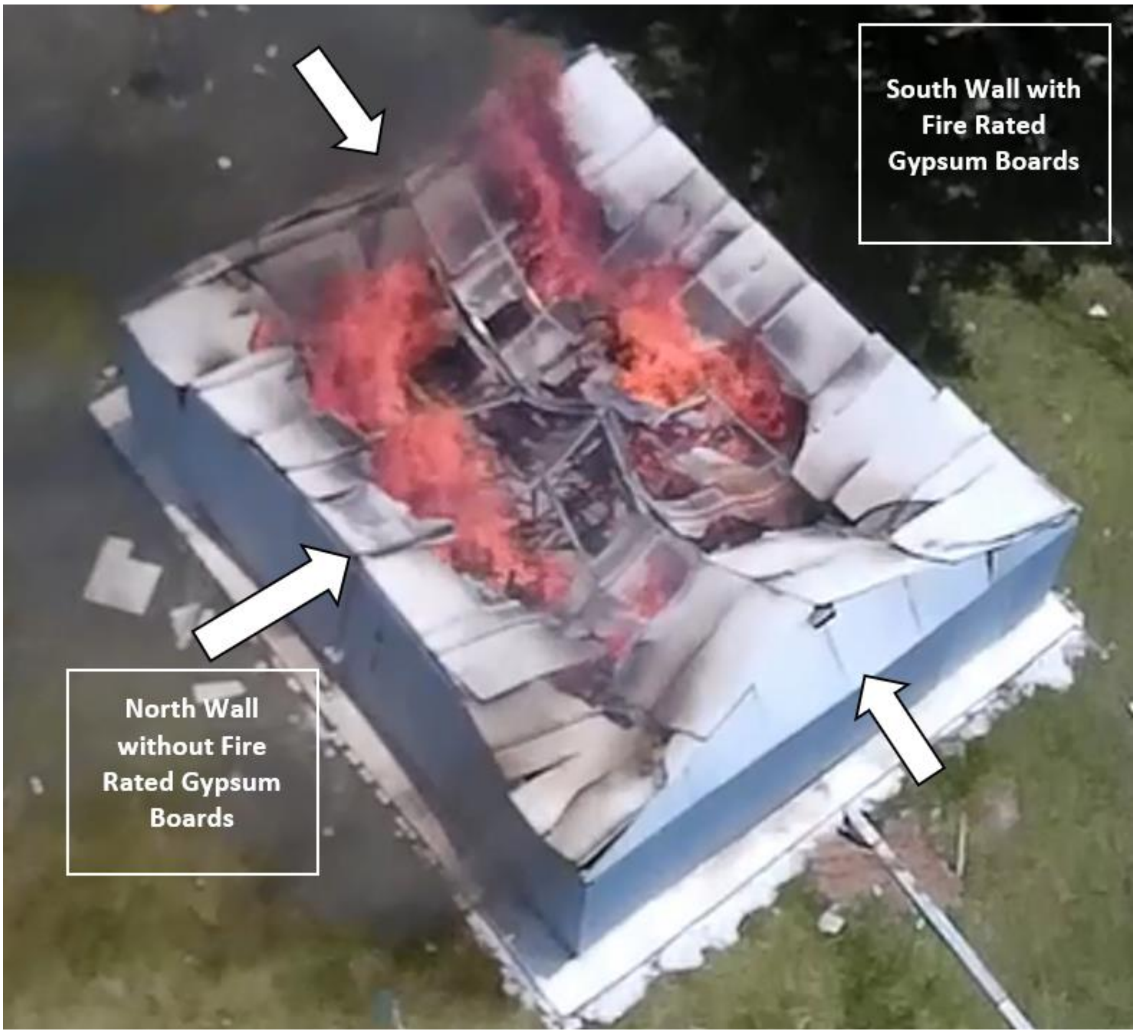

Figure 6.15: Plan View of Fire Test

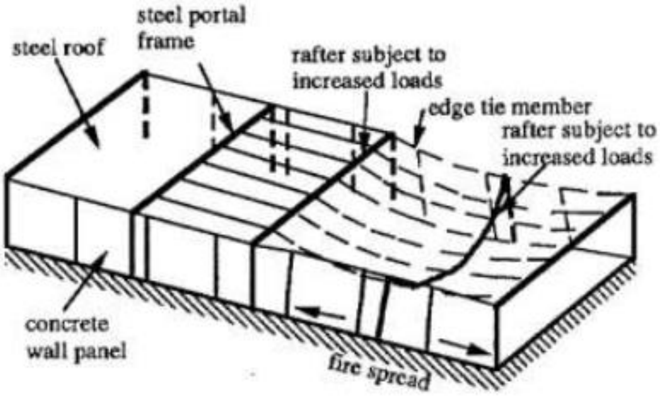

Figure 6.16: Failure Mode of Industrial Portal Frame (O'Meagher *et al.*, 1992)

The overall failure mechanism of the CFS structure as shown in Figure 6.15 is similar to collapse behaviour of steel portal frames described by O'meagher *et al*., (1992) as shown in Figure 6.16. Cold-formed steel roof trusses were heated initially, the primary and secondary members were expanding in the fire. As the fire continued to develop, the top chords of the roof trusses were critical after subjected to compression load and, the fire deteriorated the steel properties which contributed to downward deflection of roof trusses. Song (2008) highlighted the collapse of hot frames can be temporarily restrained by secondary members. Purlins were deformed in catenary shape contributed to lateral stability for the roof trusses. However, these secondary members cannot sustain longer and hence, the roof truss at the front and rear were pulled inwards as shown in Figure 6.15. Wall members were also subjected to fire load and the loads were transferred from the roof trusses. Eventually, this lead to buckling failure in wall studs and collapsed inward asymmetrically.

6.3 Heating Profiles of Roof Truss

Figure 6.17 shows the variation of temperature against time for the thermocouples placed around the central roof truss. The standard ISO 834 (ISO,1999) time-temperature curve and time-temperature curve are also shown for comparison. Since ISO curve did not consider initial fire growth, the ISO curve has been offset as shown in Figure 6.17. The highest peak of temperatures recorded in thermocouple number RT 1, RT2 and RT 3 are greater than the ISO-834 extended curve. Therefore, the ISO-curve used as prediction for any fire scenario is slightly less conservative in this case. However, the conservativeness of ISO-834 fire curve is further discussed in the research paper of Bahr (2014).

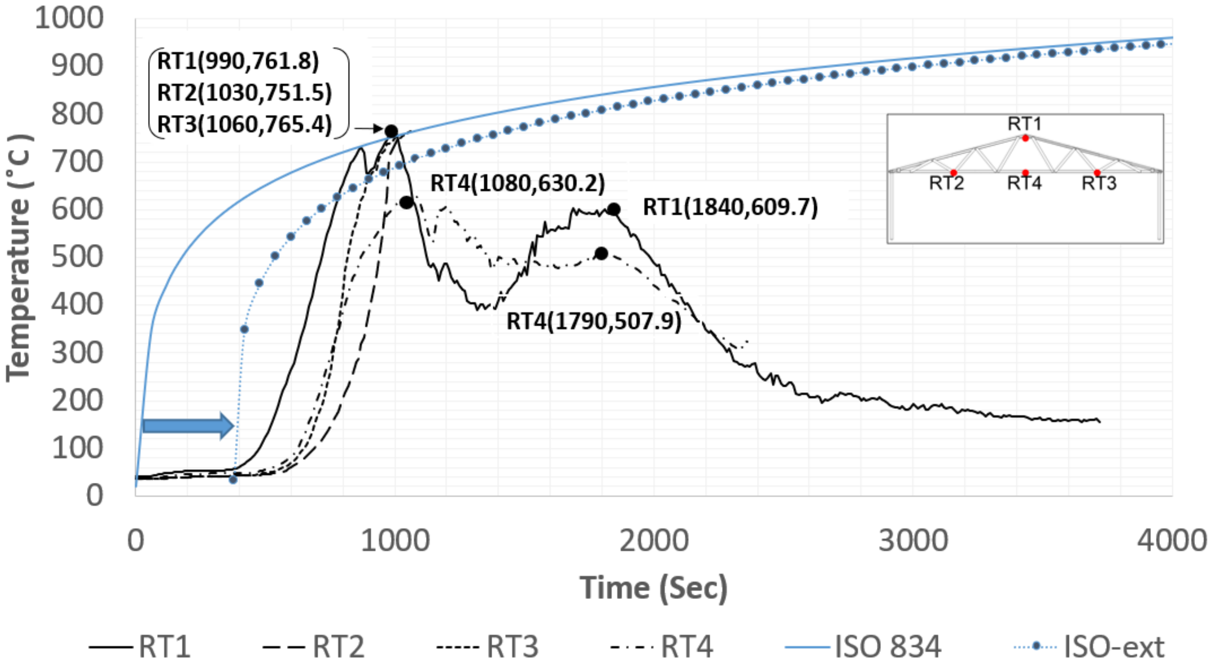

Figure 6.17: Temperature against Time Graph of Roof Central Roof Truss

The thermocouple wires provide the temperature distribution of ten location points around the structure from ignition until the point of collapse. A constraint of the experimental setup was that when the structure collapsed, the screwed connections attaching the thermocouple wire to the steel members snapped; readings taken after this point were therefore not found or invalid.

The thermocouple readings show a slow initial fire growth up to 400 seconds (or 61 °C), after which the fire growth develops rapidly. It can be noticed the temperatures recorded at point RT1 the highest temperature of 765.4 °C at a time of 1060 sec. Then, the temperature decreased from 765.4°C to 390.8°C at a time of 1350 Sec. The heat loss was due to the spalling of cement roof cladding that allowed extra openings for compartment ventilation. When the combustive material received sufficient air ventilation, the fire was again developed up to second peak temperature of 591.2 °C at a time of 1850 sec. Finally, the downward slope indicates the decay phase of the fire curve. At this stage, the available fuel for combustion is decreasing and hence, the temperature dropped. The summary of the full-scale fire test with temperature as references were tabulated in Table 14.

6.4 Heating Profiles of Cold-formed Steel Wall Framings

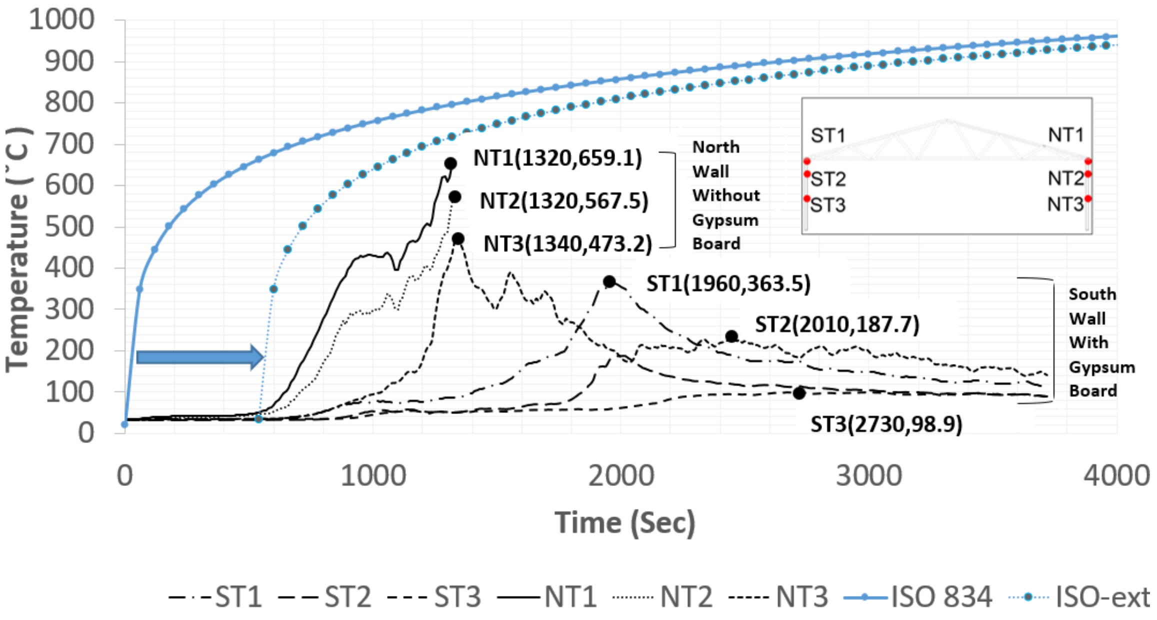

Figure 6.18: Temperature against Time Graph of Northern and Southern Wall

In addition, Figure 6.18 shows the heating profiles of northern and southern walls. Thermocouples NT1, NT2 and NT3 are the top, middle and bottom location of northern wall (without gypsum board). Similarly, ST1, ST2 and ST3 represent the top, middle and bottom thermocouple location points at southern wall (with gypsum board). In the full-scale fire test, hot gases are accumulating at the roof top. Therefore, the temperature is also diminishing from top to bottom at both northern and southern walls.

The peak temperatures of northern wall were greater than the southern wall. The peak temperature for curves NT1, NT2 and NT3 achieved earlier as compared to the curves ST1, ST2 and ST3. Considering the critical thermocouple points, NT1 and ST1, the highest temperature recorded by NT1 was 591.2 °C at the time of 1320sec. Whereby, the highest temperature recorded by ST1 was 363.5 °C at the time of 1960sec. Therefore, the fire rated gypsum board protected the southern cold-formed steel framing wall from rising temperature by 45% as compared to northern cold-formed steel framing wall, and a 48.5% of time delay in reaching the peak temperature as compared to southern cold-formed steel framing wall.

6.5 Structural Performance of Northern Wall under Natural Fire (Without Gypsum Board)

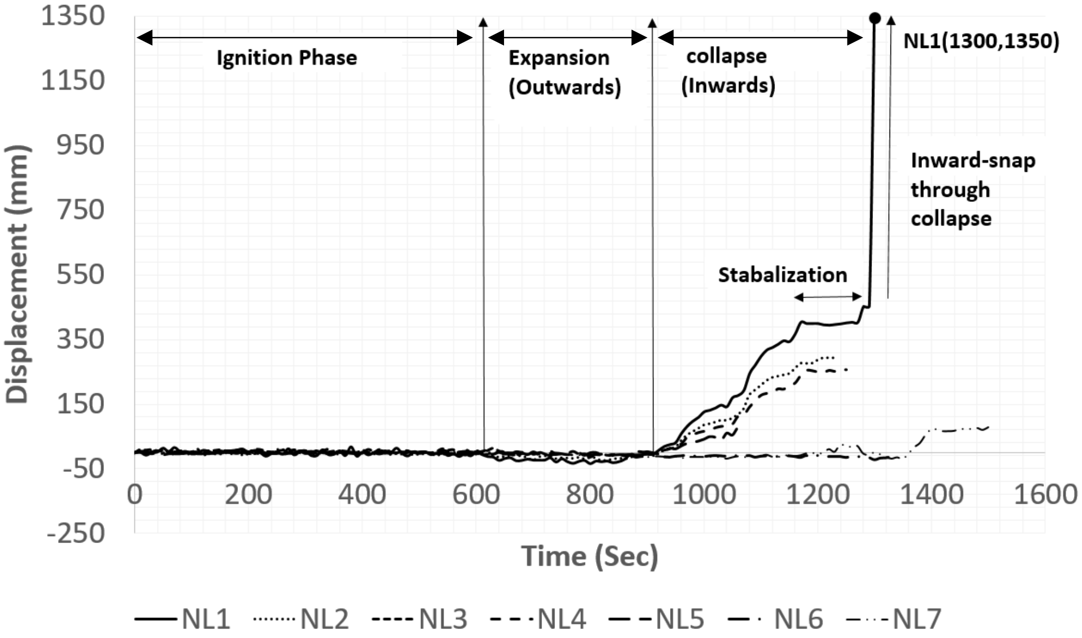

Figure 6.19: Displacement-Time Graph of Northern Wall

The displacement against time graph of northern wall was plotted as shown in Figure 6.19 to illustrate the movement of northern wall with respect to time. Laser range locations NL1 to NL7 were shown in Figure 3.48 earlier. During the ignition phase, the northern wall did not show any significant changes up to 600 second or 10 minutes. The laser range NL3 lost its contact to the wall and only recorded displacement up to 680 seconds. The corner laser range location NL 6 and NL 7 did not show any significant up to 1200 seconds until an inward displacement was recorded at 1490 seconds.

From 600 seconds to 920 seconds, the mid-wall laser range location NL1, NL2, NL4 and, NL5 shows an outward wall movement due to thermal expansion of cold-formed steel members. The curve NL 1 recorded maximum outward movement of 33 mm at 770 seconds or equivalent to 12 minutes and 50 seconds. The northern wall NL1, NL2, NL4 and, NL5 curves shows similar trends of inwards movement beyond 920 seconds. The highest point of the wall NL1 shows a gradual inward collapse from 0 mm at 920 seconds, to 400 mm at 1180seconds. The northern wall did not collapse directly as the wall stabilized itself during a period of stabilization from 1180seconds to 1270 seconds. As the strength properties of CFS wall studs continuously deteriorated by the fire, the northern wall can no longer bearing the load transferred from the roof. Eventually, the northern wall collapsed at 1350 seconds or 22 minutes with an inward deflection of 1300 mm. The structural collapse was induced by local failures or fire hinges that formed approximately at one-third of the wall height. This failure mechanism is referred as inward-snap through buckling of the wall studs.

6.6 Structural Performance of Southern Wall under Natural Fire (With Gypsum Board)

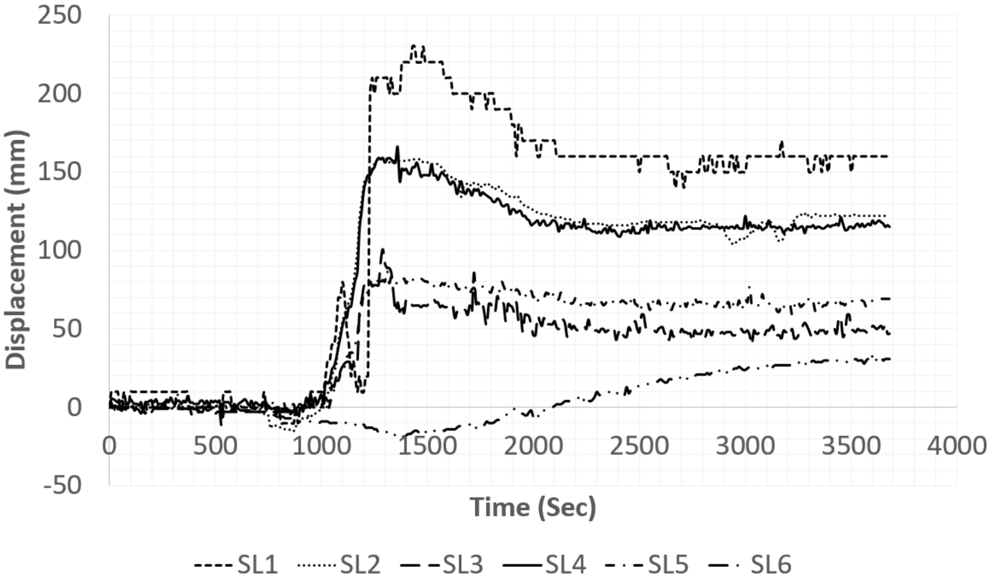

Figure 6.20: Displacement-Time Graph of Southern Wall

The displacement against time graph of southern wall was plotted as shown in Figure 6.20 which illustrate the movement of southern wall with respect to time. Laser range locations SL1 to SL6 were shown in Figure 3.59 earlier. The laser ranger target points SL1 to SL5 refers to the southern wall central locations whereas, SL6 indicated the laser range target point at the wall corner.

During the ignition phase, the southern wall did not show any significant movement up to 600 second or, 10 minutes. The laser range targets SL1 to SL5 recorded an outward movement of the wall at 600seconds to 1030 seconds. SL2 recorded maximum outward displacement of 14 mm at 840 seconds. The southern wall SL1, SL2, SL3, SL4 and SL5 curves show similar trends of inwards movement beyond 920 seconds. The southern wall did not collapse after reached its maximum displacement. The highest point of the wall, SL1 shows maximum inward displacement of 230 mm at 1430 seconds. After this maximum point, the wall moved outwards gradually at 1430 seconds to 2030 seconds. The movement of the wall remained constant at 160 mm. It is believed that the inward collapse of northern wall had pushed the southern wall moved outwards at 1430 seconds to 2030 seconds.

6.7 Structural and Thermal Performance of North wall and South Wall

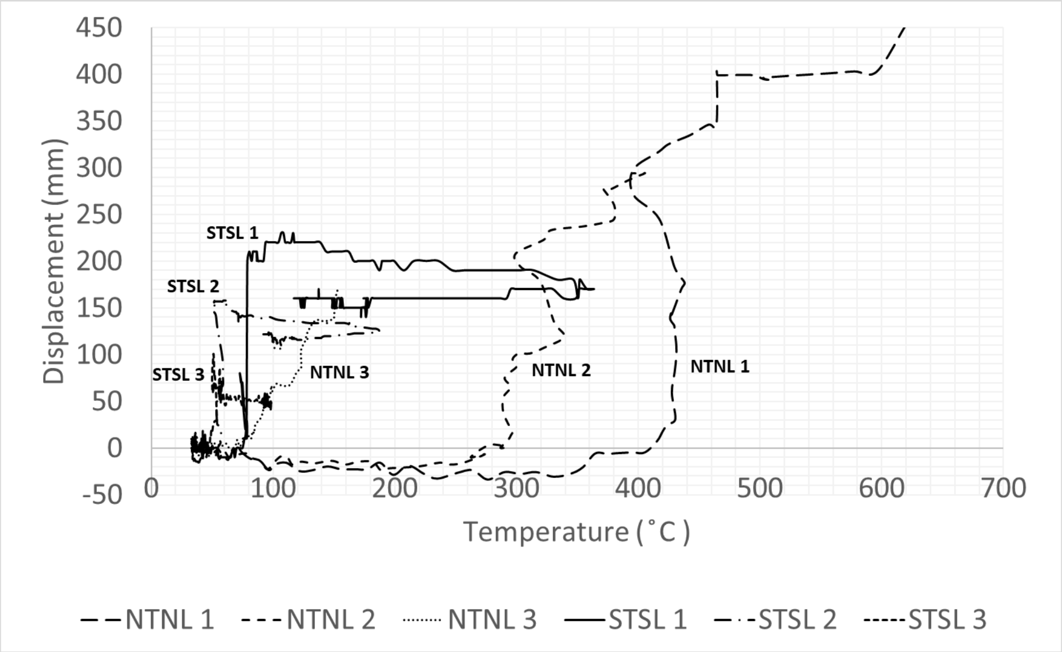

Figure 6.21: Displacement-Temperature Graph of Southern Wall

Figure 6.21 shows the lateral eaves displacement of the wall stud at top, middle and bottom positions against temperature of the central frame for the northern wall and southern wall. Initially, the temperature of the cold-formed steel roof trusses and wall studs increased due to the fire. This heating of the steel caused expansion and resulted in the stud moving laterally outwards as observed by negative values in Figure 6.21. The reduced strength and stiffness of the steel caused the cold-formed steel channel section to buckle earlier, which led to a sharp asymmetrical inwards movement.

The curve NTNL1 shows northern wall underwent a large displacement from 0mm to 399 mm within temperature interval of 410°C to 465°C. The northern wall then stabilized approximately at temperature interval of 462°C to 596°C, with a 400 mm displacement recorded. The highest displacement and temperature recorded at the northern wall were 453 mm at 622.5 °C. The temperature and displacement data beyond the maximum point were lost as the laser range targets are beyond the detectable range. The failure mode of the studs and roof trusses can be seen as asymmetrical, which can be expected since the southern wall was protected by fire rated gypsum boards, and the fire was non-uniform too. The protected steel wall framings at southern wall did not fully collapsed. Additionally, the collapse of the northern side wall at 628.23°C revealed the design of class 4 sections (cold-formed steel sections) using critical temperature of 350°C proposed by Eurocode 3 part 1.2 (CEN, 2005) is over-conservative. This is also well agreed with collapse temperature of cold-formed steel portal frame at 750 ˚C and 714 ˚C by Pyl *et al.* (2012) and Johnston *et al*., (2015) respectively showing the over-conservativeness of using critical temperature of 350°C for class 4 section design by Eurocode 3 part 1.2 (CEN, 2005).

The highest displacement recorded at the southern wall shown by curve ST SL1 was 230 mm at a temperature of 116°C. Whereby, curve STSL1 marked the highest temperature of 363 °C at a displacement of 170 mm. Initially, the southern wall expanded outwards with a displacement of 10 mm only at a temperature of 64°C. As the temperature increases to 200 °C, the southern wall moved further inwards to 82 mm whereas the northern wall collapsed with displacement of 399 mm at temperature 465°C. This is shown in the displacement against time curve where the collapse occurred at a time of 1080sec. After reaching the maximum displacement, the southern wall moving outward continuously until maximum recorded temperature of 363°C. The southern wall continues to move outward after recording the maximum displacement inwardly is mainly due to the asymmetrical collapse of northern wall. In other words, the inward collapse of northern wall pushed the southern wall to move outward.

6.8 Comparison of Full-Scale Test Result and Finite Element Results

The progressive failure mode of the cold-formed steel structure in FE model and full-scale fire test are compared at different fire growth stages. In addition, the displacement and temperature readings points for southern and northern in the FE model are shown in Figure 6.22. The critical points STSL1 and NTNL1 in full-scale test results as described in section 6.7 were used to compare with the FE analysis results.

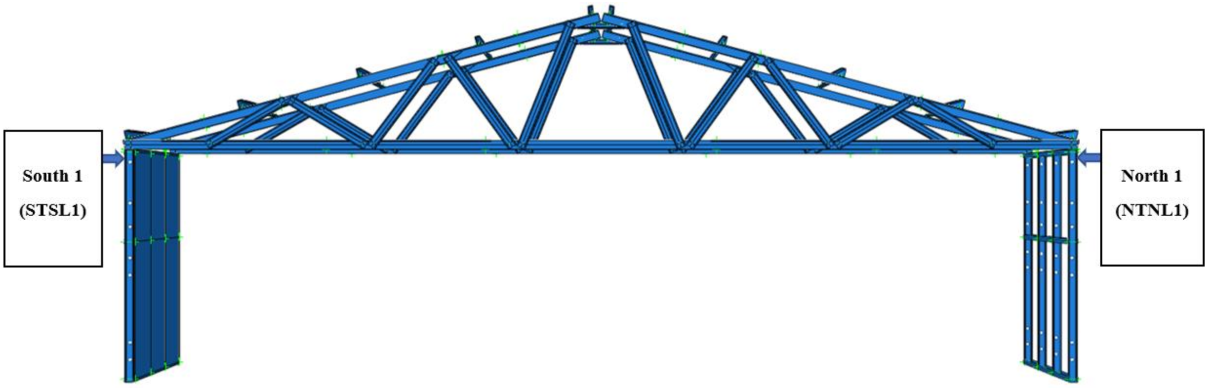

Figure 6.22: Data Reading Points for Southern and Northern Wall in FE Model

6.8.1 Deformation of Structure at Ignition Stage

Figure 6.23 and Figure 6.24 show the structural behaviour of FE model and full-scale fire test at 583 °C. The FE model illustrates most of the compression load were taken by the top chord on the right-hand side. Whereas, the bottom chord is acting in tension. The intermediate members on the right-hand side underwent buckling due to compression. The northern and southern side wall are being pushed outwards by roof trusses and due to thermal expansion of cold-formed steel.

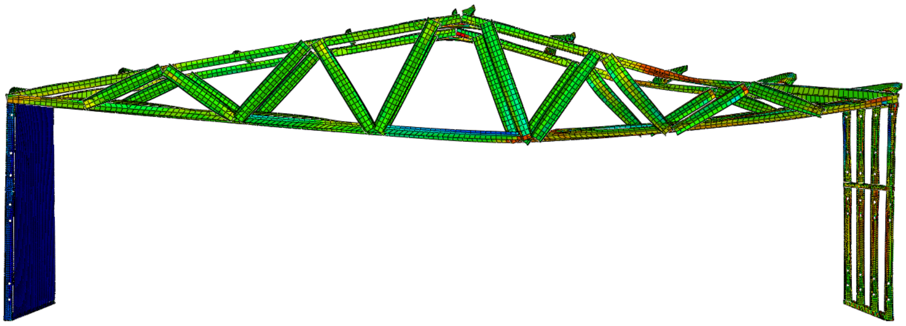

Figure 6.23: Failure Mode in FE Model (Apex Temperature at 583 °C)

Figure 6.24: Mode of Collapse in Full-Scale Fire Test (Apex Temperature at 583 °C)

6.8.2 Deformation of Structure under Fully Developed Fire

Figure 6.25 and Figure 6.26 show the deformation of the cold-formed steel structure in the FE model and full-scale fire test, where the temperature at northern wall at this stage is 550°C. The FE model shows the roof trusses deflected vertically below the eaves level, their strength and stiffness were lost and deformed to a catenary. The catenary action generated a tension force in the trusses that pulled both the southern and northern walls. The northern wall shows an inward deflection towards the compartment. However, southern wall did not deflect much compared to northern wall because of the temperatures were controlled by gypsum board. Thus, deterioration of material properties in southern wall was not severe compared to the roof trusses and northern wall.

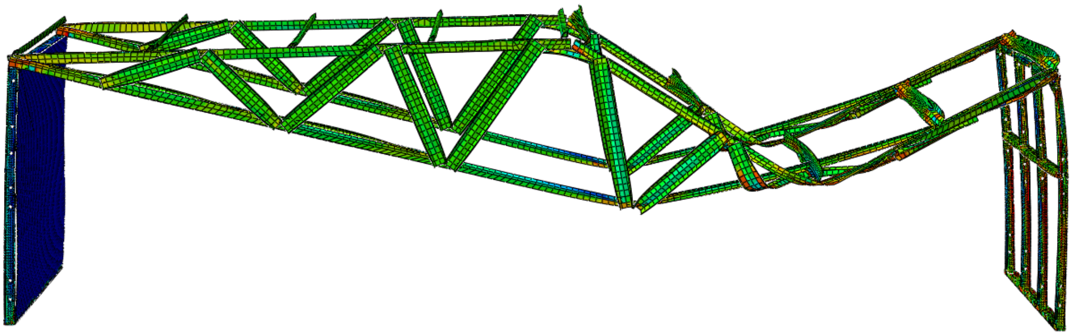

Figure 6.25: FE Model (North Wall Temperature 550 °C)

Figure 6.26: Full Scale Fire Test (North Wall Temperature 550 °C)

6.8.3 Final Deformation

The northern wall could no longer takes the roof loading as illustrated in Figure 6.25. As the yield strength of CFS deteriorated due to fire, the northern wall lost its load carrying capacity. As the fire hinge formed approximately at the two-thirds height of northern wall studs, a structural collapse was triggered and caused the upper part of the stud to rotate around the hinge. For this instance, the CFS structure changed from static to dynamic behaviour where the roof trusses collapsed under the influence gravity load. The local failure of the northern wall was identified as snap-through buckling at 628.23°C. The final collapse mechanism of the FE model and full-scale fire test are also illustrated in Figure 6.27 and Figure 6.28**.** The southern wall remained its stability and no large deformation was captured.

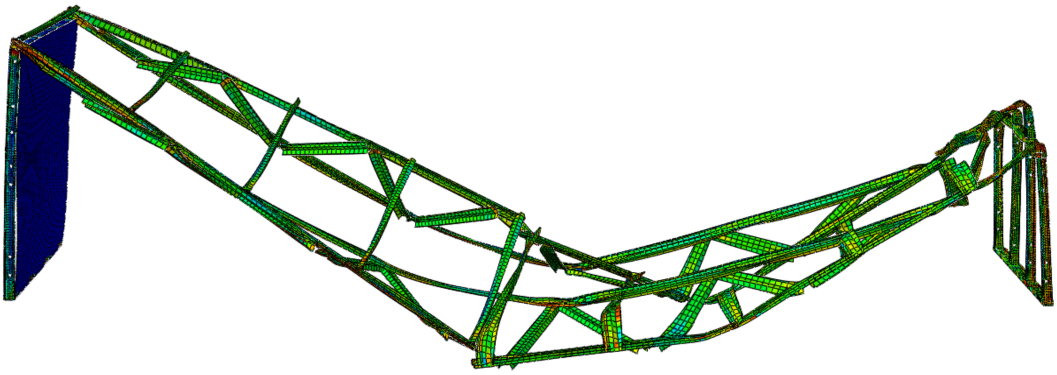

Figure 6.27: FE Model (North Wall Temperature 628.23 °C)

Figure 6.28: Final Collapse Mechanism

6.8.4 Results and Discussions of Finite Element Analysis and Full-Scale Fire Test

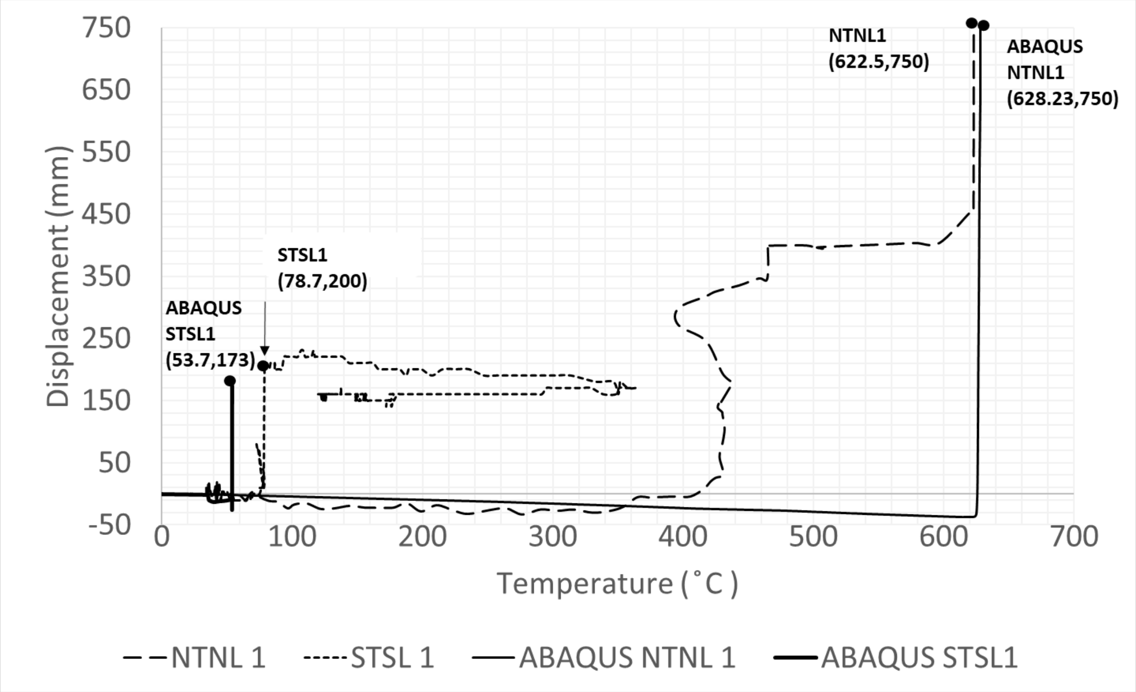

Figure 6.29: Comparison of Collapse Temperature and Displacement

Figure 6.29 shows the comparison of collapse temperature and displacement of FE results and full-scale fire test results. For northern wall, the full-scale fire test recorded collapse temperature of 622.5 °C. Whereas, the collapse temperature of northern wall in FE model was 628.23 °C. There is only a difference of 0.92%. The failure mode of the northern wall was governed by the snap-through buckling of wall studs. The comparison of failure mode for FE results and full-scale fire test are shown in Figure 6.30, Figure 6.31and, Figure 6.32. The photographs show an identical failure of snap-through buckling in vicinity to the mid-rail along the northern wall. Therefore, the FE can simulate the snap-through buckling failure of the cold-formed steel wall framings.

In addition, the southern wall in the full-scale test did not collapse as well as the FE model. The FE results for southern wall recorded an inward wall displacement of 173 mm at 53.7 °C. Whereby, the southern wall in full-scale test recorded inward wall displacement of 200 mm at 78.7 °C. Figure 6.33 and Figure 6.34 show the southern wall with and without the display of fire rated gypsum board at the end of the simulation. Figure 6.34 and Figure 6.35 show the southern wall in FE model and also the full-scale fire test did not collapse and there is no obvious buckling observed around the southern wall.

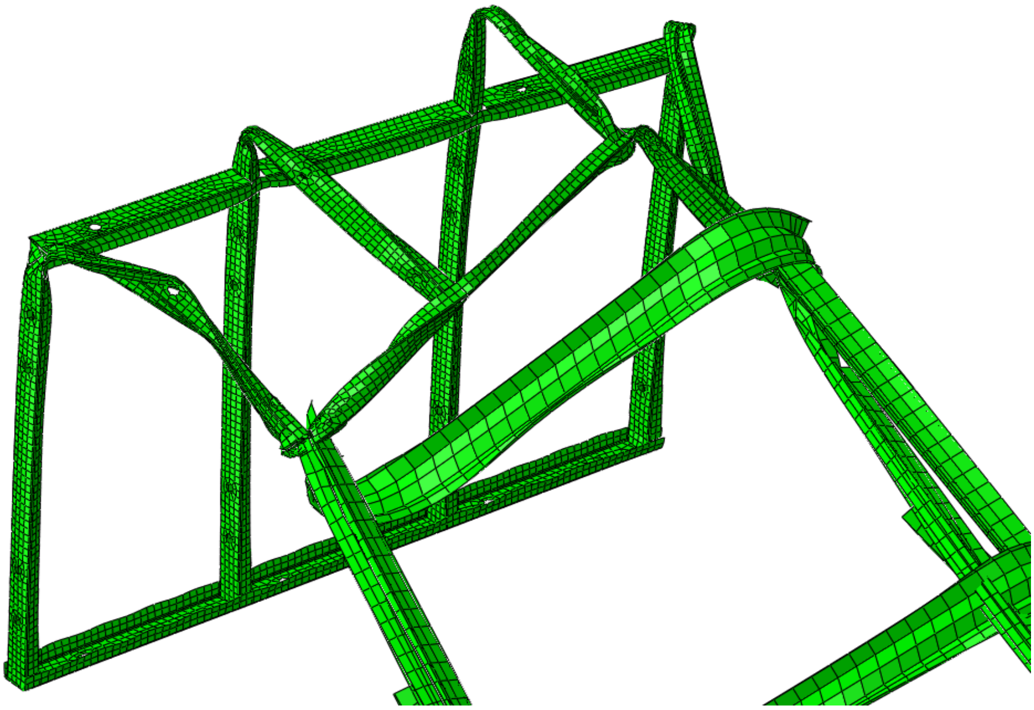

Figure 6.30: **Inward Snap-Through Buckling of Northern Wall Studs in FE Model**

Figure 6.31: **Inward Snap-Through Buckling of Northern Wall Studs in Fire Test**

Figure 6.32: Comparison of The Locations of Fire Hinge

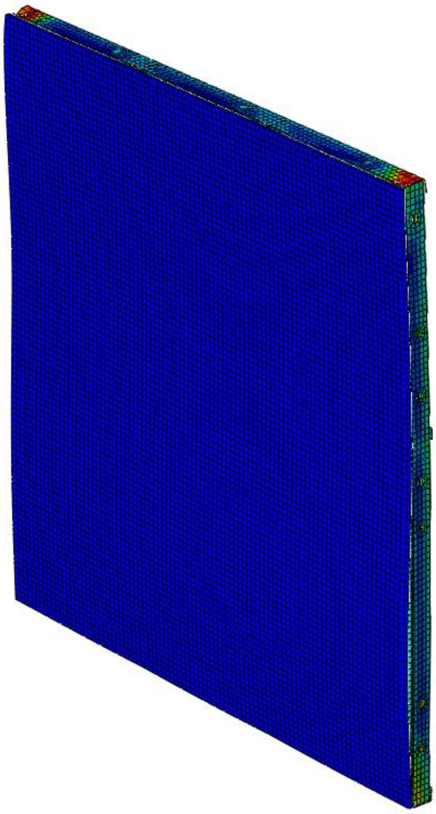

Figure 6.33: FE Model of Southern Wall

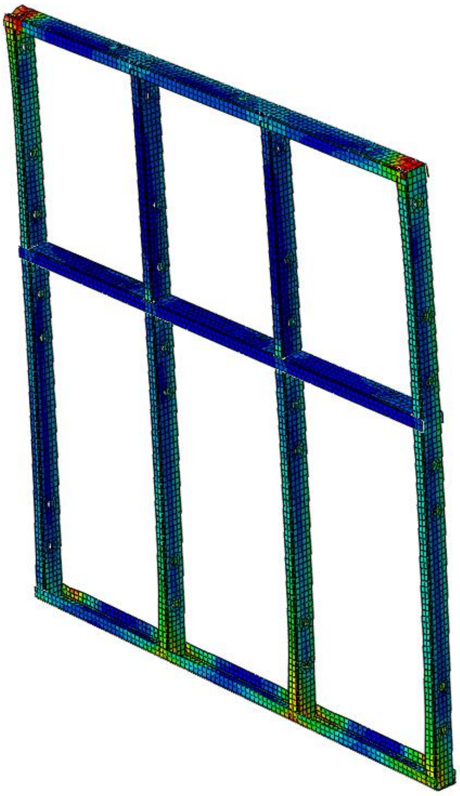

Figure 6.34: FE Model of Southern Wall (Hidden Gypsum board)

Figure 6.35: End of Full-Scale Fire Test at Southern Wall

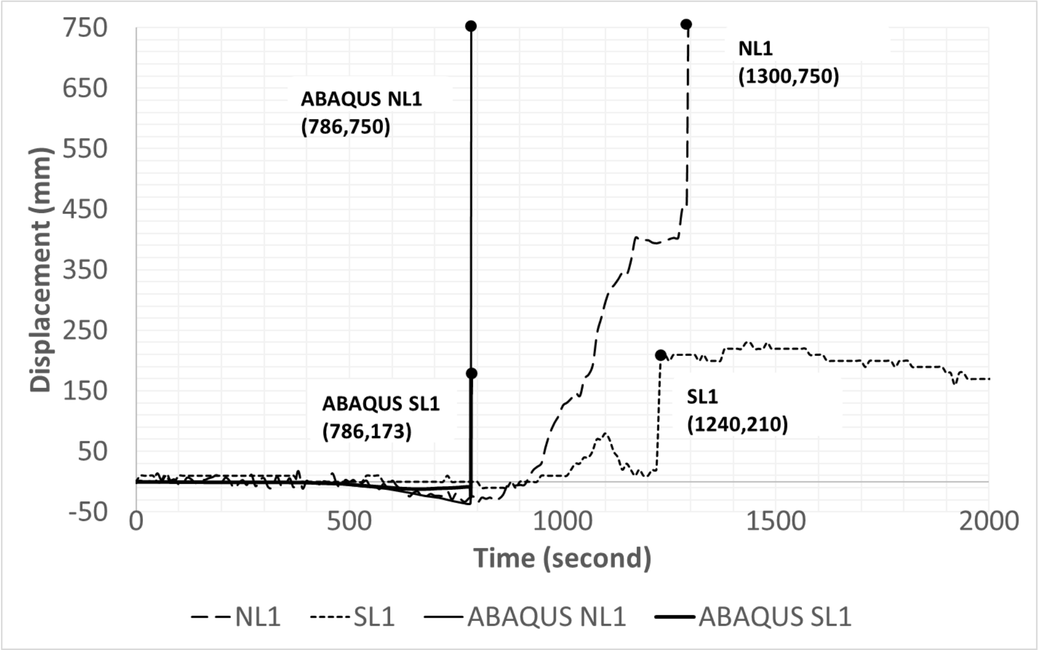

Figure 6.36: Comparison of Time of Collapse and Displacement

In relation to the time of collapse, Figure 6.36 shows displacement against time curves of northern and southern walls which compare the time of collapse in the FE model and the full-scale test results. The southern wall did not collapse however, an inward displacement was reported. The FE results show the northern wall has collapsed towards the fire compartment at a time of 786 seconds. Whereby, the time of collapse for the northern wall recorded in the full-scale fire test was 1300 seconds. Moreover, the FE results for the southern wall shows an inward displacement of 173 mm at 786 seconds. Whereas the southern wall in full-scale test recorded a significant inward displacement of 210 mm at 1240 seconds. FE model predicted an earlier time of collapse by 8 minutes and 34 seconds compared to the full-scale test results for the northern wall. Whereas for southern wall, the FE results also predicted an earlier time of collapse by 7 minutes and 34 seconds.

In overall comparison, the earlier time of wall collapse predicted was susceptible to the pinned base assumption made earlier in Section 5.1. Similarly, the ABAQUS NTNL1 in displacement against temperature curve in Figure 6.29, did not captured the stabilization effect around 400 °C to 480 °C. It is believed with inclusion of base rotational stiffness may delay the time of collapse and capture the stabilization effects during the collapse.

Figure 6.37: Tearing of Top Rail in North Wall

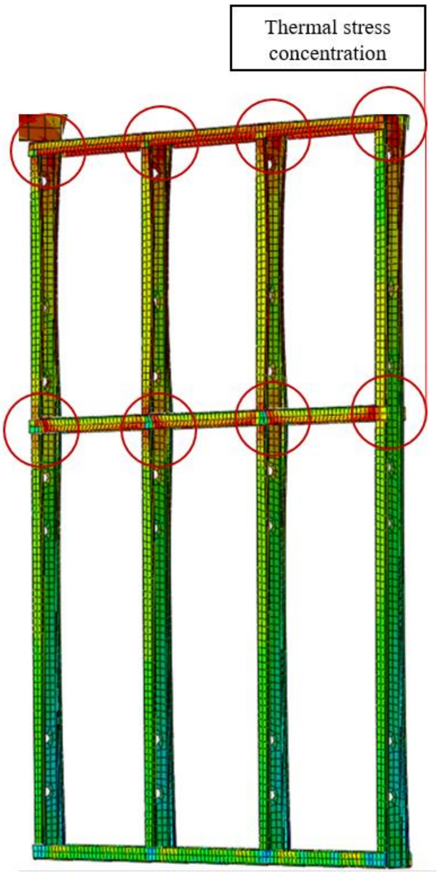

Figure 6.38: Thermal Stress Concentration on North Wall (667 sec)

Lastly, the side rails or the top, middle and bottom track played an important role in collapse mechanism of CFS structure under fire. In the full-scale fire test, the top rail of northern side wall acted in tension which prevented the wall from out of plane collapse. However, the top rail buckled severely along their length due to being pulled by roof trusses during exposed to high temperature. Figure 6.37 shows the flange of top rail at the corner was teared due to material degradation at high temperature. Thus, the top rail failed to provide lateral restraint to the wall studs. It was observed the failure of the wall were governed by the buckling of CFS member rather than failure of connections.

In the FE model, during the wall being pulled outwards by roof trusses due to thermal expansion, the top and mid rail temporarily provided laterally restrained to the compression flange. This can be evident by the FE results where the thermal stresses are concentrated on the top rail and mid rail at 667 sec as shown in Figure 6.38. The side rails had the tendency to prevent outward collapse by restraining the vertical CFS studs. However, the top and mid rail failed to provide lateral restraint to the compression flange when the north wall collapsed inward. Only the bottom rail provided lateral restrain to the north wall as it did not buckle severely. This is because most of the heat were accumulated in the roof and knee level and hence, the bottom rail was less vulnerable to fire. For south wall, all the side rails provided lateral restraint to the vertical studs as it was protected by the gypsum board.

6.9 Conclusions

The full-scale fire test results have been analysed and discussed. The cold-formed steel structure was collapsed inwards asymmetrically at 628.23°C. The collapse of the cold-formed steel structure was due to snap-through buckling of the northern wall. As predicted, the southern wall did not collapse due to the protection of fire rated gypsum boards. The full-scale fire test revealed the behaviour of cold-formed steel wall framings in a complete building differs from the component in laboratory. One of the reasons is the effects of structural continuity. In addition, the collapse of the northern wall at 628.23°C revealed the critical temperature of 350°C proposed by Eurocode 3 part 1.2 (CEN, 2005) is overly conservative.

A comparison has been made for the full-scale fire test results and the finite-element results. The finite element results show a reasonable correlation to the full-scale in terms of collapse temperature, displacement of the walls and overall collapse mechanism. Therefore, the finite element model developed in this research can facilitate further investigation for more parametric studies.

7 Conclusions and Recommendations

7.1 Introduction

A full-scale, non-uniform natural fire test was carried out on cold-formed steel structure with roof truss supported by the studs and framing wall assembled with and without fire-rated gypsum boards. A non-linear implicit dynamic finite element model has been developed to analyse and demonstrate the collapse behaviour of cold-formed steel structure with roof truss supported by the studs and framing wall assembled with and without fire-rated gypsum boards under natural fire. Finally, the finite elements model was verified with the full-scale non-uniform natural fire test results.

7.2 Conclusions

Collapse behaviour of cold-formed steel structure with roof truss supported by the studs and framing wall assembled with and without fire-rated gypsum board under elevated temperatures was studied and it was found that the structure collapsed with an inwards asymmetrical collapse mechanism at 622.5 °C where the collapse is being due to the member buckling rather than failure of the connections.

Failure of roof truss and frame is not due to the failure of the screwed connections. The failure was mainly governed by an inward snap-through of wall studs at one-third of the wall height.

The behaviours of collapse demonstrated by northern and southern walls are different as predicted where the fire–rated gypsum board is able to protect the cold-formed steel wall frames. The southern wall protected by fire-rated gypsum wall did not collapse at the end of the test. A layer of 15mm fire-rated gypsum board protected the cold-formed steel studs from 44.8 % rise in temperature and also resulted in 48.5% of time delay. The validated finite element model can predict the collapse of cold-formed steel structure where the comparison shows the

FE results correlates well with full-scale fire test results. The collapse temperature of CFS structure from the fire test and that predicted using the finite element model are 622.5 °C and 628.2 °C respectively. It is less than 1% in differences.

7.3 Recommendations for Future Work

The research met the aim and objectives set earlier in this study.
Further recommendation for future works in this research field includes:

1) Further research on the effect of initial imperfections on the performance of the cold-formed steel structure under fire.

2) Further investigation on the contact friction of cold-formed steel members experimentally to provide data for the contacts in finite element modelling.

3) Further investigation on the effect of different material properties of CFS and fire-rated gypsum board, thickness of primary structural members and effect of joint stiffness through extensive parametric study using the FE model.

4) Further development in performance-based design method for cold-formed steel roof truss in fire collapse temperature predicted using the finite element shell model through parametric study.

5) Comparison of explicit and implicit dynamic analysis in different finite element software to evaluate the computational efficiency.

6) Further research on effect of joint rigidity including actual base fixity on the performance of cold-formed steel structure under fire.

References

ABAQUS. (2014). *ABAQUS Analysis User's Manual-Version 6.14-1*. ABAQUS INC., USA.

Abreu, J. C. B., Vieira, L. M., Abu-Hamd, M. H., & Schafer, B. W. (2014). development of performance-based fire design for cold-formed steel. *Fire Science Reviews, 3*(1), 1.

Alfawakhiri, F., Sultan, M., & MacKinnon, D. (1999). Fire Resistance of Loadbearing Steel-Stud Wall Protected with Gypsum Board: A Review. *Fire Technology, 35*(4), 308-335. doi:10.1023/A:1015401029995

American Iron and Steel Institute. (2007). *North American specification for the design of cold-formed steel structural members*. American Iron & Steel Institute, Committee of Steel Plate Producers & Committee of Stainless Steel Producers.

Ariyanayagam, A., & Mahendran, M. (2014a). Experimental Study of Load-Bearing Cold-Formed Steel Walls Exposed to Realistic Design Fires. *Journal of Structural Fire Engineering, 5*(4), 291-330. doi:10.1260/2040-2317.5.4.291

Ariyanayagam, A. D., & Mahendran, M. (2014b). Numerical modelling of load bearing light gauge steel frame wall systems exposed to realistic design fires. *Thin-Walled Structures, 78*, 148-170. doi:http://dx.doi.org/10.1016/j.tws.2014.01.003

Bahr, O. (2014). A Study on the Conservativeness of ISO Standard Fire in Office Buildings. *Journal of Structural Fire Engineering, 5*(1), 35-46. doi:doi:10.1260/2040-2317.5.1.35

Bisby, L., Gales, J., & Maluk, C. (2013). A contemporary review of large-scale non-standard structural fire testing. *Fire Science Reviews, 2*(1), 1.

Bong, M. W. (2005). *Structural Fire Performance of Steel Portal Frame Buildings*. Master Thesis, University of Canterbury, New Zealand.

Bong, M. W., Buchanan, A. H., Moss, P. J., & Dhakal, R. P. (2005). *Structural fire performance of steel portal frame buildings*: Department of Civil Engineering, University of Canterbury.

Bonnier, G., & Devin, E. (1997). Couples thermoélectriques. *Caractéristiques et Mesures de Températures. Techniques de l'Ingénieur, 2*, 590.

Buchanan, A. H. (2001). *Structural Design for Fire Safety*. John Wiley & Sons, Ltd, England, UK.

Cadorin, J. F., & Franssen, J. M. (2003). A tool to design steel elements submitted to compartment fires—OZone V2. Part 1: pre-and post-flashover compartment fire model. *Fire Safety Journal*, *38*(5), 395-427.

Cadorin, J. F., Pintea, D., Dotreppe, J. C., & Franssen, J. M. (2003). A tool to design steel elements submitted to compartment fires—OZone V2. Part 2: Methodology and application. *Fire safety journal*, *38*(5), 429-451.

Chen, J., & Young, B. (2007). Experimental investigation of cold-formed steel material at elevated temperatures. *Thin-Walled Structures, 45*(1), 96-110. doi:http://dx.doi.org/10.1016/j.tws.2006.11.003

Chen, W., Ye, J., Bai, Y., & Zhao, X.-L. (2013). Thermal and mechanical modeling of load-bearing cold-formed steel wall systems in fire. *Journal of Structural Engineering, 140*(8), A4013002.

Cheng, S. (2015). *Fire performance of cold-formed steel sections.* PhD Thesis, Plymouth University.

CONSTRADO (1979). *The Study of the Behaviour of Portal Frames in Fire When Subject to Boundary Conditions.* The Constructional Steel Research and Development Organisation, UK.

Cooke, G., & Latham, D. (1987). The inherent fire resistance of a loaded steel framework. *Steel Construction Today, 1*(2), 49-58.

Cramer, S. M., Friday, O. M., White, R. H., & Sriprutkiat, G. (2003). Mechanical properties of gypsum board at elevated temperatures. In *Fire and materials 2003: 8th International Conference, January 2003, San Francisco, CA, USA. London: Interscience Communications Limited, c2003: pages 33-42.*

De Souza Junior, V., Creus, G., & Franssen, J.-M. (2002). numerical modelling of a single storey industrial building at elevated temperature-comparison between the 2d and 3d analyses. *Mecanica Computacional, 21*, 1986-1997.

Dong, Y., & Prasad, K. (2009). Thermal and structural response of a two-story, two bay composite steel frame under fire loading. *Proceedings of the Combustion Institute*, *32*(2), 2543-2550.

[DrywallTrims] [Digital image]. (n.d.). Retrieved from http://www.drywalltrims.com/product/KNEEWALLKIT-250-24.html

Ellobody, E., Feng, R., & Young, B. (2014). Chapter 3 - Finite Element Modeling *Finite Element Analysis and Design of Metal Structures* (pp. 31-55). Boston: Butterworth-Heinemann.

European Committee for Standardization (CEN). (2005). Design of steel structures—Part 1-2: General rules—Structural fire design. *Eurocode 3*.

Feng, M. (2004). *Numerical and experimental studies of cold-formed thin-walled steel studs in fire.* PhD Thesis, The University of Manchester. Retrieved from http://ethos.bl.uk/OrderDetails.do?uin=uk.bl.ethos.505857

Feng, M., Wang, Y. C., & Davies, J. M. (2003a). Structural behaviour of cold-formed thin-walled short steel channel columns at elevated temperatures. Part 1: experiments. *Thin-Walled Structures, 41*(6), 543-570. doi:http://dx.doi.org/10.1016/S0263-8231(03)00002-8

Feng, M., Wang, Y. C., & Davies, J. M. (2003b). Structural behaviour of cold-formed thin-walled short steel channel columns at elevated temperatures. Part 2: Design calculations and numerical analysis. *Thin-Walled Structures*, *41*(6), 571-594. doi:http://dx.doi.org/10.1016/S0263-8231(03)00003-X

Franssen, J. M. (2005). SAFIR: A thermal/structural program for modelling structures under fire. *Engineering Journal-American Institute of Steel Construction Inc*, *42*(3), 143-158.

Gentili, F. (2013). *Multi-physics modelling for the safety assessment of complex structural systems under fire.* PhD Thesis, Sapienza University of Rome.

Gere, J. M., & Timoshenko, S. P. (1991). Mechanics of Materials, 3rd SI ed. *UK: Chapman and Hall*.

Gerlich, J. (1995). *Design of loadbearing light steel frame walls for fire resistance.* University of Canterbury.

Grosshandler, W. L. (2007). *Fire Resistance Proficiency Testing of Gypsum/Steel-Stud Wall Assemblies.*

Gunalan, S. (2011). *Structural behaviour and design of cold-formed steel wall systems under fire conditions.* PhD Thesis, Queensland University of Technology.

Gunalan, S., & Mahendran, M. (2014). Fire performance of cold-formed steel wall panels and prediction of their fire resistance rating. Fire Safety Journal, 64(0), 61-80. doi:http://dx.doi.org/10.1016/j.firesaf.2013.12.003

Gunawan, L. (2011). *Numerical models to simulate the thermal performance of LSF wall panels*. Mphil Thesis, Queensland University of Technology.

Hilber, H. M., & Hughes, T. J. (1978). Collocation, dissipation and [overshoot] for time integration schemes in structural dynamics. *Earthquake Engineering & Structural Dynamics*, *6*(1), 99-117.

Huang, Y., & Young, B. (2014). The art of coupon tests. *Journal of Constructional Steel Research*, *96*(0), 159-175. doi:http://dx.doi.org/10.1016/j.jcsr.2014.01.010

Iqbal, N. (2016). *Analysis of Catenary Effect in Steel Beams and Trusses Exposed to Fire.* PhD Thesis, Lulea University of Technology.

ISO. (1999). *ISO 834: Fire Resistance Tests - Elements of Building Construction.* Geneva: International Standards Office.

Javed, M. F., Hafizah, N., Memon, S. A., Jameel, M., & Aslam, M. (2017). Recent research on cold-formed steel beams and columns subjected to elevated temperature: A review. *Construction and Building Materials, 144*, 686-701. doi:https://doi.org/10.1016/j.conbuildmat.2017.03.226

Johnston, R.P., Lim, J., Xu, Y., Sonebi, M., Armstrong, C., Lau, H., . . . Mei, C. (2014). Cold-formed steel portal frames in fire: full-scale testing and finite element analysis. *The Structural Engineer: journal of the Institution of Structural Engineer, 92*(10), 44-50.

Johnston, R. P., Sonebi, M., Lim, J. B., Armstrong, C. G., Wrzesien, A. M., Abdelal, G., & Hu, Y. (2015). The Collapse Behaviour of Cold-formed Steel Portal Frames at Elevated Temperatures. *Journal of Structural Fire Engineering*, *6*(2), 77-102.

Jones, B. H. (2001). *Performance of Gypsum Plasterboard Assemblies Exposed to Real Building Fires.* Master Thesis, University of Canterbury, New Zealand.

Kankanamge, N. D., & Mahendran, M. (2008). Numerical studies of cold-formed steel beams subject to lateral-torsional buckling at elevated temperatures. In *Fifth International Conference on Thin-walled Structures, Brisbane, Australia*(pp. 737-744).

Kankanamge, N. D., & Mahendran, M. (2011). Mechanical properties of cold-formed steels at elevated temperatures. *Thin-Walled Structures, 49*(1), 26-44. doi:http://dx.doi.org/10.1016/j.tws.2010.08.004

Keerthan, P., & Mahendran, M. (2012). Numerical modelling of non-load-bearing light gauge cold-formed steel frame walls under fire conditions. *Journal of Fire Sciences*, 0734904112440688.

Kesawan, S., & Mahendran, M. (2015). Predicting the performance of LSF walls made of hollow flange channel sections in fire. *Thin-Walled Structures*(0). doi:http://dx.doi.org/10.1016/j.tws.2015.03.014

Kodur, V. K. R., Garlock, M., & Iwankiw, N. (2012). Structures in fire: state-of-the-art, research and training needs. *Fire Technology*, *48*(4), 825-839.

Kolarkar, P., & Mahendran, M. (2012). Experimental studies of non-load bearing steel wall systems under fire conditions. *Fire Safety Journal, 53*, 85-104. doi:http://dx.doi.org/10.1016/j.firesaf.2012.06.009

Kontogeorgos, D., & Founti, M. (2010). Numerical investigation of simultaneous heat and mass transfer mechanisms occurring in a gypsum board exposed to fire conditions. *Applied Thermal Engineering, 30*(11–12), 1461-1469. doi:http://dx.doi.org/10.1016/j.applthermaleng.2010.03.006

Laím, L., Rodrigues, J. P., & da Silva, L. S. (2013). Numerical analysis of cold-formed steel beams in fire. In *Proceedings of the 13th International Conference and Exhibition on Fire and Materials, San Francisco, USA* (pp. 163-174).

Landesmann, A., & Camotim, D. (2016). Distortional failure and DSM design of cold-formed steel lipped channel beams under elevated temperatures. *Thin-Walled Structures, 98*, 75-93.

Lee, J. H., Mahendran, M., & Makelainen, P. (2003). Prediction of mechanical properties of light gauge steels at elevated temperatures. *Journal of Constructional Steel Research, 59*(12), 1517-1532. doi:http://dx.doi.org/10.1016/S0143-974X(03)00087-7

Lou, G., Wang, C., Jiang, J., Jiang, Y., Wang, L., & Li, G.-Q. (2018). Fire tests on full-scale steel portal frames against progressive collapse. *Journal of Constructional Steel Research, 145*, 137-152. doi:https://doi.org/10.1016/j.jcsr.2018.02.024

Makelainen, P., & Miller, K. (1983). Mechanical Properties of Cold-Formed Galvanized Sheet Steel Z32 at Elevated Temperatures. *Helsinki University of Technology, Finland*.

Mehaffey, J., Cuerrier, P., & Carisse, G. (1994). A model for predicting heat transfer through gypsum-board/wood-stud walls exposed to fire. *Fire and Materials, 18*(5), 297-305.

Manzello, S. L., Gann, R. G., Kukuck, S. R., & Lenhert, D. B. (2007). Influence of gypsum board type (X or C) on real fire performance of partition assemblies. *Fire and Materials: An International Journal, 31*(7), 425-442.

Martins, A. D., Camotim, D., Dinis, P. B., & Young, B. (2015, November). Local–Distortional Interaction in Cold-formed Steel Columns: Mechanics, Testing, Numerical Simulation and Design. In *Structures* (Vol. 4, pp. 38-57). Elsevier.

Mirambell, E., & Real, E. (2000). On the calculation of deflections in structural stainless-steel beams: an experimental and numerical investigation. *Journal of Constructional Steel Research*, 54(1), 109-133.

Moss, P., Dhakal, R., Bong, M., & Buchanan, A. (2006). Structural fire performance of steel portal frame buildings.

Newman, G. M. (1990). *Fire and steel construction: The behaviour of steel portal frames in boundary conditions*. Steel Construction Institute.

Nyman, J. F. (2002). *Equivalent fire resistance ratings of construction elements exposed to realistic fires.* Mphil Thesis, University of Canterbury.

O'Meagher, A. J., Bennetts, I. D., Dayawansa, P. H., & Thomas, I. R. (1992). Design of single storey industrial buildings for fire resistance. *Steel Construction, 26*(2).

Park, S.-H., Manzello, S. L., Bundy, M. F., & Mizukami, T. (2011). Experimental study on the performance of a load-bearing steel stud gypsum board wall assembly exposed to a real fire. *Fire Safety Journal, 46*(8), 497-505. doi:http://dx.doi.org/10.1016/j.firesaf.2011.09.001

Purkiss, J. A., & Li, L.-Y. (2013). *Fire safety engineering design of structures*: CRC Press.

Pyl, L., Schueremans, L., Dierckx, W., & Georgieva, I. (2012). Fire safety analysis of a 3D frame structure based on a full-scale fire test. *Thin-Walled Structures, 61*(0), 204-212. doi:http://dx.doi.org/10.1016/j.tws.2012.03.023

Ramberg, W. and Osgood, W. (1943). *Description of Stress-Strain Curves by Three Parameters.* NACA, Technical Note No. 902.

Rahman, M. (2012). *A computational study of the behaviour of hot-rolled portal frames in fire.* PhD Thesis, University of Strathclyde. Retrieved from http://ethos.bl.uk/OrderDetails.do?uin=uk.bl.ethos.576401

Rahman, M., Lim, J., Hamilton, R., Comlekci, T., Pritchard, D., & Xu, Y. (2009). An investigation of overturning moments of portal frames at elevated temperatures.

Rahmanian, I. (2011). *Thermal and mechanical properties of gypsum boards and their influences on fire resistance of gypsum board based systems* (Doctoral dissertation, The University of Manchester (United Kingdom)).

Rahmanian, I., & Wang, Y. C. (2012). A combined experimental and numerical method for extracting temperature-dependent thermal conductivity of gypsum boards. *Construction and Building Materials, 26*(1), 707-722. doi:http://dx.doi.org/10.1016/j.conbuildmat.2011.06.078

Ranawaka, T. (2006). *Distortional buckling behaviour of cold-formed steel compression members at elevated temperatures.* PhD Thesis, Queensland University of Technology.

Ranawaka, T., & Mahendran, M. (2009). Experimental study of the mechanical properties of light gauge cold-formed steels at elevated temperatures. *Fire Safety Journal, 44*(2), 219-229. doi:http://dx.doi.org/10.1016/j.firesaf.2008.06.006

Rasmussen, K. J. (2003). Full-range stress–strain curves for stainless steel alloys. J*ournal of constructional steel research, 59*(1), 47-61.

Rogers, C. A., & Hancock, G. J. (1997). Ductility of G550 sheet steels in tension. *Journal of Structural Engineering*, *123*(12), 1586-1594.

Rubert, A., & Schaumann, P. (1986). Structural steel and plane frame assemblies under fire action. *Fire Safety Journal, 10*(3), 173-184. doi:http://dx.doi.org/10.1016/0379-7112(86)90014-7

Rust, W. (2015). *Non-Linear Finite Element Analysis in Structural Mechanics* (pp. XIV, 363). doi:10.1007/978-3-319-13380-5

Rusthi, M., Keerthan, P., Ariyanayagam, A. D., & Mahendran, M. (2015). *Numerical studies of gypsum plasterboard and MGO board lined LSF walls exposed to fire.* Paper presented at the Proceedings of the Second International Conference on Performance-based and Life-cycle Structural Engineering (PLSE 2015).

Semitelos, G. K., Mandilaras, I. D., Kontogeorgos, D. A., & Founti, M. A. (2014). Simplified correlations of gypsum board thermal properties for simulation tools. *Fire and Materials*.

Shahbazian, A. (2013). *Simplified thermal and structural analysis methods for cold-formed thin-walled steel studs in wall panels exposed to fire from one side.* PhD Thesis, University of Manchester.

Shahbazian, A., & Wang, Y. C. (2013). A simplified approach for calculating temperatures in axially loaded cold-formed thin-walled steel studs in wall panel assemblies exposed to fire from one side. *Thin-Walled Structures, 64*, 60-72. doi:http://dx.doi.org/10.1016/j.tws.2012.12.005

Sidey, M. P., & Teague, D. P. (1988). Elevated temperature data for structural grades of galvanized steel. *British Steel (Welsh Laboratories) Report*.

Simms, W., & Newman, G. (2002). *Single Storey Steel Framed Buildings in Fire Boundary Conditions*, The Steel Construction Institute. *SCI Publication P, 313*, 2002.

Santiago, A., Simoes da Silva, L., Vaz, G., Vila Real, P., & Gameiro, L. A. (2008). Experimental investigation of the behaviour of a steel sub-frame under a natural fire. *Steel and Composite Structures*, *8*(3), 243-264.

Song, Y. (2008). *Analysis of industrial steel portal frames under fire conditions.* PhD Thesis, University of Sheffield.

Standard, A. (2007). Metallic materials—tensile testing at ambient temperature. *AS 1391-2007, Australia*.

Standard, A. (2005). AS 1530.4: Methods for fire tests on building materials, components and structures–Part 4: Fire-resistance test of elements of construction.

Standard, A. S. T. M. (1988). Designation: E119-88, standard test method for fire tests of building construction and materials. *ASTM International, USA.*

Standard, A. S. T. M. (2005). Designation: E 1269-05, standard test method for determining specific heat capacity by differential scanning calorimetry. *ASTM International, USA*.

Standard, B. (1986). BS 4360: Specification for weldable structural steels.

Standard, B. (1972). BS 476-8: Fire tests on building materials and structures. *Test methods and criteria for the fire resistance of elements of building construction*. Londres.

Steel, B. (1999). The behaviour of multi-storey steel framed buildings in fire. *British Steel, Rotherham, UK*, 82.

Sultan, M. A. (1996). A model for predicting heat transfer through non-insulated unloaded steel-stud gypsum board wall assemblies exposed to fire. *Fire Technology, 32*(3), 239-259. doi:10.1007/bf01040217

Sultan, M. A. (2010). Comparison of gypsum board fall-off in wall and floor assemblies exposed to furnace heat. In *12th Int. Conf. on Fire Science and Engineering* (pp. 1-6).

Sun, J. S., Lee, K. H., & Lee, H. P. (2000). Comparison of implicit and explicit finite element methods for dynamic problems. *Journal of Materials Processing Technology, 105*(1), 110-118. doi:https://doi.org/10.1016/S0924-0136(00)00580-X

Sun, R. R. (2012). *Numerical modelling for progressive collapse of steel framed structures in fire.* PhD Thesis, University of Sheffield.

[Supaloc Steel Building System] [Digital image]. (n.d.). Retrieved from http://supaloc.com.au/the-supaloc-system/

Swanger, W. H., & France, R. D. (1932, December). Effect of zinc coatings on the endurance properties of steel. In *Proc. ASTM* (Vol. 32, No. Part 2, pp. 430-454).

Thomas, G. (2002). Thermal properties of gypsum plasterboard at high temperatures. *Fire and Materials, 26*(1), 37-45.

Vassart, O., Brasseur, M., Cajot, L., Obiala, R., Spasov, Y., Friffin, A., . . . De la Quintana, J. (2007). Fire safety of industrial halls and lowrise buildings. *Final report, Technical Steel Research, European Commission*.

Vassart, O., Cajot, L.-G., O'Connor, M., Shenkai, Y., Fraud, C., Zhao, B., . . . Gens, F. (2004a). *3D simulation of Industrial Hall in case of fire. Benchmark between ABAQUS, ANSYS and SAFIR.* Paper presented at the Interflam2004 Proceedings. Fire Sciences and Engineering Conference.

Vassart, O., Cajot, L.-G., Franssen, J.-M., & Gens, F. (2004b). *Dynamic approach of structural fire calculation with FEM software.* Paper presented at the Proc. 5th International Conference on Performance-Based Codes and Fire Safety Design Methods.

Vassart, O., & Zhao, B. (2011). FRACOF Engineering Background. Report developed for the Leonardo Da Vinci Programme: Fire Resistance Assessment of Partially Protected Composite Floors (FRACOF). European Commission. *Education and Culture DG, Bordeaux, France*.

Vassart, O., Zhao, B., Cajot, L., Robert, F., Meyer, U., & Frangi, A. (2014). *Eurocodes: Background & Applications Structural Fire Design*. Retrieved from https://ec.europa.eu/jrc

Wakili, K. G., Hugi, E., Wullschleger, L., & Frank, T. (2007). Gypsum board in fire modeling and experimental validation. *Journal of Fire Sciences, 25*(3), 267-282.

Wang, Y., Burgess, I., Wald, F., & Gillie, M. (2012). Global modelling of structures in fire *Performance-Based Fire Engineering of Structures* (pp. 211-232): CRC Press.

Wong, S. Y. (2001). *The structural response of industrial portal frame structures in fire*. PhD Thesis, University of Sheffield.

Xiong, M.-X., Huang, Z.-Y., & Liew, J. Y. R. (2017). Modified Critical Temperatures for Steel Design Based on Simple Calculation Models in Eurocode 3. *Fire Technology, 53*(1), 227-248. doi:10.1007/s10694-015-0522-x

Yu, W.-W., & LaBoube, R. A. (2010). *Cold-Formed Steel Design* (4 ed.): John Wiley & Sons, Inc.

Zhao, B., Kruppa, J., Renaud, C., O'Connor, M., Mecozzi, E., Apiazu, W., . . . Kaitila, O. (2005). Calculation rules of lightweight steel sections in fire situations. *EUR*(21426), 1-226.

Every reasonable effort has been made to acknowledge the owners of copyright material. I would be pleased to hear from any copyright owner who has been omitted or incorrectly acknowledged.

Appendix A: Fire Load Survey Data

Table A.1

M_i	Kg
1	14
2	14
3	12
4	15
5	15
6	14
7	12
8	14
9	13
10	10
11	14
12	15
13	16
14	16
15	16
16	16
17	15
18	15
19	15
20	15
21	16
22	16
23	17
24	17
25	17
26	17
27	17
28	17
29	17
30	17
31	17
32	17
33	19
34	19
35	19

36	19
37	19
38	19
39	19
40	20
41	19
42	19
43	19
44	19
45	19
46	18
47	18
48	18
49	18
50	18
51	18
52	19
53	33
54	34
55	39
56	33
57	30
58	30
59	31
60	30
61	22
62	22
63	22
64	21
65	21
66	21
67	20
68	21
69	21
70	23
71	23
72	22
73	22
74	22
75	25
76	24
77	25
78	25
79	24
80	25

81	26
82	27
83	26
84	26
85	26
86	25
87	25
88	28
89	28
90	27
91	28
92	27
93	29
94	29
95	46
96	25
97	17
98	17
99	17
100	17
101	17
102	17
103	16
104	16
105	16
106	16
107	16
108	16
109	18
110	18
111	18
112	18
113	18
114	18
115	26
116	25
117	25
118	25
119	25
120	25
121	25
122	26
123	27
124	27

125	28
126	16
127	16
128	16
129	16
130	16
131	16
132	16
133	17
134	17
135	17
136	17
137	17
138	17
139	17
140	17
141	21
142	21
143	21
144	21
145	21
146	21
147	21
148	22
149	23
150	23
151	22
152	21
153	23
154	23
155	23
156	20
157	25
158	25
159	25
160	25
161	25
162	25
163	26
164	26
165	26
166	26
167	26
168	30
Total (Kg)	3517

A*f*	Fuel load area	47.8 m^2

Fire test wooden pallets arrangement

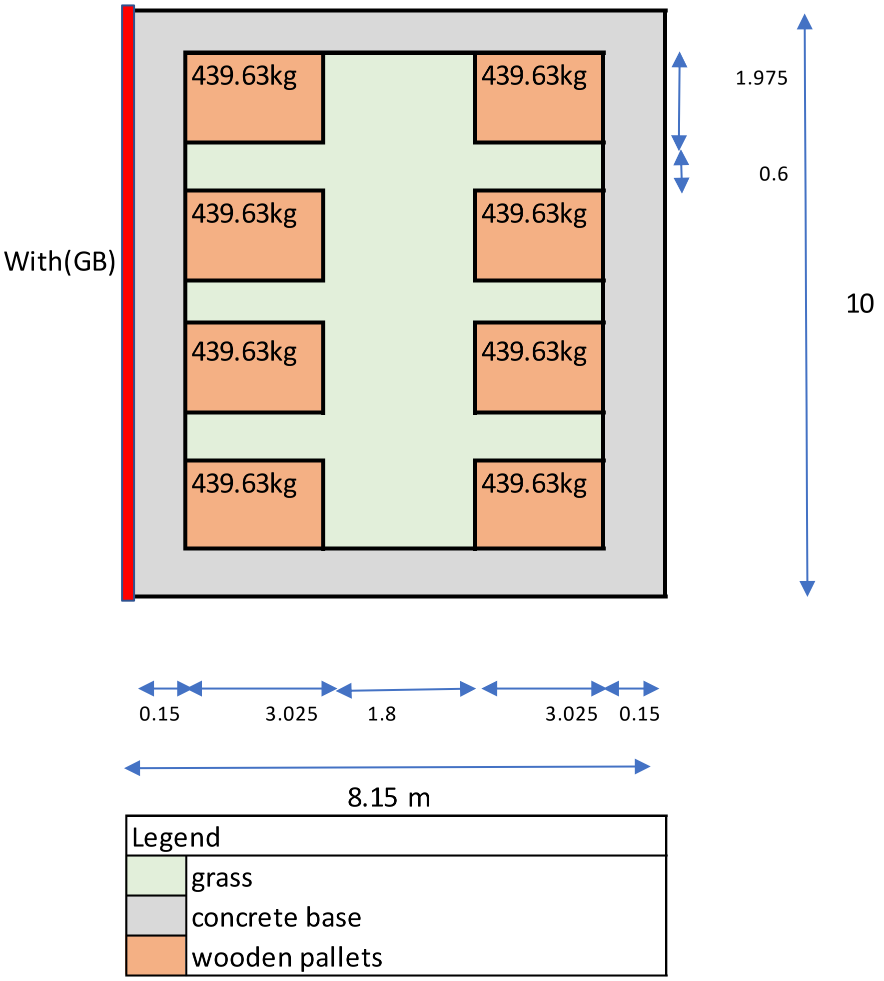

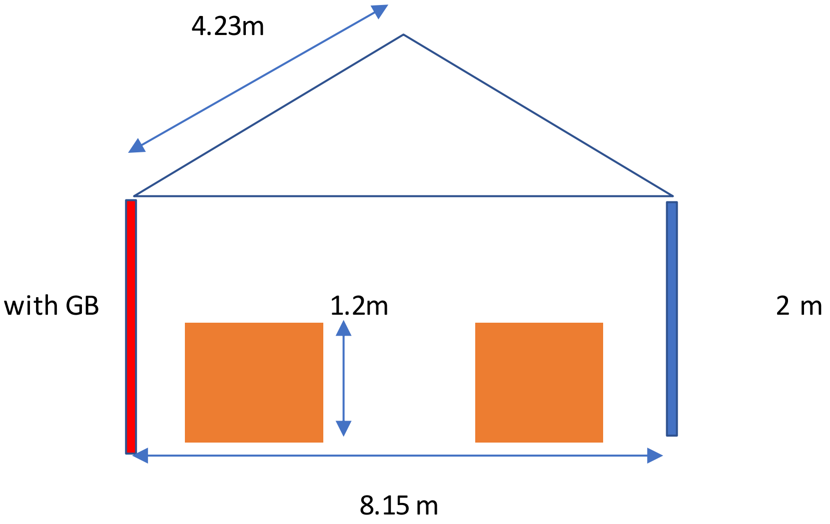

Af(fuel area)	Surface area of fuel(timber pallets)
Mi	total weight of each single combustible item in the fire compartment
Hci	effective caloric value of each combustible item
Hci (MJ/kg)	16.7

Af(floor area)	m^2	47.8
h (height of the fire compartment)	m	2.58
L (length of the fire compartment)	m	10
B (width of the fire compartment)	m	8

Hci (MJ/kg)	16.7	
$\frac{\sum M_i \Delta H_{ci}}{A_t}$	1228.743	MJ/m^2

average weight	20.93452	kg

FIRE LOAD	73.57741	kg/m^2

Time equivalence method given in Eurocode 3 was adopted to estimate the fire severity in time domain. Law (1997) stated the severity of two fire was equal if the areas under the two temperature-time curves were equal. The term “time equivalence” is usually taking to be the exposure time in the standard fire resistance test which gives the same heating effect on a structure as give compartment fire.

$t_{e,d}=q_{f,d}k_b w_f k_c$	In minutes	62.82181
$t_{e,d}$	time equivalent of exposure (min)	
$q_{f,d}$	design fire load density (MJ/m^2)	1228.871
w_f	ventilation factor	1.921863
k_c	correction factor of the member material	0.38
k_b	converstion factor related to thermal inertia of the enclosure ($min.m^2/MJ$)	0.07
kb has a value of 0.07 according to PD 7974.3 (compartment bounded with mansory and gypsum plaster For small fire compartment with floor area $Af<100m^2$ and without openings in roof For our case, $Af = 47.8\ m^2 < 100\ m^2$ and no openings in roof		

cross sectional material	**k_c**
Reinforced concrete	1
protected steel	1
unprotected steel	13.7*O

$W_f = O^{-1/2} A_f/A_t$		1.921863
$O = [A_v(h_{eq})^{1/2}]/A_t$	**(0.02< 0< 0.2) ($m^{1/2}$)**	0.027096
A_v	Total area of vertial openings on all walls (m^2)	4.971
h_{eq}	height of vertial openings (m)	1.9
A_t	total area of enclosure (m^2) (walls, ceiling and floor including openings)	252.88
A_f	Floor area (m^2)	80

Appendix B: Temperature Prediction by OZone

OZone V 3.0.3 Report

ANALYSIS

Analysis Name:

File Name:C:\Users\User\Desktop\Ozone Fire prediction\Fire test.ozn

Created: 15/07/2018 at 04:08:41 AM

Strategy

Select Analysis Strategy: 1 Zone

Parameters

Openings

Radiation Through Closed Openings: 0.8

Bernoulli Coefficient: 0.7

Physical Characteristics of Compartment

Initial Temperature: 293 K

Initial Pressure: 100000 Pa

Parameters of Wall Material

Convection Coefficient at the Hot Surface: 35 W/m²K

Convection Coefficient at the Cold Surface: 9 W/m²K

Calculation Parameters

End of Calculation: 7200 sec

Time Step for Printing Results: 60 sec

Maximum Time Step for Calculation: 10 sec

Air Entrained Model:Heskestad

Temperature Dependent Openings

Temperature Dependent: 400 °C

Stepwise Variation

Temperature	% of Total Openings
[°C]	[%]
20	10
400	50
500	100

Linear Variation

Temperature	% of Total Openings
[°C]	[%]
20	10
400	50
500	100

Time Dependent Openings

Time	% of Total Openings
[sec]	[%]
0	5
1200	100

Compartment

Compartment Geometry: Rectangular Floor

Height: 3.158 m

Depth: 8.15 m

Length: 10 m

Double Pitch Roof

Ceilling Height: 1.158

Floor

Material	Thickness	Unit mass	Conductivity	Specific Heat	Rel Emissivity	Rel Emissivity
	[cm]	[kg/m³]	[W/mK]	[J/kgK]	Hot Surface	Rel Emissivity
Peat soil	10000	700	0.29	3300	0.8	0.8

Ceiling

Material	Thickness	Unit mass	Conductivity	Specific Heat	Rel Emissivity	Rel Emissivity
	[cm]	[kg/m³]	[W/mK]	[J/kgK]	Hot Surface	Rel Emissivity
Primafelx cement board	0.45	1390	0.019	1000	0.8	0.8

Wall 1

Material	Thickness	Unit mass	Conductivity	Specific Heat	Rel Emissivity	Rel Emissivity
	[cm]	[kg/m³]	[W/mK]	[J/kgK]	Hot Surface	Rel Emissivity
Primafelx cement board	0.45	1390	0.019	1000	0.8	0.8

Openings

Sill Height Hi	Soffit Height Hs	Width	Variation	Adiabatic
[m]	[m]	[m]		
0	1.9	2.5	Constant	no

Wall 2

Material	Thickness	Unit mass	Conductivity	Specific Heat	Rel Emissivity	Rel Emissivity
	[cm]	[kg/m³]	[W/mK]	[J/kgK]	Hot Surface	Rel Emissivity
Primafelx cement board	0.45	1390	0.019	1000	0.8	0.8

Openings

Sill Height Hi	Soffit Height Hs	Width	Variation	Adiabatic
[m]	[m]	[m]		
1.8	1.9	0.04	Constant	no
1.5	1.6	0.04	Constant	no
0.8	0.9	0.04	Constant	no

Wall 3

Material	Thickness	Unit mass	Conductivity	Specific Heat	Rel Emissivity	Rel Emissivity
	[cm]	[kg/m³]	[W/mK]	[J/kgK]	Hot Surface	Rel Emissivity
Primafelx cement board	0.45	1390	0.019	1000	0.8	0.8

Wall 4

Material	Thickness	Unit mass	Conductivity	Specific Heat	Rel Emissivity	Rel Emissivity
	[cm]	[kg/m³]	[W/mK]	[J/kgK]	Hot Surface	Rel Emissivity
Gypsum board [EN12524]	15	900	0.25	1000	0.8	0.8
Primaflex cement board	0.45	1390	0.019	1000	0.8	0.8

Fire

Compartment Fire: Annex E (EN 1991-1-2)

Max Fire Area: 81.5 m^2

Fire Elevation: 2 m

Fuel Height: 1.2 m

Occupancy	Fire Growth Rate	RHRf	Fire Load qf,k	Danger of Fire Activation
		[kW/m²]	80% Fractile [MJ/m²]	
User Defined	150	3280	1228.8	1

Active Fire Fighting Measures

Automatic Water Extinguishing System	δ_1=1
Independent Water Supplies	δ_2=1
Automatic Fire Detection by Heat	$\delta_{3,4}$=1
Automatic Fire Detection by Smoke	
Automatic Alarm Transmission to Fire Brigade	δ_5=1
Work Fire Brigade	$\delta_{6,7}$=1
Off Site Fire Brigade	
Safe Access Routes	δ_8=1.5
Staircases Under Overpressure in Fire Alarm	
Fire Fighting Devices	δ_9=1.5
Smoke Exhaust System	δ_{10}=1.5

Fire Risk Area: 81.5 m^2 $\delta_{q,1}$ = 1.32

Danger of Fire Activation:$\delta_{q,2}$ = 1

Active Measures:$\Pi\delta_{n,i}$ = 3.375

$q_{f,d}$ = 5474.3

Combustion Heat of Fuel: 17.5MJ/kg

Combustion Efficiency Factor: 1

Combustion Model:Extended fire duration

RESULTS

Fire Area: The maximum fire area (81.50m²) is greater than 25% of the floor area (81.50m²). The fire load is uniformly distributed.

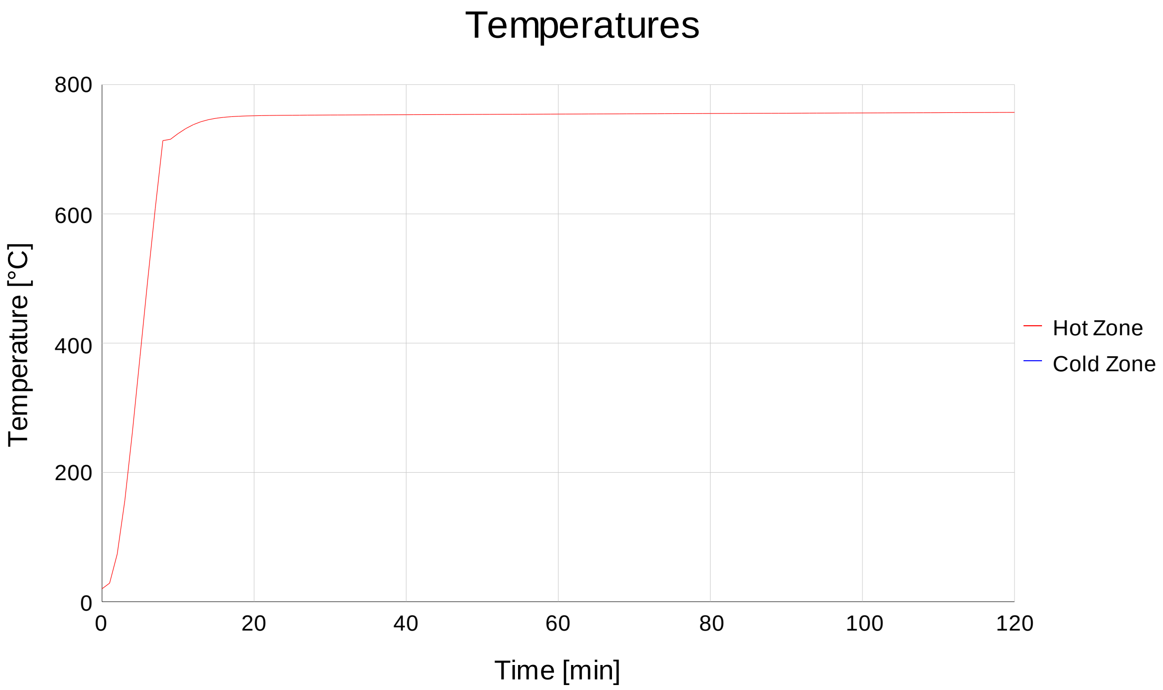

Figure B.1 Temperature against Time Curve of Gas in Compartment

Max: 757°C At:120 min

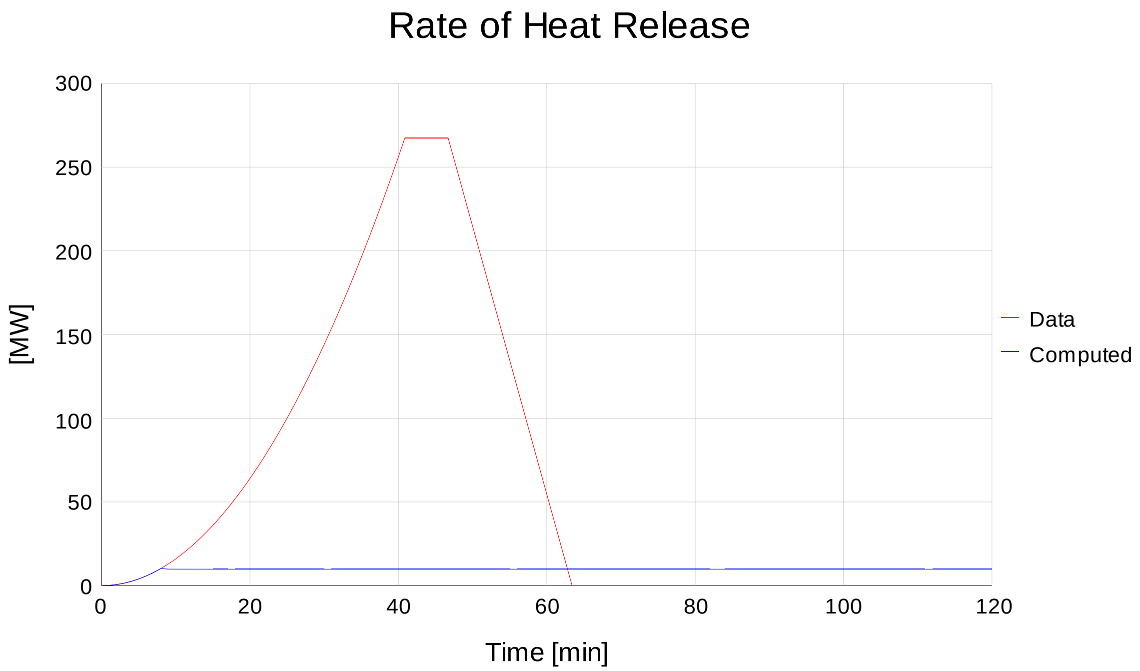

Figure B.2 RHR Data and Computed

Max: 267.32MW At:40.9 min

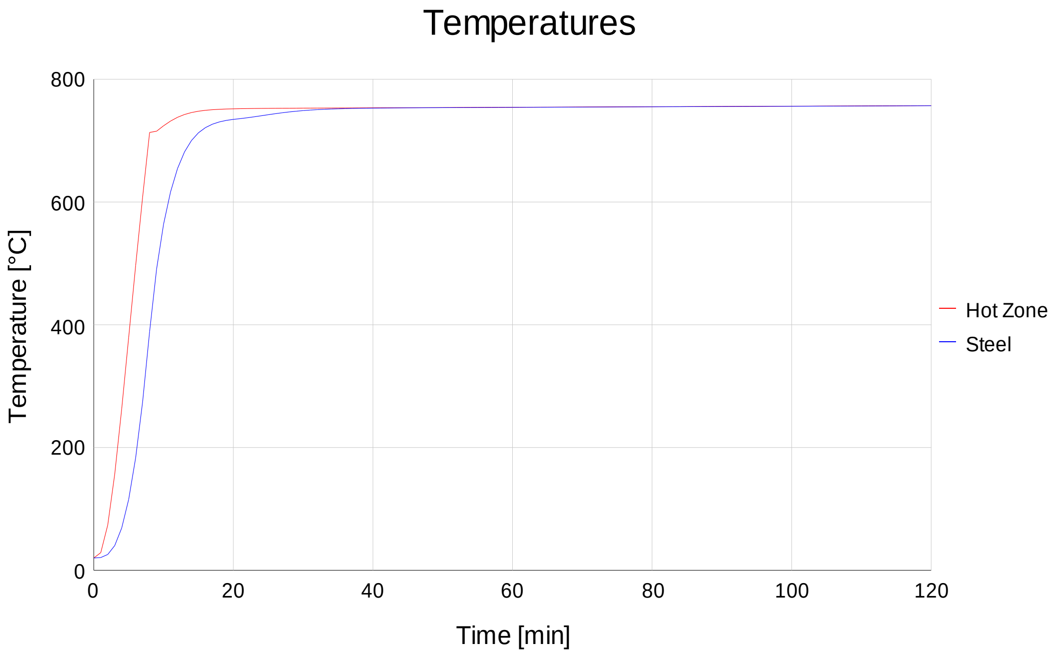

Figure B.3 Compartment Temperature and Steel Temperature

Max: 757°C At:120 min

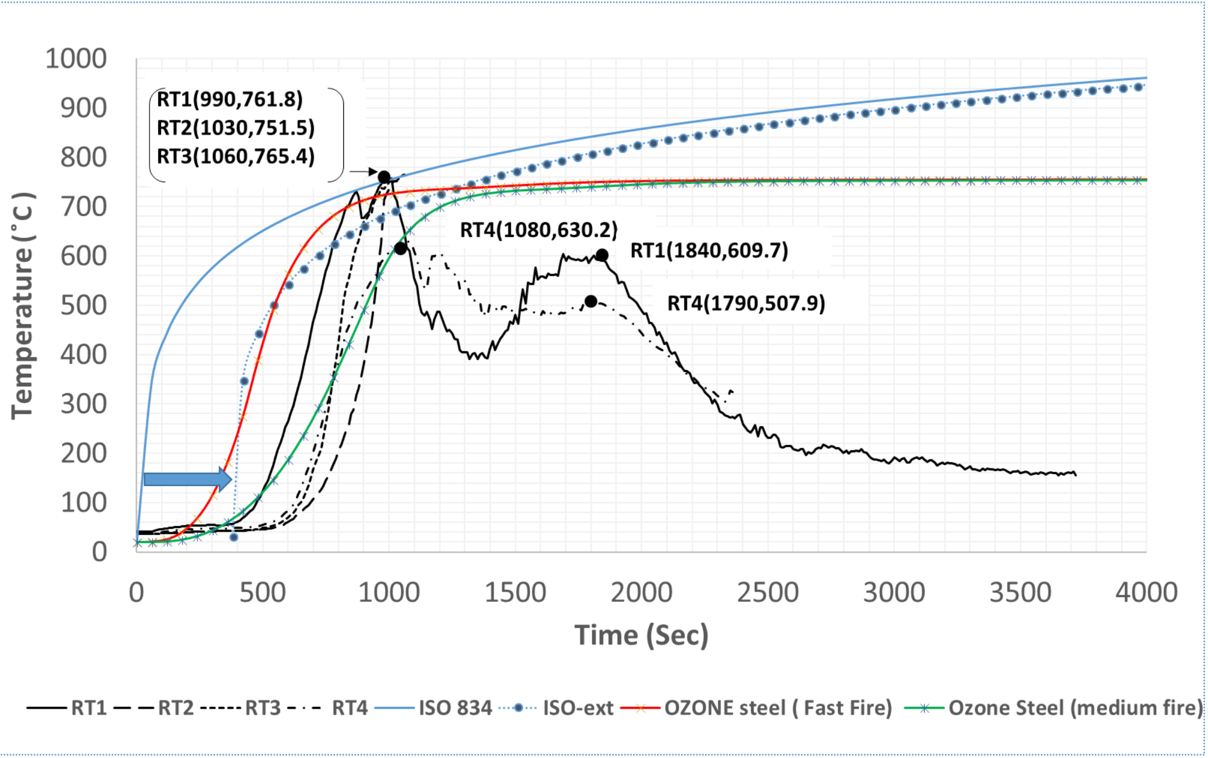

Figure B.3 Ozone Prediction for Fast Fire and Slow Fire Compared to Roof Truss Temperatures

Appendix C: Calculations of Permanent Load

The following shows the detailed calculations of permanent load acts on the top of purlins:

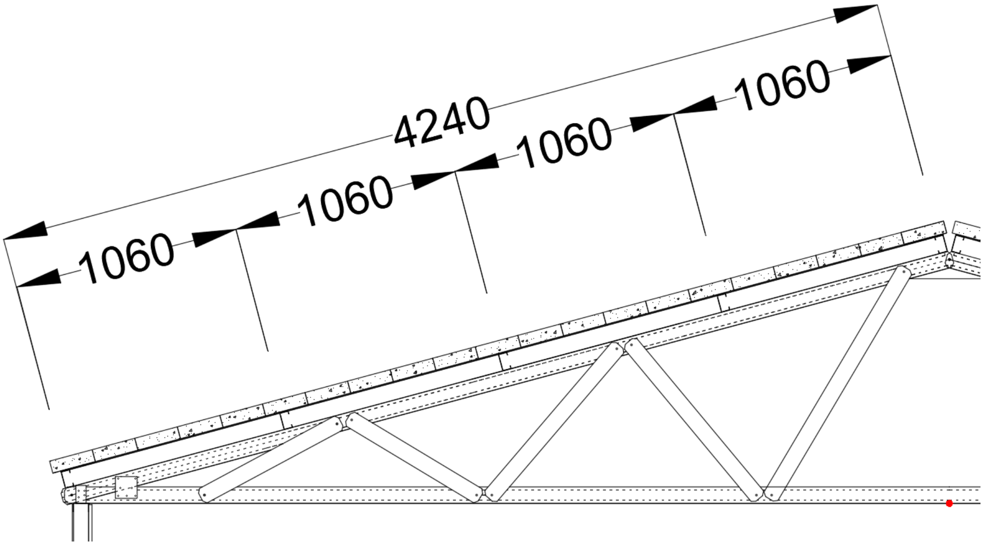

Figure C.4 Bricks on Roof

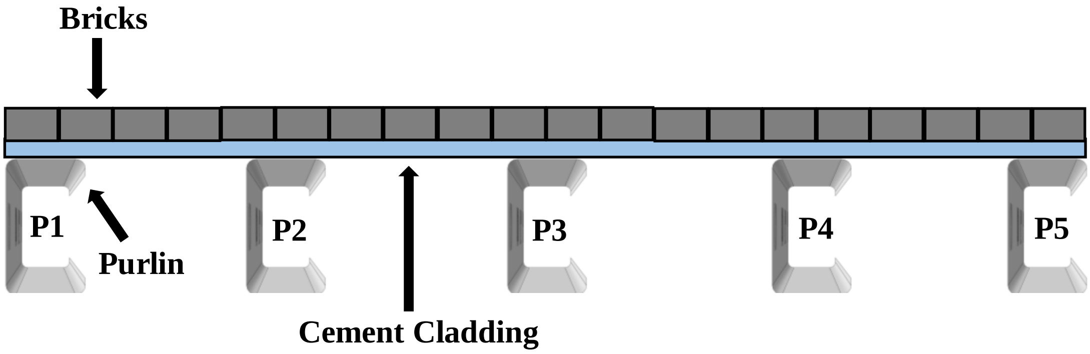

Figure C.5 Details of Bricks on Roof

Single Span of Double-Pitch Roof

To determine load acts on each purlin due to the weight of cement cladding:

$Density\ of\ Cement\ Cladding = 1390\ kg/m^3$

$Thickness\ of\ Cement\ Cladding = 0.0045m$

$Length\ of\ cladding = 1.667m$

$Purlin\ Spacing = 1.06m$

$$Total\ Volume\ of\ Cement\ Cladding = Thickness \times Length \times Spacing$$

$$= 0.0045 \times 10 \times 1.06$$

$$= 0.0477\ m^3$$

$$Mass\ of\ Cement\ Cladding = Volume \times Density$$

$$= 0.0477 \times 1390$$

$$= 66.03\ kg$$

$$Weight\ of\ Cement\ Cladding = Mass \times Gravitational\ Acceleration$$

$$= 66.03 \times 9.81$$

$$= 650.43\ N$$

$$\text{UDL of cement cladding on purlin} = \frac{650.43}{10 \times 1000} = 0.065\ \text{kN/m}$$

$$UDL\ on\ P1 = Load\ on\ P5 = \frac{Weight\ of\ Cement\ Cladding}{2}$$

$$P1\ and\ P5\ take\ half\ of\ the\ load = \frac{0.065}{2}$$

$$= 0.0325\ kN/m$$

$$UDL\ on\ P2 = P3 = P4 = 0.065\ \text{kN/m}$$

Each purlin is supported by seven trusses and spanned evenly at 1.667m

The purlin lapped at 5m hence adopting the 3-span formula,

The focus of this calculation was the load on the mid frame (4th truss)

Therefore,

Concentrated load on P1 = 2× 0.4× UDL_{p1}×1.667= 0.0433 kN =43.342 N

Concentrated load on P2=P3=P4 = 2× 0.4 × UDL_{p2} ×1.667= 0.0867 kN =86.68 N

To determine the load acts on each purlin due to weight of bricks:

$$Mass\ of\ Single\ Brick = 2\ kg$$

$$\begin{aligned} Length\ of\ Purlin\ Placed\ with\ Brick &= Purlin\ Spacing \times 4\ Spans \\ &= 1.06 \times 4 \\ &= 4.24m \end{aligned}$$

$$Length\ of\ Brick = 0.203m$$

$$height\ of\ Brick = 0.057m$$

$$\begin{aligned} Amount\ of\ Brick &= \frac{Length}{Breadth\ of\ Brick} \\ &= \frac{4.24}{0.203} \\ &= 20.887 \quad say\ 21\ Bricks \end{aligned}$$

$$\begin{aligned} Total\ Mass\ of\ Brick &= Amount\ of\ Brick \times Mass\ of\ Single\ Brick \\ &= 21 \times 2 \\ &= 42\ kg \end{aligned}$$

$$\begin{aligned} UDL\ of\ Brick\ along\ Purlin &= \frac{Total\ Mass\ of\ Brick}{Span\ Length\ of\ Purlin} \\ &= \frac{42}{4.24} \\ &= 9.852217 \frac{kg}{m} \\ &= 9.852217 \times 9.81 \\ &= 96.7\ N/m \end{aligned}$$

The distributed load on each purlin was calculated based on Figure C.6 below:

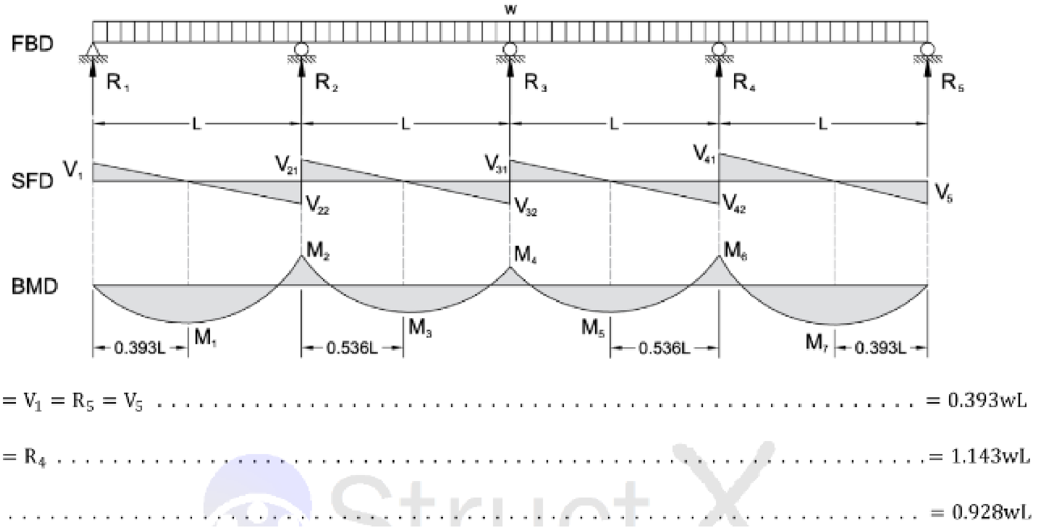

$R_1 = V_1 = R_5 = V_5$ . . . . = 0.393wL

$R_2 = R_4$ . . . . = 1.143wL

R_3 . . . . = 0.928wL

Figure C.6 Coefficient of load on four spans continuous beam (Struct X, 2016)

$$Load\ on\ P1 = Load\ on\ P5 \qquad = 0.393\ wL$$

$$= 0.393 \times 96.7 \times 1.06$$

$$= \mathbf{40.28\ N}$$

$$Load\ on\ P2 = Load\ on\ P4 \qquad = 1.413\ wL$$

$$= 1.143 \times 96.7 \times 1.06$$

$$= \mathbf{117.16\ N}$$

$$Load\ on\ P3 \qquad = 0.928\ wL$$

$$= 0.928 \times 96.7 \times 1.06$$

$$= \mathbf{95.12\ N}$$

Table C2 shows the total load acts on each purlin:

Table C2 Total load acts on each purlin

Purlin	P1	P2	P3	P4	P5
Cement Cladding, N	43.34	86.68	86.68	86.68	43.34
Brick, N	40.28	117.16	117.16	117.16	40.28
Total Load, N	83.62	203.84	203.84	203.84	83.62

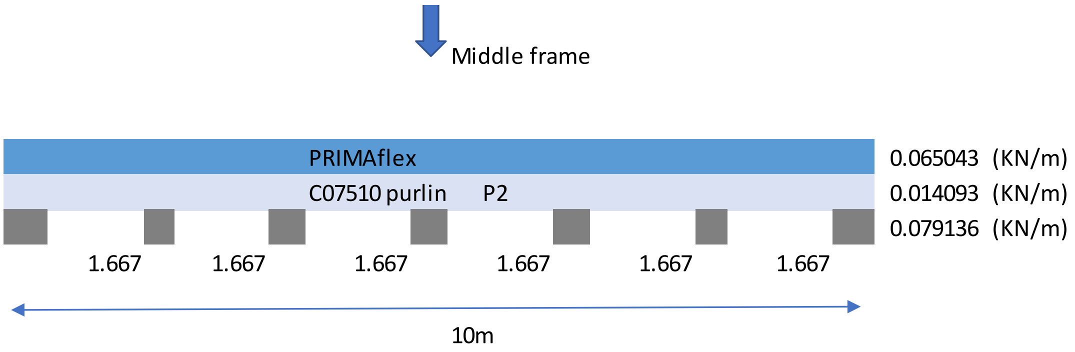

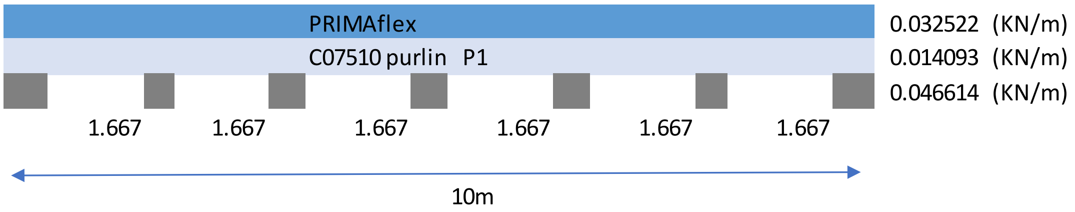

	T		T		T		T		T		T		T	
p2	1		2		3		4		5		6		7	
		0.05277		0.11927		0.11927		0.105536		0.11927		0.11927		0.052768
p1		0.03108		0.08548		0.085476		0.062165		0.085476		0.062165		0.031082

Legend			Density(Kg/m3
▭	CFS purlins		7850
⬛	CFS Rafter		7850
╱	PRIMAflex cement board		1390
🟧	Bricks		
⟷	load path of cladding onto purlins		

View

elevation

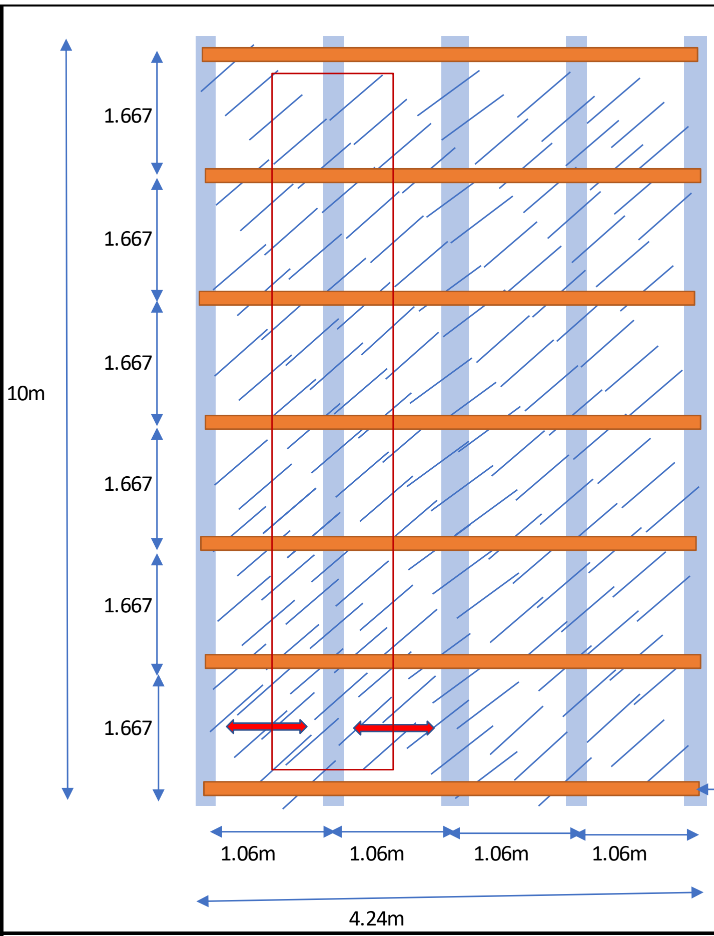

20 bricks, 1 brick 2kg

Front

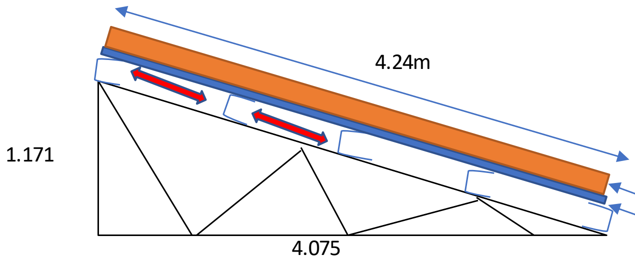

Brick UDL 0.092547 KN/m
20 bricks, 1 brick 2kg
4.5mm thick Primaflex

Dead load on mid truss

		p 1	p 2	p 3	p 4	p 5
Brick load KN		0.0385533	0.112128	0.091037	0.112128	0.038553
Purlin+cement KN		0.0621647	0.105536	0.105536	0.105536	0.062165
	Total KN	0.100718	0.217664	0.196572	0.217664	0.100718
Site	N	100.71797	217.6638	196.5723	217.6638	100.718
ABAQUS	N	81.924134	198.87	177.7785	198.87	81.92413

(excluded purlin self-weight)
Because purlins are modelled
in ABAQUS)

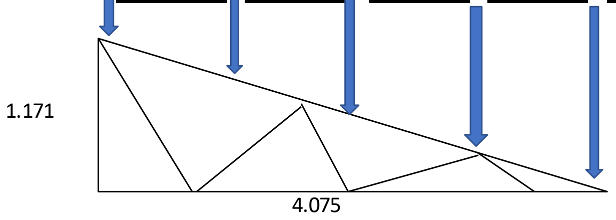

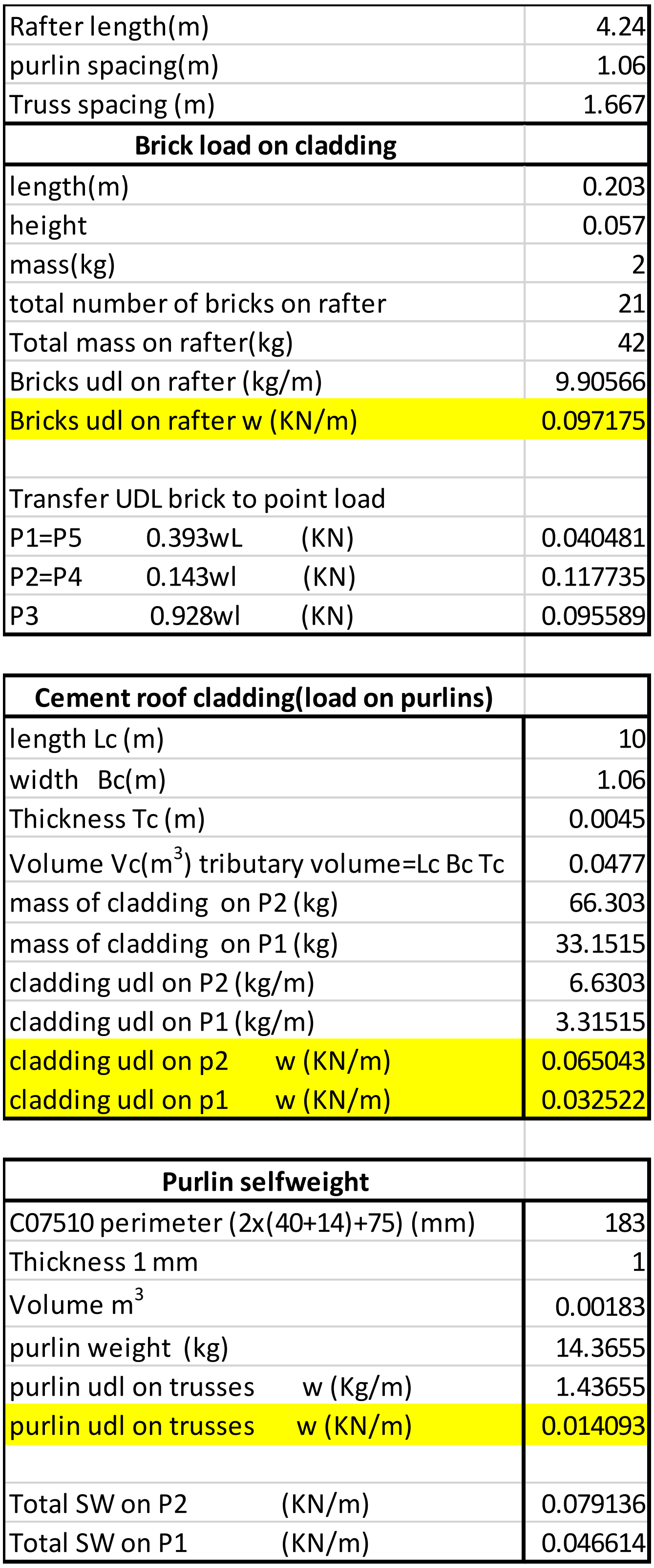

Rafter length(m)	4.24
purlin spacing(m)	1.06
Truss spacing (m)	1.667
Brick load on cladding	
length(m)	0.203
height	0.057
mass(kg)	2
total number of bricks on rafter	21
Total mass on rafter(kg)	42
Bricks udl on rafter (kg/m)	9.90566
Bricks udl on rafter w (KN/m)	0.097175
Transfer UDL brick to point load	
P1=P5 0.393wL (KN)	0.040481
P2=P4 0.143wl (KN)	0.117735
P3 0.928wl (KN)	0.095589

Cement roof cladding(load on purlins)	
length Lc (m)	10
width Bc(m)	1.06
Thickness Tc (m)	0.0045
Volume Vc(m^3) tributary volume=Lc Bc Tc	0.0477
mass of cladding on P2 (kg)	66.303
mass of cladding on P1 (kg)	33.1515
cladding udl on P2 (kg/m)	6.6303
cladding udl on P1 (kg/m)	3.31515
cladding udl on p2 w (KN/m)	0.065043
cladding udl on p1 w (KN/m)	0.032522

Purlin selfweight	
C07510 perimeter (2x(40+14)+75) (mm)	183
Thickness 1 mm	1
Volume m^3	0.00183
purlin weight (kg)	14.3655
purlin udl on trusses w (Kg/m)	1.43655
purlin udl on trusses w (KN/m)	0.014093
Total SW on P2 (KN/m)	0.079136
Total SW on P1 (KN/m)	0.046614

Appendix D: Details of Thermocouple Tree and Gypsum Board Connections

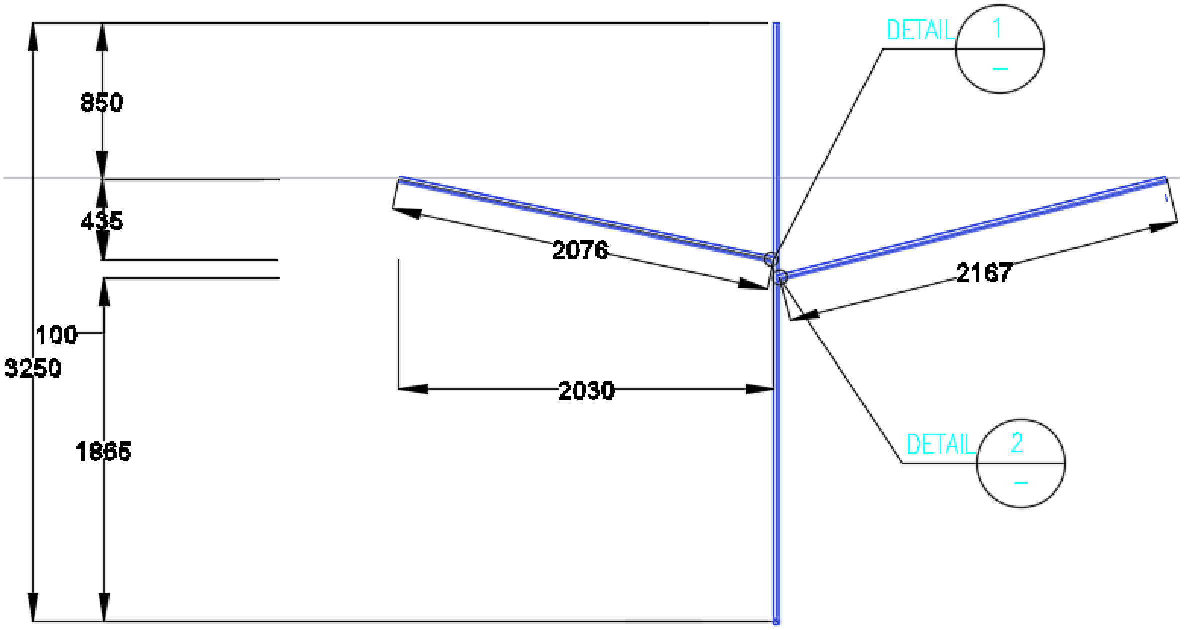

Figure D.7 Thermocouple Tree

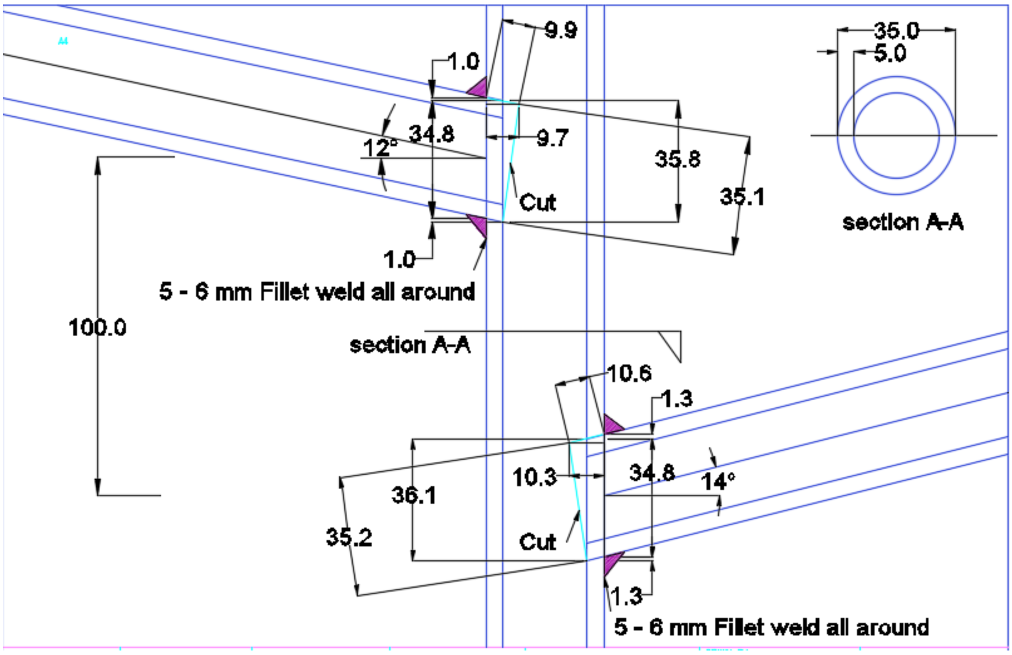

Figure D.8 Joint Details of Thermocouple Tress

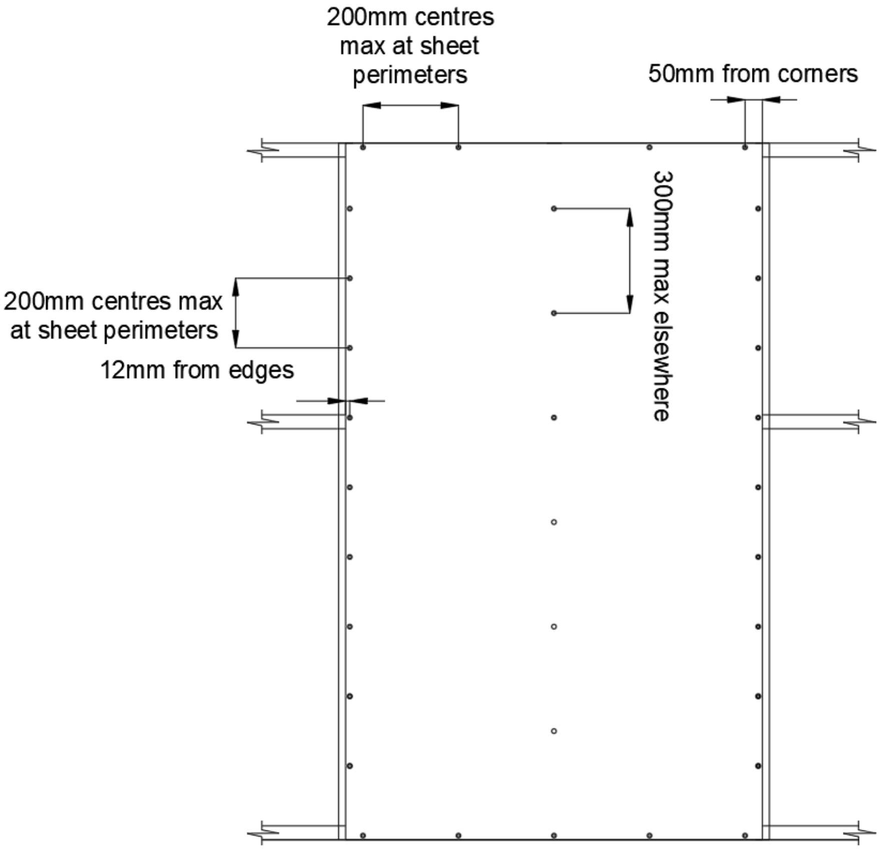

Figure D.9 Details of Gypsum Board Connections

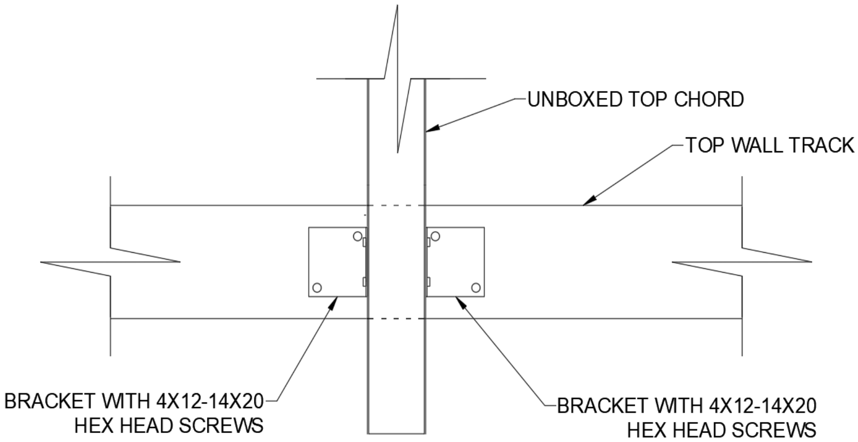

Figure D.10 Details of Eave Connection

Appendix E: Gypsum Board Small-Scale Test Observations and Results

Figure E.10 Initiation of Charring of Gypsum Board (Specimen 2)

Figure E.11 Cracks Developed on Ambient Surface of Gypsum Board(Specimen 2)

Table E3

Time (minutes)	Observations at the ambient surface of specimen 1
13	Steams are observed, this was due to dehydration of water content in gypsum board.
20	Smoke was emitted from the gypsum board, the paper on the ambient side turned dark brown.
35	Cracks developed at the centre of gypsum board
40	No visible changes after the gypsum board cracked
80	End of the test

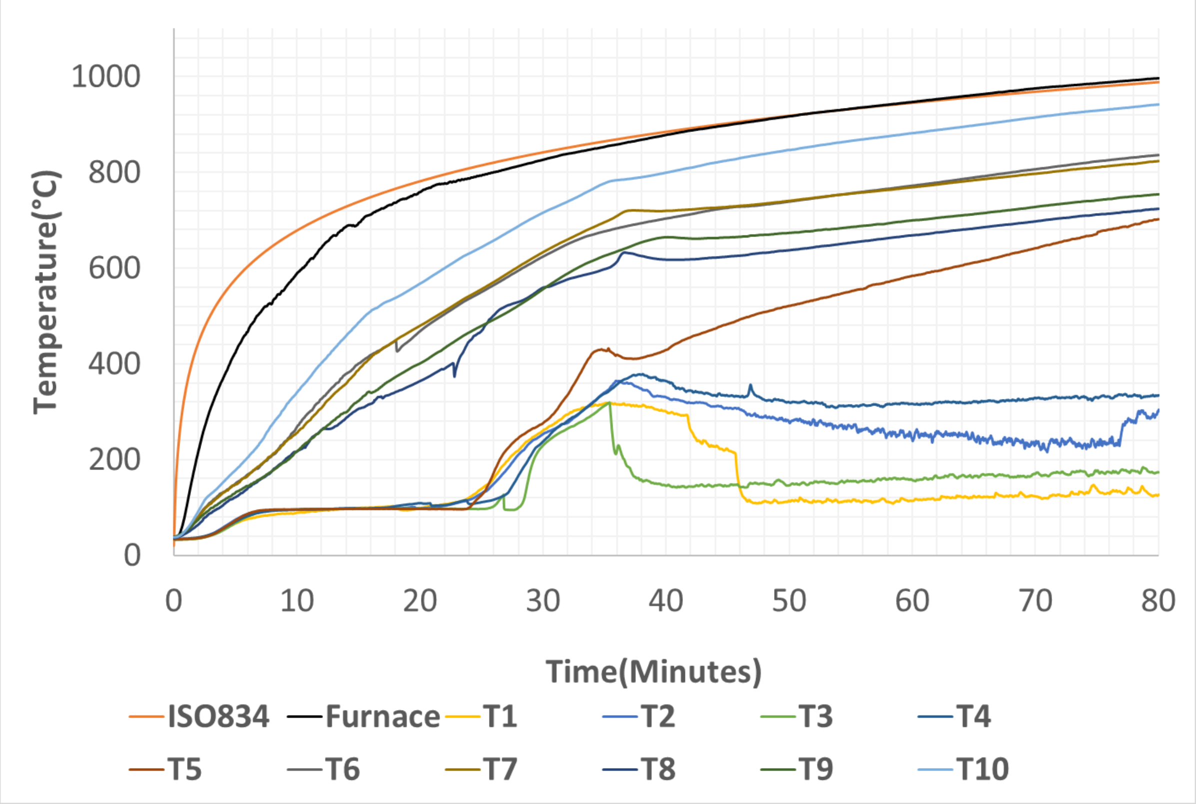

Figure E.12 Small-Scale Test Results Specimen 1

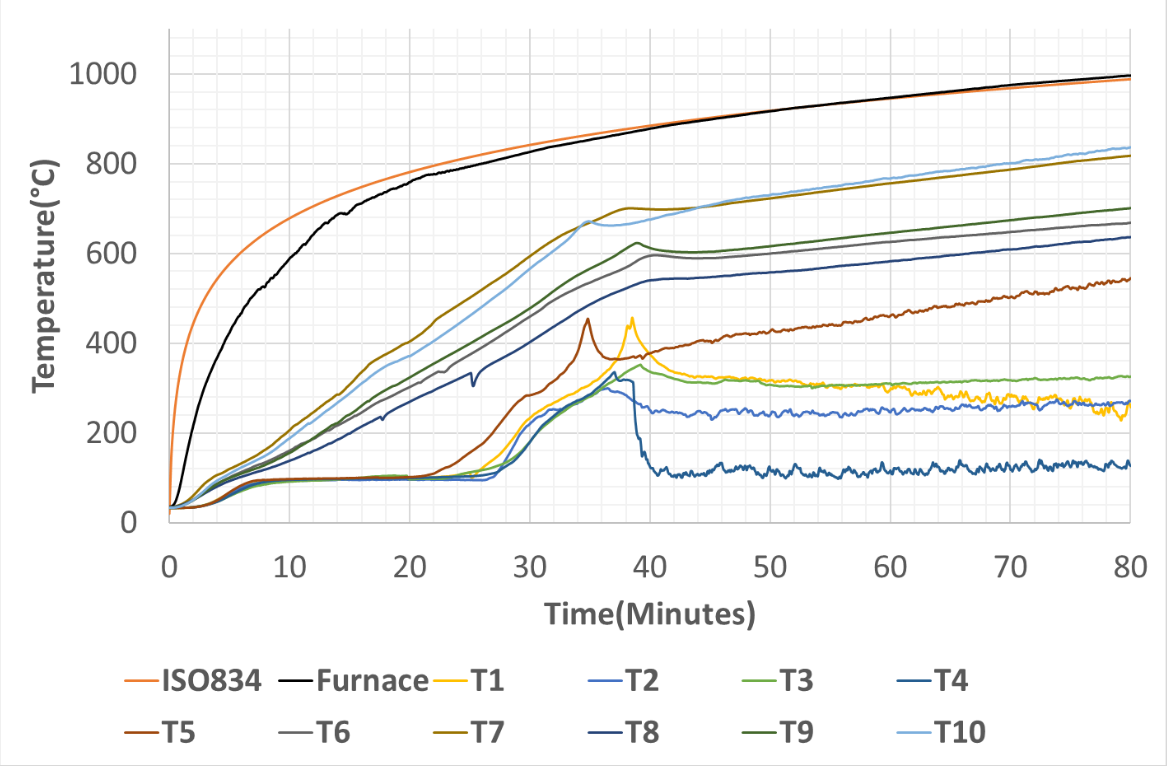

Figure E.13 Small-Scale Test Results Specimen 3

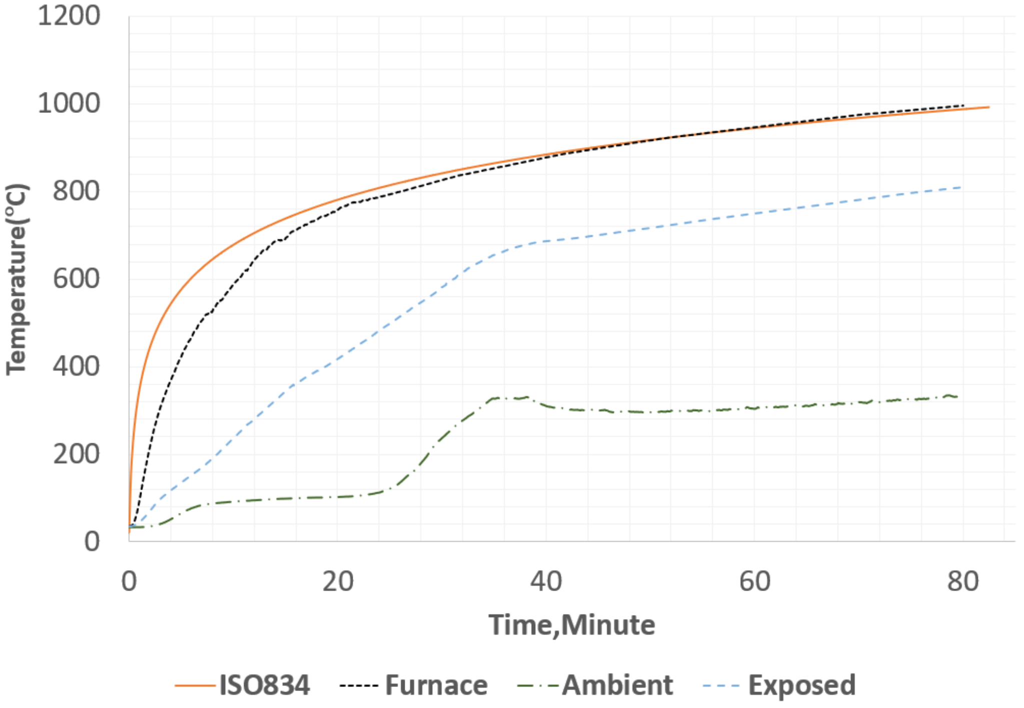

Figure E.14 Small-Scale Test Results Specimen 1 (Averaged Temperatures at Ambient Side)

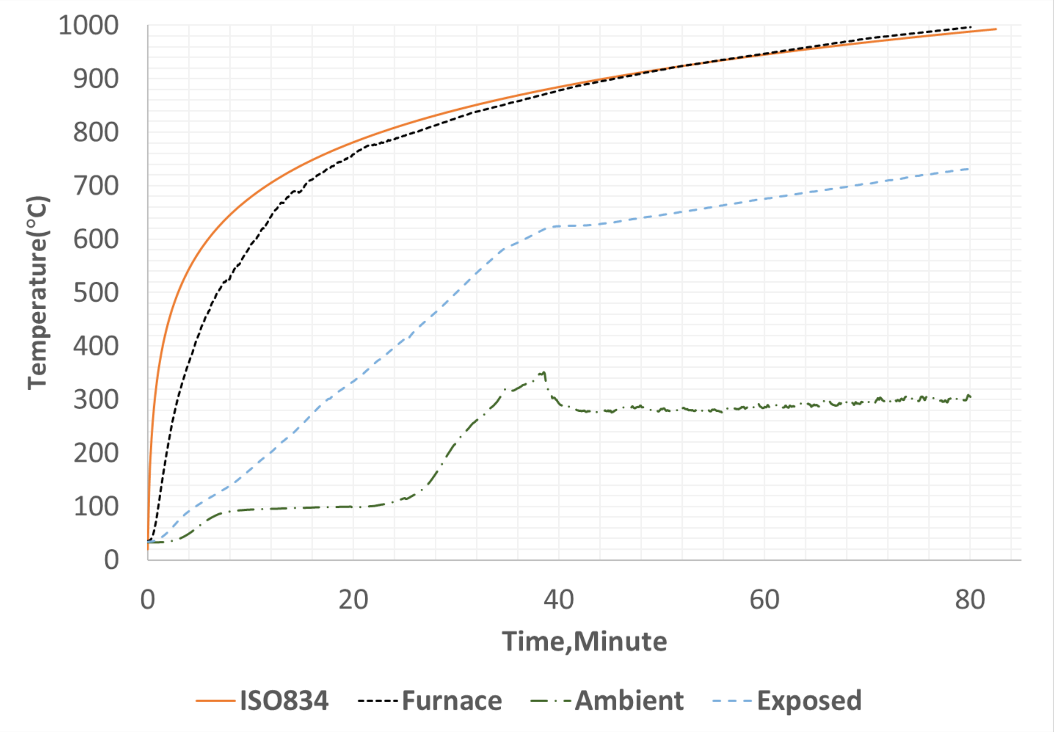

Figure E.15 Small-Scale Test Results Specimen 3(Averaged Temperatures at Ambient Side)

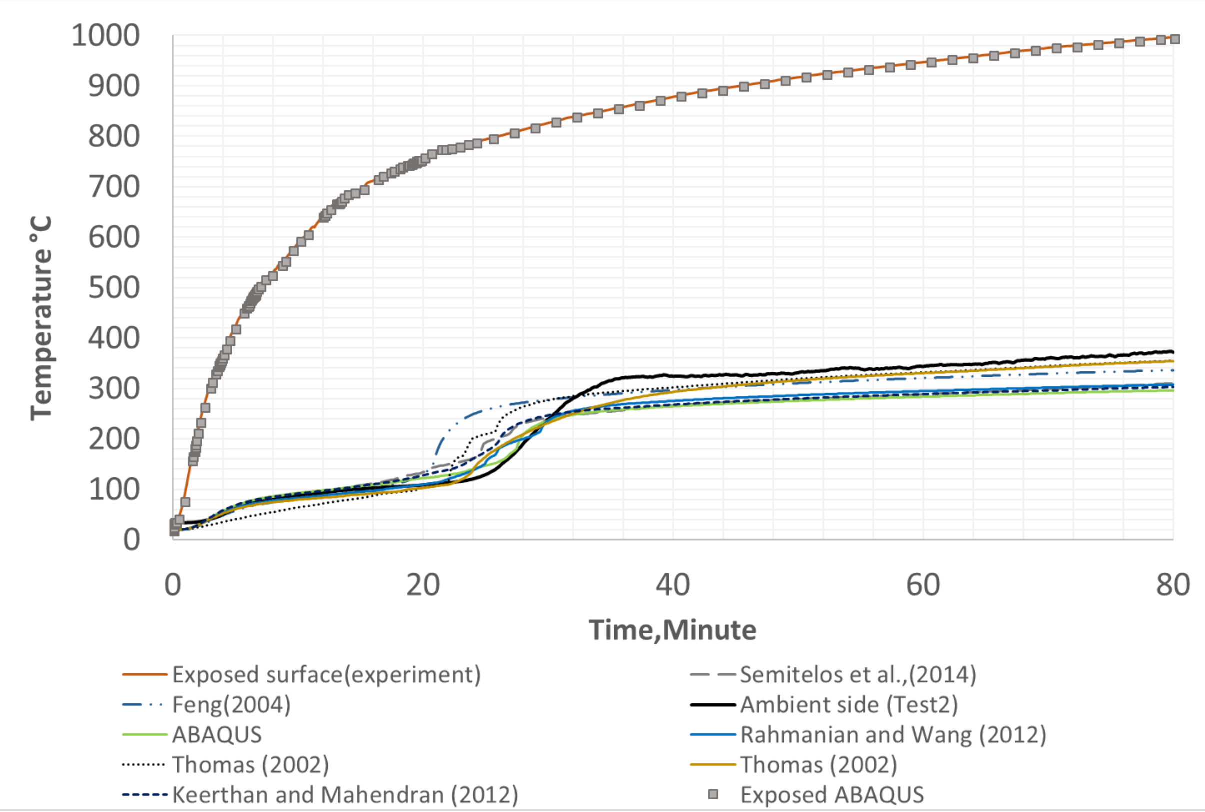

Figure E.16 Finite Element Validation for Small-Scale Fire Test Specimen 2

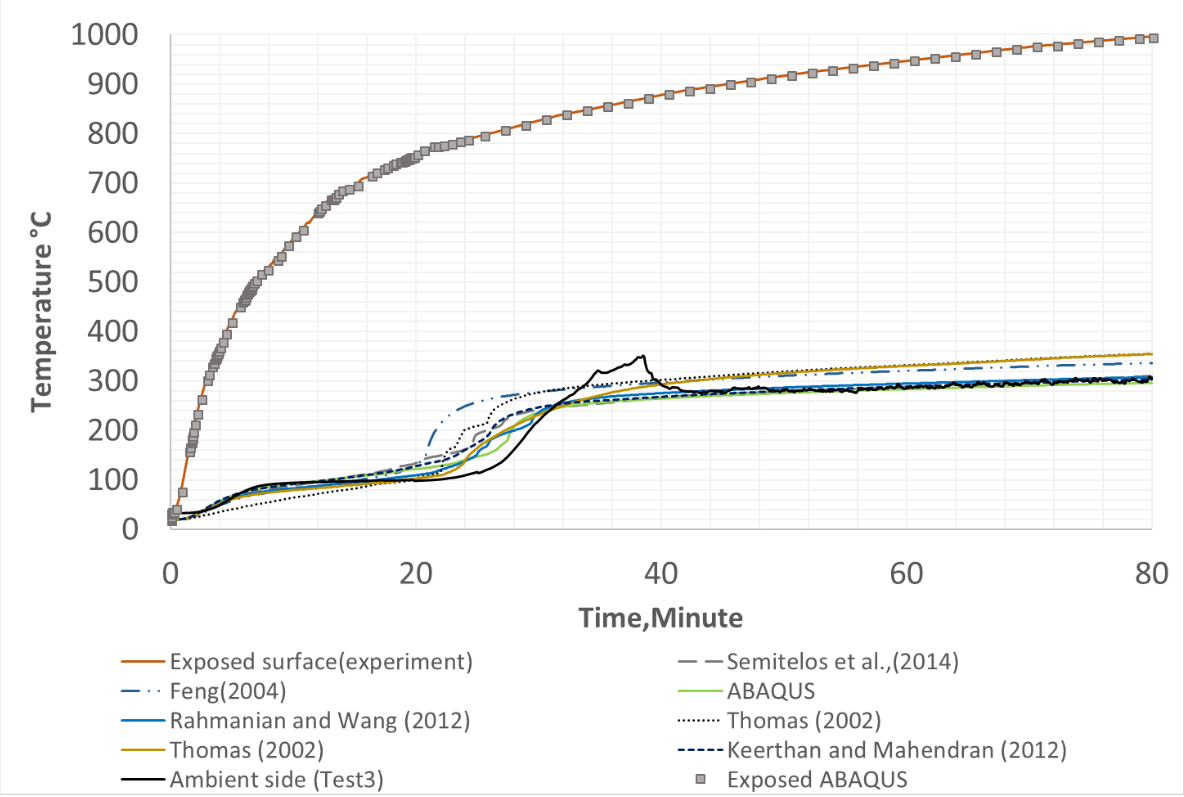

Figure E.17 Finite Element Validation for Small-Scale Fire Test Specimen 3

Appendix F: Laser Range Meter Specifications

Bosch GLM 80 Specifications

Laser Distance and Angle Measurer

GLM 80

Benefits: GLM 80 Laser Distance and Angle Measurer

- Precision Distance and Angle Measuring Technology
- Indirect Length Measurement Mode Backlit Display with Tilt Screen Technology Integrated Li-ion Battery Min./Max. Measurement Mode Multi-Surface Area Mode
- Backlit Display with Tilt Screen Technology
- Integrated Li-ion Battery
- Min./Max. Measurement Mode
- Multi-Surface Area Mode

Specifications: GLM 80 Laser Distance and Angle Measurer

Battery	3.7 Li-ion Battery
Laser Diode	Class II 630 - 670 nm
Leveling Accuracy (Vial)	+/- 0.2°
Measuring Accuracy	Typ. +/-1/16-in (1.5 mm)
Range	2-in (50 mm) to 265-ft (80 m)
Weight (oz.)	5 oz. (0.14 kg)

Includes

Li-ion Battery
Charger
Belt Pouch

FLUKE 424D Specifications

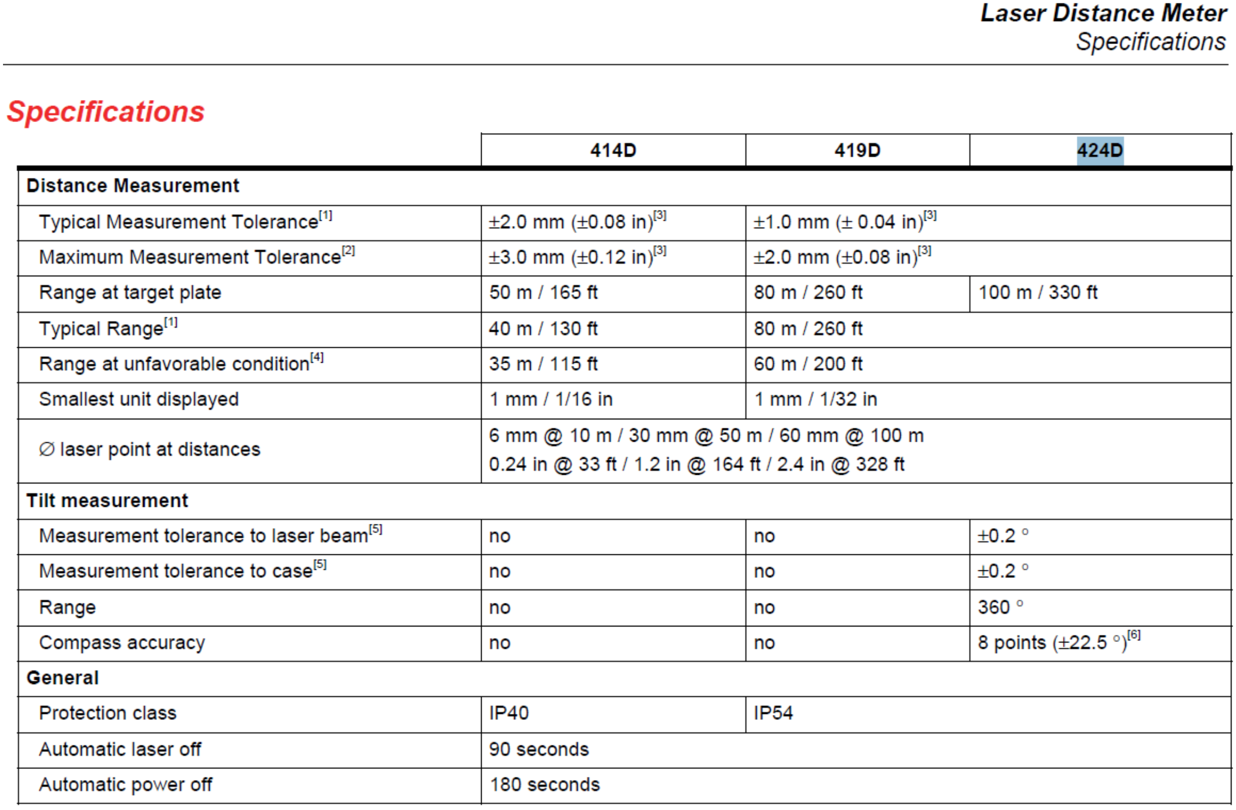

Laser Distance Meter
Specifications

Specifications

	414D	419D	424D
Distance Measurement			
Typical Measurement Tolerance[1]	±2.0 mm (±0.08 in)[3]	±1.0 mm (± 0.04 in)[3]	
Maximum Measurement Tolerance[2]	±3.0 mm (±0.12 in)[3]	±2.0 mm (±0.08 in)[3]	
Range at target plate	50 m / 165 ft	80 m / 260 ft	100 m / 330 ft
Typical Range[1]	40 m / 130 ft	80 m / 260 ft	
Range at unfavorable condition[4]	35 m / 115 ft	60 m / 200 ft	
Smallest unit displayed	1 mm / 1/16 in	1 mm / 1/32 in	
∅ laser point at distances	6 mm @ 10 m / 30 mm @ 50 m / 60 mm @ 100 m 0.24 in @ 33 ft / 1.2 in @ 164 ft / 2.4 in @ 328 ft		
Tilt measurement			
Measurement tolerance to laser beam[5]	no	no	±0.2 °
Measurement tolerance to case[5]	no	no	±0.2 °
Range	no	no	360 °
Compass accuracy	no	no	8 points (±22.5 °)[6]
General			
Protection class	IP40	IP54	
Automatic laser off	90 seconds		
Automatic power off	180 seconds		